DESIGN AND DEVELOPMENT OF A MULTIFUNCTIONAL COMPOSITE RADIATION SHIELD FOR SPACE APPLICATIONS

By

ADEBAYO EMMANUEL

A Thesis submitted to the Faculty of Graduate Studies of the University of Manitoba in partial fulfillment of the requirements of the degree of

DOCTOR OF PHILOSOPHY

Department of Mechanical Engineering
University of Manitoba
Winnipeg, Manitoba, Canada

ABSTRACT

A Canadian Polar and Communication (PCW) satellite mission has been proposed by the Canadian Space Agency (CSA) in conjunction with the other departmental agencies and industrial partners. PCW mission will provide essential communications and meteorological services to the Canadian Arctic, as well as space weather observations of ionizing radiation along the orbit. The CSA has identified three potential Highly Elliptical Orbits (HEOs) for a PCW satellite constellation. One of which is Molniya orbit, which provides good satellite coverage and high orbital stability at reasonable altitude. But owing to low apogee of Molniya orbit, its trajectory passes through high radiation Van Allen belts subjecting the satellites in such orbit to highly energetic radiation particles requiring radiation shields to protect the satellite electronics and space bus. The commonly used aluminium alloy - based shield would be heavy and costly for the satellite mission and a lighter alternative material has not been developed in the past. Hence, the objective of this thesis is to develop a multifunctional hybrid composite shield that is lighter than aluminium and meets the mission requirements on radiation shielding and mechanical properties. Using MULASSIS, a particle transport code within European Space Agency's SPENVIS, and the TID (Total Ionization Dose) transmitted through, and absorbed by a radiation shield, for a 15-year mission in Molniya, was predicted as a function of its areal weight. Using a design approach involving methodical study of homogeneous materials and polymer composite materials made up of two or more materials, and hybrid composite made up of composites and homogeneous materials, hybrid composite compositions that meet the radiation requirements were identified. Using lamination theory, the mechanical properties of these compositions were predicted and compared with the properties of the currently used Al 6061 alloy to choose the composition of the

multifunctional hybrid composite that is lighter than Al by 13%. A two-step manufacturing cycle was developed to manufacture this composite. Using proton beam at TRIUMF (UBC Campus, BC) and the electron beam at Acsion Inc. (Pinawa, MB), the TID under electrons and t_{WET} (equivalent to TID) under protons were measured for the three constituents (Al, PFC, and CFC) of the hybrid composite. These correlates very well (within 6% for protons and 2% for electrons for shields with thickness < 6.4 mm) with predictions validating the MULASSIS. These experimental results also demonstrate that the hybrid composite was lighter than Al shield by a maximum of ~19.4% under protons and by ~5.6% under electrons. Experimentally measured mechanical properties of the hybrid composite demonstrate that while some properties are comparable or better than Al 6061, others could be improved through appropriate choice of another carbon fiber composite constituent. In summary, the multifunctional hybrid composite that is lighter than Al, that meets both radiation and structural requirements, has been designed and the design has been experimentally validated.

ACKNOWLEDGMENT

I would like to express my sincere gratitude to my thesis advisor **Dr. Raghavan Jayaraman**, for his invaluable guidance, academic support and financial assistance throughout my thesis work.

I would like to thank **Magellan Aerospace** and **Canadian Space Agency** for funding this research work.

I would also thank **Mike Boskwick** and **Trevor Smith**, both of Mechanical Engineering Department, for their technical assistance during my research.

Finally, my very special thanks to **my wife**, **Jumoke**, **my family** and **friends** for their constant support and encouragement during my graduate studies.

TABLE OF CONTENTS

LIST OF FIGURES

LIST OF TABLES

ABBREVIATIONS

ASP	Aluminum Sandwich Panel
ATOX	Atomic Oxygen
CFC	Carbon Fiber Composite
CME	Coronal Mass Ejections
CSA	Canadian Space Agency
DFC	Hybrid Face Sheet
DSP	Hybrid Sandwich Panel
ESD	Electro-Static Discharge
GCR	Galactic Cosmic Radiation
GEO	Geo-stationary Earth Orbit
GPS	Global Positioning System
GSO	Geo-Synchronous Orbit
HEO	Highly Elliptical Orbit
ISS	International Space Station
JPL	Jet Propulsion Laboratory
LEO	Low Earth Orbit

LET	Linear Energy Transfer
MEO	Medium Earth Orbit
MMOD	Micrometeoroids and Orbital Debris
MULASSIS	Multilayered Shielding Simulation Software Tool
NIEL	Non-Ionizing Radiation Energy Loss
PCW	Polar Communications and Weather Satellite
PFC	Polyethylene Fiber Composite
RAD	Radiation Absorbed Dose
RDM	Radiation Design Margin
SEU	Single Event Upset
SPE	Solar Particle Event
SPENVIS	Space ENVironment Information System
TAP	Three Apogee orbit
TID	Total Ionizing Radiation
$TID_{Absorbed}$	Absorbed TID within shield
$TID_{Critical,\ Transmitted}$	Critical transmitted Absorbed TID within shield
$TID_{Critical,\ Transmitted}$	Critical transmitted TID through shield

$TID_{Transmitted}$	Transmitted TID through shield
UHMWPE	Ultra-High Molecular Weight Polyethylene

CHAPTER ONE

INTRODUCTION

1.1 Space Environment

Satellite technologies have re-defined many aspects of human endeavours, such as reliable communication services, global weather monitoring, air and land navigation, security and defence, space exploration, remote sensing, and technological advancements. Communication satellites provide easy access to telecommunication and internet services all over the globe. Thanks to the Broadcast satellites that are encircling our world, we are able to watch thousands of TV stations streaming contents via satellite. Satellite systems such as the Global Positioning System (GPS) enable air and maritime navigation easier and these days even cars and mobile devices make use of GPS for maps, assistance with driving, etc. In addition, remote-sensing satellites are used for meteorology services, allowing accurate weather forecasting and predicting of natural disasters like hurricanes and cyclones.

Space, in which these satellites operate, is a dynamic and complex environment filled with various types of hazards:

- Harsh radiation environment, consisting of trapped charged protons and electrons, solar protons, galactic cosmic radiation (GCR), neutrons, that can cause satellite electronics (bus and payload) to fail or malfunction.
- Micrometeoroids and orbital debris (MMOD) that can cause severe impact damage and destruction of satellite components

- Very high vacuum (10^{-6} to 10^{-9} torr) that can cause outgassing of organic materials used in satellites and deposition as a thin contaminant layer on critical optical components impairing the performance of the latter
- Extreme thermal cycling, when a satellite switches, a number of times a day, between the Earth shadow region (cold temperature of -150°C during solar eclipse) to direct sunlight region (hot temperature of +150°C during Sun illumination) [1], that cause thermal fatigue and failure of satellite components
- Atomic oxygen (ATOX) at low Earth orbits that can erode a material and impair its integrity
- Electric and magnetic fields, which along with interaction with radiation can cause surface and internal charging of materials, resulting in dangerous discharge (arching) damaging the satellite electronics.

These hazards can result in loss of performance or satellite itself. Satellites, operating in LEO (Low Earth Orbits) and GEO (Geo-stationary Earth Orbit), employ a variety of strategies to mitigate these hazards at minimal weight. Satellites are not as common in HEO (Highly Elliptical Orbits) [2] and hence, studies on hazard mitigation strategies for this orbit are rare. Satellite in HEO is the focus of this study.

The type and the level of radiation in the environment outside the Earth's atmosphere, in which most satellites and ISS (International Space Station) operate, depend on the orbit and mission duration of the satellite. The extremely harsh radiation environment in space can destroy (or reduce the life-time of) the on-board microelectronics of the satellite`s payload and space bus. Currently, radiation hardened (rad-hard) materials are used in developing these payloads. That is,

space bound electronic components and systems are rated to withstand the radiation below a critical level, which is typically expressed as the critical level of TID (Total Ionization Dose) deposited on the electronics components during the mission duration. Dose is the measure of energy and expressed in units of krad or kGy (Gy is "Gray", 100 rad = 1 Gy).

The total dose deposited on the satellite electronics during a mission would be hundreds to thousands of times higher than the critical TID that the satellite electronics can withstand [3, 4]. Currently, the cumulative dose incident on the satellite electronics during the mission is reduced to the dose less than the critical level by packaging them in an enclosure constructed with panels (referred in this thesis as radiation shield or shield) manufactured using radiation shielding material.

Furthermore, the shielding material should ideally meet other functional property requirements to mitigate the other space hazards identified above, such as negligible outgassing, resistance to oxidation due to atomic oxygen (ATOX), high thermal conductivity to dissipate away heat generated by satellite electronics as well as solar heat, high electrical conductivity to avoid internal charging and discharging though arcing, low thermal expansion coefficient to reduce the thermal stresses due to extreme thermal cycling and resistance to impact damage due to orbital debris. Additionally, it may be required to have sufficient mechanical properties if it also serves the structural function. Therefore, a satellite shielding material with multifunctional properties, minimal weight and reasonable cost is desired.

Traditionally, aluminum has been the de facto material used in space applications, meeting both the radiation shielding and the structural functional requirements [3–5]. In many satellites, polymer composites have replaced aluminum only to serve the structural function, but not the

radiation shielding function. Polymer composites offer weight savings over aluminum due to their high specific properties (property divided by its density). Launch cost increases exponentially with weight and hence, reducing the structural weight has been the main factor driving the use of composites in space applications.

1.2 PCW mission in HEO and its relevance to this Thesis

This study has been initiated to support the current need to provide satellite coverage to Canadian Arctic region. Canadian Arctic represents the large percentage of total Canadian landmass and is generating immense interest due to its vast resources, rapid change in climatic conditions and territorial integrity of Canadian borders [6, 7]. Hence, the Canadian Space Agency (CSA), in conjunction with the Department of Defence (DOD), the Environment Canada (EC) and other government and industrial partners, has proposed the Polar Communications and Weather (PCW) satellite mission. The objective of this mission is to provide continuous satellite communication services throughout the Canadian Arctic region, weather monitoring and meteorological Earth observation, air and marine navigation, Arctic science, and support efforts to maintain the security and the territorial integrity of the Canadian border [6–8].

The mission has planned to use a 2-satellite constellation in a Highly Elliptical Orbit (HEO) to provide the required continuous coverage of the Canadian Arctic region as illustrated in Figure 1.1.

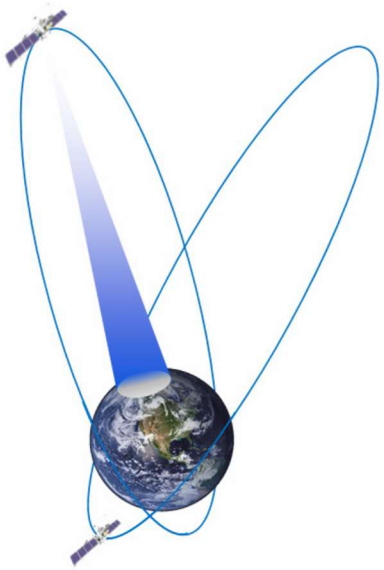

Figure 1.1: Two satellite constellation for continuous coverage of Canadian Arctic region [8]

A HEO satellite is preferable to a geo-synchronous (GSO) satellite since the latter lacks the capacity for continuous coverage of the polar region above 60°N latitude from its orbital plane. Low Earth Orbit (LEO) satellites would require 23 and 32 satellites to observe the Arctic in 15 and 10 minutes intervals respectively [6] and hence, is not preferred over HEO satellites.

The CSA has currently identified [8, 9] three highly elliptical orbits (HEOs) for the PCW mission, namely a 12-hr Molniya orbit, a 16-hr Triple Apogee and a 24-hr Modified Tundra, which are based on studies by Trishchenko et al. [6, 10]. An illustration of these orbits is shown in Figure 1.2 and the orbital parameters are tabulated in Table 1.1.

While Molniya orbit offers superior imaging due to lower apogee altitude and high stability [6], it passes through Van Allen radiation belts, during each perigee pass, that would expose the satellite to trapped particles of highly energetic electrons and protons, Galactic Cosmic Rays (GCRs), and solar energetic particles. The radiation levels are substantially higher than that experienced in LEO and GEO orbits, hence previous mission in Molniya orbit (Russian satellites) has been limited to 2-4 years [2, 11]. The envisaged mission duration for PCW missions is 15 years. Hence, the thickness of aluminium shields in Molniya orbits would be substantially higher than that used in LEO or GEO orbits, resulting in higher launch and mission cost. Therefore, the modified Tundra has been proposed as an alternative. Due to the higher perigee, this orbit avoids the inner Van Allen belt, thus providing the satellite with excellent longevity of 24-hour orbital period. However, due to higher apogee altitude, imaging is relatively poorer than the Molniya orbit. Hence, a compromise orbit, namely TAP (Three Apogee) has been suggested. However, it is less optimal than Molniya.

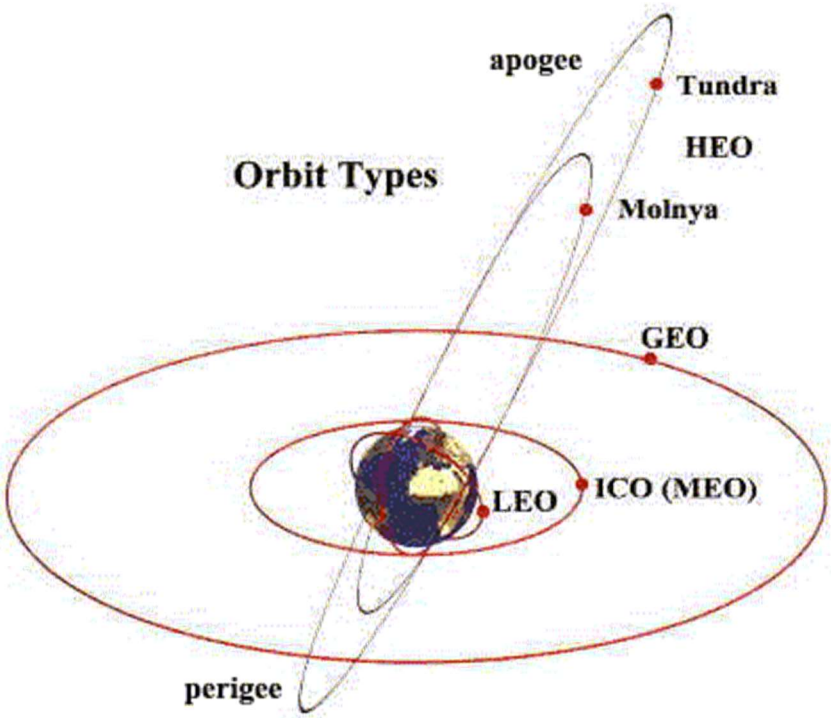

Figure 1.2: Schematic of HEO orbits relative to LEO, MEO and GEO

[http://sattracker.mrtian.com/aeimages/orbtypesr.gif].

Table 1.1 : Orbital properties for three HEOs identified for PCW Mission [10]

	Period	Perigee Altitude (km)	Apogee Altitude (km)	Inclination angle í (°)	Eccentricity
Molniya	12 hrs	500	39850	63.4	0.74
TAP	16 hrs	8100	43493	63.4 – 70	0.55
Mod. Tundra	24 hrs	23144	48442	90	0.3

Although Molniya is the best orbit for PCW mission, the aluminium shields will be much heavier than that needed for the TAP or Modified Tundra orbits. Hence, an alternate material is required if Molniya has to be used for the PCW mission. NASA researchers have developed several shielding concepts (e.g. regolith) for interplanetary missions [12]. Recent studies have shown that lightweight multilayer hybrid composite consisting ceramic and polymer composite is effective in shielding against radiation while offering protection during re-entering of space vehicles [12, 13]. However, there are no published studies on the design of multifunctional radiation shields for HEO orbits. Hence, further study is required in developing an appropriate multi-functional radiation shielding for the PCW mission.

Despite its good structural properties, aluminium is marginally effective at shielding of electrons, since it has a lower electron density. Also, in radiation environments such as the one observed in Molniya, the chances of generating secondary radiation particles by metallic shield materials increases with increase in atomic number (Z) [14]. Thus, aluminum and other metal shields can themselves turn lethal when hit by heavy energetic radiation particles. In contrast, low Z materials such as polymers and carbon fibers found in polymeric composites are better than Al in shielding against protons, although they are not as effective as aluminum in shielding against electrons. Moreover, the risk of production of secondary electrons is less due to their lower Z. However, low Z materials may have poor mechanical properties. Hence, a hybrid material is required.

1.3 Thesis Goal and Scope

Hence, the overall goal of this thesis is to design and develop a multifunctional hybrid composite shielding that meets the PCW mission requirements of radiation shielding, mechanical properties, and functional properties such as electrical conductivity and resistance to thermal cycling. Resistance to outgassing would be met by appropriate selection of shielding material. Other hazards such as orbital debris impact and ATOX are not the focus of this study.

Although this study would be focusing on Molniya orbit, the results of this study would be applicable for other missions beyond this orbit such as deep space and inter-planetary missions. In addition, the study would contribute to the body of knowledge with detailed information and step by step approach in designing radiation shields for HEO satellites. This is a critical knowledge gap that this study set out to address.

The envisaged outcomes of this research are (i) design and development of a multifunctional shield for Molniya orbit and PCW mission, (ii) development of new knowledge in the area of design of multifunctional radiation shield for missions beyond LEOs, and (iii) development of new knowledge in the area of manufacturing of these shields.

1.4 Thesis Organization

This thesis is organized as follows:

Chapter 2 provides an overview of radiation environment encountered by satellites in space including a discussion on the components of this radiation environment and their sources. A detailed review of application of composites in space and radiation damage effects applicable to

satellite composite shield structure is presented. Based on the literature review, knowledge gaps are identified in support of the three thesis objectives presented at the end of this chapter.

In Chapter 3, the design of multi-functional hybrid composite radiation shield is presented.

Chapter 4 presents details on materials selection and manufacturing of the hybrid composite shield designed in Chapter 3. This is followed by details on radiation and mechanical tests, employed to validate the design.

In Chapter 5, Results from radiation and mechanical tests are presented and compared with the simulations presented in Chapter 3 to validate the designed multi-functional hybrid composite radiation shield.

In Chapter 6 the results are summarized and the conclusions based on the results are presented in support the thesis objectives.

A list of reference is presented at the end of this thesis.

CHAPTER TWO

LITERATURE REVIEW

The chapter is divided into four sections. Section 2.1 is dedicated to providing background information through a comprehensive review of radiation environment in space and the hazards posed by it to satellites during their mission. The review covers published literature on satellite orbits and space radiation environment, radiation – materials interactions, radiation damage and space hazards relevant to polymeric composite materials. The section 2.2 is focused on review of published literature on composite radiation shielding for application in various satellite orbits and space. The knowledge gaps, based on review in section 2.2, are identified in section 2.3.

2.1 Background Information

2.1.1 Earth Satellite Orbits

The response of material to environment in space depends on the orbit in which the material is expected to function and the type of radiation encountered in such orbit. The characteristics of the radiation environment are highly dependent on the type of mission. To effectively design a shield for satellites, the first consideration is to have knowledge of orbital parameters. Hence various satellite constellations applicable to Earth's orbit are reviewed first. The Earth satellite orbits, shown in the schematic in Figure 2.1, can be classified into the following:

- Low Earth orbit (LEO)
- Medium Earth Orbit (MEO)

- Geostationary orbit (GEO)
- Highly elliptical orbit (HEO)

(i) Low Earth Orbit (LEO): The altitude of this orbit ranges from 500 – 2000km [15]. This orbit is below the Van Allen radiation belts and mostly used by satellites. The orbital time to complete a cycle period varies between ninety minutes and two hours. Most radiation effects in LEO are caused by trapped protons from the inner Van Allen radiation belt. In addition, satellites in LEO are also exposed to a mixture of electrons, galactic cosmic radiation (GCR), and secondary radiation products produced by collision of the primary radiation particles (electrons and protons). GCR and SPE (Solar Particle Event) at LEO depend on the inclination of the spacecraft's orbit. An increase in the angle of inclination results in increase in GCR and SPE exposure. Surface charging and deep dielectric charging are not hazards for satellites in LEO regions. Satellites pass in and out of the trapped electron regions of the Van Allen Belt too quick for charge accumulation to be effective. High concentration of atomic oxygen is also present in this orbit. Atomic oxygen erodes aluminium and it interacts with polymers causing the surface to convert to volatile oxidation products [16].

(ii) Medium Earth Orbit (MEO): Also known as Intermediate Circular Orbits (ICO), MEO is a circular orbit located at an altitude in the range of 10, 000 – 20,600 km, between the Van Allen belts. It is above inner Van Allen belt and below outer Van Allen belt. Satellites in this orbit are affected by radiation from the inner belt during launching; therefore, the fluence of proton is higher than that in LEO and GEO. Cosmic radiation is lower in this orbit leading to

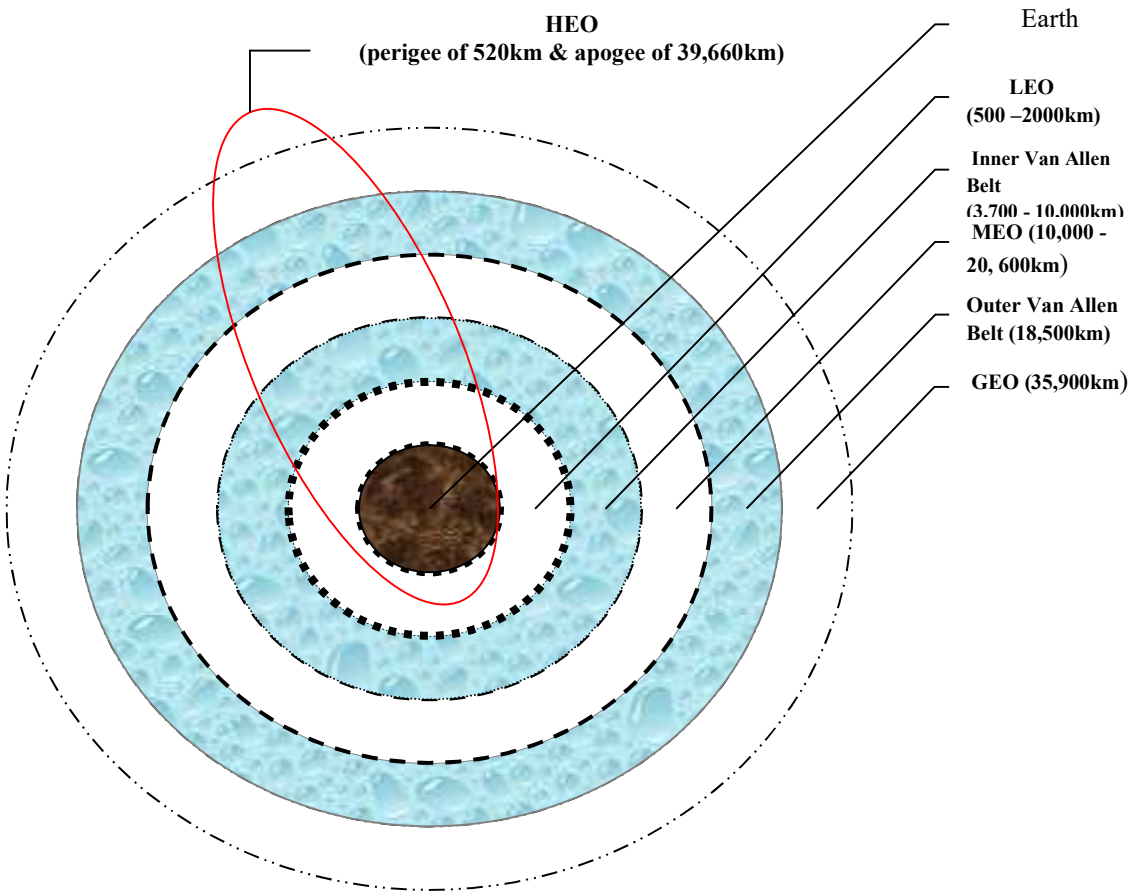

Figure 2.1: Schematic Diagram of Earth's Satellite Orbits

longer life expectancy [11]. Radiation in this orbit varies by several orders of magnitude due to changes in the magnetosphere induced by solar and magnetic storms.

(iii) Geostationary orbit (GEO) or Geosynchronous Orbit (GSO): The radius of the orbit is typically 35,753 km and it is beyond the Van Allen radiation Belts. The satellite's orbital plane is very close to the equatorial plane of the Earth thus the inclination is near zero. The orbit is as circular as possible, and eccentricity is almost zero. Electron concentration in outer Van Allen belt dominates the radiation exposure in GEO orbit. Although beyond peak particle level of the outer belt, the satellites still encounter highly energetic electrons and ionizing effects. High levels of low energy trapped protons also occur in this orbit even though the Earth's magnetosphere offers some protection against solar proton, SPE and GCRs.

(iv) Highly Elliptical Orbit (HEO): This elliptical orbit approaches the Earth's surface within several hundred kilometres, crosses both Van Allen belts, and goes beyond GEO. It has perigee of 520 km and an Apogee of 39,660 km [2]. The orbits are inclined at 63.4^0 and owing to the high eccentricity of the orbit, a satellite in a highly elliptical orbit spends most of the time near the apogee. Examples of this orbit are Molniya and Tundra orbit. HEO satellite constellation is mainly designed to cover the area under the apogee. The drawback of this orbit is that it is energetically costly to maintain satellite in the circularization elliptical orbit and the allowable weight of the payload drastically reduced. Due to the orbital inclination of HEO, it gives better coverage far from the Earth but the satellite transverse the Van Allen radiation belts twice at each perigee pass.

The summary of the characteristics properties of Earth satellite orbits is shown in Table 2.1.

Table 2.1: Summary of Standard spacecraft orbits

Designation	Orbit	Altitude (km)	Inclination (°)	Type of Orbit
LEO	Low Earth Orbit	500 – 2000	0	Circular
MEO	Medium Earth Orbit	10000 – 20 600	0	Circular
GEO	Geostationary	35 790	0	Circular
HEO	Highly Elliptical Orbit	500 – 39 660	65	Elliptical

Note, not all orbits are included in Table 2.1. (Other example includes higher Earth orbits and polar orbit of LEO & GEO).

2.1.2 Radiation Environment in Space

Satellites operate in environmental conditions that are much different from terrestrial condition on Earth. The space environment contains many hazards to satellite operation as highlighted in Chapter 1. Chief among them is the intense radiation that is incomparable to what could be experienced within Earth atmosphere. Radiation in space is generated by particles emitted from a variety of sources both within and beyond our solar system. Radiation effects from these particles cannot only cause degradation, but can also cause failure of the electronic and electrical systems in space vehicles or satellites. Therefore, radiation is one of the important factors in space environment, that may lead to the failure of the satellite's mission.

A radiation environment specification for a mission is established wherein all types of radiation particles are considered, reflecting general and mission-specific radiation susceptibilities; this specification is then used for component selection, material selection and shielding optimisation. In designing a radiation shield structure, the choice of shielding material depends on the type of radiation to be encountered on the mission, the energy of the radiation flux and the required level of reduction in radiation when it encounters the electronics behind the shield. In the following sub-sections, types of space radiation and their sources are reviewed.

2.1.3 Sources of Radiation in Space

Satellites located in the Earth's orbit will be required to operate in the radiation environment of space and in the process, be exposed to different types and fluencies of radiation particles. Knowing the sources and types of radiations that would be encountered by the satellites is necessary for safe design and operation of the latter.

The ionizing radiations in space affecting Earth's satellites are of three distinct sources: Trapped Radiation Belts, Galactic Cosmic Rays (GCRs) and Solar Particle Events (SPE). The energy and flux of energetic particles from these sources vary with time due to variation in solar activities. Solar activities influence the Earth's magnetosphere, which directly impact these three sources of ionizing radiation.

2.1.3.1 Trapped Radiation Belts

Energetic electrons and protons are magnetically trapped within the confines of the Earth's geomagnetic field forming the radiation belts. They are often called Van Allen radiation belts, named after head of first US satellite (Explorer I) exploration that discovered the radiation regions. The Van Allen radiation belts consist of two concentric doughnut shaped regions of energetically charged particles as shown in Figure 2.2. The main source of these charged particles is from outburst of ionized plasma from the outer surface of Sun's corona.

The inner belt extends to 2.5 Earth radii (R_E = 6, 371 km) comprising of primarily energetic protons with energy ranging from 100s of MeV. Also small numbers of electrons with energy in the 10s of MeV range and ions are present in the inner belt [17, 18]. The inner belt is located at low altitude and the particles' population are fairly stable from the influence of solar activity [19].

The outer belt comprises primarily electrons with energy range of 0.1 – 7 MeV. The outer belt radiation fluctuates depending on the solar activity. Electron flux may cause problem for spacecraft depending on its altitude and orbital inclination (The angle between orbital plane and equatorial planes). The northern and southern regions where the outer radiation belt goes down to

very low altitudes, are called the polar horns and pose a possible radiation hazard to spacecraft in high-inclination orbits similar to HEO. Due to less protective coverage of the Earth's geomagnetic field, the outer Van Allen belt is more influenced by solar disturbances. These two trapped radiation belts around the Earth forms a region that is hazardous to spacecrafts.

The dense atmosphere of the Earth's surface reduces radiation experienced by satellites in Low Earth Orbit (LEO) but due to tilt of the Earth's magnetic pole from the geographic pole and the displacement of the magnetic field from the centre, there is a region in the South Atlantic where the trapped proton radiation increases. This anomaly is known as the South Atlantic Anomaly or Brazilian Anomaly and it dominates the radiation received in LEO and high-inclination orbits [18, 20].

The flux and energy of inner trapped proton belt and outer trapped electron belt are usually predicted using NASA's AP8 and AE8 models [21, 22] accessible online via European Space Agency (ESA) Space ENVironment Information System (SPENVIS). Both have two versions namely AP8MIN / AE8MIN and AP8MAX / AE8MAX. The minimum (MIN) corresponds to data during solar minimum while the maximum (MAX) relates to data during solar maximum. These models are the standard models used in modeling trapped radiation belts based on measurements by several spacecraft during 1960 -70s. Current versions of AE9 and AE9 are presently available within SPENVIS (SPace ENVironment Information System) for evaluation purpose.

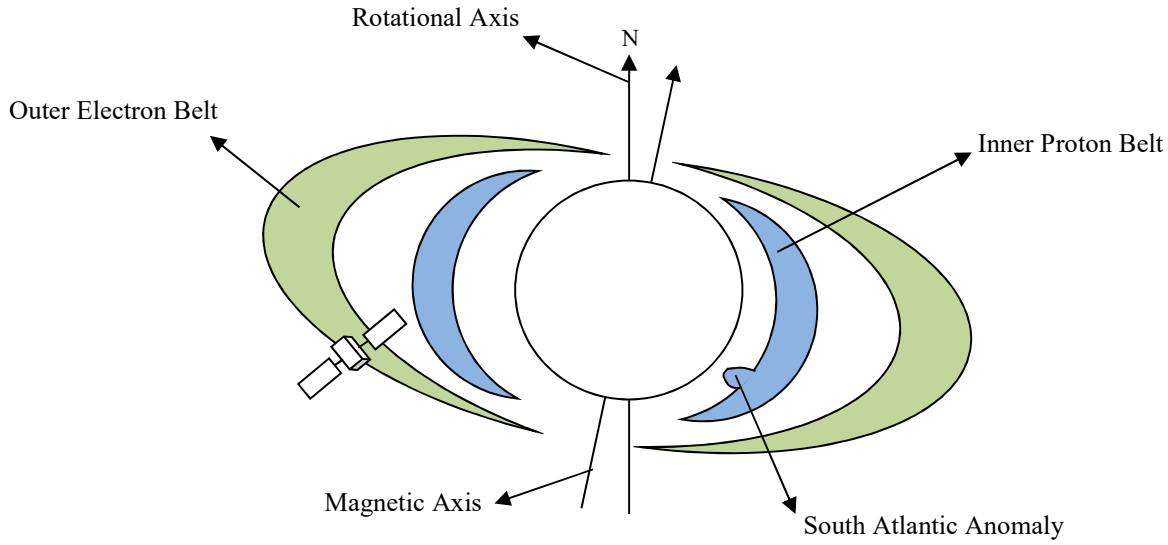

Figure 2.2: Trapped Van Allen radiation belts. (The inner belt consists of mostly protons, whereas the outer belt consists of electrons - Adapted from [23]).

2.1.3.2 Solar Particle Events

Solar Particle Events (SPEs) are high-energy particles that are encountered in interplanetary space and close to the Earth. SPEs are the result of acceleration of energetic particles in the Sun's outer layers. These particles are transported to the Earth under influence of the solar wind. The frequency of SPE is governed by the Sun during the solar activities such as solar flares and coronal mass ejection. Solar flares are made up of high speed solar protons emitted by the Sun and are probably the most potent of the radiation hazard to space satellites [24]. Due to their high energies (from a few tens of keV to GeV ranges with the fastest particles reaching relativistic speeds), they are difficult to shield and endanger life of electronics in outer space. Coronal mass ejections (CME) consist of a cloud of charged particles and plasma arising from the Sun's surface. It is composed of mainly of protons, alpha particles and heavy ions. When a solar flare or a coronal mass ejection occurs, large amounts of high-energy protons are released, often in the direction of the Earth. These high energy protons reach the Earth's poles and high latitude in a matter of minutes or hours often leaving little time to prepare for their arrival. Solar particle events are relatively rare and occur most often during the solar maximum phase of 11-years solar cycle. The Sun has an 11-year cycle, which culminates in a dramatic increase in the number and intensity of solar flares, especially during periods when there are numerous sunspots.

The Earth's geomagnetic field decreases the probability of solar particles to penetrate to Earth's satellites orbit altitudes, especially at lower latitudes, thus offering some protection from SPE particles as well as GCRs. SPE will pose serious hazards to space flight most especially for flight outside the Earth's orbit [25]. Some of the models in predicting long term solar proton fluencies are King [26] and JPL-91 [27] and ESP [28, 29] models.

2.1.3.3 Galactic Cosmic Rays (GCRs)

Galactic Cosmic Rays, (GCRs) are high-energy charged particles that originate from beyond our solar system. They are thought to enter the solar system from distant parts of the galaxy, primarily from exploding stars. They are composed of protons, electrons, and fully ionized nuclei. Main fluence composition is around 87% protons, 12% alpha particles and remaining 1% heavy ions of charge elements from ^{3}Li – ^{92}U [20]. There is a continuous and isotropic flux of Galactic Cosmic Ray (GCR) ions. The intensity of GCRs decreases monotonically as the energy increases. Although the flux is low, GCRs include energetic heavy ions, typically referred to as HZE particles, which can deposit significant amounts of energy in sensitive volumes and so cause problems to spacecraft electronics and humans in space. The GCR energy spectrum ranges from 10^{3} – 10^{12} MeV and peaked around 1 GeV within the solar system [30]. Shielding GCR with high Z absorber leads to production of secondary particles radiation [17]. The presence of Earth geomagnetic field largely deflects most charged GCR particles and provides up to certain protection to Earth`s orbiting satellites. The significant of GCR on the radiation contribution to this mission is greatly reduced by the Earth`s geomagnetic field. Commonly used models for predicting GCRs include Nymmik model (also known as CREME96) [31] and ISO-15390 model [32]. The summary of different radiation sources experienced in space flight is given in Table 2.2

Table 2.2: Sources of radiation encountered in space. Data sourced from ECSS-E-ST-10-04C [17] and Battiston et. al. [33]

Radiation Sources		Composition	Energy Range
Trapped Radiation Particle Belts	Inner belt	Mainly high energy protons and few electrons and ions	0.1 – 400 MeV
	Outer Belt	Mainly electrons	0.1 – 7 (MeV)
Solar Particle Events (SPE)		Transient bust of low to medium protons and alpha particles	Few MeV - 100s of MeV
Galactic Cosmic Rays, (GCRs)		High energy protons, alpha particles and heavy nuclei	10 MeV 10^{19} GeV/nuc

2.1.4 Radiation Damage to Satellite Payload

The presence of highly energetic particle radiations in space posses risks to critical satellite payload and microelectronics on-board the space bus. Radiation effects from these particles not only cause permanent damage but can also cause operational failure in electronic and electrical systems in space vehicles and other satellites components. Examples of such failure includes: catastrophic device failure, reduction in output power of solar arrays, noise generation in photonic and electro-optic integrated circuits such as charge-coupled devices (CCDs) and opto-isolators. There are three major types of radiation effects that are of concern to space electronics explained by Johnson et al. [25].

(A) Total Dose Effects

The result from the interaction of ionizing radiation with device materials, generating charges or charged centre, which can influence the functioning of the electronic devices. These effects depend upon the total ionizing dose (TID) absorbed in the material. This cumulative long term ionizing damage is mainly due to trapped protons and trapped electrons in Van Allen radiation belts. The absorption of TID creates electron-hole pairs in dielectric materials (e.g. silicon or silicon dioxide). The electrons have higher mobility than the holes and are rapidly swept out of the oxide layer. The holes which are much less mobile are trapped within the dielectric and at Si/SiO_2 interface. The trapped holes and interface defects created results into leakage currents, loss of noise immunity and eventual functional device failure [12, 24, 34]. Total ionizing radiation can also produce changes in material properties such as discolouration of solar panel cover glasses and

embrittlement of polymer materials. In this thesis, one objective is to reduce the ionizing dose deposited in satellite microelectronic payload below radiation design margin (RDM).

(B) Displacement Damage (Non-Ionizing Energy Loss- NIEL)

Energetic particles such as protons, electrons, neutrons, α-particles, and heavy ions can create cumulative long term non-ionizing damage in microelectronics by displacing atoms in the crystal lattice of semiconductors. Displacement damage results in displacement or dislodging of atoms from their crystal lattice of a material structure by the interaction of energetic particles thereby creating a vacancy in the material. This leads to Frenkel defects, reduction of minority carrier lifetime, change of the majority carrier charge density, and reduction of carrier mobility [35, 36]. The displacement damage is proportional and measured by non-ionizing radiation energy loss, (NIEL). This is not covered in this thesis.

(C) Single Event Effects (SEE)

Single event effects are caused by a single charged particle (heavy ions and/or protons) traversing the active volume of semiconductor devices causing either transient or permanent effects. Charge collection as a result of the ionization interactions can cause changes in circuit operation or in the information stored. Single-Event Upsets (SEU) or soft errors only alter the logic state of the device leading to change of information stored in the device. In the case of Single Event Disturb (SED), there is momentary disruption of the information stored in memory bit. Single-Event Burnout (SEB) is caused by high excessive current leading to permanent device burnout. Single-Event Gate Rupture (SEGR) is caused by heavy ions hitting the neck regions of electronic devices, leading to

a flow of electrons towards the drain, short-circuiting the oxide field [36]. This is not covered in this thesis.

2.1.5 Interactions of Materials with Radiation

In order to design effective radiation shielding structure, knowledge on the interaction of incident radiation with shield materials is required. High energy particles collide with material atoms via various interactions, during their transport through the shield. The attenuation of the energy of the particles in the radiation, due to the interaction between penetrating radiation and matter is not a straight forward process and there are various processes involved. The interactions of radiating particles with materials differ considerably depending (a) the type of radiation (energy and charge of the particle) and (b) type of interaction the incident radiation experiences before annihilation.

Photons have no charge and therefore travel a long distance in a medium without interacting with medium atoms. Their limited interactions lead to attenuation with generation of secondary electrons. On the other hand, electrons which are negatively charged and protons which are positively charged travel only a short distance before interaction with the medium atoms along their trajectories. Therefore, the transport of photons, electrons and protons is coupled due to the fact that incident photons produce electrons, electrons produce photons and sometimes photons produce proton - electron pair or this pair produces photons in different interactions with medium atoms [36]. Radiation - material interaction can be explained under two categories: (i) photon – material interaction (ii) particle - material interaction.

i) Photon – Material Interaction

High energy photons like x-ray and gamma rays transfer their energy to the electrons of the atoms in the material during interaction. During this process, the energy of the photons is attenuated through (a) photon scattering, (b) photoelectric effect and (c) pair production.

(A) Photon Scattering

An incident photon is scattered in a collision with the electrons in a medium through either elastic scattering (Rayleigh scattering) or inelastic scattering (Compton scattering) depending on the energy of the incident photon. Rayleigh or coherent scattering involves collision of incident photon with the whole atom so that the photon is scattered with no change in internal energy to the scattering atom of the medium and the photon. The scattering occurs without any loss of energy and makes little contribution to the absorption coefficient. Rayleigh scattering is more significant at low energies and more effective with shield materials of low Z. The second photon scattering is the Compton (inelastic) scattering which is a dominant interaction at energies below 30 MeV in which the incident photon imparts some of its energy into an electron of an atom of the material. After the collision, the incident photon energy and direction changes while the electron is ejected from the medium based on the laws of conservation of energy and momentum. Attenuation of energy due to Compton Effect is proportional to the atomic number (Z) of the material [37].

(B) Photoelectric Effect

Due to photoelectric effect, an incident photon ejects the core electrons from the target shield and gets annihilated in the process. The ejected electrons have kinetic energy as given by:

$$E_e = h\nu - E_b \qquad 2.1$$

where E_e is the kinetic energy of the particle, E_b is the work function/barrier to eject a particle from the surface of a material, h is Planck's constant, and v is frequency of the photon. The photoelectric effect is dominant at low energies below 20 KeV for low Z materials. The energy range increases as Z increases. The probability of occurrence of photoelectric effect increases at lower energies as the energy of the incident photon increase such that $E_e > E_b$. The probability of occurrence is proportional to $[Z^4/(hv)^3]$ [37].

(C) Pair production

In pair production, an incident photon with minimum energy of $2E_0 = 1.02$ MeV interacts with nucleus or electron of a target atom resulting in the disappearance of the photon and creating of positron and electron pair, based on the mass-energy equivalence equation ($E= mc^2$). An opposite interaction to pair production is an annihilation process, in which electron and positron combine to produce two annihilation photons of equal energy. Effect of pair production varies directly as Z^2 [37].

ii) Particle – Material Interaction

Interaction of incident particles present in space radiation environment with material takes place through several specific atomic and nuclear processes. Among these possible processes, two are of particular importance from radiation shielding point of view: (a) energy loss and (b) fragmentation.

(A) Energy loss

Interaction of charged particles with materials differs from that of photon [37]. Photon undergoes few interactions to dissipate all its kinetic energies while electron interaction probabilities are much higher before dissipating its kinetic energy. Charged particles lose their kinetic energy gradually in steps along its trajectories. The energy loss varies with particle energy. Charged particles like electron and positron loses their kinetic energy upon collision with electron of target material in their path through ionization or excitation of the electrons of the atoms of the target material. The resulting energy loss of charged particles per unit length in a given material traversed (also known as stopping power or linear energy transfer – LET) is directly proportional to the square of the Z and inversely proportional to the energy of the incident charged particle.

$$\mu = \frac{AZ^2}{E} \qquad 2.2$$

where μ is linear energy transfer (LET), Z is atomic number of the material, A is constant parameter, and E is energy of the incident charged particle. The critical parameter is the maximum particle energy to be stopped, since it defines the required thickness and consequently the mass of the shield.

Proton is a positively charged particle with rest mass $m_p = 1.67 \times 10^{-27}$ kg ($m_p = 1836\ m_e$), which is not easily deflected by electron in the atoms of the shielding material. Energy loss is mainly due to ionization and excitation. Since proton energy loss is proportional to Z^2, low Z materials tend to attenuate proton effectively per unit areal density [14]. This makes low-Z material effective shield material in proton rich environment such as LEO and HEO. At lower velocities, the LET increases as incident proton traverses the shield material until it reaches a maximum which is referred to as Bragg peak, after which it decreases abruptly.

Electrons, which dominates the outer Van Allen belt and poses a major radiation risk in GEO, has relatively small mass (m_e = 9.11 $\times 10^{-31}$ kg). Ionization is favored at low energies for inelastic scattering when the electron energy E_e is less than the critical energy of collision E_c.

The bremsstrahlung process dominates at high energies whereas the inelastic scattering dominates at low electron energies in high Z materials. The bremsstrahlung process occurs when incident electron collides with atomic nucleus leading to inelastic radioactive interaction. The incident electron is deflected and decelerated and, the decelerated electron converts its kinetic energy into production of photons. The generated photons can have energies in the range of 0 keV up to the energy of the incident electron, depending on the amount of deceleration. Production of bremsstrahlung within shielding material (most especially in high- Z materials) in a high energetic particle environment like GCR and SPE environment results in emission of highly penetrative photons that requires addition shielding. This increases the total thickness and mass of the material required for shielding, which increases the mission cost.

(B) Fragmentation

Fragmentation arises as a result of elastic collision between incident heavy particles and target material leading to formation of smaller fragments moving at the same speed as the incident particle but less ionizing due to lower atomic number [38]. Neutrons are also produce from the aftermath of the collision. In addition, secondary particles are produced in the shielding material upon fragmentation of its nucleus resulting in more radiation. The breaking up of heavy primary ions in GCRs flux into smaller fragments with lower ionizing power while reducing shielding material's bremsstrahlung is the only realistic solution for developing effective shield against high energetic particles [13]. The use of hydrogen-rich materials, such as water or polyethylene,

reduces the production of fragment nuclei, protons and neutrons by spallation, and lowers the radiation risk for a given amount of shielding weight [33]. Table 2.3 gives a summary of various radiation particle interactions with shield material.

Table 2.3: Radiation interaction processes with shield material [37]

Incident Radiation	Target	Type of Collision		
		Elastic	Inelastic	Complete Absorption
Alpha	Nucleus	Rutherford scattering	Bremsstrahlung production (negligible)	Transmutation
	Orbital Electron	(negligible)	Ionization & Excitation	(none)
Electrons/ Protons	Nucleus	Rutherford scattering (Principal cause of backscattering)	Bremsstrahlung production important with high Z absorbers	Electron capture (K-capture)
	Orbital Electron	Causes some scattering	Ionization & Excitation (characteristic x-ray production)	Annihilation (if incident electron is a proton)
Photons	Nucleus	Thomson Scattering (negligible)	Nuclear resonance Mossbauer effect	Photodisintegration
	Orbital Electron	Rayleigh Scattering (coherent) Thomson Scattering	Compton scattering (partial absorption of photon energy)	Photoelectric effect
	Field	Interaction/ scattering (negligible)	(negligible)	Pair production (mainly at high energy photon)

2.1.6 Particle Transport Prediction Tools for Studying Radiation Shielding Efficiency of Materials

The most efficient method of protecting against radiations is the use of shield. The use of material barriers to reduce the intensity of radiation seems only feasible means of mitigating the impact of radiation on astronauts and satellite's payloads. The shielding effectiveness of different materials could be studied using particle transport codes. The particle transport codes model the propagation of charged particles in space radiation environment through various shielding materials and the various interactions between the radiation and the material.

Common particle transport simulation codes includes NASA BRYNTRN [39], HZETRN [40], MNCP [41, 42], SHIELDOSE-2 [43], GEANT4 [44, 45], SRIM [46]. BRYNTRN and HZETRN are based on solving 1- dimensional Boltzmann equations for radiation fields as particles transverse shield material of known areal density. SHIELDOSE-2, MNCP, and GEANT4 are based on general purpose Monte Carlo method of using probability in solving numerical problems.

Most of these codes are available as standalone application or could be accessible within all inclusive software packages like ESA's SPENVIS or NASA's OLTARIS. The software packages provide a framework for linking various models for space environment. The models for radiation flux are also available within these two software packages. Two radiation transport codes employed in this study are SHIELDOSE and MULASSIS. While SHEILDOSE can simulate shielding effectiveness of Aluminium only, MULASSIS can simulate shielding effectiveness of a variety of materials including Aluminium. Additionally, the latter allows simulation of layered structures, suited for the analysis of composites. These are discussed further in Chapter-3

2.1.7 Polymer Composites in Space Application

Since this thesis is focused on developing a hybrid composite shield based on polymer composites, the background information and literature review will be limited to this. Polymer materials offer wide range of useful properties desirable in space application. Apart from being used as the matrix of polymer composites, polymeric materials are used as adhesives, in thermal blanket, in circuits' boards, in electrical installation, as lubricants and as thermal coatings.

Several space hazards affect polymeric material and hence polymeric composites must meet following requirements for use in-space [47, 48]. It should be noted that many of these space hazards are also applicable to metals and ceramics too.

(a) Vacuum outgassing: The loss of mass of polymer through volatilization in vacuum is known as outgassing. This volatilized material can deposit on critical components such as solar arrays or other optical components and degrade their performance. According to NASA specification, the Total Mass Loss (TML) should be < 1% while Collected Volatile Condensable Materials (CVCM) should be < 0.1% [49].

(b) Atomic oxygen: Spacecraft / satellite in low Earth orbit (LEO) altitudes (200 km to 700 km) are exposed to a flux of atomic oxygen which can cause erosion and oxidation of materials used in the spacecrafts and satellites. Therefore, polymer composites must have resistance to erosion from atomic oxygen with erosion yield less than ~ 3×10^{-24} cm^3/atom [50].

(c) Thermal cycling: Structure made of polymer composites must be able to withstand induced thermal stresses and endure wide range of temperature. There should be no significant or visible degradation at -100°C to 100°C [47, 51].

(d) Space charging: External surfaces of geostationary satellites can be charged to several thousand volts, depending on the environment, electrical properties of materials and surface geometry. A satellite system must be designed such that electrostatic discharge (ESD) due to surface charging is prevented. ESD can result in structural damage, degradation of spacecraft components, and operational anomalies. Since polymer composites have poor conductive properties, ESD is one major concern [52–54].

(e) Intense radiation: In addition to shielding the electronics from intense radiation, the polymer composites must not be damaged by the radiation and its properties must not be degraded. This study has focused on intense radiation and impact of radiation on polymer composite.

(f) Structural Properties: Polymer composites must meet the structural requirements of the satellite design.

2.1.8 Radiation Shielding Efficiency of Polymer Composites

Polymeric materials enjoy significant property advantages that make them excellent candidates for use in aircraft and spacecraft structural applications. Properties such as specific tensile strength, specific tensile modulus, fatigue resistance, damage tolerance, and design flexibility, all make these materials very attractive for aerospace applications. In addition, a wide range of fiber reinforcement types and matrix resin systems are available to the engineer and designer for specific application.

2.2 Literature Review of Radiation Shielding

2.2.1 Radiation Shielding of Polymer Composites

Since the discovery of radioactivity, there have been several published studies focused on shielding materials for medical industries and terrestrial nuclear facilities. Sufficiently thick slab of carefully chosen material are used without any concern for the weight of the shield. However, radiation attenuation in space is required shield that are lighter since increase in weight increases mission cost exponentially.

Previous space missions have depended on aluminium and its alloy for both structural and radiation protection of the spacecraft their availability, good machinability, and cost effectiveness [Li et. al, 2013]. Few studies have investigated multilayer configuration of different materials to achieve effective shielding of spacecrafts. These are highlighted here in this review.

A hybrid composite material was developed by Abusafieh et al [55] for electron dominated GEO and Global Positioning Satellite (GPS) orbits. A low Z/high Z/low Z multilayer configuration was used to obtain 28% weight saving over aluminium. The low Z material was graphite-cyanate ester, which reduced secondary particles production while tungsten a high Z material was used for electron attenuation. The study shows that multiple shield materials are at least a factor of two more effective than a single shield material for the same areal weight (equal to density × thickness).

Similar design concept of low Z/high Z/low Z configuration was employed for ESA Advanced Equipment Design (AED) study by Brander et. al. [56] and Garcia et. al.[57]. These studies investigated the development of electronic housing using hybrid panel of carbon fiber and tungsten for PROBA 2 satellite in LEO. The studies show better radiation shielding effectiveness

of aluminium when compared with carbon fiber reinforced epoxy laminate with tungsten at the same areal mass. This is partly due to strong proton environment in LEO where high Z materials (such as tungsten) have less shielding effectiveness. Though radiation shielding effectiveness was reduced, the use of K1100 carbon fiber improves the thermal conductivity of the structure. Atwell [58] studied radiation shielding of "graded-Z" shield material in Jupiter environment that has similar trapped protons and electrons like Earth. He concluded that arrangement of materials with descending atomic number (Z,) has greater potential in absorbing characteristic x-ray produced by adjacent high Z layer in the configuration.

NASA has also developed several radiations shielding concepts among which is multifunctional composite architecture for deep space mission. Sen et al [13] manufactured a multifunctional polyethylene composite for radiation, ballistic and thermal protection. The outer layers of the polyethylene composite were reinforced with open cell carbon foam and plasma-deposited B_4C. The ultra-high molecular weight (UHMW-PE) polyethylene fiber composite with epoxy matrix has higher specific ultimate tensile strength (2.8 times lighter) and higher specific modulus (2.5 – 4 times greater) when compared with aluminium alloys such Al 2024 and Al 219. These alloys are typically used for space application such as International Space Station (ISS) and space shuttle fuselage. Polyethylene based composite are distinctively better shielding material for SPE and GCRs in deep space mission. Since breaking up the heavy ions in GCR flux into smaller fragments with lower ionizing power is the only realistic solution for passive radiation design for interplanetary radiation environment, shielding with polyethylene (a low Z) material maximize likelihood of projectile fragmentation while producing minimum number of target fragments. The incorporation of open cell carbon foam and plasma deposition of B_4C coating on the exterior of

surface of the polyethylene composite enhanced the multifunctional nature of the composite by addressing thermal management and ballistic impact resistance properties.

Recent study by Kaul et. al. [12] have shown that lightweight multilayer hybrid composite consisting of ceramic and polymer composite is effective in shielding against cosmic and solar flare radiations while offering protection during re-entering of space vehicles. Kaul et. al. [12] studied a tri-layer hybrid structure for shielding against cosmic and solar radiation as shown in Figure 2.3. The inner layer made up of inter-ply or intra-ply layers of ultra-High molecular weight polyethylene (UHMW-PE) fibers (V_f = 30 - 42%) and graphite fiber ((V_f = 18 - 30%) in an epoxy matrix. The presence of UHMW-PE fibers provided radiation shielding while the combination of UHMW-PE fiber and graphite fiver provided strong lightweight composite.

The middle layer is composed of UHMW-PE fiber (68%) in a polyethylene matrix which provided both radiation shielding attributes and micrometeoroid (MMOD) protection. The outermost layer comprises of ceramic materials (e.g. aluminium oxide, boron carbide or silicon carbide) which provided MMOD protection. This makes the configuration truly multi-functional which can be exploited for space habitat modules or re-entry vehicles.

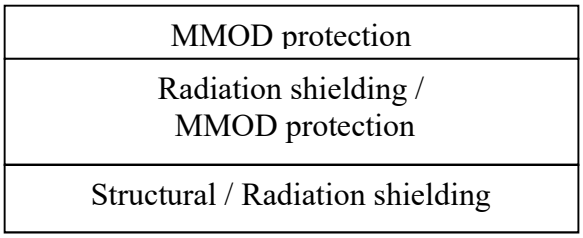

Figure 2.3: Schematic of multi-functional layered structure having structure and radiation shielding attributes [12].

Zhou et al. [59] studied the use of in-situ lunar/Martian materials for shielding against proton and neutron radiation encountered on Mars. Soil representing Martian regolith was bonded using polyimide to manufacture composite. The composites with regolith content reduced the fluence of low energy proton but did not provide adequate shielding for payload electronics under neutron exposure.

2.2.2 Radiation Damage in Polymeric Composites

One of the main concerns with the use of polymeric composite materials in space application is the effect of long term radiation exposure on the molecular structure of the polymer composite. Radiation induced damage is not major concern for metals and ceramic in space within certain energy range. The mechanical properties of structural metals or ceramics will not be significantly degraded following exposure to proton fluencies $< 10^{17}/cm^2$ (E>1MeV), neutron fluence $< 10^{17}/cm^2$ (E > 1keV), and electron fluence $< 10^{18}/cm^2$ (E >1keV) [60]. It is expected, therefore, that the space radiation will not constitute a significant hazard to metals and ceramics, because such fluencies can only be accumulated only on extremely long missions (hundreds of years). Polymeric materials are considerably more sensitive to radiation which can result in significant degradation of the mechanical properties of polymeric composites.

When energetic particles and photons interact with solids, energy is transferred from the incident radiation to the target. The major consequences of energy transfer from incident radiation to materials are ionization, electronic excitations and atomic displacement, all of which can result in serious degradation [61]. In polymer, composite irreversible chain scission can occur, which are manifested as changes in appearance, chemical and physical states, and mechanical, electrical, and

thermal properties. However, not all properties of a polymer are affected to the same degree by radiation.

Fibre reinforced polymer composites experience diverse radiation environments during service in space. While fibers are not affected significantly (polymeric fibers are an exception) by radiation environment, the polymer matrix in a fiber reinforced composite is highly susceptible to radiation with significant influence on matrix dominated composite properties like transverse tensile modulus (E_{22}) and shear modulus (G_{12}). Milkovich et. al. [62] studied the effect of 1 MeV electron radiation at a dose rate of 1.8E9 Gy/s to a total dose of 100 MGy on graphite/epoxy. This radiation exposure corresponds to dose absorbed within Van Allen radiation belts. The authors reported that the electron radiation degraded the in-plane strength properties as a result of radiation interaction with epoxy matrix. At elevated temperature, radiation increased the ductility of the epoxy matrix, specifically in matrix dominated laminates layup sequences suggesting reduction in molecular weight through chain scission.

Egusa [63] also compared the irradiation effect of 2MeV of electron and ^{60}Co γ-ray on glass fabric composite with regard to the dose dependence of the composite strength. The author observed that radiation damage to polymers was independent to first order of the type of ionizing radiation and dose rate but depended only on the total dose of ionizing radiation. He concluded that the dose dependence of the composite strength followed identical pattern regardless of the type of radiation. This study showed that the composite strength is virtually determined by a change in the matrix ultimate strain due to irradiation. Chartuvedi and Chai [64] also observed that elastic modulus of irradiated matrix at room temperature exhibited an increase when compared

with non-irradiated matrix while the glass transition temperature T_g of both the composite and resin decreased due to irradiation.

Based on these results, it can be concluded that the interaction of radiation with polymer composite affects mainly the matrix through chain scission and chain cross-linking reducing the matrix dominated properties. Cross linking is the formation of new and irreversible chemical bonds between two adjacent polymer chains while chain scission involves fracture of polymer chains resulting in a decrease in the molecular weight of the polymer and hence, reduction in strength and heat resistance [65]. Both of these mechanisms compete against each other and are present in a polymer undergoing irradiation, with an overall effect determined the dominant mechanism. A summary of dose ranges for significant alteration of properties of various polymeric materials is given in Figure 2.4.

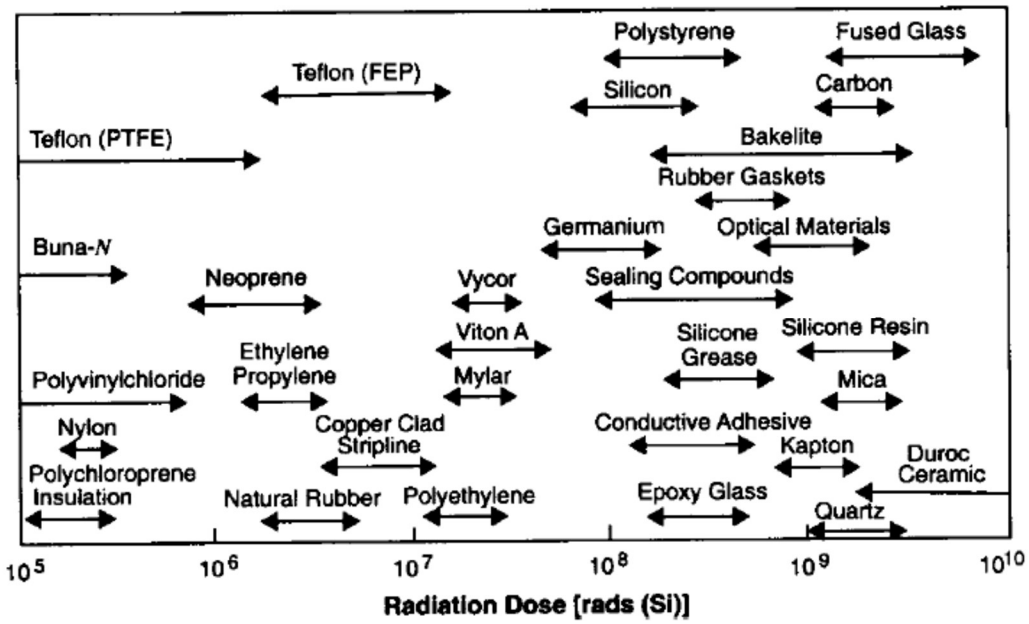

Figure 2.4: Radiation dose tolerances of materials [66]

[*http://www.dsri.dk/roemer/pub/Cubesat*.]

2.3 Literature Review Summary and Knowledge Gaps

There have been few attempts in replacing aluminium as structural and radiation shield for space application. Multifunctional capability of the structural shielding is desired to reduce the overall weight of satellite structure and provide more room for other spacecraft components.

Most of the published studies have focused on LEO, GEO, and interplanetary mission. LEO is a proton dominated environment. Few design configurations with composite structure has been able to obtain lighter radiation shielding than aluminium with significant improvement in structural and thermal properties has been achieved. These improvements coupled with design flexibility has sustained the interest in the use of composite structure in LEO. An example is in the development of deployable telescope for optical imaging [67].

In GEO and GPS orbit, electron is the major threat to satellite operation. The use of low Z/high Z/low Z design configuration has improved radiation attenuation with significant weight reduction in the primary structure. In the tri-layer shield structure, each layer is designed to attenuate preferentially a particular type of radiation particle. A very important inference from the literature is that low Z materials are more effective in shielding protons through fragmentation while high Z absorbers are efficient against electrons through energy loss.

While there are few studies [6, 7] on optimization of HEO orbits for CSA's PCW mission (discussed in Chapter 1) as well as mention about few Russian missions in HEO [11], there are no published studies on shielding concepts for this orbit. A recently published patent [68] discusses multifunctional composite radiation shielding concept for space applications. However, it is very generic without specifics; for example, it does not define how radiation shielding

effectiveness is quantified. Moreover, the concept does not consider the limit to absorbed dose in constituent materials.

Based on the literature review, the following knowledge gaps can be identified.

- There are no published studies on radiation shielding concepts for HEO to replace traditionally used Al. While published radiation shielding concepts in LEO and GEO are very useful, the response of material shield in a multi particle species environment like HEO is expected to be different. However, knowledge on optimized radiation shielding concept that would meet multi-functional requirements (radiation, structural, electrical, thermal) in HEO is not available but are highly needed for the CSA's PCW mission discussed in Chapter 1.
- Limited available studies on composite radiation shielding does not offer any insight into effect of structure (such as fiber volume fraction within a layer, thickness of a layer and stacking sequence) on radiation shielding. While focusing on radiation shielding, few published studies on composites have not focused on optimizing other properties such as mechanical properties, thermal cycling or space charging.
- While focusing on radiation shielding through modelling, validation of the design through radiation experiments is extremely limited.
- While there are many studies on comparison of various particle transport codes identified in 2.1.6, there are no published studies on systematic approach to design of radiation shields (specifically composite shields) using these transport codes. Moreover, experimental validation of accuracy of software such as the one used in this thesis is not available.

2.4 Thesis Objectives

Based on the knowledge gaps highlighted in the previous section the overall goal of this thesis is to design and develop a multifunctional hybrid composite shielding that meets the PCW mission requirements of radiation shielding, mechanical properties, and functional properties such as electrical conductivity and resistance to thermal cycling. In order to meet this goal, the following three objectives have been proposed and realized:

1. Develop a design methodology for the development of a multifunctional composite radiation shield and demonstrate it by developing a radiation shield tailored to specific requirements in HEO.

2. Develop a process cycle for manufacturing the composite radiation shield designed in Objective 1.

3. Radiation and mechanical testing of the manufactured shield panels to validate its designed shielding and structural properties.

CHAPTER THREE

DESIGN OF MULTIFUNCTIONAL HYBRID COMPOSITE RADIATION SHIELD

Development of multi-functional satellite radiation shield depends on knowledge of the satellite service environment in space. For the PCW mission identified in Chapter 1, the desired shield requirements include effective radiation shield at minimum shield weight, desired mechanical properties without any degradation due to radiation, atomic oxygen resistance, space charging and out-gassing compliant, and be able to withstand repeated thermal cycling and micro meteoroid impact.

The primary focus of this thesis was to design and develop a hybrid composite shield with desired radiation shielding and mechanical properties. Secondary design requirements that are not explicitly focused on, such as atomic oxygen resistance, space charging, and out-gassing compliance were implicitly satisfied through appropriate material selection. The effect of thermal cycling on mechanical properties was studied experimentally and is discussed in Chapter 4. Micro-meteoroid impact was not studied in this thesis.

Sections 3.1 to 3.8 discusses the various steps leading to the final hybrid composite design, which have been published as three journal papers as identified in section – in Chapter 1. The final hybrid composite design to meet radiation shielding requirements is discussed in section 3.9. The refinement of this design to meet the desired mechanical properties is discussed in section 3.10.

The material discussed in Sections 3.9 and 3.10 have been submitted as a manuscript for possible publication in Composites Science and Technology (see Publications.)

3.1 Design Methodology

A flow chart detailing the design methodology is presented in Figure 3.1.

This general design methodology has been applied in the following sections for a specific PCW mission for reasons discussed in Chapter 1. However, this methodology can be applied to other missions and radiation environment. Due to the limitations imposed by the simulation software, a layered material structure (in case of hybrid composites) has been used. However, this could be extended to a real material microstructure if the simulation software allows it. This is discussed as "Recommendations for Future Work" in Chapter 6.

The Step 1 in the flow chart on mission selection and input is presented in 3.2. Step 2, on the determination of radiation fluences for the chosen mission is discussed in 3.3. Simulation of TID transmitted through, and absorbed in the shield made of homogenous materials (Steps 3and 3.1) is presented and discussed in 3.4. Radiation shielding analysis of hybrid composite shield made up of 2 homogenous materials to satisfy both criteria identified in Step 1 is discussed in 3.5 and 3.7 (Steps 4 and 4.1).

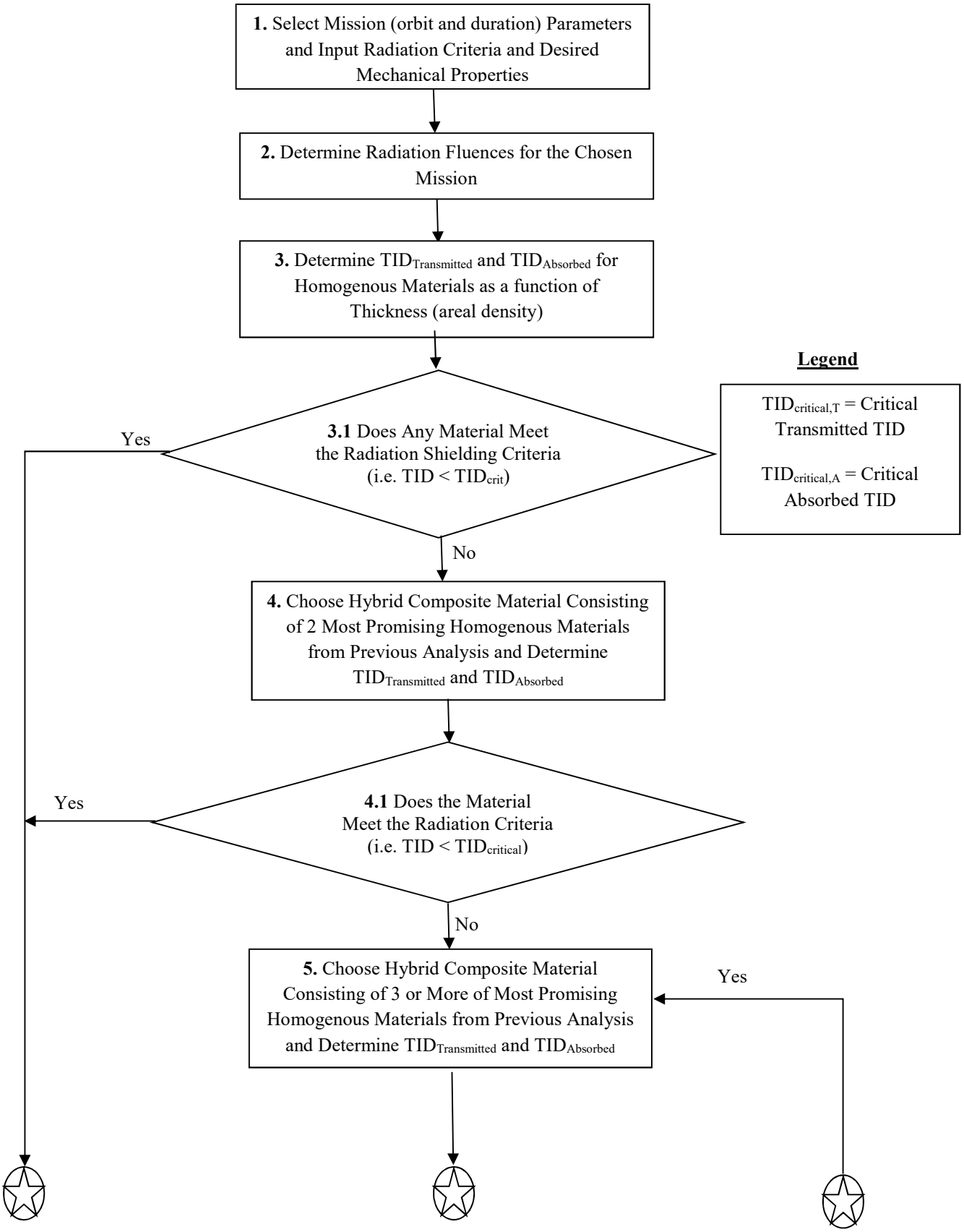
1. Select Mission (orbit and duration) Parameters and Input Radiation Criteria and Desired Mechanical Properties
2. Determine Radiation Fluences for the Chosen Mission
3. Determine $TID_{Transmitted}$ and $TID_{Absorbed}$ for Homogenous Materials as a function of Thickness (areal density)
Legend
$TID_{critical,T}$ = Critical Transmitted TID
$TID_{critical,A}$ = Critical Absorbed TID
3.1 Does Any Material Meet the Radiation Shielding Criteria (i.e. TID < TID_{crit})
Yes
No
4. Choose Hybrid Composite Material Consisting of 2 Most Promising Homogenous Materials from Previous Analysis and Determine $TID_{Transmitted}$ and $TID_{Absorbed}$
4.1 Does the Material Meet the Radiation Criteria (i.e. TID < $TID_{critical}$)
Yes
No
5. Choose Hybrid Composite Material Consisting of 3 or More of Most Promising Homogenous Materials from Previous Analysis and Determine $TID_{Transmitted}$ and $TID_{Absorbed}$
Yes

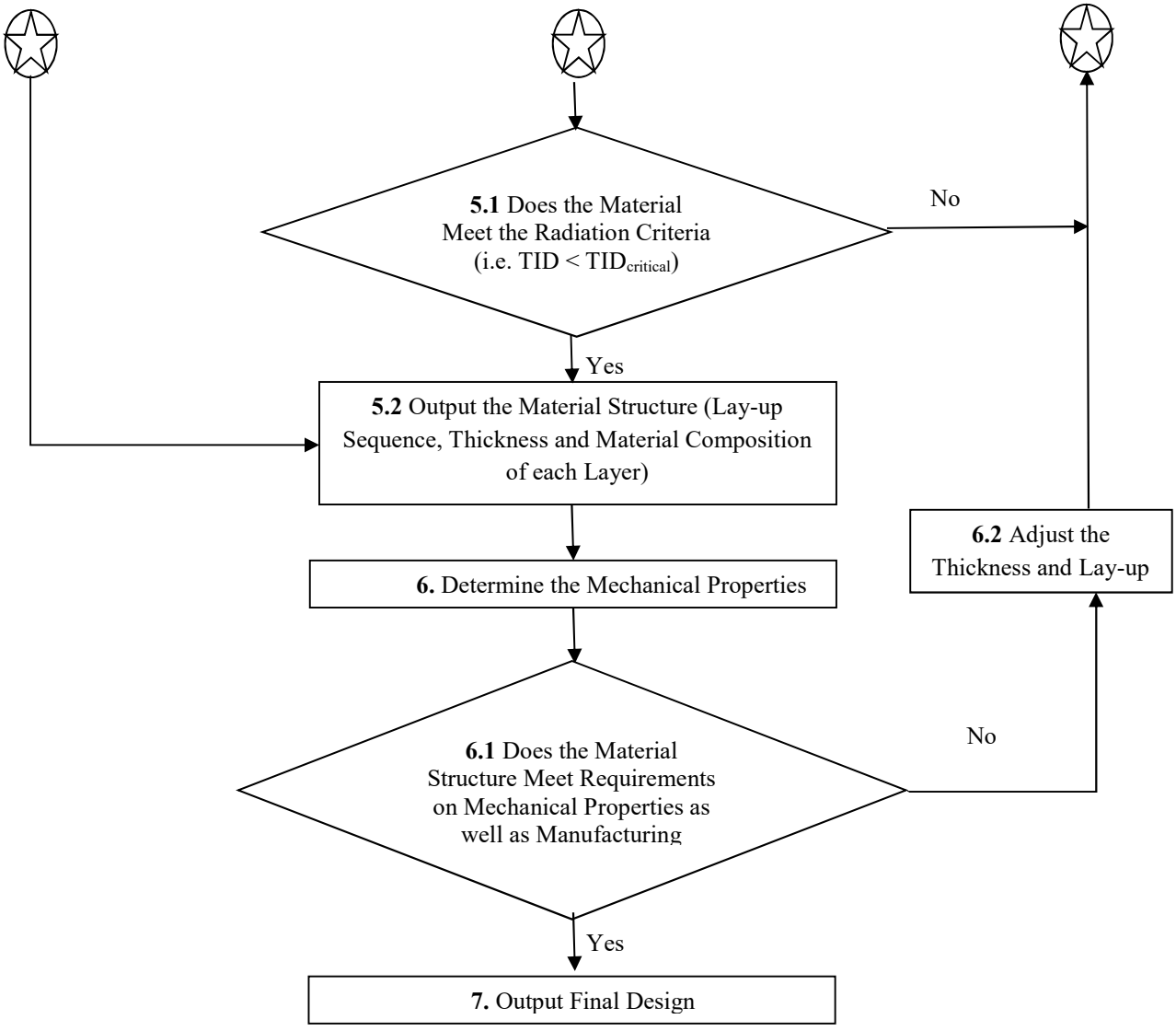

Figure 3.1: The design methodology flowchart

The effect of lay-up sequence of two material layers and their thickness on radiation shielding effectiveness is discussed in 3.6. Based on the recommendations from 3.5 and 3.6, the final composite shield design that meets both criteria identified in Step 1 is discussed in 3.7 (Steps 5, 5.1, and 5.2).

Section 3.8 (Steps 6, 6.1, and 6.2) discusses the mechanical properties of the design determined in 3.7 and tweaking of the structure to meet radiation and mechanical property criteria as well as manufacturing requirements.

Final step 7 outputs the final design.

3.2 Orbital / Mission Parameters and Radiation Shielding Criteria

3.2.1 Definition of Orbital and Mission Parameters

The radiation environment experienced by a satellite depends on its orbital trajectory, angle of inclination, the altitude of its perigee and apogee, and mission duration. These have to be accurately defined to realistically simulate the radiation shielding response of a material.

The three HEOs defined for the PCW mission are Molniya, Modified Tundra and Three Apogee (TAP) orbits. The radiation shielding effectiveness of various homogenous materials in these environments were simulated and compared to justify (i) the selection of composites over homogenous materials as the shielding material, and (ii) focus on Molniya over other two orbits for further development of the shield.

3.2.2 Radiation Shielding Criteria

The required resistance of satellite electronics and space bus to radiation is often defined in terms of Total Ionizing Dose (TID) and Linear Energy Transfer (LET). Total Ionizing Dose (TID) is the cumulative ionizing radiation that an electronic device receives over a specified period of time. TID is the integral of the product of the particle energy spectrum and the stopping power of each particle type as a function of incident energy It is measured in RAD (Radiation Absorbed Dose), which is defined as 1.0×10^{-5} J/g (100 ergs/gm) of materials. Satellite electronics will be damaged beyond a threshold TID. The radiation shield should limit the TID transmitted ($TID_{Transmitted}$) through it and deposited on the electronics below this threshold value ($TID_{Critical,Transmitted}$). While blocking the radiation, the radiation shielding material would absorb the radiation and this absorbed TID ($TID_{Absorbed}$) value should be less than a critical value, beyond which the material properties would degrade.

Linear Energy Transfer (LET) is measure of energy deposited in a solid state material by a radioactive particle over the length of its decay track. The particle range/length is the distance travelled by an energetic particle in the material before coming to a rest. The LET (sometimes refers to as stopping power) is expresses as charge deposited per unit track length, $MeV.cm^2$ /mg. Passage of high LET radiation such as alpha and beta particles, disturbs state of electronic circuits causing malfunction of silicon based devices.

In this thesis, the threshold TID for the electronics has been chosen over LET and hence, the design is based on this threshold TID. Based on this, the following radiation shielding criteria have been chosen and used in the design of the radiation shield.

(i) The cumulative TID transmitted through the shield ($TID_{Transmitted}$) during the mission period must be less or equal to an arbitrary TID value of 50 krad ($TID_{Crititcal,\ Transmitted}$).

(ii) The cumulative TID absorbed by the shield ($TID_{Absorbed}$) must be less than the threshold TID ($TID_{Crititcal,\ Absorbed}$) for onset of radiation-induced-degradation of the shield materials. The ($TID_{Crititcal,\ Absorbed}$) for various materials considered in this study are tabulated in Table 3.1

3.2.3 Desired Mechanical Properties

The desired mechanical properties for the hybrid composite shield is that its properties should be equivalent to currently used Aluminum based radiation shield. Presently, the alloys of aluminum represent the majority of spacecraft structural materials. An example is Al-6061-T6. The materials properties of Al (Al-6061-T6) are given in Table 3.2.

3.3 Determination of the Radiation Environment for the Chosen Mission

The radiation environment for a given orbit and mission duration was predicted using standardized models available in European Space Agency's (ESA) Space ENVironment Information System (SPENVIS) software [69, 70] for a mission duration of 15 years, from 2017 - 2031. SPENVIS is a web-based tool for assessing environmental effect on spacecraft systems. It has interfaces to various models that can be used to define the space environment (the models are updated periodically using data from various satellite missions) and predict its effects on spacecraft and components.

The major source of intense radiation environment in HEOs is due to Van Allen belts (both proton and electron belts). Energetic electrons and protons are magnetically trapped around the Earth forming the radiation belts. Other sources of radiation are from solar particle Events (SPE) and galactic cosmic rays (GCRs). The trapped proton and the trapped electron fluxes were calculated, for the satellite's orbital trajectory, using NASA's AP8 and AE8 models. "Worst case" condition was simulated using AP8 MAX proton model and AE8 MAX electron model [17, 21, 22]. The "Worst case" condition represents the highest radiation fluxes that the satellite could experience during its mission period of 15 years. AP8 Max and AE8 MAX correspond to the averaged protons and electrons fluxes at solar maximum. (It is worth noting that latest version of electron and proton models, AE9 and AP9 models respectively are now available within SPENVIS. However, it was not used to be consistent with previous analysis on this project. Also, sample analysis with AE9 and AP9 shows no drastic difference between from AE8 and AP8 results).

Table 3.1: Onset of radiation induced damage ($T_{Critical,\ Absorbed}$) in some selected materials [60].

Materials	$T_{Critical,\ Absorbed)}$ (rad)
Aluminum	1.0×10^{17}
Tantalum	1.0×10^{19}
Tungsten	1.0×10^{19}
Epoxy	1.0×10^{8}
Polyethylene	2.0×10^{7}
Phenol – formaldehyde	3.9×10^{9}
Unfilled Phenolic	5.0×10^{7}
Teflon	2.0×10^{4}
Polyvinylchloride	5.0×10^{6}

Table 3.2: Material properties of Al-6061 commonly used in space structures [71].

Properties	Values
Modulus (GPa)	68.9
Ultimate Tensile Strength (MPa)	314.92
Yield Strength (MPa)	276.89
Shear Modulus (GPa)	26.0
Shear Strength (MPa)	207.0
Poisson Ratio	0.33

NASA's Jet Propulsion Laboratory's (JPL) model [27], available within SPENVIS, was used to determine the long-term solar particle events (SPE) fluence into the shielding structure while ISO-15390 model [32] was used to determine the galactic cosmic ray flux (GCR) based on 2 solar cycles of the 15- years mission duration, which included a solar maximum cycle for 9.87 years and a solar minimum cycle for 5.13 years. The presence of geomagnetic shielding was assumed using rigid cut-off by Størmer with eccentric dipole model. This is referred to as quiet magnetospheric condition within SPENVIS, and this provides less geomagnetic protection at the low energy end of the proton spectrum. The fifteen years' mission from 2017 to 2031 includes solar maximum cycle for 9.87 years and a solar minimum cycle for 5.13 years.

The fluences for various radiation particles were determined using the models identified above, as detailed in the flow chart in Figure 3.2.

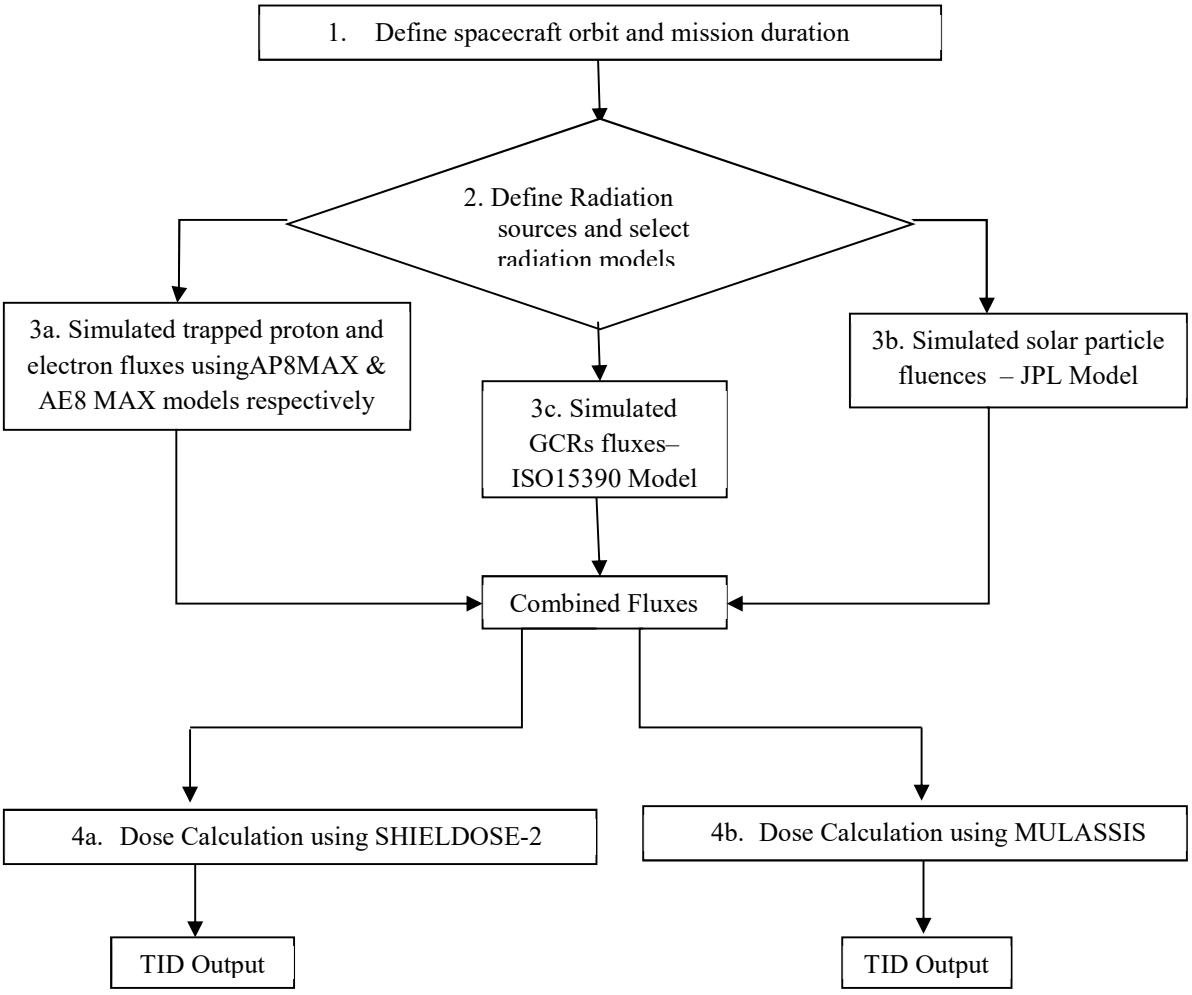

Figure 3.2: Flowchart for predicting fluences for the mission and TID for a given shield

3.3.1 Simulated Results for Radiation Fluxes for the Radiation Environment in HEOs

The total mission average fluxes for the four simulated radiation environments are shown in Figure 3.3 – 3.6 for protons, electrons, solar protons and galactic cosmic rays (GCRs) respectively. These fluxes were obtained using the models highlighted in Section 3.3. As observed in Figure 3.3, trapped protons have energies in the range of 0 – 400MeV while trapped electrons have energies in the range of 0 – 7 MeV as shown in Figure 3.4. Figure 3.4 also suggests that a satellite in Molniya orbit is subjected to a significant amount of highly energetic protons with energies above 10 MeV as compared with TAP and Modified Tundra. Earlier reports on HEO analysis [13] has attributed this to low perigee pass of Molniya orbit (~ 500km) as it passes through region of energetic trapped proton belt with high peak proton density flux in the inner Van Allen belt. Perigee refers to the elliptical orbit position when the satellite is closest to the Earth while Apogee is the farthest point on the elliptical orbit to the Earth. The high perigees of Modified Tundra (~23,144 km) and TAP (~8100 km) orbits ensure that their trajectories deviate from this region resulting in little contribution from proton flux to TID.

It can be inferred from Figure 3.5 that the TAP has the highest average flux of energetic electrons while the Modified Tundra has the lowest average flux of low energetic protons of the three orbits. The magnitude of electron flux in Molniya orbit lies between the values of the other two orbits. As observed in Figure 3.5, Modified Tundra has slightly higher average flux of solar particles when compared with Molniya and TAP due to higher apogee of 48442 km exposing it into more influence of geomagnetic storm from outer Earth magnetic radiation. The fluxes due to GCRs as shown in Figure 3.6 are fairly constant for the three orbits as a result of effective protection by the Earth's geomagnetic shield deflecting much of the outer galaxy radiation particles.

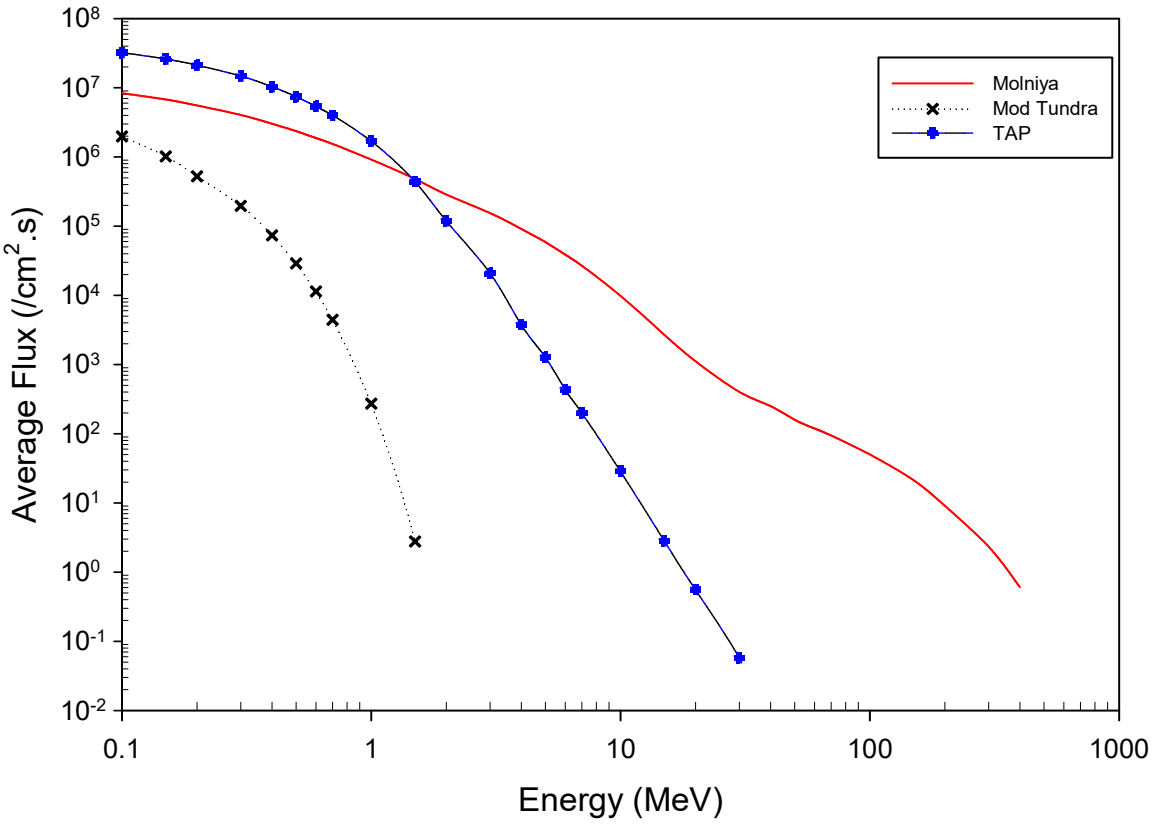

Figure 3.3: Comparison of average proton radiation flux in the three HEOs

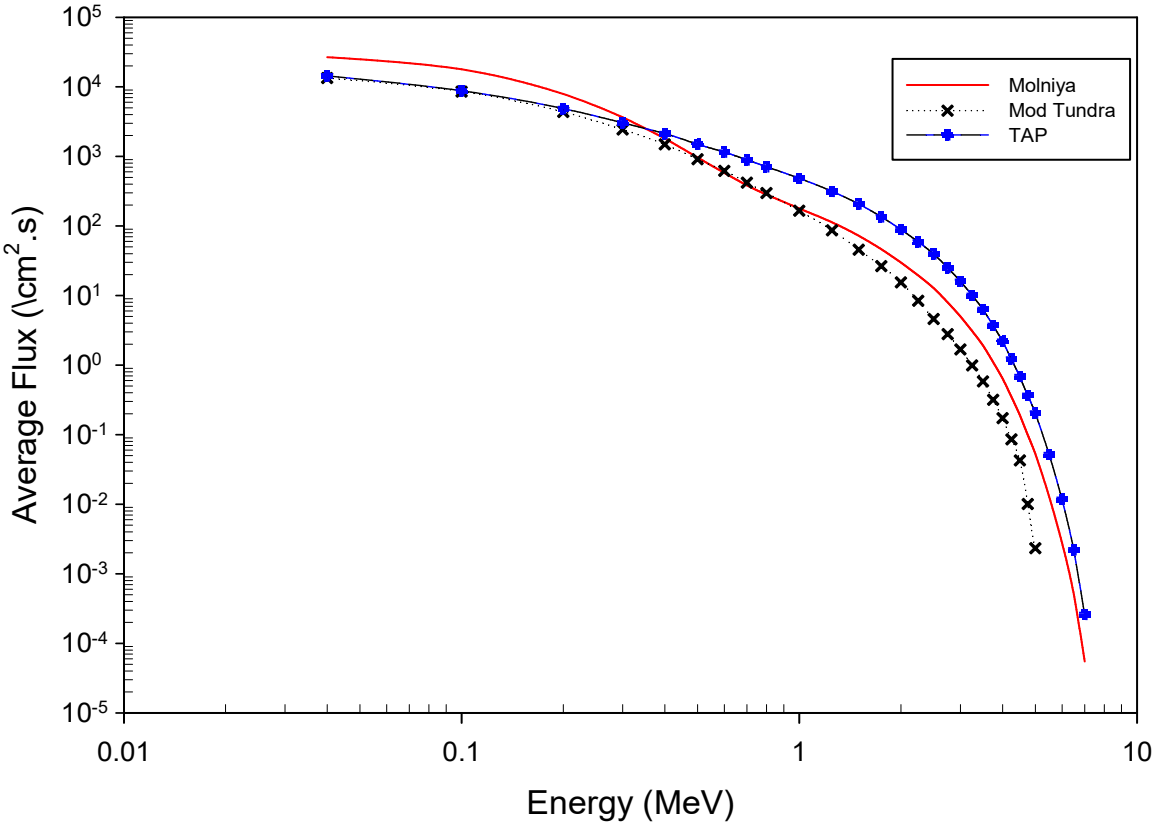

Figure 3.4: Comparison of average electron radiation flux in the three HEOs

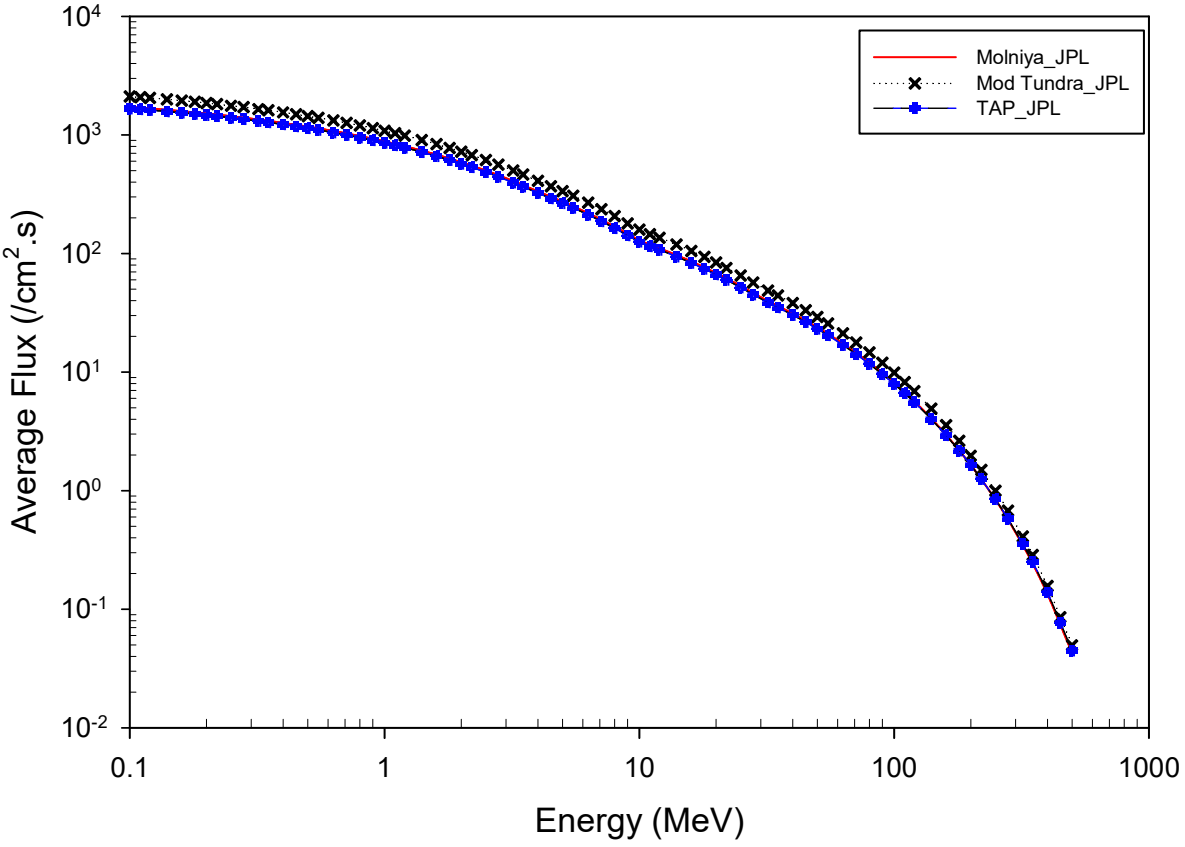

Figure 3.5: Comparison of average solar electron radiation flux in the three HEOs

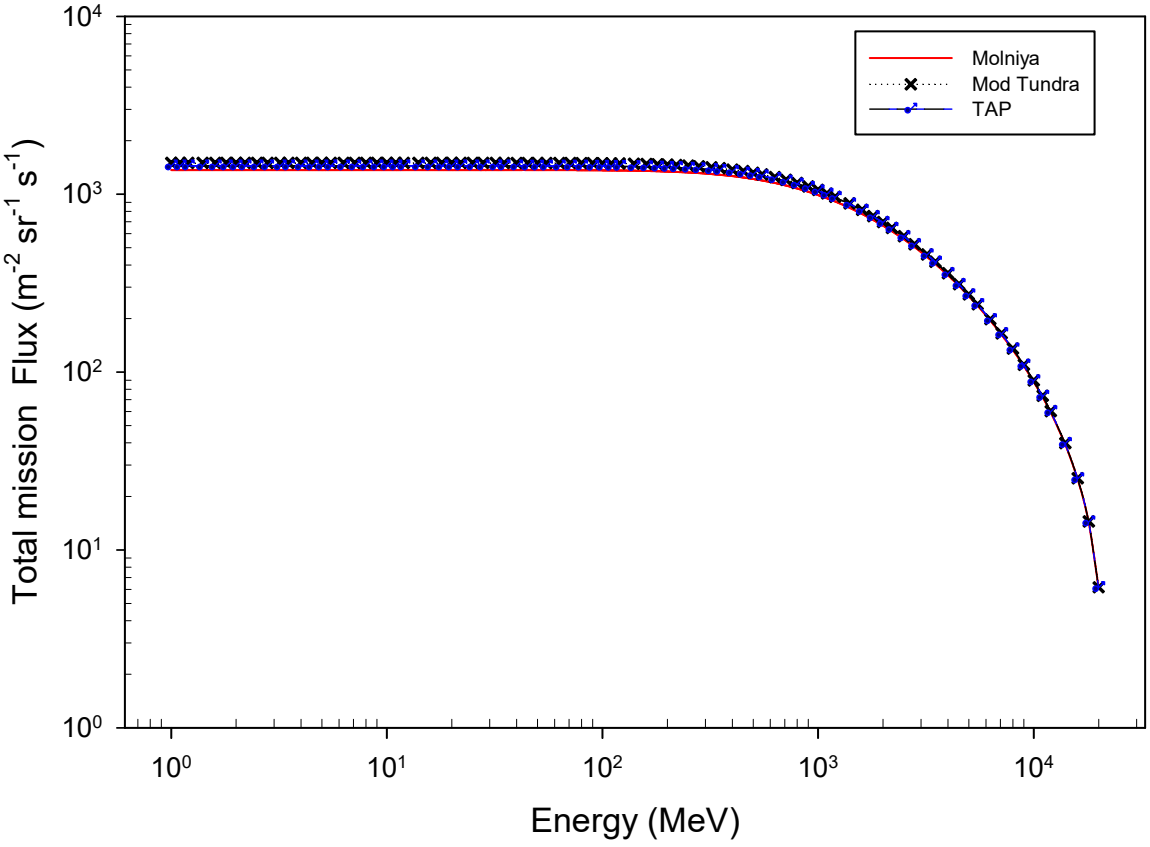

Figure 3.6: Comparison of total mission flux of galactic cosmic rays (GCRs) flux in the three HEOs

In summary, the TAP is electron dominated, Molniya is proton dominated and Modified Tundra has least electrons and protons. Fluences in Figures 3.3 – 3.6 were used as input for radiation shielding analysis of homogeneous and composite materials discussed below.

3.4 Simulation of Transmitted and Absorbed TID for Homogenous Shielding Materials

3.4.1 Shield and Detector Geometry

The shield and detector geometry were defined to be planar layers. In case of homogeneous materials, a single planar layer of homogeneous material was used. The composite shield consisted of laminated layers of various homogenous constituents as shown in Figure 3.7. The detector geometry was also planar and had the same dimensions as the shield as shown in Figure 3.7.

The material in each shield layer was defined by its density and elemental/isotropic composition. The area of the shield perpendicular the incident radiation is of no consequence since the radiation shielding simulation software is particle transport analysis software in 1-D. The effect of volume of these materials in the shield on radiation shielding (i.e. transmitted or absorbed TID) was varied by varying their thickness or the areal density (density ×thickness). The radiation transmitted through these shield panels was recorded by a 10 μm thick silicon detector (t_s) placed behind the shield as shown in Figure 3.7.

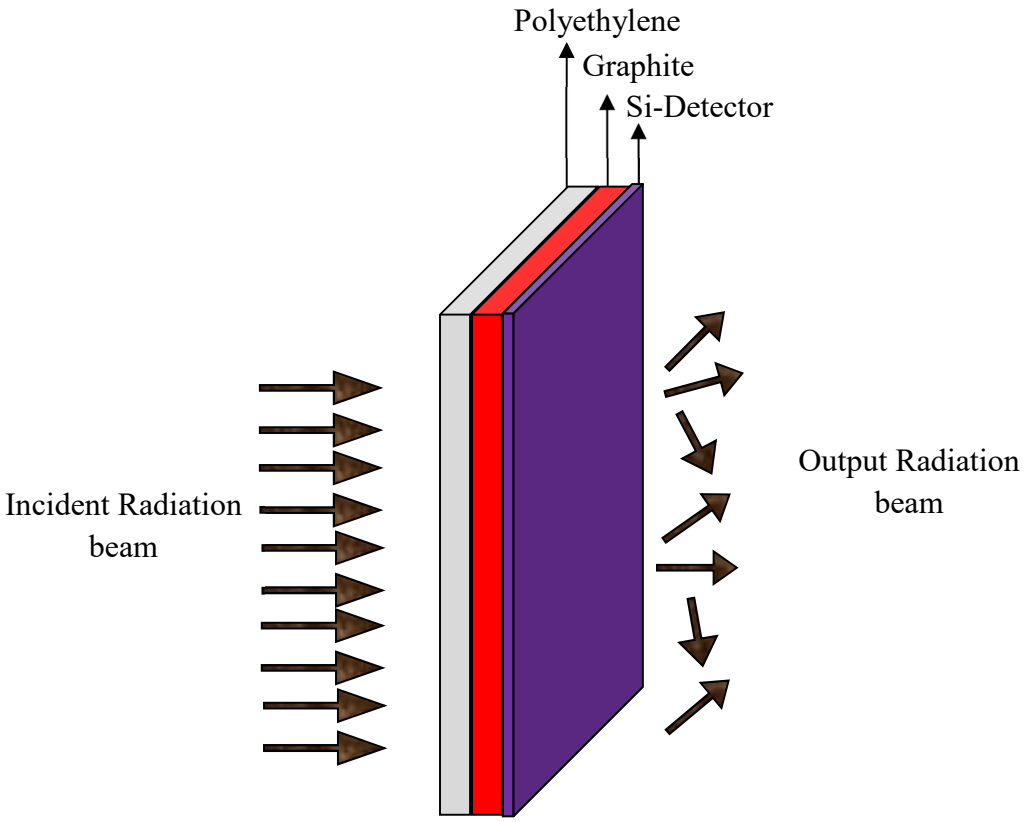

Figure 3.7: The schematic of radiation shielding calculation in the simulation (t_S = shield thickness)

3.4.2 Materials

Homogenous material of metals and polymers were utilized as shielding materials in the analysis. Metals included Aluminium, (Al - 2.699 g/cm^3), Tantalum (Ta -16.654 g/cm^3), and Tungsten (W - 19.3g/cm^3). Metals has been commonly used materials for space application, polymers on the other hand are made of elements with low atomic numbers (Z), primarily carbon (C), hydrogen (H), oxygen (O), and nitrogen (N) which provide the best shielding from galactic cosmic rays (GCR).

In particular, hydrogenous composites are being preferred as radiation shielding radiation especially in weight sensitive application for deep space radiation shielding. Hydrogen-containing polymers are not only effective in interacting with GCR particles; they are also effective in reducing the energy of the neutrons formed in the interactions. The best shield for this radiation would be liquid hydrogen, which is not feasible. For this reason, hydrogen-containing polymers make the most effective practical shields [72, 73]. Polymers included Polyethylene (PE - 0.94 g/cm^3) and Epoxy (1.28 g/cm^3).

In addition, Carbon (1.7 g/cm^3) and ultra-high molecular weight PE fibers (0.97 g/cm^3) was used as the reinforcement material. Additional trials using liquid hydrogen (0.07085 g/cm^3) were also completed to explain the effects of secondary particle production and how it affected trends observed in the simulated results.

3.4.3 Simulation Details

A key aspect of developing effective and lightweight radiation shielding materials is the understanding of the transport phenomenon and the nature of interactions between space radiation and shielding materials [74]. These interactions vary for different charged particles, which add to the complexity of radiation shield development. Accurate prediction of the transport of radiation thorough spacecraft material yields accurate prediction of the TID.

NASA's SHIELDOSE-2 and ESA's MULASSIS (Multilayered Shielding Simulation Software Tool), which is a variant of GEANT4, were used in simulating the transport and interaction of charged particles with the shielding material and the resulting TID. Both are accessible within SPENVIS and results from both codes are presented and compared in this study to justify the use of MULASSIS for the design of multifunctional materials. SHIELDOSE-2 makes use of Monte Carlo code ETRAN, which treats radiation processes with straight ahead, continuous slowing down approximation. This makes SHEILDOSE-2 fast and accurate for dose estimation for relatively thin shield. But the code is limited with a lot of straight forward approximation [75]. Also, secondary particles generated due to interaction of the radiation with the shield are not accounted for in SHIELDOSE-2. In addition, definition of shield material in SHIELDOSE-2 is limited to mainly Aluminium and some few metals. The code cannot be used in defining shields and detectors with non-metals such as polymers and graphite. MULASSIS, a GEANT4-based Monte Carlo (M-C) simulation tool for ionising dose and particle fluence analysis of radiation shields, can be applied to a wide range of materials. GEANT4 is a result of international collaboration among ESA (European Space Agency), CERN (European Organization for Nuclear Research) and several universities and institutes, to develop an accurate and sophisticated treatment of individual radiation particles and their interaction probabilities with target atoms and

nuclei along their trajectories. Application of GEANT4 ranges from space physics to high energy physics to medical physics. GEANT4 simulation toolkit provides a comprehensive physics modeling capabilities for particle transport simulation. In addition, GEANT4 contains a comprehensive list of physics models to simulate interactions for all relevant particles and allows selection of these models for defined simulation. This approach allows multiple interactions to be monitored.

For the radiation environment in HEO, the physics lists used for simulation were the standard electromagnetic interaction and decay physics processes such that all relevant physics scenarios were treated. The range of available electromagnetic processes in GEANT4 is extensive such that all possible interactions are covered and these have been discussed in Section 2.1.5. Example includes Compton Effect, pair production, photo electric effect for photons, electrons interaction via bremsstrahlung process, multiple coulomb scattering and ionization process, positron interaction similar to electron interaction with discrete annihilation processes, ions integration based on coulomb scattering, and ionization and nuclear fragmentation through decay processes. The Geant4 radiation transport toolkit in MULASSIS uses these interaction models to account for the interaction of electrons, protons, solar particles and GCRs, as well as other secondary radiation generated during collision of primary particles the materials.

The radiation fluencies for various charged particles predicted in 3.3 (as detailed in Figure 3.2), were input to SHIELDOSE-2 and MULASSIS, which performs the particle transport analysis for the chosen shield geometry and composition and outputs the absorbed and transmitted TID. The step-by-step procedure used in particle transport simulation using MULASSIS is described in

Appendix A. This process is repeated for various shield thickness (i.e. areal density) to obtain TID as a function of thickness or areal density.

3.4.4 Results and Discussion for Transmitted TID of Homogenous Materials

It should be noted that the radiation attenuation results presented in this section is for 15 years' mission duration. Figure 3.8 shows representative result of predicted transmitted Total Ionizing Dose (TID) with Al shield thickness, determined using NASA's SHILEDOSE-2, for the three identified orbits. Since the thickness of a shield is directly proportional to its areal density, the latter is plotted in the figure to allow direct comparison of the shielding effectiveness of different materials at a constant shield weight. The TID varies inversely with the areal density of the shield. The dose also varies with the orbit. The orbit that requires minimum Al shield weight depends on the desired level of radiation protection. For example, it can be inferred from Figure 3.8 that the TAP orbit would require the lightest Al shield to yield any transmitted TID < 30 krad, while the Modified Tundra orbit would require the lightest Al shield for transmitted TID > 30 krad. Therefore, the suitability of an orbit to the PCW mission depends on the one offering good imagery altitude and minimum shield weight at certain dose limit.

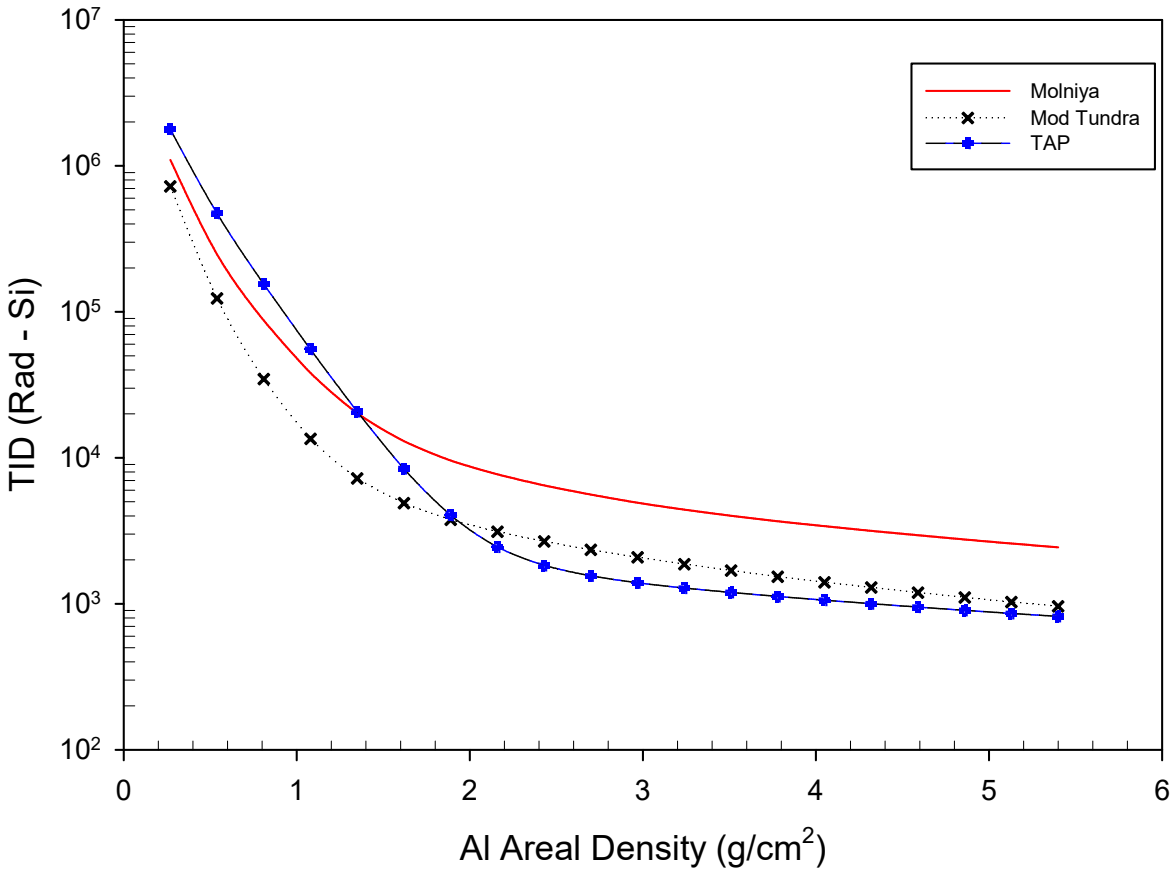

Figure 3.8 TID absorbed by the Si-detector as a function of areal density of aluminum shield in the 3 orbits, simulated using SHIELDOSE-2

3.4.4.1 Comparison of Predictions of Transmitted TID using SHEILDOSE-2 and MULASSIS

While simple radiation tool such as SHIELDOSE-2 (a simple look-up table approach) has been the de-facto standard in rapid calculation of the TID for a shield, it has limited library of materials that can be used in the detector library and the shield. It can be used with Aluminium only and cannot be used to model other homogenous materials and composite materials as shield. However, MULASSIS allows calculation of TID behind a shield made up of variety of homogenous materials and composite materials. Results of simulation, using the two codes, for the Aluminum in Modified Tundra orbit were compared to highlight the difference between the two codes and to highlight the relative accuracy of MULASSIS. The TID for Al calculated using MULASSIS is compared with the prediction using SHIELDOSE-2 and presented in Figure 3.9.

Both codes yield essentially the same result with variance observed at higher thickness. The TID predicted using MULASSIS fluctuates at higher thicknesses. This fluctuation is due to the production of secondary bremsstrahlung photons and neutrons. With increase in thickness, the attenuation of radiation increases. However, the production of Bremsstrahlung radiation also increases with increase in thickness, which would increase the TID. Hence, the observed fluctuation is believed to be due the production of secondary bremsstrahlung photons.

Bremsstrahlung radiation is the main secondary product especially for energetic trapped electrons and MULASSIS accounts better for the production of bremsstrahlung radiation from all species when compared to SHIELDOSE-2 [75]. In order to confirm this, the shielding effectiveness of hydrogen gas, with an atomic number Z = 1, in the Molniya orbit was simulated using MULASSIS and compared in Figure 3.10 with the results for PE and AL.

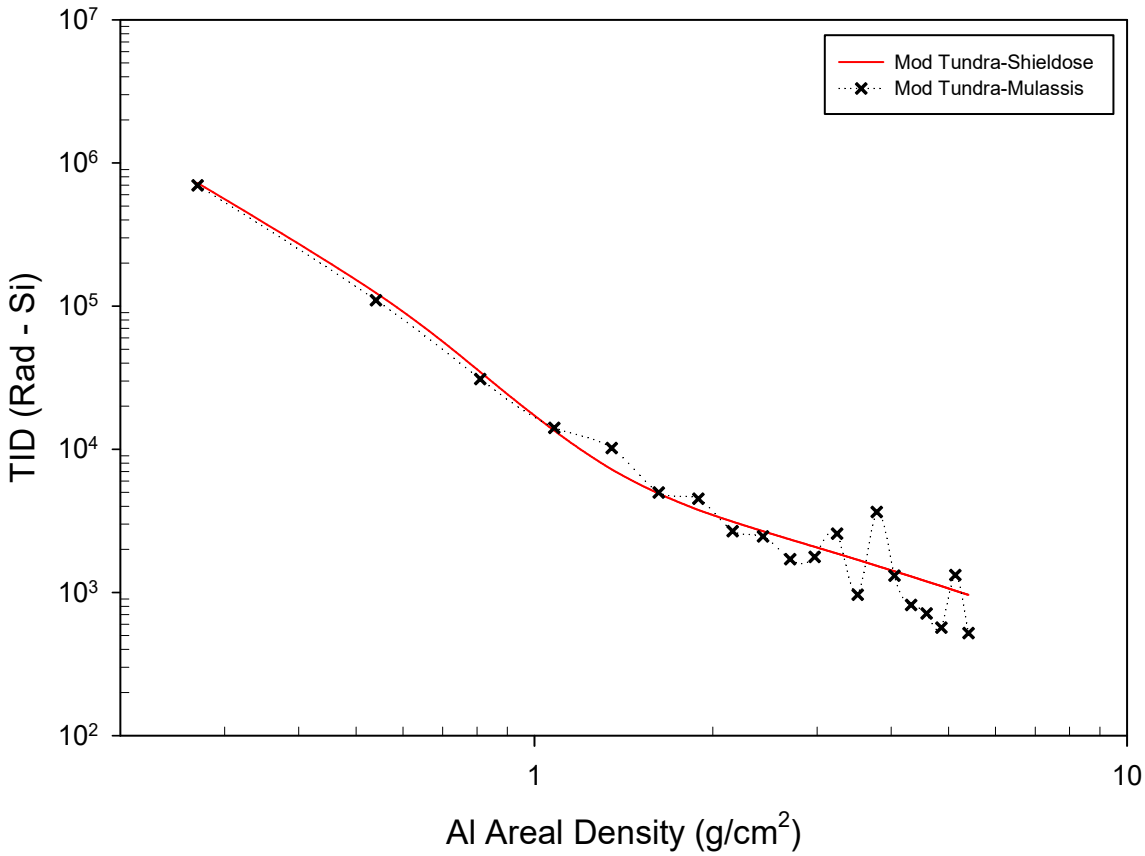

Figure 3.9 TID Transmitted through the shield and absorbed by the Si-detector as a function of areal density of aluminum shield in Modified Tundra orbit, simulated using SHIELDOSE-2 and MULASSIS.

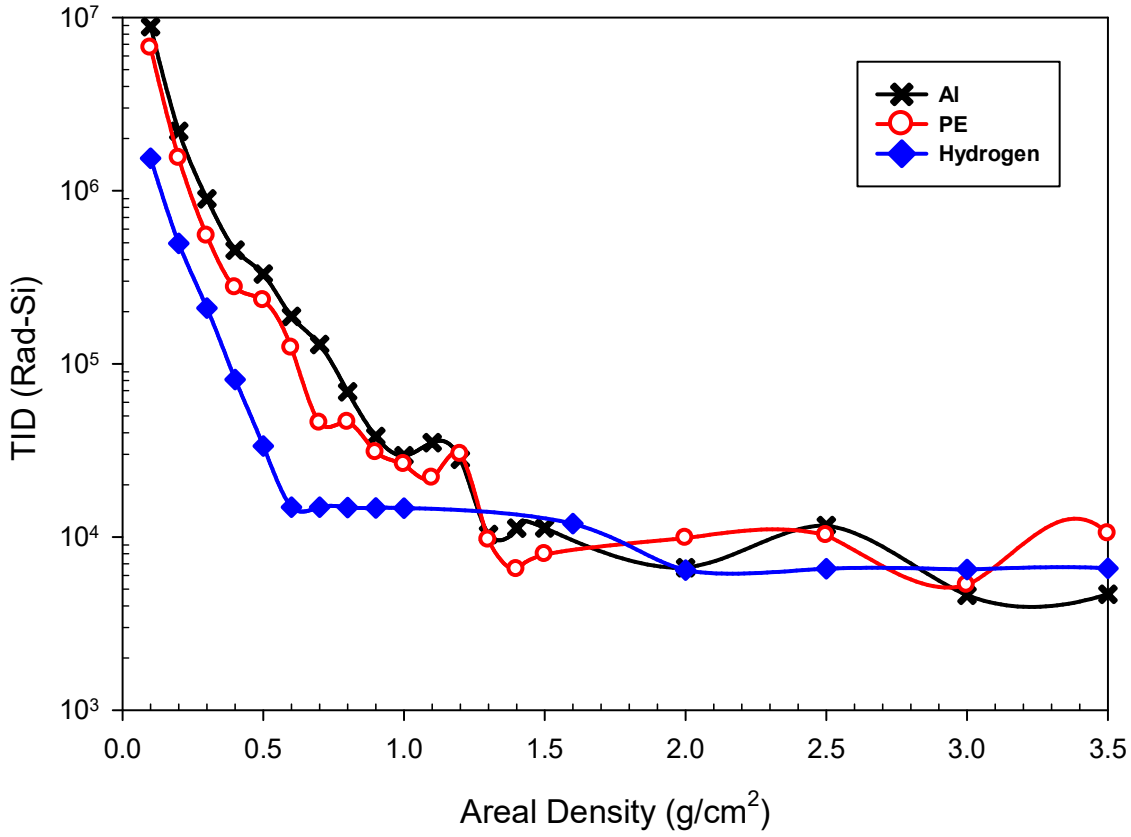

Figure 3.10: Influence of generation of bremsstrahlung photons and secondary particles on the TID behind H_2, Al, and PE, simulated using MULASSIS, in the Molniya orbit

Lack of oscillation in the simulated curve for hydrogen suggests that the fluctuations observed in the curves for PE and Al in Figure 3.10 and figures in the rest of this chapter are due to the effect of secondary particles. While the generation of secondary particles increases with thickness, their fragmentation and energy loss within the shield also increases with increase in thickness. The competition between these two processes is believed to be the reason for the observed fluctuations. The areal density of 1.0 g/cm^2 in Fig. 6 corresponds to a thickness of 3.7 mm, 10.6 mm, and 11940.6 mm of Al, PE, and H_2 respectively. It has been confirmed through simulation that the initial decrease in the TID in the curve for H_2 is due to the shielding of trapped protons and the observed plateau beyond 0.6 g/cm^2 is due to contributions from SPE and electrons. Another linear decrease in the TID due to shielding of SPE by H_2 is observed at much higher thickness values.

Following this, the subsequent TID prediction results presented in this thesis have been obtained using MULASSIS due to its ability to accommodate various homogenous and composite materials as well as to account for secondary particles.

3.4.4.2 Effect of Individual Radiation Particles on Transmitted TID for Homogenous Materials

The four charged particles found in the radiation environment of the HEO are trapped protons, trapped electrons, SPE and GCR. Firstly, the effects of each of these particles in the HEOs on the five homogenous materials were studied. The radiation shielding effectiveness of five homogenous shield materials in the HEO's electron and proton radiation environments are compared in Figures 3.11 and 3.12 respectively. The five shield materials are aluminium (Al),

tantalum (Ta), tungsten (W), polyethylene (PE) and epoxy. The results are limited to an areal density of 1.5 g/cm^2 since comparative evaluation are done for TID greater than 10 krad. It can be inferred in Figure 3.11, that high atomic number (Z) materials such as W and Ta, are more effective in attenuating the electrons. That is, for a given areal density, the TID behind the W and the Ta shields are lower than that of low Z materials. This reinforces the reported observation that high Z materials are effective in shielding against electron [14, 76]. Low Z materials such as PE and Epoxy are more effective in attenuating proton particles as shown in Figure 3.12.

It can also be observed from Figure 3.11 that PE and epoxy performs slightly better than Al (with a higher Z) even in an electron environment. Two major competing processes in passive shielding are energy loss and fragmentation. Although the magnitude of energy loss would be higher with high Z materials, they could also increase the TID through generation of secondary particles. In contrast, fragmentation, which will be higher with low Z materials, results in minimal production of secondary particles and hence, minimal contribution to TID due to secondary particles. Low Z materials have more nuclei in the path of the radiating particles for the same shield thickness per unit mass and per unit cross-sectional area, which increase fragmentation and decrease the production of bremsstrahlung photons. This accounts for the lower required shielding thickness for PE and Epoxy when compared with Al in the electron environment.

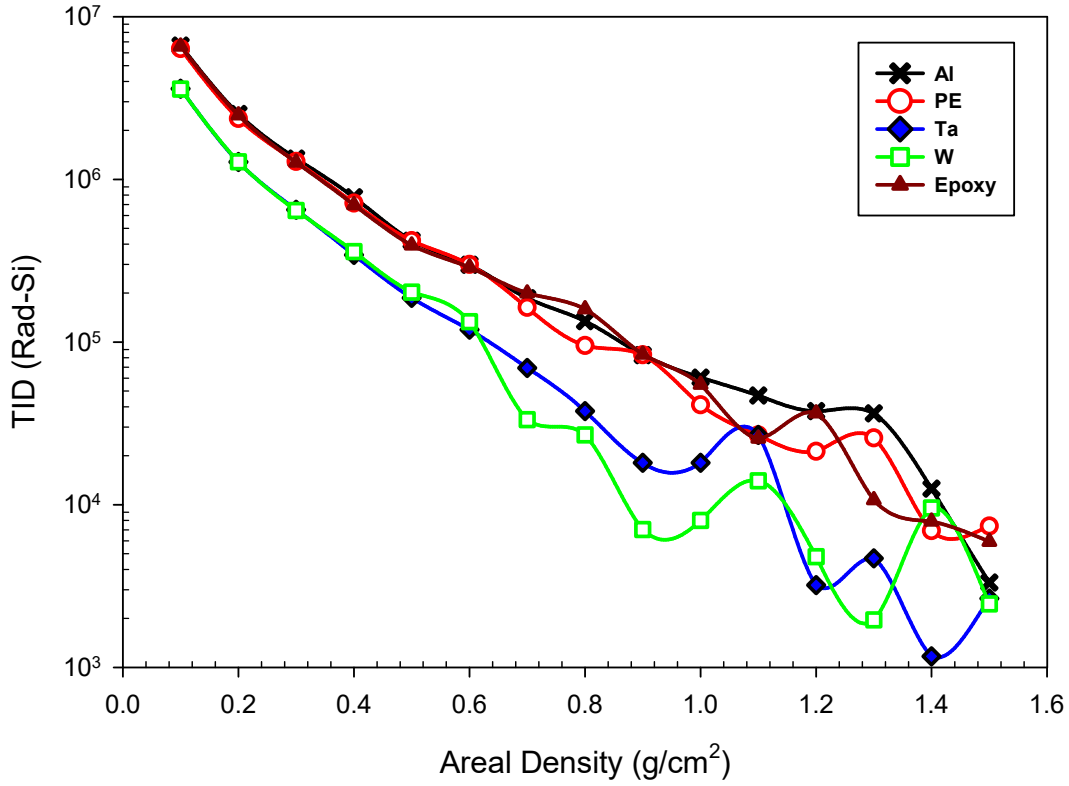

Figure 3.11: $TID_{Transmitted}$ for five different materials in the electron radiation environment in TAP orbit.

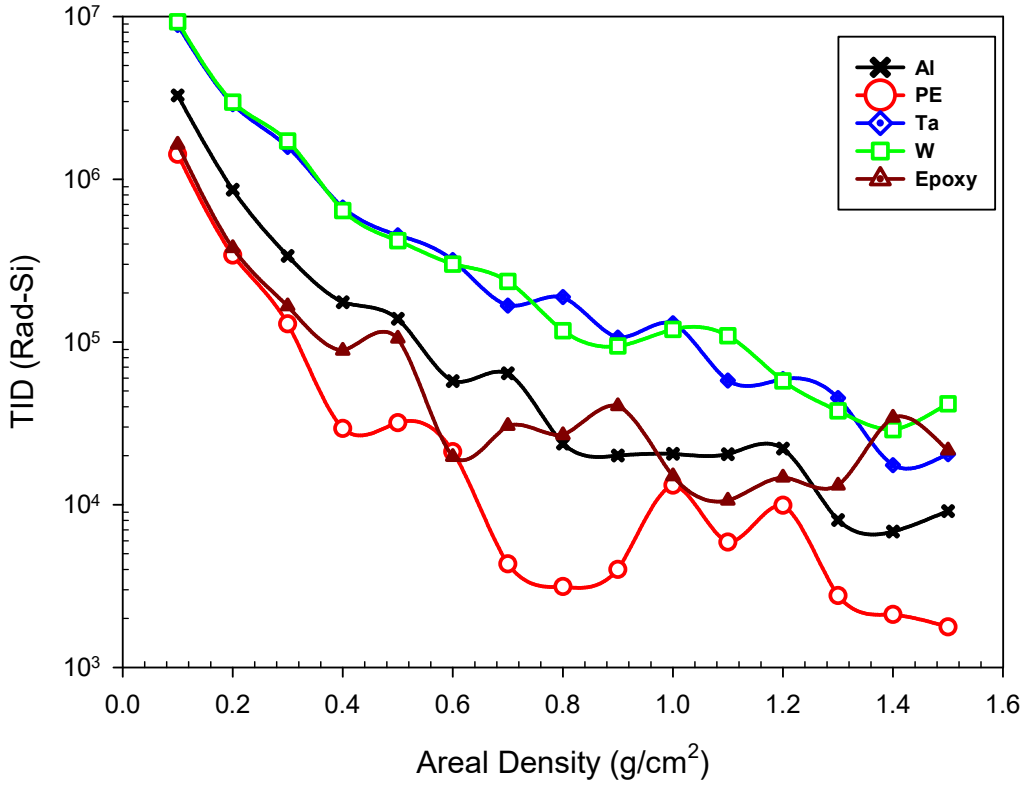

Figure 3.12: $TID_{Transmitted}$ for different materials in the proton radiation environment in Molniya orbit.

The efficiency of Low Z materials in shielding against protons was also observed in solar particles environment. As shown in Figure 3.13 for Modified Tundra, low Z material like PE and Epoxy have better shielding efficiency in stopping solar particles. Satellites in Modified Tundra would experience the highest average flux of solar due to higher apogee (~42,488 km). Solar particles primarily contain low energy protons with some heavy ions [18]. PE and Epoxy perform better in shielding against heavy nuclei through fragmentation in addition to shielding low energetic protons in SPE spectra. A number of recent publications [13, 77] have identified PE with high concentration of hydrogen atoms to shield better against protons and solar particles than materials with low concentration of hydrogen atoms.

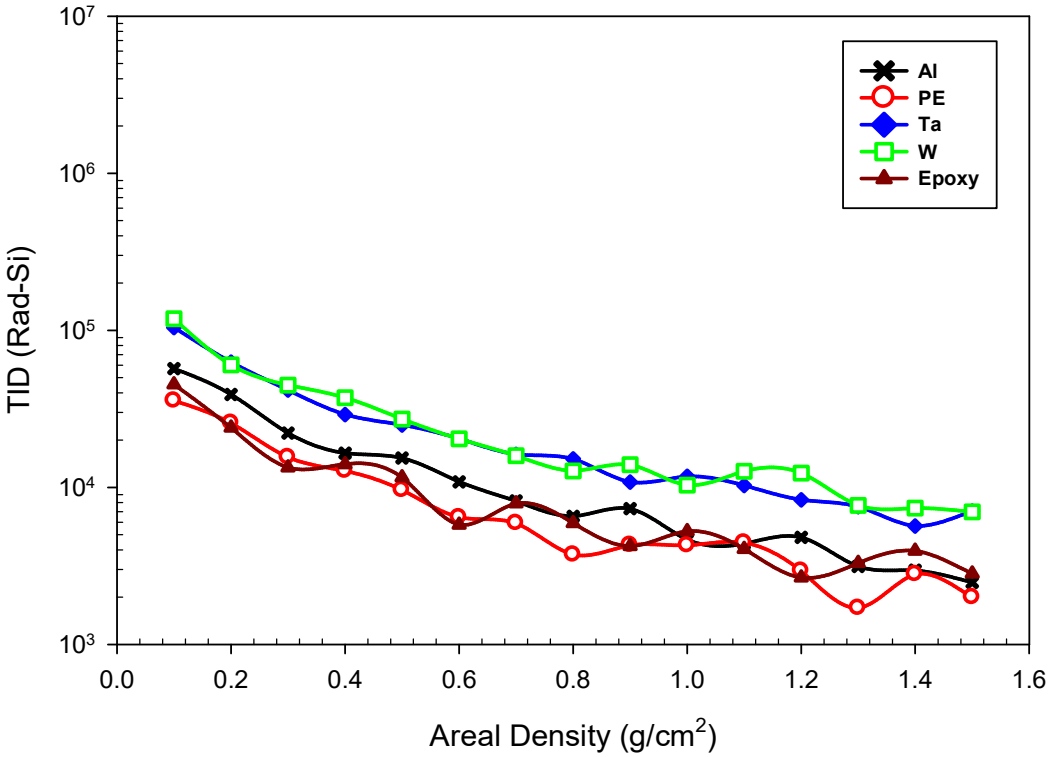

Figure 3.13: $TID_{Transmitted}$ for five different materials in the solar particles radiation environment in Modified Tundra orbit.

3.4.4.3 Combined Effect of All Radiation Particles on Transmitted TID for Homogenous Materials

The effect of combined radiation environment of electrons, protons, solar particles and GCRs encountered in the three HEOs on the transmitted TID through five homogenous materials on a Si detector was studied using MULASSIS. The transmitted TID is plotted as a function of areal density for the five homogeneous materials in Figures 3.14 – 3.16 for Molniya, Modified Tundra and TAP orbits, respectively. The TID due to combined radiation environment decreases with areal density (i.e. thickness) of the shield. The fluctuation increases significantly beyond the areal density of 1g/cm^2. Due to large fluctuation in the TID at higher shield areal density, selection of one material over other based on the TID is rather difficult. In most cases, satellite design engineers require certain TID limit within the space bus. If a TID limit corresponding to an areal density in the range of 0 – 1 g/cm^2 is acceptable, then a material's suitability as shielding material can be discerned with relative ease.

Radiation design margin (RDM) is the radiation tolerance level of a component or a system used in a satellite, during a mission. For the PCW mission, a RDM of 50 krad was arbitrarily chosen. Hence the areal density values required to achieve an arbitrary dose of 50 krad was extracted from Figures 3.14 - 3.16 and tabulated in Table 3.3 for the five different materials.

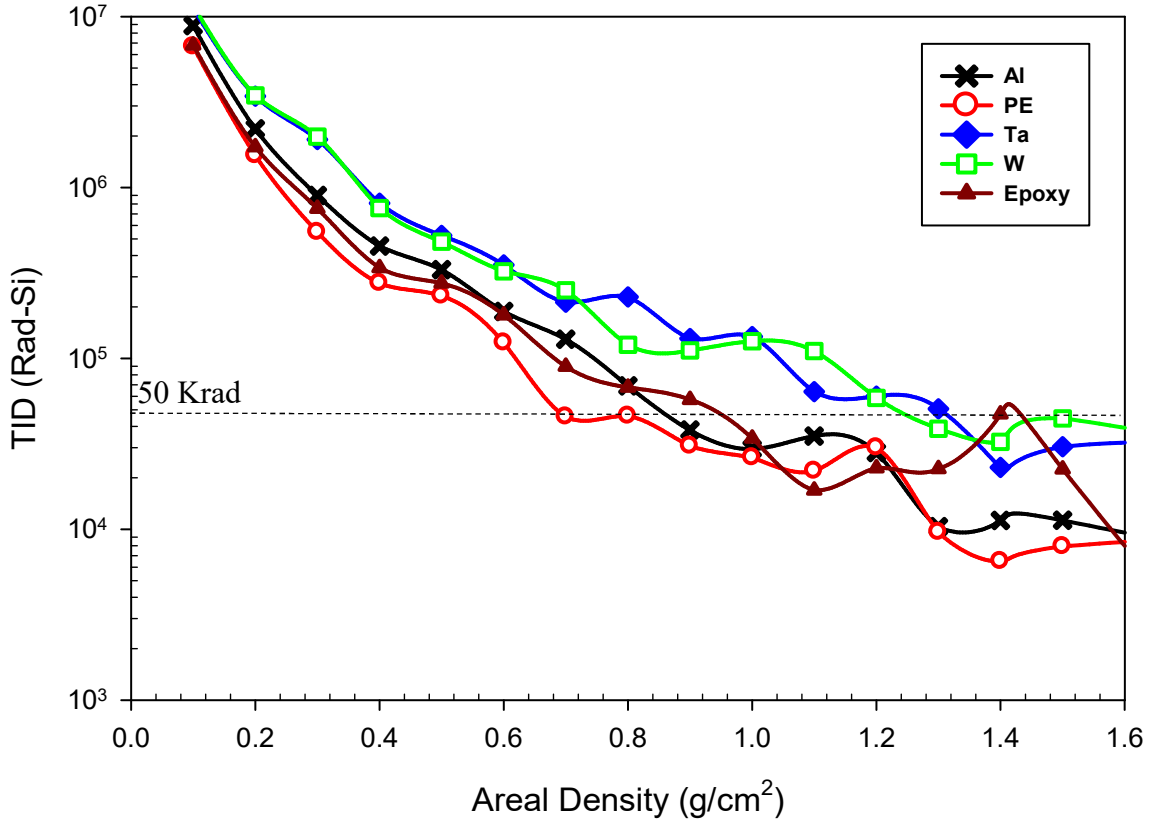

Figure 3.14: $TID_{Transmitted}$ for five materials in a combined environment of electrons, protons and solar particles in Molniya.

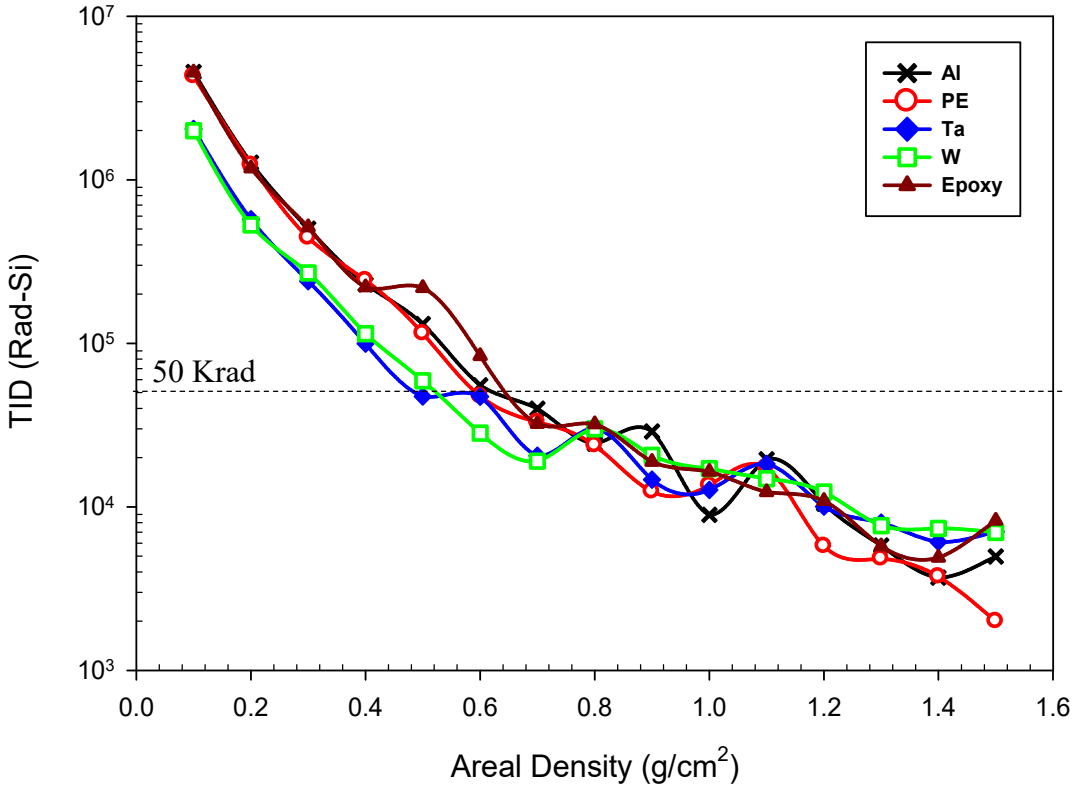

Figure 3.15: $TID_{Transmitted}$ for five materials in a combined environment of electrons, protons and solar particles in Modified Tundra

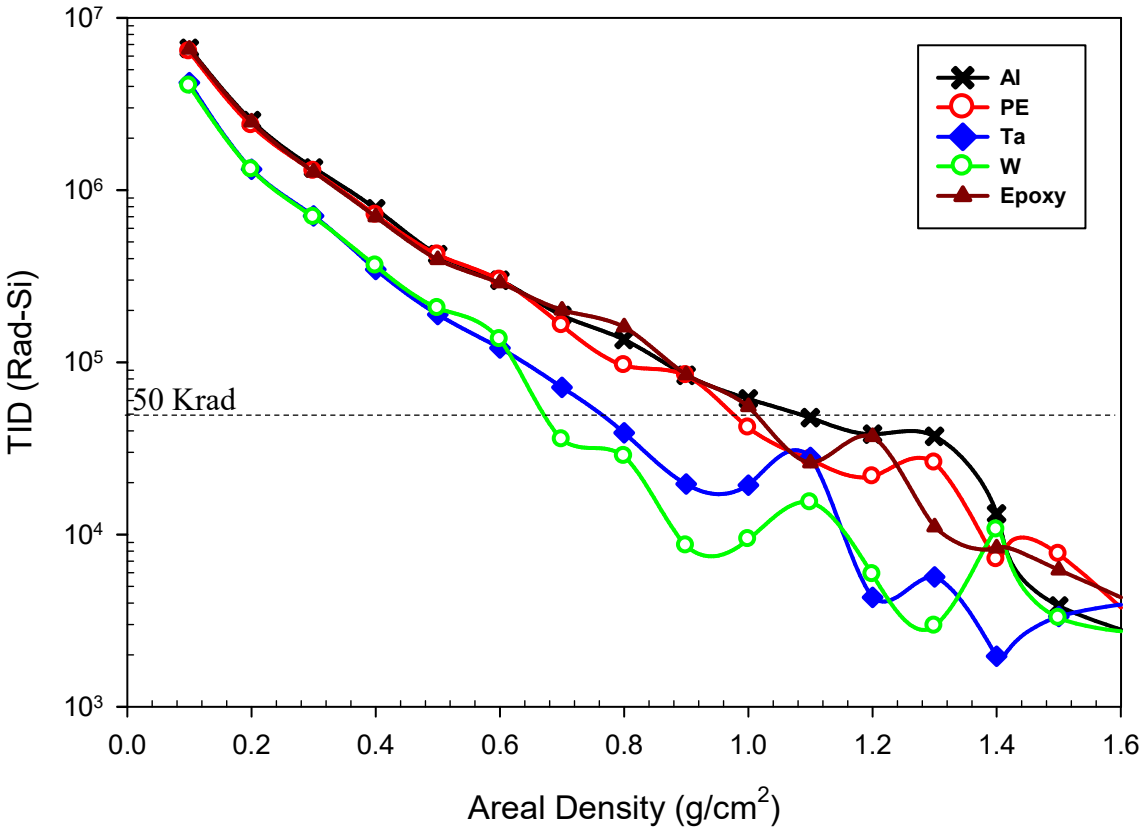

Figure 3.16: $TID_{Transmitted}$ for five materials in a combined environment of electrons, protons and solar particles in TAP

Among the 5 materials studied, Ta would result in the lightest shield (0.49 g/cm^2) in Modified Tundra Orbit. Unfortunately, Modified Tundra could not meet other mission requirements such as high cost of high Z materials and limited coverage for the mission [10]. The next material to offer the lightest shield is W (0.68 g/cm^2) in TAP orbit. While meeting other orbital requirement, TAP may also result in higher cost of shield due to cost of high Z material – W, identified to be optimal. Slightly behind is PE that offers the lightest shield (0.7 g/cm^2) in Molniya orbit. PE shields are lighter than Al shields in all the three HEOs, with a maximum weight saving of 26% in the Molniya orbit. Thus, Molniya orbit would satisfy both the mission and the shield weight requirements provided PE is used.

Regardless of the orbit selected, it is important to note that PE consistently represents a lighter shielding option than Al. It is interesting to note that, for a PE shield, it is the TAP orbit, not the Molniya that require the heavier shield, despite the higher proton fluxes found in Molniya. The Modified Tundra orbit requires the lightest PE shield, reflecting the comparatively low proton and electron flux levels at higher orbit altitudes. Based on the consideration for radiation shielding in Molniya, the results show that PE shield is lighter than the Al shield, resulting in weight savings while meeting the desired TID tolerance. This weight savings for the RDM (50 krad) chosen is 26%.

A weight savings of 26% in Molniya combined with better performance of PCW spacecraft (better imaging, shorter communication path lengths, shorter delay times in communication, etc.) and longer mission time (15 years used in the simulation) would justify the development of polymer based shields to replace the traditional Al shields.

Table 3.3: Required areal density to meet a TID of 50 krad for five materials in 3 HEO orbits

Orbit	Shield Areal Weight (g/cm^2)				
	Al	PE	Ta	W	Epoxy
Molniya	0.95	0.70	1.30	1.22	0.94
Modified Tundra	0.62	0.6	0.49	0.52	0.65
TAP	1.10	0.98	0.76	0.68	1.02

While the results in this section conforms the ability of PE to meet the transmitted TID criterion, its ability to meet the absorbed TID criterion was studied next.

3.4.5 Effect of Radiation Damage in PE in Molniya Orbit

Exposure to radiation, during long term space mission, may be sufficient to degrade critical properties of some materials if the absorbed dose $TID_{Absorbed}$ of such material is greater than its $TID_{Critical\ Absorbed}$. Table 3.4 shows the $TID_{Critical\ Absorbed}$ of the five materials studied and their corresponding $TID_{Absorbed}$ at areal densities needed to meet a TID of 50 krad in Molniya orbit.

As observed from table 3.4, radiation-induced damage is not of much significance for metals while polymeric materials such as PE and Epoxy are more sensitive to radiation resulting in significant degradation of their mechanical properties.

As observed in Table 3.5, at 0.7 g/cm^2 of PE the transmitted TID through PE meets the RDM criterion of 50 krad but the $TID_{Absorbed}$ in PE is greater than $TID_{Critical,\ Absorbed}$ for the chosen mission of 15 years in Molniya. Increasing the areal density of PE to 0.9 g/cm^2 would reduce the absorbed TID ($TID_{Absorbed)}$ below the $TID_{Critical,\ Absorbed}$. However, his would negate any weight savings attained by PE when compared with Al in Table 3.5.

Hence, efforts were made to hybridize PE with other materials to reduce the absorbed dose in PE while meeting the $TID_{critical,\ transmitted}$ in Molniya orbit. Details on the PE hybridization are discussed in the next Section.

Table 3.4: Comparison of $TID_{Critical\ Absorbed}$ with $TID_{Absorbed}$ of the selected five materials

Materials	$T_{critical,\ Absorbed}$ (rad)	$T_{Absorbed}$ (rad)
Aluminum	1.0×10^{17}	2.03×10^{7}
Polyethylene	2.0×10^{7}	2.52×10^{7}
Tantalum	1.0×10^{19}	1.01×10^{7}
Tungsten	1.0×10^{19}	1.32×10^{7}
Epoxy	1.0×10^{8}	1.75×10^{7}

Table 3.5: $TID_{Transmitted}$ and $TID_{Absorbed}$ through PE in Molniya orbit

PE Areal Density (g/cm^2)	$TID_{Transmitted}$ (rad) - Si	$TID_{Absorbed}$ (rad)- PE
0.1	2.43E+06	1.70E+08
0.2	8.49E+05	8.72E+07
0.3	4.10E+05	5.85E+07
0.4	2.66E+05	4.40E+07
0.5	1.39E+05	3.52E+07
0.6	8.20E+04	2.94E+07
0.7	5.01E+04	2.52E+07
0.8	3.24E+04	2.37E+07
0.9	2.38E+04	1.96E+07
1	2.43E+04	1.77E+07
1.1	2.11E+04	1.61E+07
1.2	1.60E+04	1.47E+07
1.3	8.82E+03	1.36E+07
1.4	7.30E+03	1.26E+07
1.5	6.77E+03	5.75E+06

3.5 Radiation Shielding Effectiveness of Two-layer Hybrid Material Shields

The radiation shielding effectiveness is defined in this thesis as the ability of a material to meet the radiation shielding requirements on $TID_{Critical,Transmitted}$ and $TID_{Critical,Absorbed}$ while weighing the least. In order to reduce the absorbed TID in the PE, another layer was added before PE. Such a multilayer concept has been employed in the past for radiation shielding analysis for interplanetary mission [13, 55, 58], where the main radiation particle concern is GCR. With the focus of this research in HEO, a multi particle space environment, multilayer concept refers to the order and arrangement of layers with various atomic numbers (Z) to increase the radiation shielding effectiveness of multi- layered structure against electrons, protons, solar particles and GCRs.

The two-layer (High Z / Low Z) configuration was employed to reduce the absorbed TID in PE. The high Z metallic layer is good at electron attenuation while the low Z PE layer is good at attenuating the protons. The radiation environment in HEO is dominated by both electrons and protons and thus, a high Z metallic layer placed before the PE layer would attenuate the electrons, resulting in the reduction of the radiation entering the PE layer and thus the absorbed TID in the PE layer. High Z layer of Al, Ta and W were placed in front of the PE layer and the volume fraction of both layers were varied by varying their thickness to determine the volume fraction of the metallic layer required to meet the radiation shielding criteria. The TID transmitted through the shield and the TID absorbed by the PE layer are plotted as a function of volume fraction of the PE layer in Figure 3.17 for a representative composite aerial density of 0.75 g/cm^2.

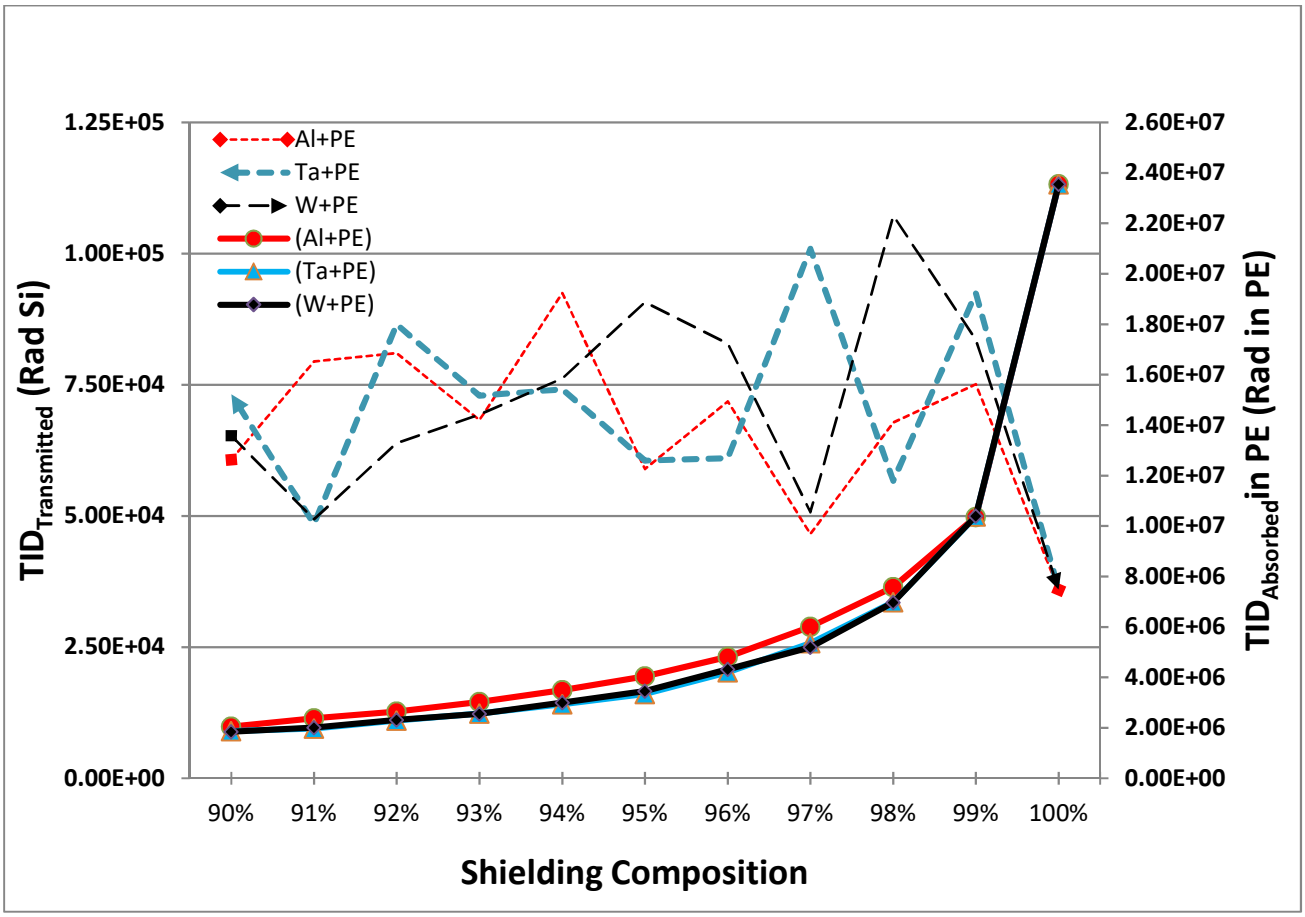

Figure 3.17: Absorbed TID in PE and Transmitted TID through the three two-layer shields at 0.75 g/cm^2. (*The volume fraction of PE is shown in the x-axis and the rest is that for the metal layer;)*

Note: Dotted lines are for $TID_{Transmitted}$ *while solid lines are for* $TID_{Absorbed.}$

The transmitted TID is the plotted along the primary Y- axis while the absorbed TID in PE is plotted along the secondary Y-axis. The total areal density of the composition was kept constant at 0.75 g/cm^2 while the volume fraction of PE was varied between 100% and 90% as noted on the x-axis of the plot.

It can be inferred that 3% Al-97% PE, 9%Ta-91% Al, and 9% W-91% PE meet the two criteria namely (a) Transmitted TID is ≤ 50 krad and (b) absorbed TID < $TID_{Critical}$ (see Table 3.1). These correspond to thicknesses of 84 μm, 41μm, and 35 μm for Al, Ta, and W respectively. The corresponding PE thicknesses are 2.716 mm, 4.146 mm, and 4.146 mm respectively.

Thus, above analysis confirms that adding a thin layer of a metal before PE would reduce the absorbed TID in PE below the threshold level. Aluminum was chosen for subsequent analysis due to its low cost and due to its history in space performance.

However, due to inferior mechanical properties of PE, the majority constituent of the 2-layer composite shield, the latter does not meet the structural requirements. Hence, the effect of reinforcing the PE layer with fibers, which would increase the mechanical properties, on the radiation shielding effectiveness was studied next. Due to the limitation imposed by MULASSIS, this fiber was added as a layer to the PE layer and the effect of volume fraction and arrangement of the reinforcing layers (with respect to the PE layer) on the radiation shielding effectiveness of the PE layer was studied.

3.6 Radiation Shielding Effectiveness of Carbon Fiber Reinforced Polymer Composite – Effect of Composition and Structure

Few published studies have examined the shielding effectiveness of PE fiber reinforced epoxy composite [12, 13, 78, 79]. In these studies, ultrahigh molecular weight PE fibers have been used as reinforcement in epoxy matrix. However, mechanical properties of this composite are inferior to those of carbon fiber reinforced epoxy composites owing to inferior properties of PE fibers when compared to those of carbon fibers. However, carbon and epoxy have lower radiation shielding effectiveness than PE. Hence, in this study two types of composites, that maximized PE content, were considered: (a) PE fibers reinforced PE matrix composite and (b) Carbon fiber reinforced PE matrix composite. Since the radiation shielding effectiveness of PE matrix is not affected by the introduction of the PE fiber, the carbon fiber reinforced PE matrix composite was the focus in this study.

Carbon is also a low Z material with density value of 1.7 g/cm^3. It is commonly used in form of carbon fiber to reinforce polymeric matrices. Though its shielding effectiveness is less than PE, it has high specific modulus and tensile strength. However, the effect of volume fraction of reinforcing fibers and its arrangement within the composite (i.e. structure of composites) on shielding effectiveness of PE is not known and hence was studied in this thesis.

The building block of a continuous fiber composite laminate is a unidirectional tape prepreg with parallel fibers impregnated with a matrix or a fabric prepreg with fibers woven in two orthogonal directions (0° and 90°) and impregnated with matrix. The fiber volume fraction (V_f) in the prepreg would be in the range of 55 – 65%. The prepreg, ~ 0.2 – 0.4 mm in thickness, is stacked in a particular stacking sequence to form a multidirectional composite of required thickness, as shown in Figure 3.18(a). The stacking sequence defines the orientation of fibers in

various layers with respect to loading direction (X-axis in Figure 3.18(a)) as well as location of these layers within a laminate. The number of layers per orientation is determined by dividing the required thickness per orientation (dictated by the mechanical properties) by the thickness of the prepreg. The volume fraction of a layer with an orientation ($V_{[0]}$ or $V_{[90]}$ in Figure 3.18(a)), determined by the ratio of the total thickness of all layers with an orientation to the total composite thickness, the stacking sequence, and volume fraction of the fibers (V_f) in each layer, determine the in-plane mechanical properties of composite laminates. A change in the thickness of each layer (i.e. prepreg), would not affect the in-plane properties as long as the volume fraction of each orientation ($V_{[0]}$ or $V_{[90]}$ in Figure 3.18(a)) is maintained.

Similarly, the interchanging the location of each layer within the composite (for example, [90/0/0/90] instead of [0/90/90/0] shown in Figure 3.18(a)) would not affect the in-plane properties. However, same cannot be said about the radiation shielding effectiveness of the composite material.

The level of attenuation of an incident radiation, within a material with a given areal density, depends on its path length (i.e. thickness) in that material and the atomic number of atoms in that material. In addition, it would depend on the sequence of interaction if a shield contains more than one material; for example, in a two-layered composite made up of polyethylene (PE) and Carbon (C,) the intensity and the energy of the beam incident on PE in PE/G lay-up would be different from that incident on PE in C/PE lay-up resulting in difference in attenuation and TID behind the shield.

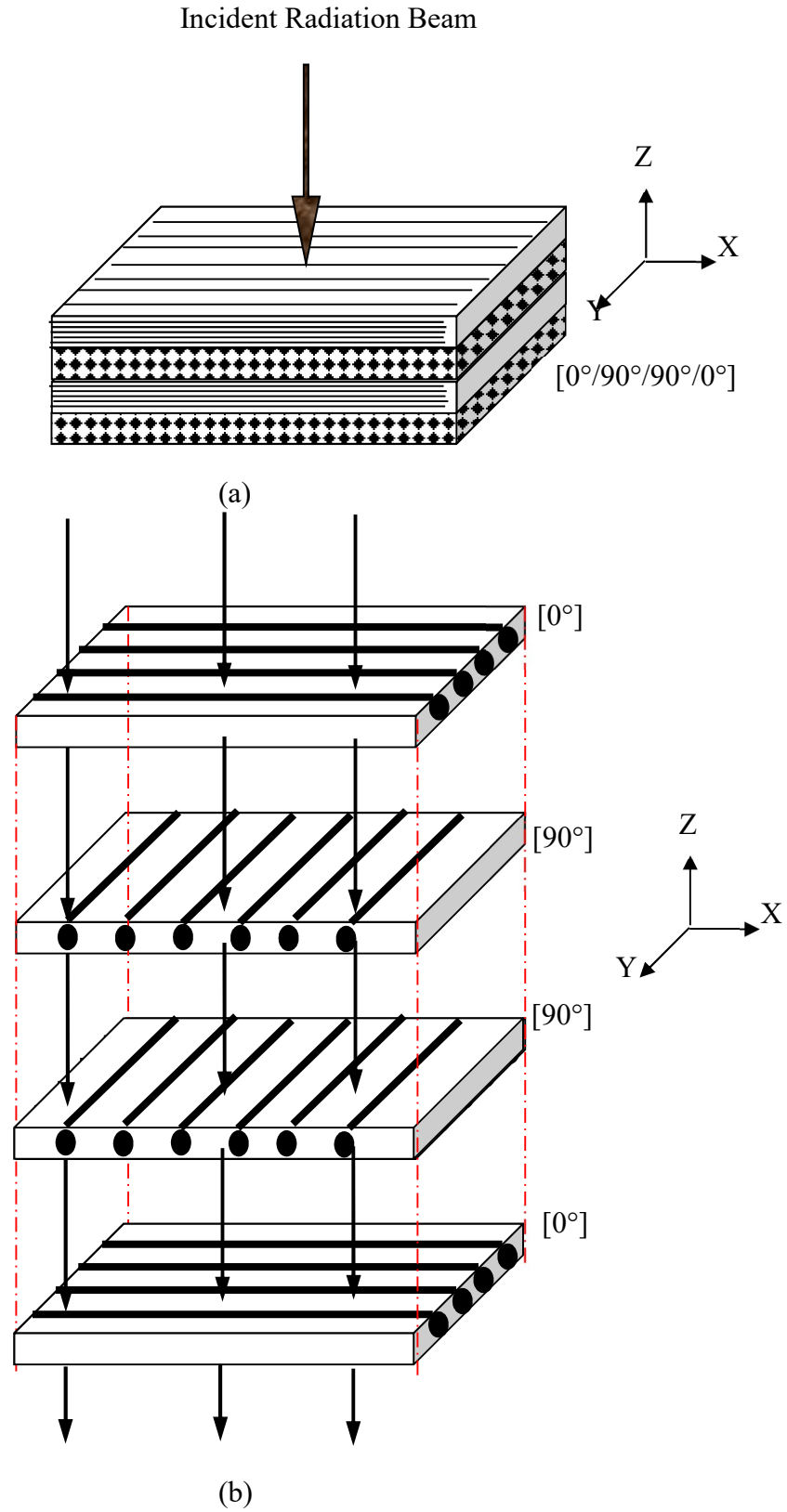

Figure 3.18: Schematic of (a) a four-layer [0°/90°/90°/0°] composite shield and (b) attenuation paths for energetic particles transport through layers of the composite shield.

The path length and the sequence of interaction in a composite consisting of materials with differing Z would vary in a complex manner as illustrated in Figure 3.18(b) irradiating along the Z axis. The beam could travel parallel to the reinforcing fibers in the matrix of the composite without intercepting the fibers or travel alternatively between the fiber and the matrix or in a complex manner depending on the scattering angle. Thus, the TID behind a composite laminate shield would depend on its structure characterized by (a) the V_f of fibers in a composite layer (b) the thickness of each layer, (c) the orientation of fibers within a layer, (d) $V_{[\theta]}$ of layers with fiber orientation [θ], and (e) the stacking sequence.

In this design, the effect of composite laminate structure, as described above in different size scales, on its radiation shielding effectiveness (determined as TID behind the shield) was studied through particle transport simulation of energetic particles through a material. Due to the limitation of the simulation software in defining the composite structure, the composite was modeled as a layered structure made-up of two materials, the polyethylene (PE) matrix and the carbon (C) reinforcing fibers. While this simplification does not capture the effect of ALL features associated with a composite structure as discussed above, it provides an insight into the effect of thickness, volume fraction and stacking sequence of each phase (PE and C) on the TID behind a PE-C composite shield with a given areal density.

To demonstrate this effect of composite laminate structure, composite shields with 2, 4, 8 and 16 layers were defined and used in the simulation. The procedure for deriving the composition and structure of a composite shield can be understood using Table 3.6 for a 2-layer shield consisting of one layer each of PE and C.

Table 3.6: Composition and structure of a two-layer composite shield with an areal density of 0.2 g/cm^2

Composite Composition (Volume fraction)	Composite Density (g/cm^3)	Composite Thickness (mm)	PE layer thickness (mm)	Carbon Layer Thickness (mm)
100% PE	0.940	2.128	2.128	0.000
70% PE; 30% Carbon	1.168	1.712	1.199	0.514
50% PE; 50% Carbon	1.320	1.515	0.758	0.758
30% PE; 70% Carbon	1.472	1.359	0.408	0.951
100% Carbon	1.700	1.176	0.000	1.176

For a given areal density (0.2 g/cm^2 in Table 3.6), the composite density was determined using rule of mixtures for various volume fractions of PE and C, in the range of 0 -100%. The density was divided by the areal density to yield composite thickness. The thickness of individual layers was determined by multiplying the composite thickness by the volume fraction. The thickness data in Table 3.5 allowed the simulation of the effect of volume fraction of PE or C on TID behind a two-layer composite with an areal density of 0.2 g/cm^2. The effect of stacking sequence was studied by the interchanging the position of PE and C in the path of the beam. This procedure was repeated for by varying the areal density of the two-layer composite in the range of 0.2 to 1 g/cm^2. The areal density range was chosen based on the result from Section 3.4.4.3 and represents the range in which PE shield can be lighter than Al shield.

The 4-layer composite consisted of 2 layers each of PE and C, and the thickness of each layer was determined by dividing the thickness of a layer, determined for the 2-layer composite with a given areal density, by two. The four layers were inter-dispersed to study the effect of layer thickness and stacking sequence at a constant volume fraction and areal density. The various stacking sequences studied were [PE/C/PE/C] abbreviated as $[PE/C]_2$, [C/PE/C/PE] abbreviated as $[C/PE]_2$, [PE/C/C/PE] abbreviated as $[PE/C]_s$, and [C/PE/PE/C] abbreviated as $[C/PE]_s$. The subscript "s" stands for "symmetric" and refers to stacking sequence above the reference plane is a mirror image of the stacking sequence below the reference plane. Such symmetric lay-up is required to prevent warping of a composite laminate during manufacturing as well as during temperature cycling while in orbit.

Similar procedure was used to define the composition and structure of a 8-layer composite shield. Lay-ups, [PE/C/PE/C/PE/C/PE/C] abbreviated as $[PE/C]_4$, [C/PE/C/PE/C/PE/C/PE] abbreviated as $[C/PE]_4$, [PE/C/PE/C/C/PE/C/PE] abbreviated as $[PE/C]_{2s}$ and

[C/PE/C/PE/PE/C/PE/C] abbreviated as $[C/PE]_{2s}$) were used to study the effect of layer thickness and stacking sequence on TID behind a 8-layer composite. In addition, four configurations of 16-layer composite, $[PE/C]_8$, $[C/PE]_8$, $[PE/C]_{4s,}$ and $[PE/C]_{4s,}$ with an areal density of 1.0 g/cm^2 and PE volume fraction of 50%, were used to understand the effect of layer thickness.

The simulated TID, behind a two-layer PE-G composite is plotted in Figures 3.19 (a) – (e) as a function of volume fraction of PE, for various areal densities in the range of 0.2 g/cm^2 to 1.0 g/cm^2, along with the values for 100% PE and 100% C. It can be inferred from this figure that the magnitude of TID behind the shield, for a given volume fraction of PE, decreases with increase in areal density. This is due to increase in the attenuation of incident irradiation due to increase in the thickness of both PE and C with increase in areal density.

Since the shielding effectiveness of PE is better than C, the TID behind the two-layer composite is expected to decreases monotonically with increase in the volume fraction of PE for a given areal density. While this trend is observed at the areal density of 0.2 g/cm^2, the TID varies non-monotonically with increase in the volume fraction of PE at areal densities higher than 0.2 g/cm^2. In addition, it is also influenced significantly by the stacking sequence. The TID behind a PE/C lay-up is lower than the TID behind a C/PE lay-up for all volume fractions of PE at 0.2 g/cm^2 and 0.4 g/cm^2, and for volume fraction of PE < 70% at 1 g/cm^2. However, the TID behind the C/PE lay-up is lower than that for PE/C lay-up for all volume fractions of PE at 0.6 g/cm^2 and below 50% volume fraction of PE at 0.8 g/cm^2.

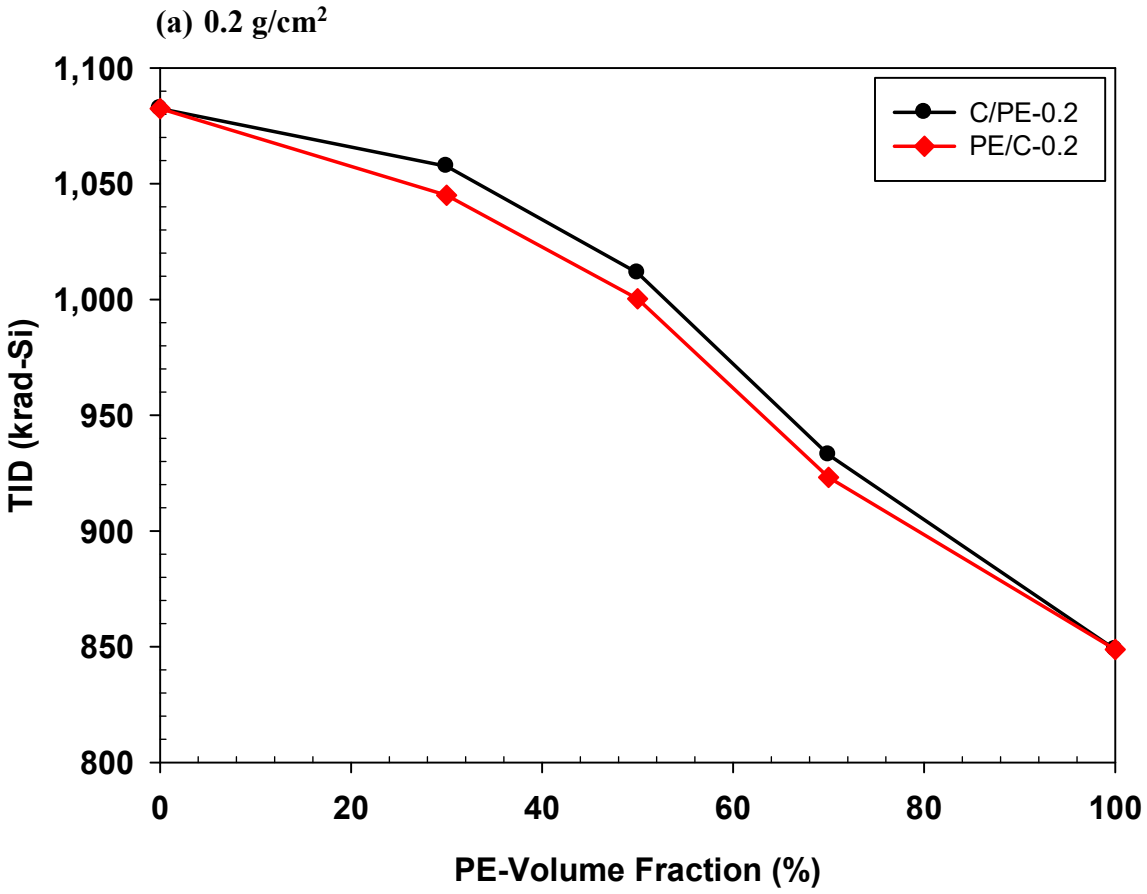
(a) 0.2 g/cm2
1,100
1,050
1,000
950
900
850
800
TID (krad-Si)
0
20
40
60
80
100
PE-Volume Fraction (%)
C/PE-0.2
PE/C-0.2

(b) 0.4 g/cm^2

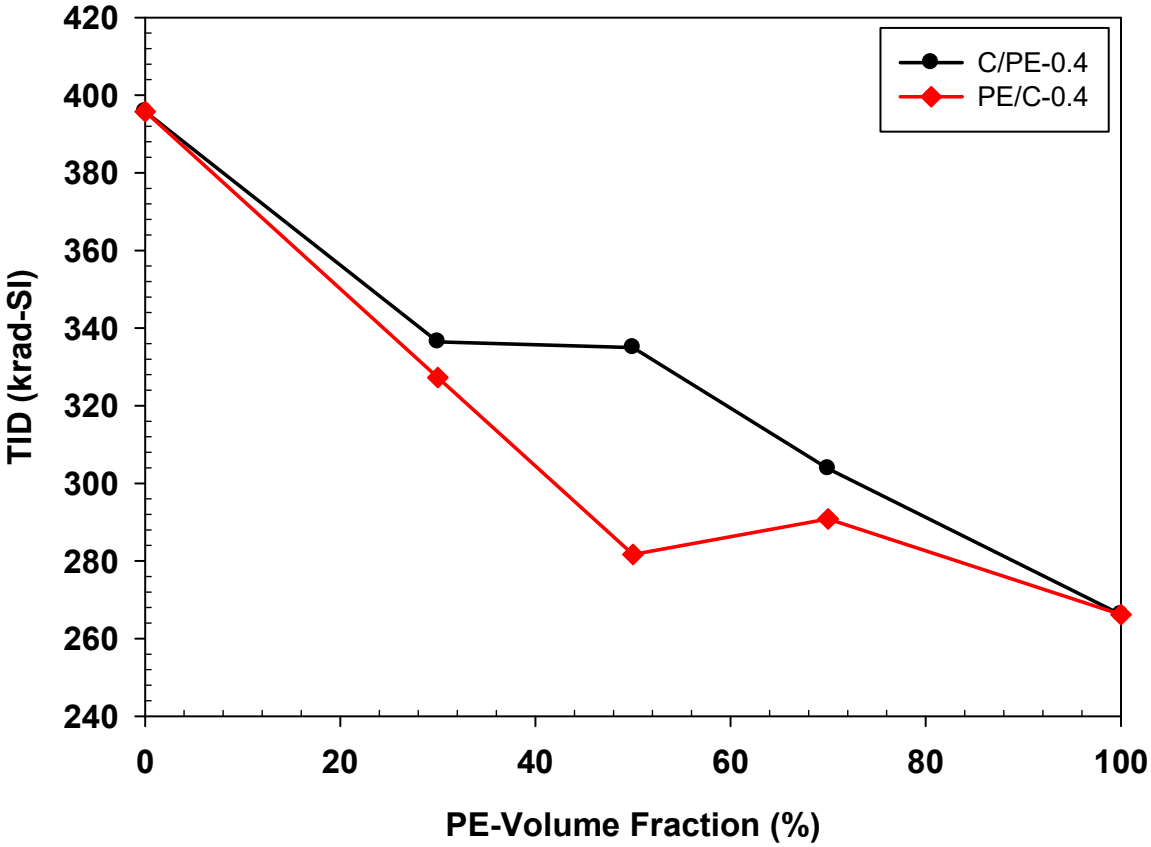
C/PE-0.4
PE/C-0.4
TID (krad-Si)
PE-Volume Fraction (%)
420
400
380
360
340
320
300
280
260
240
0
20
40
60
80
100

(c) 0.6 g/cm^2

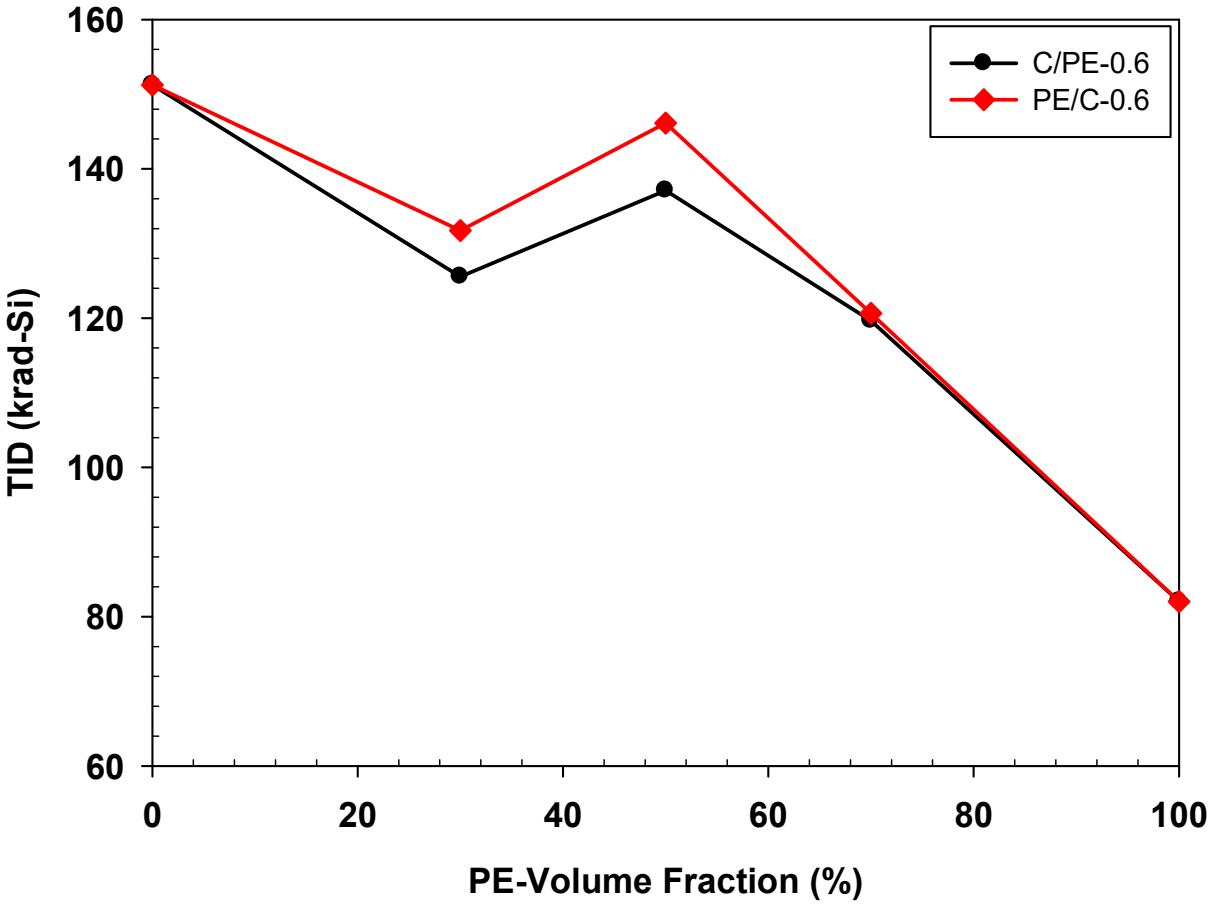
160
140
120
100
80
60
TID (krad-Si)
0
20
40
60
80
100
PE-Volume Fraction (%)
C/PE-0.6
PE/C-0.6

(d) 0.8 g/cm^2

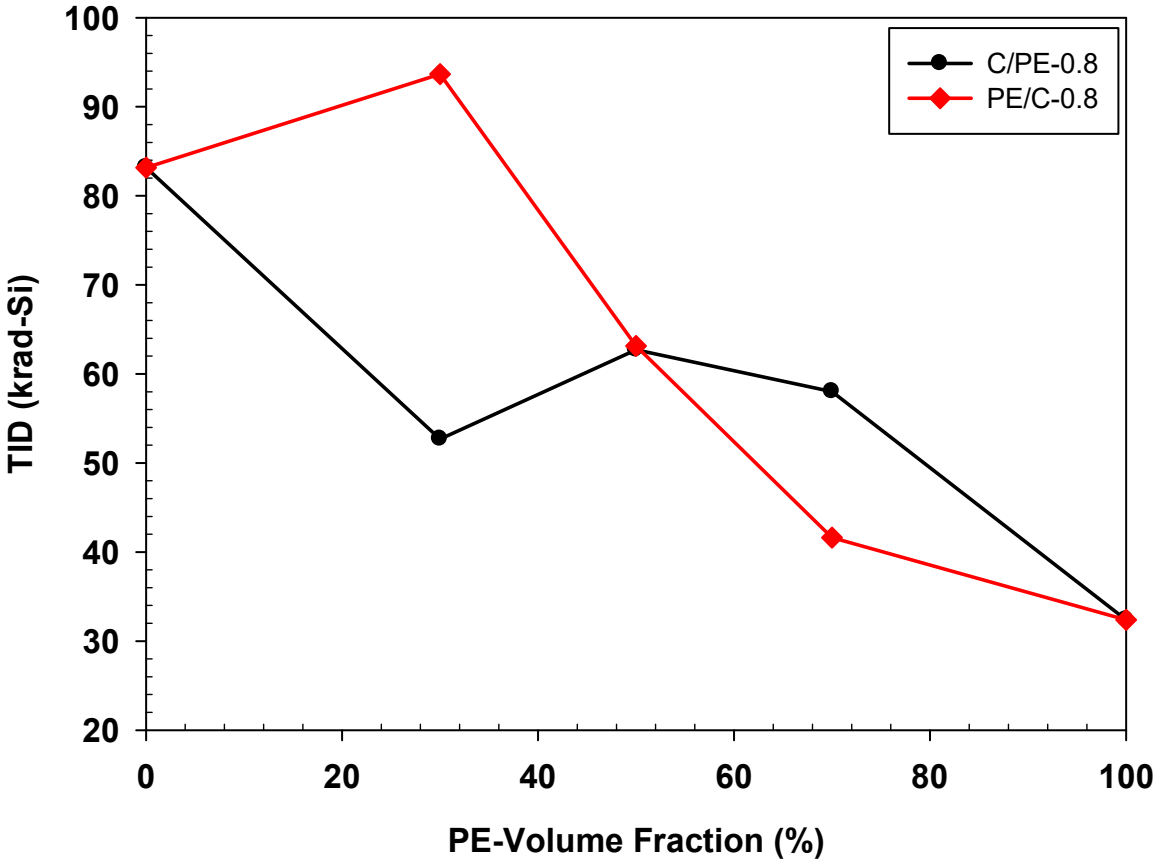
C/PE-0.8
PE/C-0.8
TID (krad-Si)
PE-Volume Fraction (%)
100
90
80
70
60
50
40
30
20
0
20
40
60
80
100

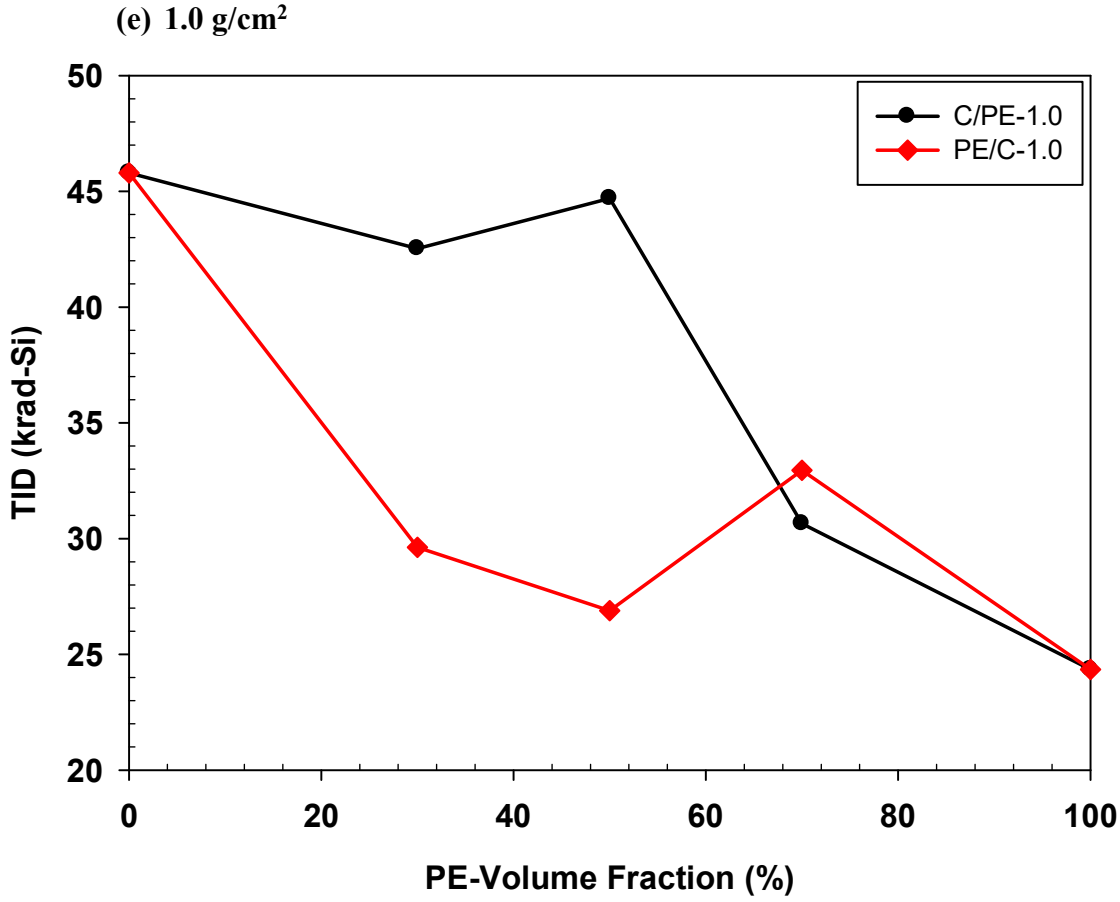

Figure 3.19: Effect of volume fraction of PE and lay-up sequence at (a) 0.2 g/cm^2, (b) 0.4 g/cm^2, (c) 0.6 g/cm^2, (d) 0.8 g/cm^2, (b) 1.0 g/cm^2 on transmitted TID behind a two layer PE-C composite

In addition to attenuation of the incident radiation, secondary (Gamma) particles are generated and absorbed, which depends on the energy of the incident beam, the atomic number of the material in a layer, and the thickness of the layer. Hence, the fluence and the energy of the primary (i.e. attenuated) and secondary particles going into PE behind C in C/PE lay-up would be different from those going into C behind PE in PE/C lay-up. Hence, the fluence and the energy of primary and secondary particles output from PE in a C/PE lay-up and the TID deposited by them in the Si detector behind PE would be different from those outputs from C in a PE/C lay-up and the TID deposited in the Si detector behind C. This is confirmed by results shown in Figure 3.20(a) and (b), for the interaction of electrons with a composite shield that has a PE volume fraction of 30% and an areal density of 0.8 g/cm^2. The fluence and the energy of the attenuated beam of electrons output from the shield (but before entering the Si-detector) are plotted in Figure 3.20(a). Similarly, the fluence and the energy of output secondary (gamma) particles are plotted in Figure 3.20(a). Results for 100% graphite are also included for comparison. It should be noted that the spectrums are not continuous and the data points are connected by a line to facilitate reading. The attenuated electron spectrum for the three shields differed significantly more than the gamma particle spectrum.

The fluence and the energy of the attenuated electrons and the gamma particles output from C in a PE/C lay-up are very different from that output from PE in a C/PE lay-up, resulting in the observed difference in TID between PE/G and G/PE lay-ups. The TID deposited in the silicon detector by the attenuated electrons and gamma particles generated by them is tabulated in Table 3.7 under “trapped electrons”. Similarly, the TID deposited by trapped protons and solar protons are also calculated and included in this table. The total TID plotted in Figure 3.19(d) for the three shields (C, PE/C with 30% PE and C/PE with 30% PE) is a sum of the TID due to these particles.

It can be inferred from this table that the contribution from electrons to the total TID plotted in Figure. 3.19(d) is higher for [PE/C] when compared to [C/PE], which is due to the spectrums of the attenuated electrons and the gamma particles observed in Figure 3.20 (a) and (b) for the two lay-up sequences. Higher fluence of attenuated electrons at many energy levels output from PE/C when compared to C/PE is believed to have contributed to the higher TID behind PE/C when compared to that behind C/PE.

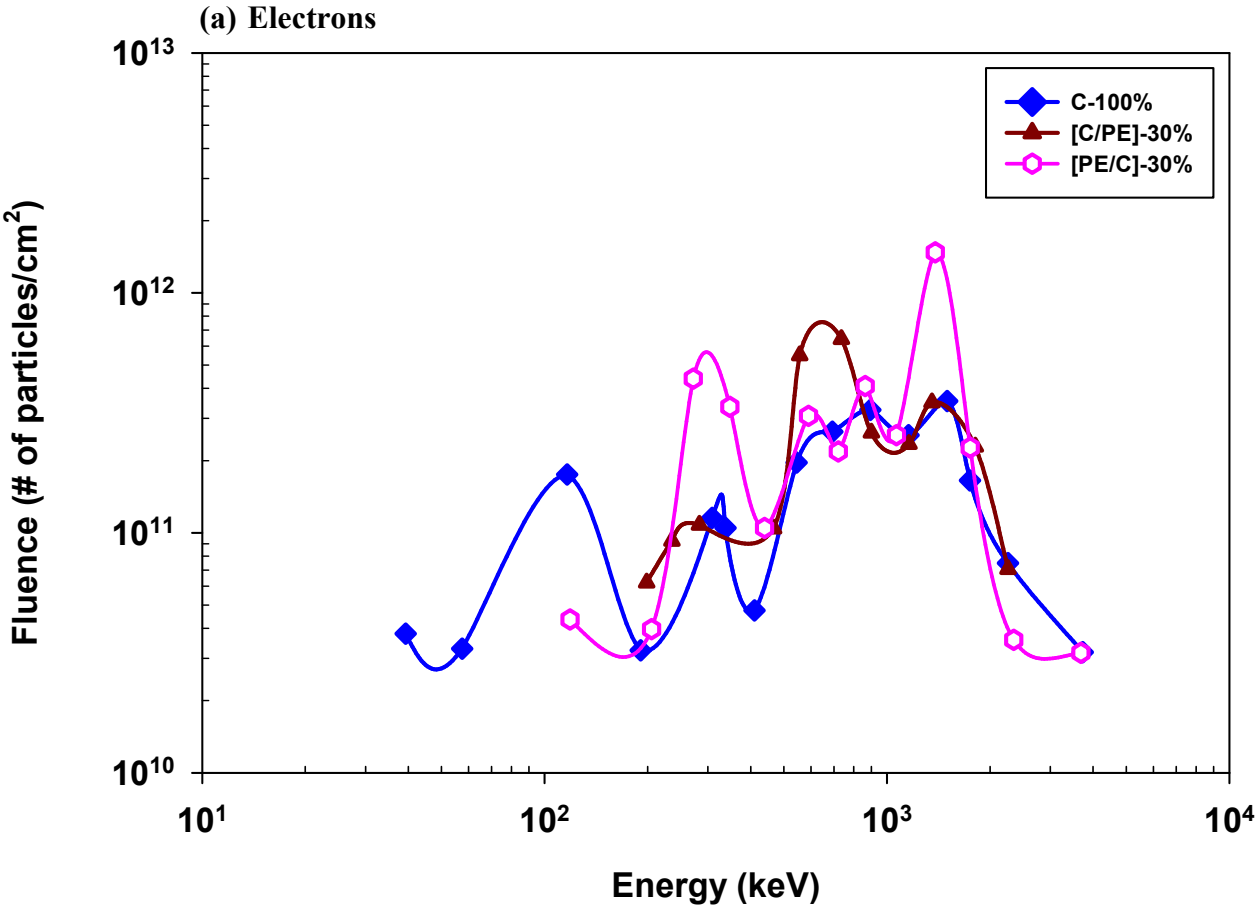
(a) Electrons
C-100%
[C/PE]-30%
[PE/C]-30%
Fluence (# of particles/cm2)
Energy (keV)
10^13
10^12
10^11
10^10
10^1
10^2
10^3
10^4

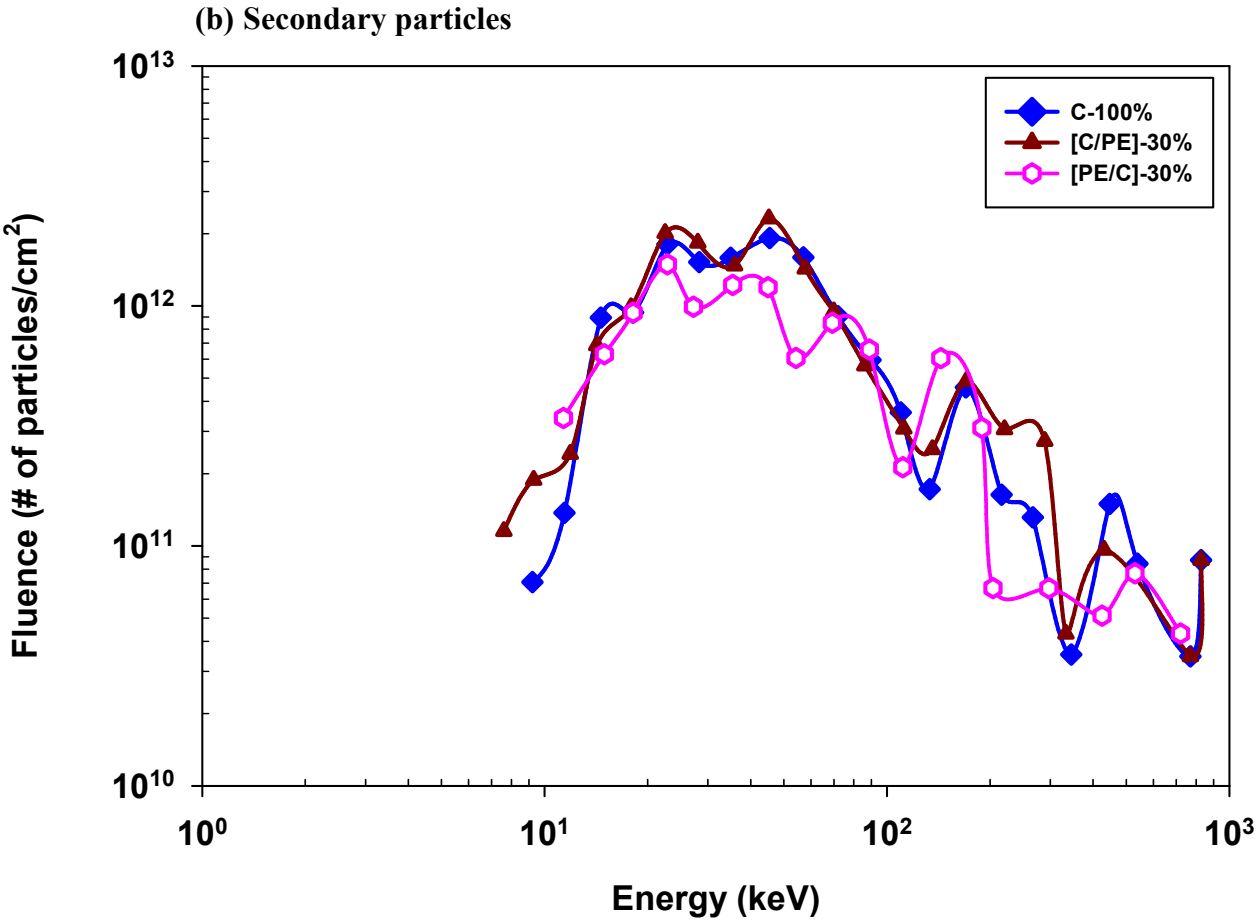

Figure 3.20: Output radiation spectrum (a) electrons and (b) secondary particles behind a PE-C composite shield with 30% volume fraction of PE and an areal density of 0.8 g/cm^2

While the spectrums of gamma particles are similar, the spectrums for the attenuated electrons and the gamma particles are different for 100% G and G/PE; while attenuated electrons with energy levels below 200 keV are output from 100% G, these are completely absent in the output from G/PE. This is believed to be the reason for slightly higher TID behind 100% G when compared to G/PE. In addition, higher contribution from trapped protons results in higher TID for 100% C when compared to [C/PE] in Table 3.7 and Figure 3.19(d).

It is interesting to observe, in Figure 3.19(d) and (e) that a composite with a certain composition and lay-up can result in a TID higher than that for C (PE/C with 30% PE and 0.8 g/cm^2 areal density) or in a TID close to that for PE (PE/G with 50% PE and 1 g/cm^2 areal density). Aerospace composites normally have a reinforcement volume fraction in the range of 50-70% (i.e. the matrix volume fraction in the range of 50 – 30%), to meet the requirements on mechanical properties. The results in Fig. 3.19(e) suggest that PE-G composites, with PE volume fraction in the range of 30-50%, can result in a TID similar to that achievable with 100% PE and that an appropriate lay-up sequence is critical to achieving this. Hence, further analysis was focused on PE volume fractions of 30%, 50%, and 70%.

The simulated TID for the four lay-ups of the four-layer composite is plotted in Figure 3.21 as a function of areal density for constant PE volume fractions of 30 % (Figure 3.21(a)), 50% (Figure 3.21(b)), and 70% (Figure 3.21(c)).

Table 3.7: A comparison of TID deposited, in the Si-detector behind a PE-C composite with an areal density of 0.8 g/cm^2 by various particles in the incident radiation.

Shield Lay-up	TID (krad-Si)			
	Trapped Electrons	Trapped Protons	Solar Protons	Total
C	46.2	36.3	0.722	83.22
[PE/C] with 30% PE	82.3	8.32	3.0	93.62
[C/PE] with 30% PE	36.0	13.9	2.79	52.69

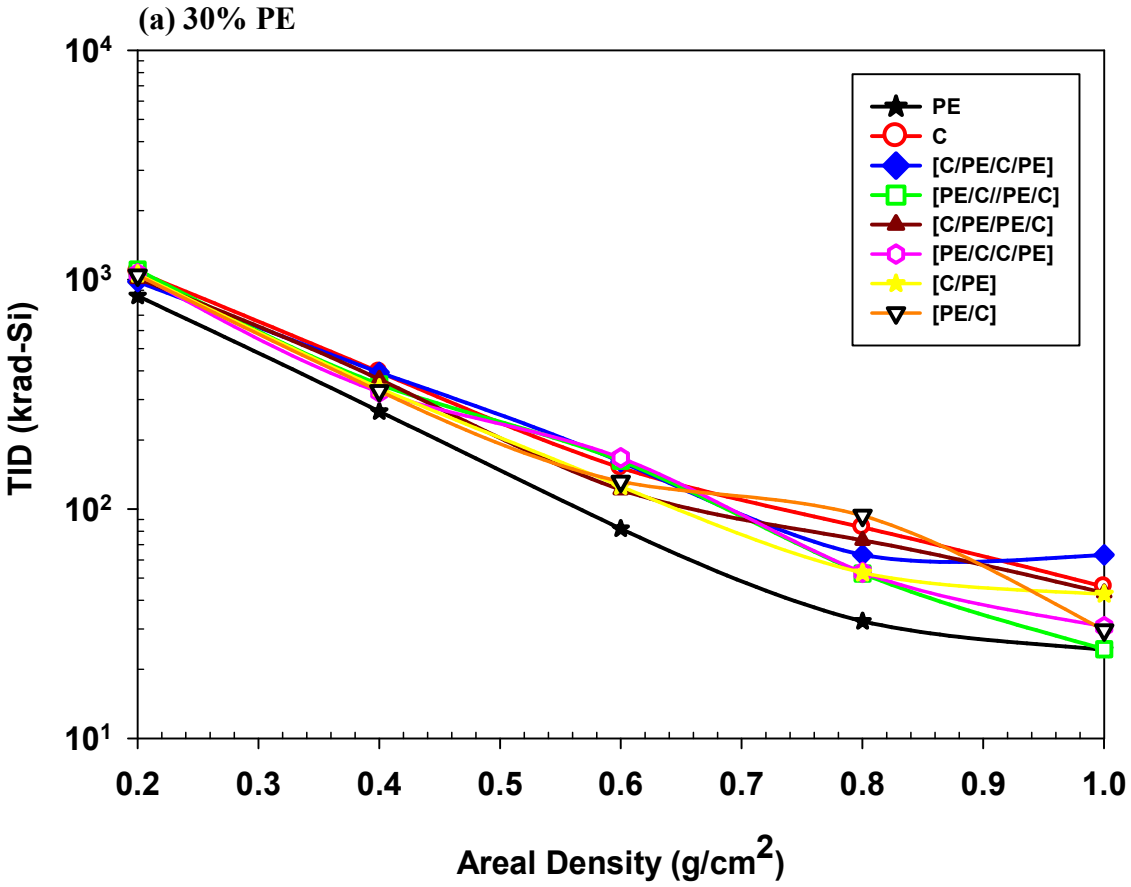
(a) 30% PE
TID (krad-Si)
Areal Density (g/cm2)
PE
C
[C/PE/C/PE]
[PE/C//PE/C]
[C/PE/PE/C]
[PE/C/C/PE]
[C/PE]
[PE/C]

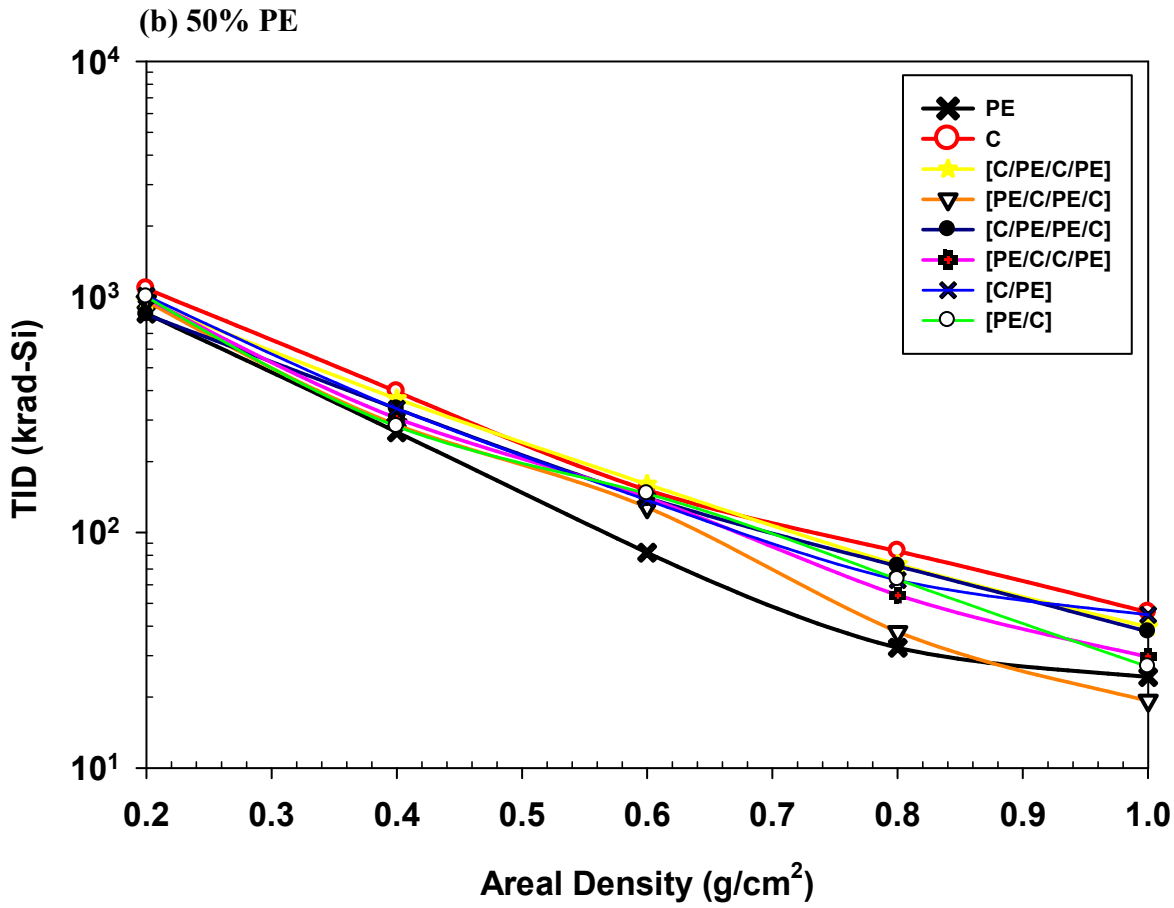
(b) 50% PE
TID (krad-Si)
Areal Density (g/cm2)
PE
C
[C/PE/C/PE]
[PE/C/PE/C]
[C/PE/PE/C]
[PE/C/C/PE]
[C/PE]
[PE/C]

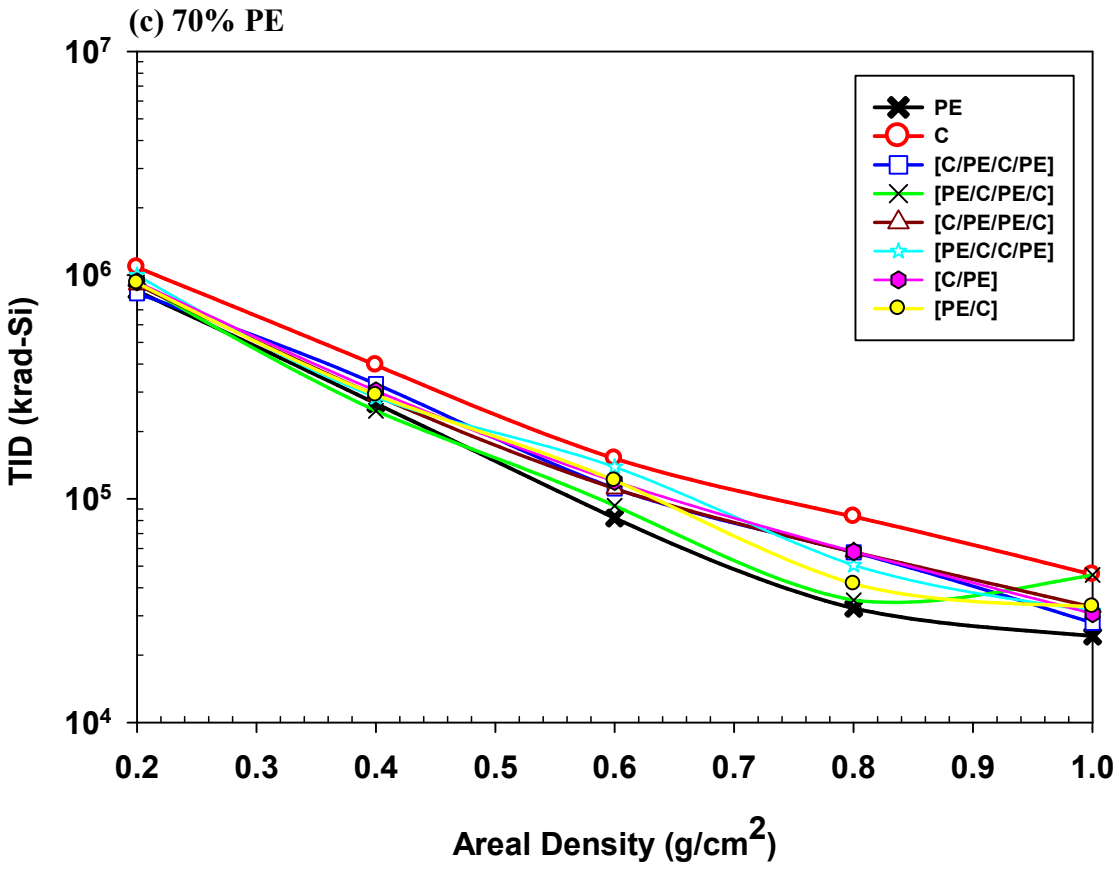

Figure 3.21: Comparison of TID for 2-layer and 4-layer composite shields (a) 30% PE; (b) 50% PE; (c) 70% PE.

It should be noted that the thickness of PE and C in these composites is half the thickness of PE and C in 2-layer composite. TID values for the two-layer composite as well as 100% PE and 100% C are also plotted for comparison. The TID values for 4-layer composites are between those for PE and C except for $[PE/C]_2$ with 30% and 50% volume fraction of PE, which results in a TID value lower than that for PE at the same areal density of 1.0 g/cm^2. It is observed that PE/C with 30% and 50% of PE results in TID values (29.6 krad and 26.9 krad respectively) slightly higher than the TID (24.3 krad) for 100%. The $[PE/C]_2$ composite with the same total thickness (i.e. mass) as the PE/C, reduces this TID further to a value (24.5 krad at 30% and 19.3 krad at 50%) lower than that for PE, highlighting the effect of thickness and lay-up on radiation shielding effectiveness of composites. The $[PE/C]_s$ and $[C/PE]_s$ composites, which are preferred from the manufacturing and service (thermal cycling) point of view, results in a TID higher than that for $[PE/C]_2$, PE/C, and PE. The TID for $[PE/C]_s$ is lower than that for $[C/PE]_s$.

The TID for 8-layer composites, with symmetric lay-up and various volume fractions of PE, is plotted in Figure 3.22 as a function of areal density for various constant volume fractions of PE. It should be noted that the thickness of PE and C in these composites is one-fourth the thickness of PE and C in 2-layer composite and half the thickness of PE and C in the 4-layer composite. The TID values are between the values for PE and C for all volume fractions of PE and for all values of areal density. Even the non-symmetric lay-ups (not shown in the figure) of $[PE/C]_4$ with an areal density of 1g/cm^2 results in a TID (37.4 krad for 30% PE and 33.6 krad for 50% PE) higher than that for 100% PE.

However, the TID value for the 16-layer $[PE/C]_8$ composite with 50% PE at 1g/cm^2 is 24.9 krad, which is closer to that for 100% PE, highlighting the effect of thickness of layer. Figure 3.23 summarizes the effect of layer thickness on the TID behind a non-symmetric composite shield with

a volume fraction of 50% PE and an areal density of 1 g/cm^2. It should be noted that all data points correspond to composites with same mass. The TID varies non-monotonically with the thickness of the layer. The four-layer $[PE/C]_2$ composite results in the lowest TID of 19.3 krad, which is also lower than that for 100%PE. A comparison of TID for $[C/PE]_n$ with those of $[PE/C]_n$ suggests that using low Z material such as PE, as the surface layer of a composite shield, to interact first with incident radiation, results in a lower TID than using C as the surface layer. Similar conclusion has been reached by Mangeret et al. [1996] for a trilayer multi-metallic shielding structure.

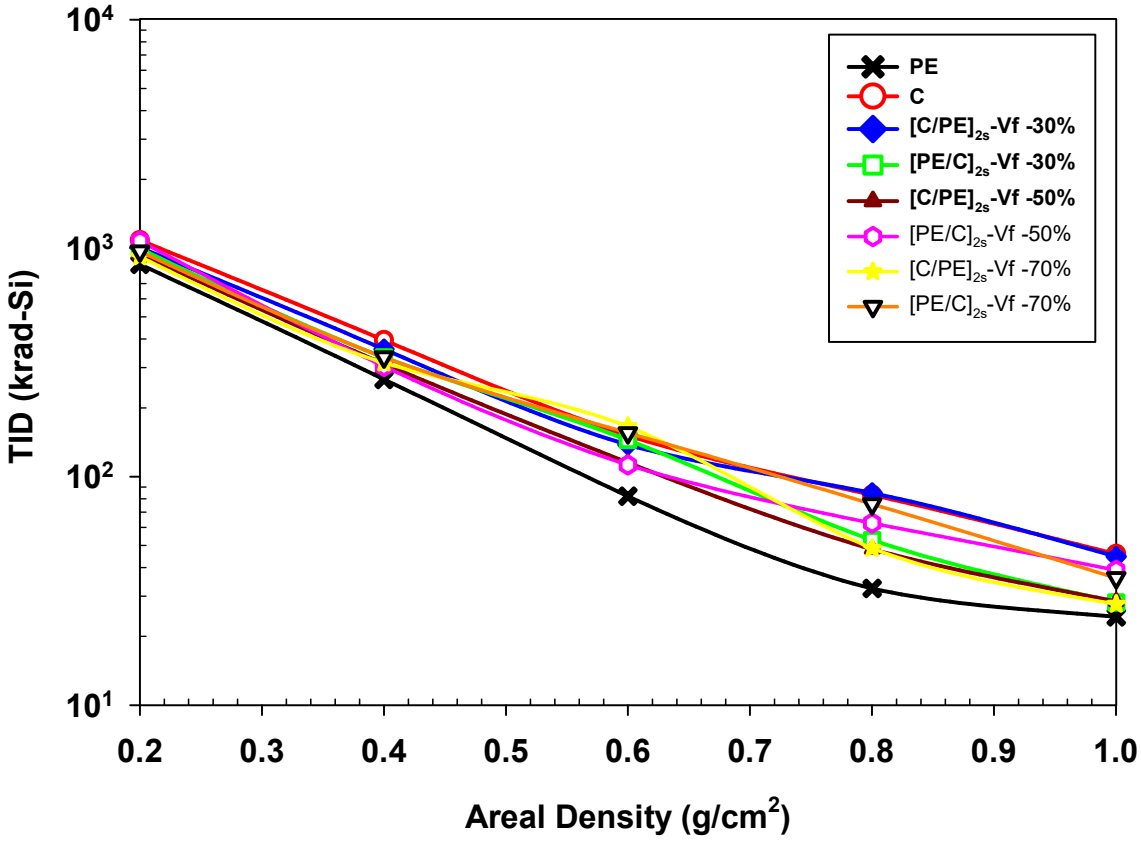

Figure 3.22: TID for 8-layer composite

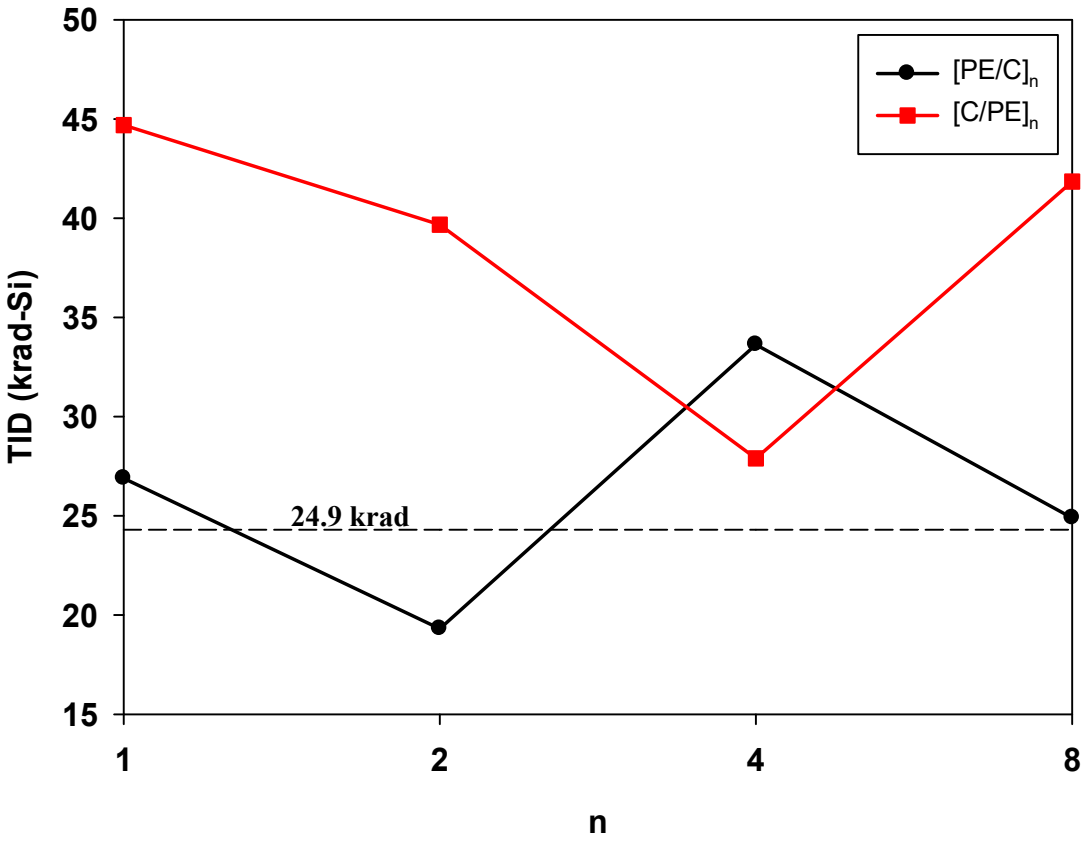

Figure 3.23: Effect of thickness on the TID behind non- symmetric composite shields with 50% PE volume fraction and areal density of 1 g/cm^2

Symmetric stacking sequence, which is preferred from the manufacturing and service point of view, results in a TID higher than that for non-symmetric stacking sequence. The effect of layer thickness on the TID behind symmetric composite shields with an areal density of 1 g/cm^2 is summarized in Table 3.8. The TID varies non-monotonically with the thickness of the layer. The 8-layer $[PE/C]_{2s}$ composite and the 16-layer $[PE/C]_{4s}$ composite result in the lowest TID for 30% and 50% volume fractions of PE, respectively. However, the TID values are higher than the TID for 100% PE.

The path length for the radiation in a given phase of a real composite would be of the order of microns while the minimum thicknesses of the layers used in this study are of the order of hundreds of microns. The sequence of interaction and attenuation would be more complex in a real composite than the layered composite used in this study. Nevertheless, this study highlights the effect of the structure of a composite on its radiation shielding effectiveness and possibility of tailoring the latter by controlling the former.

This analysis presented in this section was concerned only about the transmitted TID to elucidate the effect of structure. Based on this, composites with a minimum of 16 layers were chosen for further analysis. The absorbed TID in the first PE and Carbon layers for the 16-layered composite is summarized in Table 3.9. These as well as the results presented in section 3.5 were used in the next section to arrive at the final design.

Table 3.8: Effect of layer thickness on the transmitted TID behind symmetric composite shields with an areal density of 1 g/cm^2.

Lay-up	TID (krad-Si)		
	PE - 100%; C - 0%	PE - 30%; C - 70%	PE - 50%; C - 50%
[PE]	24.3	-	-
$[PE/C]_s$	-	30.7	29.6
$[C/PE]_s$	-	43.1	37.9
$[PE/C]_{2s}$	-	28.2	39.0
$[C/PE]_{2s}$	-	44.7	28.4
$[PE/C]_{4s}$	-	55.0	27.6
$[C/PE]_{4s}$	-	67.7	31.1

Table 3.9: Absorbed TID in the first PE and carbon layers for the 16 layer composite identified in Table 3.6.

AD = 1.0 g/cm^2	$TID_{Absorbed}$ in 1st layer of PE (rad)		$TID_{Absorbed}$ in 1st layer of C (rad)	
PE-V_f	$[PE/C]_{4s}$	$[C/PE]_{4s}$	$[PE/C]_{4s}$	$[C/PE]_{4s}$
30	5.88E+08	1.13E+07	2.95E+07	1.65E+08
50	3.53E+08	1.33E+07	1.81E+07	2.03E+08

3.7 Design of Hybrid Composite Shield

In addition to radiation and mechanical property requirements detailed in sections 3.2.2 and 3.2.3, manufacturing requirements, as listed below were also considered to come up with the final design.

- Availability of Materials: While carbon fiber reinforced epoxy (CFC) prepregs are readily available, carbon fiber reinforced polyethylene (PFC) prepregs are not available. Similarly, the UHMWPE fibers can be purchased either without matrix or with only polyurethane matrix. Prepregs consisting of the PE matrix reinforced with either carbon or UHMWPE fibers have to be manufactured in house. The thinnest Aluminum foil available for purchase is about 80 μm in thickness and is made up of Al alloy.
- Bonding: The bonding between the carbon fibers and the epoxy matrix (required for high mechanical properties of the composite) has been optimized by the pre-preg manufacturers while PE is known to bond poorly with other materials. In addition, the chosen composite should bond readily with the surface metal (Al) layer. While epoxy matrix of the CFC is known to bond well with the Al, an adhesive is required to bond PFC to the Al layer, which would add to the weight of the panel. In addition, it has been found that the available adhesive is very costly and yields lower bond strength than epoxy while bonding the composite to the Al layer.

3.7.1 Materials

Based on the above requirements and results from sections 3.4, 3.5, and 3.6, three materials were chosen: Al foil, CFC prepreg, HDPE reinforced with UHMWPE fibers (PFC) manufactured in-house. The amount of PE reduced by using epoxy in the CFC has been compensated by using UHMWPE fibers instead of carbon in the PFC. The volume fraction of carbon fiber in CFC was 60%, and the volume fraction of UHMWPE fiber in PFC was 70%.

3.7.2 Shield Composition and Weight

Based on the results from section 3.6, the volume fraction of CFC in the shield was varied between 30% and 70% to maximize the mechanical properties. The volume fraction of PFC was varied between 70% and 30% to maximize the radiation shielding effectiveness. Results in 3.17 suggest that 84 mm thick Al layer would reduce the absorbed TID in PE below the $TID_{Critical,Absorbed}$ while meeting the requirement on transmitted TID through the PE layer. Since symmetric composite lay-up was used, two layers of Al (80 μm in thickness) on either surface of the composite correspond to a minimum volume fraction of 2.5%. Thus, the volume fraction of Al was varied between 2.5 – 7%; the upper bound was arbitrarily chosen. From Table 3.3, it can be observed shields made up of 100% Al and PE would require areal densities of 0.7 g/cm^2 and 0.95 g/cm^2 to meet the required $TID_{Critical,Transmitted}$ of 50 krad for a 15-year mission in Molniya. Hence, the areal density of the hybrid composite was varied between 0.8 to 1.0 g/cm^2 to determine the final aerial density.

3.7.3 Shield Structure

Based on the results from sections 3.5 and 3.6, a symmetric hybrid composite consisting of metal and polymer composite layers was chosen: Al/ $[CFC/PFC]_{4s}$/Al. In addition to reducing the absorbed TID in the underlying PE, the Al layer on either surface also enables (i) bonding with honeycomb cores using adhesives currently in use and (ii) meet surface resistivity requirements to reduce surface charging to acceptable levels. The PE was reinforced with ultra-high molecular weight PE fibers, instead of carbon fibers, to yield the PFC layer. This maximized the amount of PE with enhancement in both radiation shielding and mechanical properties. Carbon fiber, chosen to provide additional enhancement in mechanical properties to required level, was impregnated with epoxy material to yield the CFC layer. Also, CFC could be readily sourced to manufacture the hybrid composite. Since the epoxy bonded with Al better than PE did, the CFC was placed between the Al and the PFC.

10 laminate sequences, identified below, were used. Since it is not possible to continuously vary the volume fraction, discrete volume fractions were chosen. Firstly, the volume fraction of Al was increased in steps of 1% for each sheet (a total of 2%) from 1.5%. Laminate 1 with 1.25% Al corresponds to the minimal Al foil thickness available for purchase. The volume fraction of PFC was varied between 50% - 67.5% to retain the radiation shielding properties in the laminate while CFC make up the remaining volume fraction (30% - 47%) for improved structural properties.

1. $Al^{1.25\%}/ ([PFC / CFC]_{4s})^{67.5\%/30\%}/Al^{1.25\%}$
2. $Al^{1.5\%}/ ([PFC / CFC]_{4s})^{67\%/30\%}/Al^{1.5\%}$
3. $Al^{1.5\%}/ ([PFC / CFC]_{4s})^{60\%/37\%}/Al^{1.5\%}$
4. $Al^{1.5\%}/ ([PFC / CFC]_{4s})^{50\%/47\%}/Al^{1.5\%}$
5. $Al^{2.5\%}/ ([PFC / CFC]_{4s})^{65\%/30\%}/Al^{2.5\%}$
6. $Al^{2.5\%}/ ([PFC / CFC]_{4s})^{60\%/35\%}/Al^{2.5\%}$
7. $Al^{2.5\%}/ ([PFC / CFC]_{4s})^{50\%/45\%}/Al^{2.5\%}$
8. $Al^{3.5\%}/ ([PFC / CFC]_{4s})^{63\%/30\%}/Al^{3.5\%}$
9. $Al^{3.5\%}/ ([PFC / CFC]_{4s})^{60\%/33\%}/Al^{3.5\%}$
10. $Al^{3.5\%}/ ([PFC / CFC]_{4s})^{50\%/43\%}/Al^{3.5\%}$

For each of these laminates, the thicknesses of the three constituent layers, for a given aerial density of the laminate, were determined as follows.

- Determine the density of the laminate using the rule of mixtures, densities of Al (2.69 g/cm^2), CFC (1.5 g/cm^2), and PFC (0.94 g/cm^2), and volume fraction of each layer identified for the chosen laminate. The density of Al corresponds to that of commercially available Al 1100. The density of CFC was determined using densities of carbon fiber (1.7 g/cm^2), epoxy (1.2 g/cm^2), and volume fraction of fiber in the composite (60%), which correspond to commercially available prepreg. The density of PFC was determined using densities of UHMWPE fiber (0.97 g/cm^2), HDPE (0.94 g/cm^2), and volume fraction of fiber in the composite (70%), which correspond to commercially available materials.
- Using the chosen aerial density and the calculated laminate density, determine the thickness of the laminate.

- Using the thickness of the laminate and the volume fractions of Al, CFC, and PFC, determines the total thickness of each. Divide each value by the number of layers for that ply group, as identified in each laminate configuration, to determine the thickness of each layer.

3.7.4 Simulation details

MULASSIS software allows simulation of a shield with a maximum of 20 layers. If each composite layer is modeled as a 4-layer symmetric layer to ensure that the shield is symmetric, a minimum of 68 layers (including two detectors – one behind the first PE layer and another behind the shield) is required to model the hybrid composite structure. Since this is not possible with MULASSIS, each composite layer was replaced with one with equivalent chemical composition. This allowed simulation of the shield with 20 layers.

The equivalent chemical formula for CFC layer, determined as per procedure described in Appendix B, and equivalent PFC and Al layer are tabulated in Table 3.10. The simulation procedure, discussed earlier in Section 3.4.3, was used to simulate the results presented below,

Table 3.10: Compositional table showing thicknesses of each lamina in a hybrid laminate with an areal density of 0.88 g/cm^2 and various volume fractions of PFC.

Shield Areal Density (g/cm^2)	Composition and Structure	Thickness			
		Al (μm)	PFC (μm)	CFC (μm)	Composite Laminate (mm)
0.88	$Al^{1.25\%}/[PFC/CFC]_{4s}^{67.5\%/30\%}/Al^{1.25\%}$	81	242	545	6.462
0.88	$Al^{1.5\%}/[PFC/CFC]_{4s}^{67\%/30\%}/Al^{1.5\%}$	97	241	539	6.434
0.88	$Al^{1.5\%}/[PFC/CFC]_{4s}^{60\%/37\%}/Al^{1.5\%}$	99	306	497	6.624
0.88	$Al^{1.5\%}/[PFC/CFC]_{4s}^{50\%/47\%}/Al^{1.5\%}$	104	406	432	6.916
0.88	$Al^{2.5\%}/[PFC/CFC]_{4s}^{65\%/30\%}/Al^{2.5\%}$	158	237	514	6.324
0.88	$Al^{2.5\%}/[PFC/CFC]_{4s}^{60\%/35\%}/Al^{2.5\%}$	161	282	484	6.454
0.88	$Al^{2.5\%}/[PFC/CFC]_{4s}^{50\%/45\%}/Al^{2.5\%}$	175	349	436	6.730
0.88	$Al^{3.5\%}/[PFC/CFC]_{4s}^{63\%/30\%}/Al^{3.5\%}$	218	233	490	6.218
0.88	$Al^{3.5\%}/[PFC/CFC]_{4s}^{60\%/33\%}/Al^{3.5\%}$	220	260	472	6.292
0.88	$Al^{3.5\%}/[PFC/CFC]_{4s}^{50\%/43\%}/Al^{3.5\%}$	229	352	410	6.555

3.7.5 Results and Discussion

The transmitted TID for the ten laminates is plotted as a function of areal density in Figure 3.24 for Al/[PFC/CFC]$_{4s}$/Al. It can be observed that the transmitted TID decreases monotonically with increase in areal density for some, while varies non-monotonically for others. The effect of volume fraction (i.e. thicknesses) of various layers on the transmitted TID is substantial. Since the incident radiation level is same for all laminates, the amount of transmitted TID depends on the radiation absorbed by the layers of the laminate as well as any secondary particles generated by the interaction between the incident radiation and the material in a layer. With increase in areal density of a laminate, the thickness of various layers in it also increases. With increase in thickness, the ability of a layer to absorb radiation as well as generate secondary radiation would increase. The competition between these two, as discussed in section 3.4.4.1 to explain the results in Figure 3.9 and 3.10, is believed to have caused the observed non-monotonic changes observed in Figure 3.24

It can be observed that a number of laminate configurations of Al/[PFC/CFC]$_{4s}$/Al with areal density ≥ 0.88 g/cm^2 have transmitted TID less than 50 krad. Al$^{1.5\%}$ /$[PFC/CFC]_{4s}^{67.5\%/30\%}$ /Al$^{1.5\%}$ yields the best combination of low transmitted TID and weight (0.88 g/cm^2) while Al$^{3.5\%}$ /$[PFC/CFC]_{4s}^{63\%/30\%}$/Al$^{3.5\%}$ offers the lowest TID among the 10 configurations but with a weight penalty at 1.0 g/cm^2.

However, none of the 10 configurations yields an absorbed TID in the first PFC layer less than the threshold value of 20 Mrad as shown in Figure 3.25. It should be noted that in Figure 3.17, an Aluminum layer, 84 mm in thickness, was able to reduce the absorbed TID in the PFC layer beneath it to a value below 20 Mrad. However, the thickness of the PE layer was 2.716 mm in

contrast to the PFC thickness of 0.2 – 0.4 mm in all 10 configurations. Normally more volume of material absorbing the same radiation means less transmitted TID. This is the reason for the monotonic reduction in absorbed TID with increase in areal density in Figure 3.25 since the thickness of the PFC layer increases with increase in aerial density of the shield. Normally, a layer sandwiched between two layers would receive both incident radiation passing through the top layer and as well as any radiation backscattered from the layer beneath it. The PE used in generating the results in 3.17 did not have any layer beneath it. However, the PFC layer had CFC layer beneath and hence, any back-scattered radiation from CFC could have been another reason for higher absorbed TID (than 20 Mrad) in the first PFC layer of the 10 configurations. While the thickness of the Al was in configuration # 1 was the lowest at 81 μm, it was much higher at other configurations. An increase in the thickness of Al layer would have resulted in the production of secondary particles, due to its interaction with the incident radiation, resulting in an increase in the amount of radiation incident on the PFC layer beneath it. This would have resulted in an increase in the interaction and absorption of radiation and hence the absorbed TID within the PFC, since its thickness hardly changes for the 10 configurations for a given areal density.

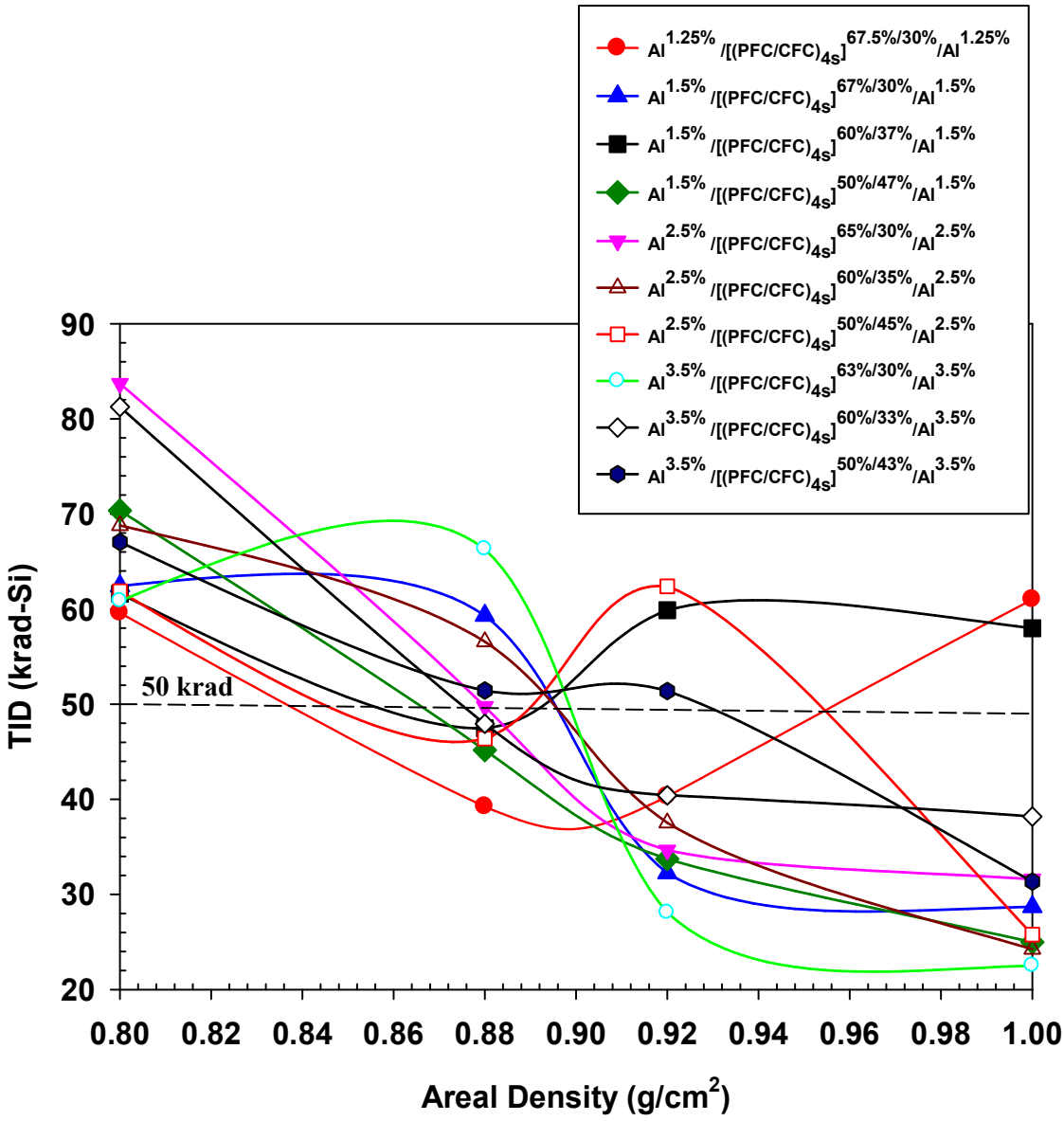

Figure 3.24: Transmitted TID for 10 laminate configurations of Al/[PFC/CFC]$_{4s}$/Al

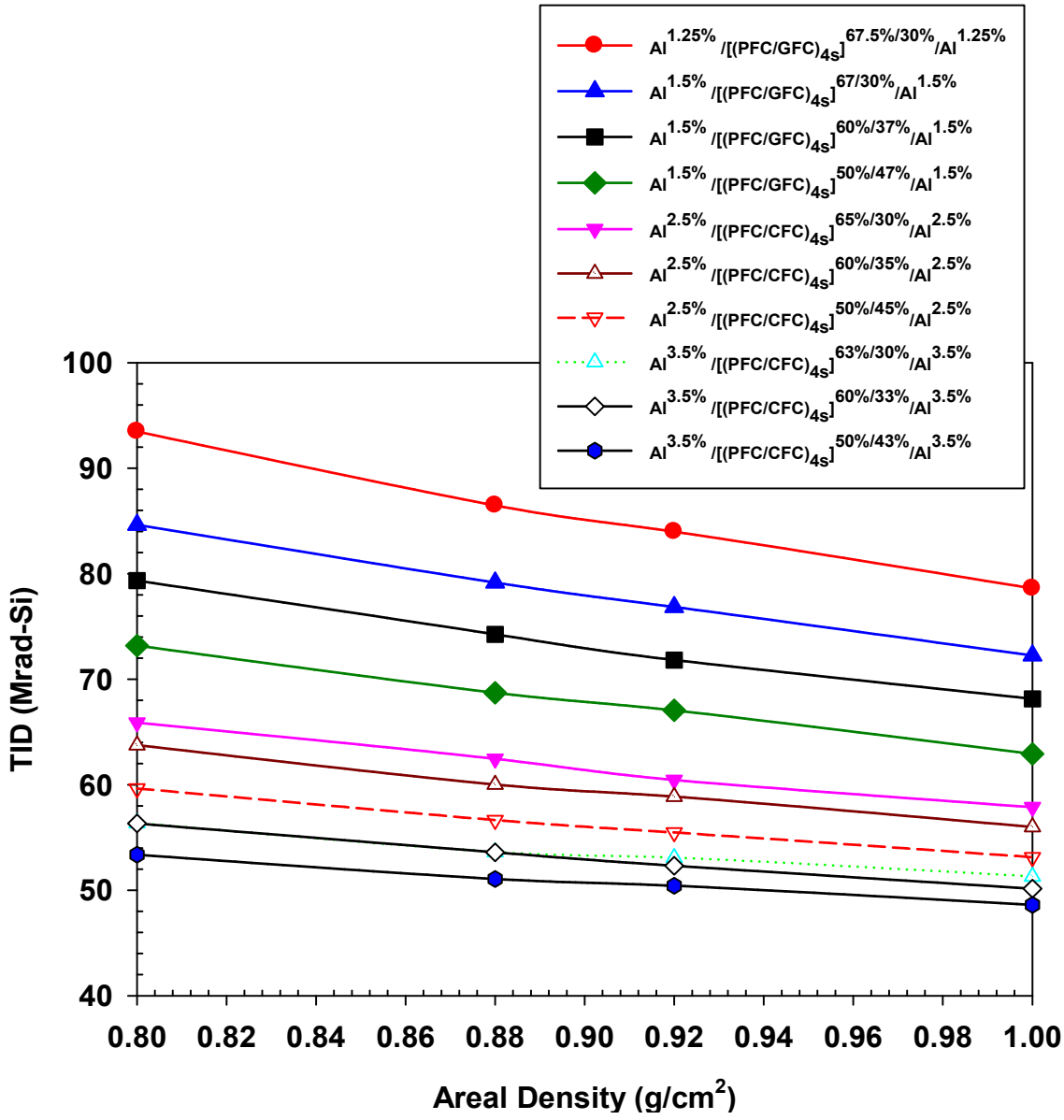

Figure 3.25: Absorbed TID in the first PFC layer of Al/[PFC/CFC]$_{4s}$/Al

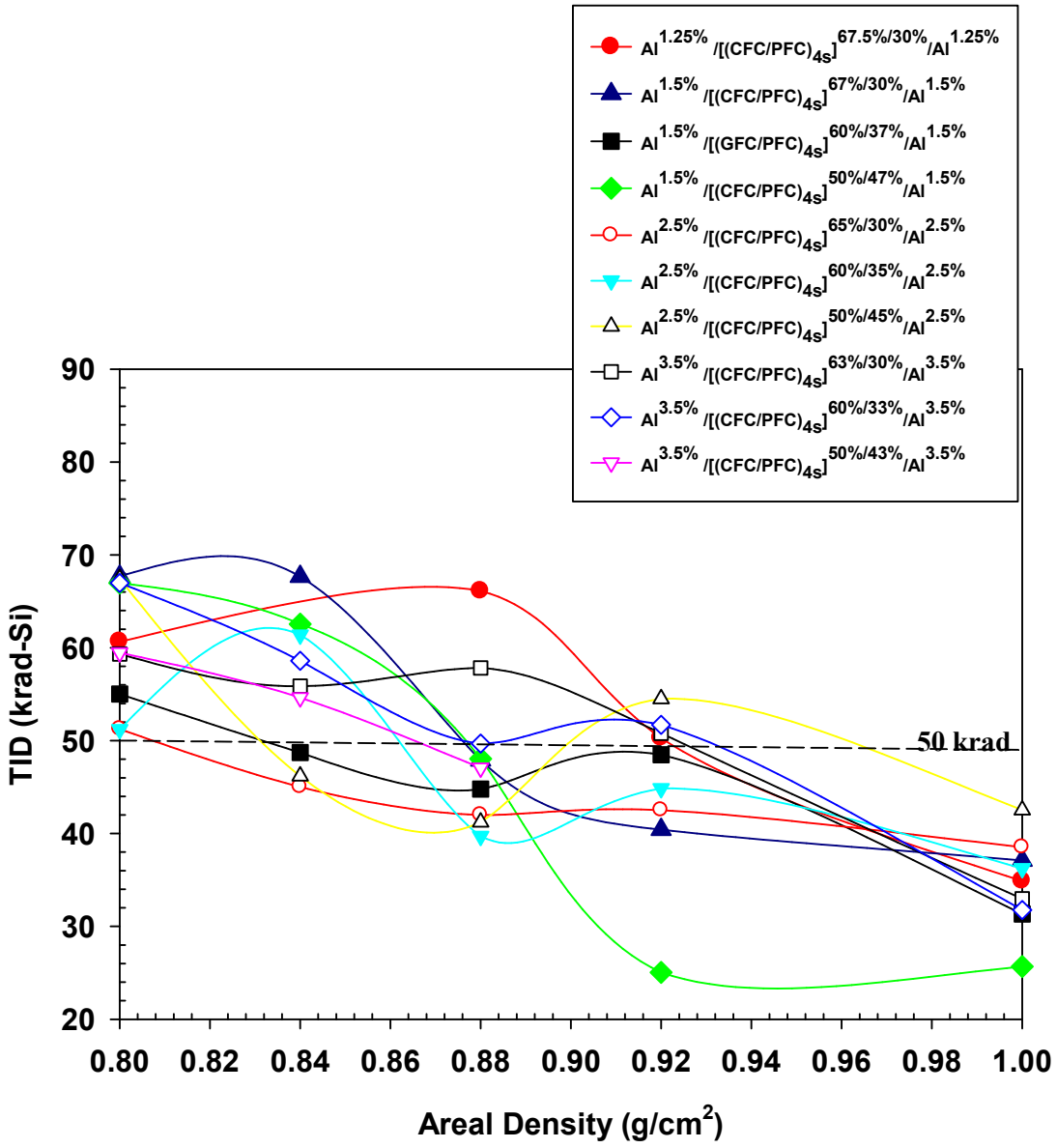

Figure 3.26: Transmitted TID for 10 laminate configurations of Al/[CFC/ PFC]$_{4s}$/Al

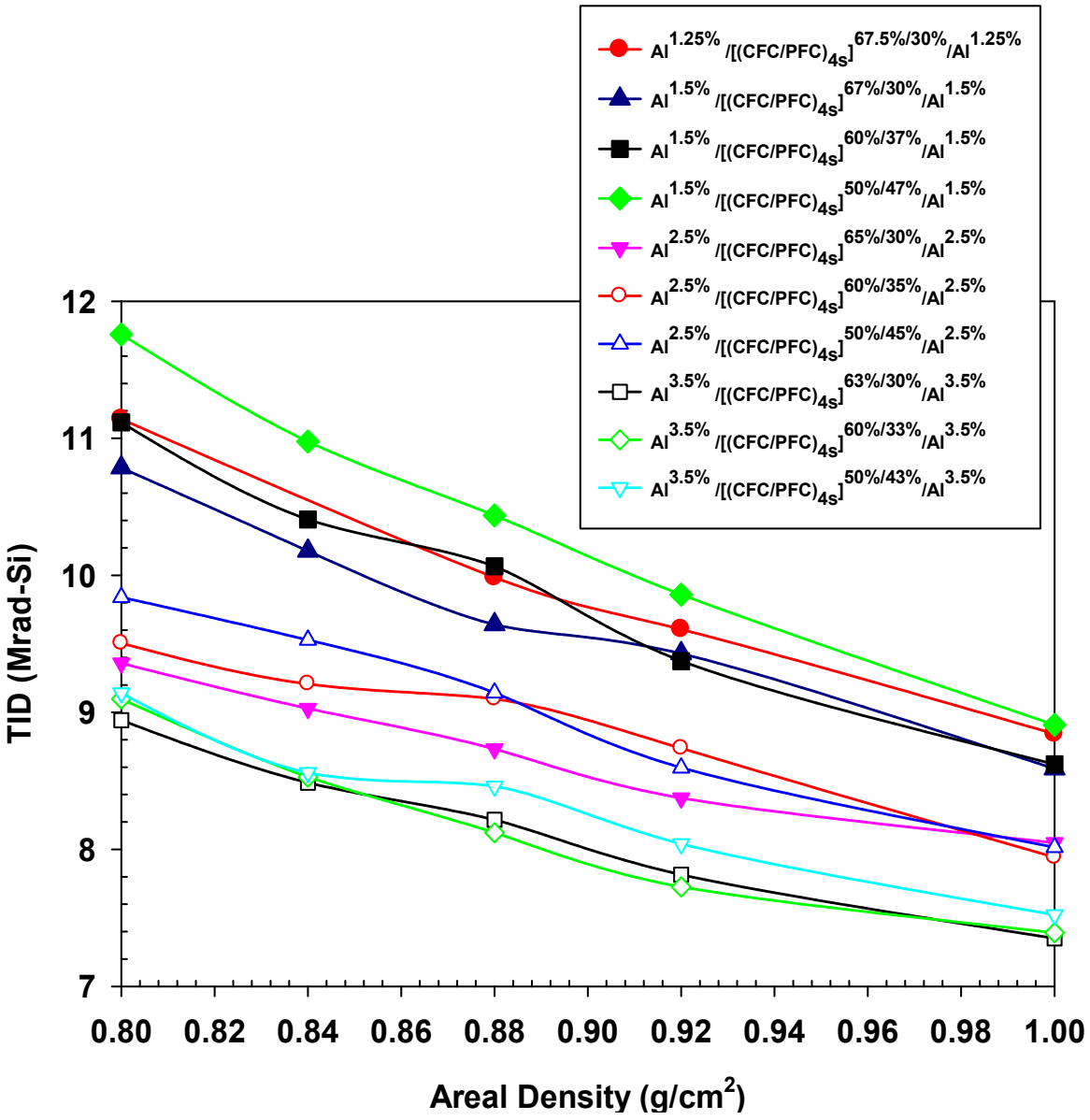

Figure 3.27: Absorbed TID in the first PFC layer of Al/[CFC/ PFC]$_{4s}$/Al

Hence, another material has to be placed between the Al and the PFC layer to reduce the absorbed TID in the PFC layer. The positions of the PFC and the CFC layers were interchanged to yield Al/[CFC/PFC]$_{4s}$/Al shield. The transmitted TID for the ten laminates of this shield is plotted as a function of aerial density in Figure 3.26. It can be observed that a number of configurations of Al/[CFC/PFC]$_{4s}$/Al with areal density ≥ 0.84 g/cm^2 yield a transmitted TID less than 50 krad. While $Al^{2.5\%}$ /$[PFC/CFC]_{4s}^{65\%/30\%}$/$Al^{2.5\%}$ offers the best combination of low transmitted TID and weight (0.84 g/cm^2), $Al^{1.5\%}$ /$[PFC/CFC]_{4s}^{50\%/47\%}$ /$Al^{1.5\%}$ yields the lowest transmitted TID among all configurations although with a weight penalty (≥0.92 g/cm^2).

The absorbed TID of the first PFC layer is less than the threshold value of 20 Mrad for all 10 configurations of Al/[CFC/ PFC]$_{4s}$/Al as shown in Figure 3.27. Unlike the Al/[PFC/ CFC]$_{4s}$/Al shield, the additional CFC layer placed between the Al and PFC layers absorb the radiation transmitted through Al, resulting in the lowering of the level of radiation incident on the PFC layer and thus the absorbed TID in PFC.

In addition to meeting the $TID_{Critical,Absorbed}$ criterion for the PFC layer, this shield configuration also satisfies the $TID_{Critical,\ Absorbed}$ criterion for the epoxy matrix of the CFC; for example, the maximum absorbed TID in CFC is 4.91 × 10^7 rad, which is far less than $TID_{Critical,\ Absorbed}$ for the epoxy matrix of the CFC (1.0 × 10^8 rad).

In summary, Al/[CFC/ PFC]$_{4s}$/Al shield has been able to satisfy both $TID_{Critical,\ Absorbed}$ and $TID_{Critical,\ Transmitted}$ criteria. The laminate configurations (out of the 10 used in the simulation) that satisfy these criteria at distinct areal densities are listed below in Table 3.11.

Table 3.11: Selected Al/[CFC/ PFC]$_{4s}$/Al configurations that satisfy both $TID_{Critical,Absorbed}$ and $TID_{Critical,\ Transmitted}$ criteria at various areal densities (0.8 g/cm^2 – 1.0 g/cm^2)

Structure	0.8 g/cm^2	0.84 g/cm^2	0.88 g/cm^2	0.92 g/cm^2	1.0 g/cm^2
$Al^{1.25\%}/ ([CFC / PFC]_{4s})^{67.5\%/30\%}/Al^{1.25\%}$	-	-	-	-	Satisfy
$Al^{1.5\%}/ ([CFC / PFC]_{4s})^{67\%/30\%}/Al^{1.5\%}$	-	-	Satisfy	Satisfy	Satisfy
$Al^{1.5\%}/ ([CFC / PFC]_{4s})^{60\%/37\%}/Al^{1.5\%}$	-	Satisfy	Satisfy	Satisfy	Satisfy
$Al^{1.5\%}/ ([CFC / PFC]_{4s})^{50\%/47\%}/Al^{1.5\%}$	-	-	Satisfy	Satisfy	Satisfy
$Al^{2.5\%}/ ([CFC / PFC]_{4s})^{65\%/30\%}/Al^{2.5\%}$	-	Satisfy	Satisfy	-	Satisfy
$Al^{2.5\%}/ ([CFC / PFC]_{4s})^{60\%/35\%}/Al^{2.5\%}$	-	-	Satisfy	Satisfy	Satisfy
$Al^{2.5\%}/ ([CFC / PFC]_{4s})^{50\%/45\%}/Al^{2.5\%}$	-	Satisfy	Satisfy	-	Satisfy
$Al^{3.5\%}/ ([CFC / PFC]_{4s})^{63\%/30\%}/Al^{3.5\%}$	-	-	-	-	Satisfy
$Al^{3.5\%}/ ([CFC / PFC]_{4s})^{60\%/33\%}/Al^{3.5\%}$	-	-	Satisfy	Satisfy	Satisfy
$Al^{3.5\%}/ ([CFC / PFC]_{4s})^{50\%/43\%}/Al^{3.5\%}$	-	-	Satisfy	-	Satisfy

Three configurations namely, $Al^{1.5\%}/ ([CFC\ /\ PFC]_{4s})^{60\%/37\%}/Al^{1.5\%}$, $Al^{2.5\%}/ ([CFC\ /\ PFC]_{4s})^{65\%/30\%}/Al^{2.5\%}$ and $Al^{2.5\%}/ ([CFC / PFC]_{4s})^{50\%/45\%}/Al^{2.5\%}$ at 0.84 g/cm^2 satisfies both criteria with least weight penalty. But the required Al thicknesses of 95 μm, 151 μm and 161 μm respectively, were not available in the market for procurement, therefore, the next alternative was considered which were 8 configurations at 0.88 g/cm^2.

The listed eight configurations at areal density of 0.88g/cm are used in the next section to compare their mechanical properties.

1. $Al^{1.5\%}/ ([PFC / CFC]_{4s})^{67\%/30\%}/Al^{1.5\%}$
2. $Al^{1.5\%}/ ([PFC / CFC]_{4s})^{60\%/37\%}/Al^{1.5\%}$
3. $Al^{1.5\%}/ ([PFC / CFC]_{4s})^{50\%/47\%}/Al^{1.5\%}$
4. $Al^{2.5\%}/ ([PFC / CFC]_{4s})^{65\%/30\%}/Al^{2.5\%}$
5. $Al^{2.5\%}/ ([PFC / CFC]_{4s})^{60\%/35\%}/Al^{2.5\%}$
6. $Al^{2.5\%}/ ([PFC / CFC]_{4s})^{50\%/45\%}/Al^{2.5\%}$
7. $Al^{3.5\%}/ ([PFC / CFC]_{4s})^{60\%/33\%}/Al^{3.5\%}$
8. $Al^{3.5\%}/ ([PFC / CFC]_{4s})^{50\%/43\%}/Al^{3.5\%}$

3.8 Hybrid Composite Shield Design for Structural Requirements

In addition to meeting the radiation criteria, the hybrid composite should have properties comparable to or better than the currently used Al composite. Sandwich composite made up of aluminum honeycomb sandwiched between two 6061 Aluminum skins are currently used. Since the same aluminum honeycomb was used in this thesis, the properties of the hybrid composite laminates were compared with those of Al - 6061, presented in section 3.2.3.

The mechanical properties of the eight laminates identified in the previous section were determined using the lamination theory [80] and the properties of its constituents, which are tabulated in Table 3.12. Since Al 6061 foil is not available for procurement in the market, Al 1100 foils were used in the manufacturing of the composite. Hence, properties of this material were used in the simulation. The properties of the CFC and PFC were measured experimentally (as per details in the next Chapter 4) and used. These two composites were manufactured using plain weave fiber fabric and hence, had fibers in 0º and 90º orientations with respect to the loading axis. Since the shear modulus of the PFC could not be measured, this value for UHMWPE fiber reinforced PE composite was taken from the literature [81]. The elastic properties and longitudinal tensile strength were predicted and compared with those for the Al 6061 in Table 3.13.

It can be inferred from this table that the two laminates with properties close to that of Al 6061 are $Al^{1.5\%}/ ([CFC/ PFC]_{4s})^{67\%/30\%}/Al^{1.5\%}$ and $Al^{2.5\%}/ ([CFC/ PFC]_{4s})^{65\%/30\%}/Al^{2.5\%}$. The latter laminate has a slightly lower transmitted TID than the former. Hence, these two compositions represent the final design for the hybrid composite radiation shield and the manufactured hybrid composite had a composition between these two.

The longitudinal modulus of the composite is less than that of the Al 6061 due to low modulus of the PFC, which could be compensated using high modulus carbon fiber composites. Similarly, the low shear modulus is due to 0/90 orientation of the fibers, which could be increased to the required value by using +45º/-45º fiber orientations in the CFC and PFC. Thus, the chosen laminates are considered to meet the structural requirements.

Table 3.12: Material Properties of Carbon epoxy composite (CFC), Polyethylene fiber composite (PFC) and Aluminum.

Properties	Al 1100	CFC	PFC
Longitudinal Modulus (GPa) = E_1	68.9	63.8	15.1
Transverse Modulus (GPa) = E_2	68.9	63.8	15.1
Tensile Strength (MPa)	110	836	500
Shear Modulus (GPa)	26.0	3.07	1.75[82]
Shear Strength (MPa)	75.8	90	-
Poisson's Ratio	0.33	0.28	0.38[82]
Thickness (mm)	0.075	0.203	0.240

Table 3.13: Predicted Mechanical Properties for Different Volume Fractions

No	Stacking Sequence	# of Plies	E_{11} (GPa)	E_{22} (GPa)	ν_{12}	G_{12} (GPa)	σ_{11} (MPa)
1.	All Al 6061	-	68.9000	68.9000	0.3300	25.9023	310.9200
2.	$Al^{1.5\%}/ ([CFC/ PFC]_{4s})^{67\%/30\%}/Al^{1.5\%}$	18	50.0681	50.0681	0.0801	3.3617	692.5113
3.	$Al^{1.5\%}/ ([CFC/ PFC]_{4s})^{60\%/37\%}/Al^{1.5\%}$	18	46.7338	46.7338	0.0928	3.2664	655.2727
4.	$Al^{1.5\%}/ ([CFC/ PFC]_{4s})^{50\%/47\%}/Al^{1.5\%}$	18	41.9780	41.9780	0.1142	3.1389	602.8644
5.	$Al^{2.5\%}/ ([CFC/ PFC]_{4s})^{65\%/30\%}/Al^{2.5\%}$	18	50.2740	50.2740	0.0889	3.8200	701.8956
6.	$Al^{2.5\%}/ ([CFC/ PFC]_{4s})^{60\%/35\%}/Al^{2.5\%}$	18	47.8805	47.8805	0.0982	3.7518	675.6616
7.	$Al^{2.5\%}/ ([CFC/ PFC]_{4s})^{50\%/45\%}/Al^{2.5\%}$	18	43.1124	43.1124	0.1196	3.6209	623.0364
8.	$Al^{3.5\%}/ ([CFC/ PFC]_{4s})^{60\%/33\%}/Al^{3.5\%}$	18	49.0214	49.0214	0.1034	4.2380	695.6834
9.	$Al^{3.5\%}/ ([CFC/ PFC]_{4s})^{50\%/43\%}/Al^{3.5\%}$	18	44.2373	44.2373	0.1247	4.1046	642.8329

3.9 Design of Sandwich Hybrid Composite Radiation Shield

In order to replace the currently used Al sandwich panel, the solid hybrid composite laminate discussed in the previous section was used as skins sandwiching the Al alloy aerospace grade honeycomb currently used. The honeycomb would slightly lower the TID. However, it does not affect the shield design presented above. The simulated TID transmitted through the sandwich hybrid composite radiation shield is compared with experimental results in Chapter 5.

CHAPTER FOUR

MATERIALS, MANUFACTURING AND TESTING

The design of the hybrid composite radiation shield was verified through mechanical and radiation testing. This chapter presents details on materials and manufacturing of the hybrid composite shield designed in Chapter 3. In addition, details on test coupon preparation and radiation mechanical testing are presented and discussed.

4.1 Materials

Commercially available materials with properties like those of materials used in designing the hybrid composite were procured. Ultra-high molecular weight polyethylene (UHMWPE) unidirectional fibers were procured from a supplier in USA. The unidirectional UHMWPE fibers were converted into woven plain weaved fabric. The fibers were woven in a criss – cross (0/90°) orientation. This was impregnated during manufacturing using a commercially available low-density polyethylene (LDPE) film, which served as the matrix. The LDPE had a film thickness that nearly corresponds to the volume of matrix needed to fill the voids within the UHMWPE fabric. Known properties of the UHMWPE fiber and the LDPE matrix are tabulated in Table 4.1.

Table 4.1: Properties of polyethylene fabric and polyethylene films

Properties	UHMWPE Fiber	LDPE Film
Density (g/cm^3)	0.975	0.92
Tensile Strength (GPa)	3.3	N/A
Elastic Modulus (GPa)	113	N/A
Melting point (°C)	147.5	122.6

A plain weave commercially available carbon fabric pre-preg was procured from USA supplier. Commercial purity grade aluminium alloy thin foil, with a thickness of 75 μm, was purchased from a local supplier.

4.2 Manufacturing Method and Process Cycle Development

The manufacturing method for the designed hybrid composite should accomplish the following:

a) Curing of the pre-impregnated carbon fiber fabric composite, under recommended temperature and pressure, to yield a high quality composite layer.

b) Complete impregnation of the PE fiber fabric by the LDPE matrix, which requires melting of the LDPE film but not the PE fiber. This means the process temperature must be between the melting temperatures for the PE fiber and the LDPE matrix. The impregnation also requires adequate pressure due to the high viscosity of LDPE matrix.

c) Bonding between the Al and CFC layers and between the CFC and PFC layers, which requires adequate pressure for interdiffusion epoxy and PE.

In order to accomplish all these tasks, compression molding of stacked layers of these three constituent layers was chosen.

Although the cure temperature of the CFC prepreg is close to the chosen process temperature for melting of LDPE, steps (a) and (b) could not be accomplished in one step due to the following reason: Impregnation of PE fabric with high viscosity LDPE matrix requires very high pressure. However, the epoxy matrix, within the carbon fiber fabric pre-preg, with much lower viscosity would bleed out at this high pressure resulting in dry spots within the carbon fiber

composite. To avoid excessive resin bleed out, carbon fiber composites are normally cured at low pressure. Hence, a two-step lamination process was developed.

a) Low Pressure Lamination Step: In this step, the stacked layers were heated to the required cure temperature under low pressure to allow the epoxy matrix of the CFC layers to flow resulting in a well consolidated and cured CFC layer. A vacuum was also applied to aid in the removal of volatile and entrapped air and consolidation. Some impregnation of PE fabric with PE matrix may have occurred since the cure temperature was same as the temperature chosen for melting of LDPE. In addition, bonding of CFC layers with Al layers and with PFC layers would have occurred in this step.

b) High Pressure Lamination Step: Subsequent to low pressure lamination, the stacked layers were subjected to the same temperature as in Step 1 but to a much higher lamination pressure. This LDPE melted, flowed and impregnated the PE fiber fabric resulting in well consolidated hybrid composite.

The process temperature and the lamination pressure for both steps were determined using manufacturer recommended cure temperature for the CFC, the melting temperatures of the LDPE film and UHMWPE fibers determined using Differential Scanning Calorimeter (DSC) and manufacturing trails using various pressures. These values are not revealed here to protect the intellectual property.

4.3 Hybrid Composite Face Sheet Manufacturing

Compression molding was used to manufacture the hybrid composite panels. The chosen materials were stacked in the desired sequence and laminated under heat and pressure using the

two-step lamination process cycle discussed in the previous section. The various steps in manufacturing the hybrid composite panel are as follows:

(a) Phosphoric Acid Anodization (PAA): Aluminium foils were anodized according to ASTM D3933 – 98. After anodization, an industrial grade primer was applied several times on both surfaces, followed by air drying and oven drying. Immediate priming of the surface was done to minimize the possibility of inadvertent contamination. The primed foils were safely stored in a craft paper until hand layup stage.

(b) Hand layup: The carbon fiber pre-preg, packed in a vacuum – sealed bag and stored in a freezer at -25°C, was removed and allowed to thaw to room temperature. Then, it was cut into 16.51 cm × 16.51 cm sheets. The PE fiber fabric and the LDPE film were also cut to into same dimension as carbon fiber pre-preg, that is 16.51 cm × 16.51 cm sheets. The average thickness of PFC was 0.240 mm while average thickness of CFC was 0.203 mm. A total of 15 layers were stacked together so as to maintain symmetric lay-up designed in the previous chapter, $[\mathrm{Al}/(\mathrm{CFC}_2/\mathrm{PFC})_2\mathrm{CFC}_{1/2}]_s$. Each UHMWPE fabric was sandwiched between two LDPE films. Cut sheets were manually stacked as per desired stacking sequence.

(c) Lamination: The stacked layers were subjected to the 2 - step lamination cycle discussed in the previous section and a Carver Hydraulic press as shown in Figure 4.1.

An image of typical well compacted hybrid composite face sheet manufactured using the steps above is shown in Figure 4.2

Figure 4.1: Carver hydraulic hot press used in manufacturing of hybrid composite panels

Figure 4.2: Typical hybrid composite panel

4.4 Hybrid Composite Sandwich Panel Manufacturing

Hybrid composite sandwich panel was manufactured by sandwiching an aerospace grade Al alloy aerospace grade honeycomb structure between two hybrid composite panels (referred here as face sheets) manufactured as per procedure discussed in 4.3. Aerospace grade honeycomb core was supplied by the industrial sponsor of this project. An aerospace grade adhesive films, were cut into size and laid between the composite face sheet and the Al honeycomb core. The assembly was held between the platens of the Carver hydraulic press at a known pressure and cured as per the cure cycle recommended by the adhesive manufacturer for the adhesive. The details off the process cycle for the manufacturing of the hybrid composite sandwich panel is not revealed to protect Intellectual Property (IP) rights. The manufactured hybrid composite sandwich panel is shown in Figure 4.3.

Similarly, two Al face sheets (Commercially available Al foil obtained from a local supplier) with a total areal density of 1 g/cm^2 were bonded with the Al honeycomb core the using same curing process to yield an Al sandwich composite, which served as a reference for comparative evaluation of the designed hybrid composite panel.

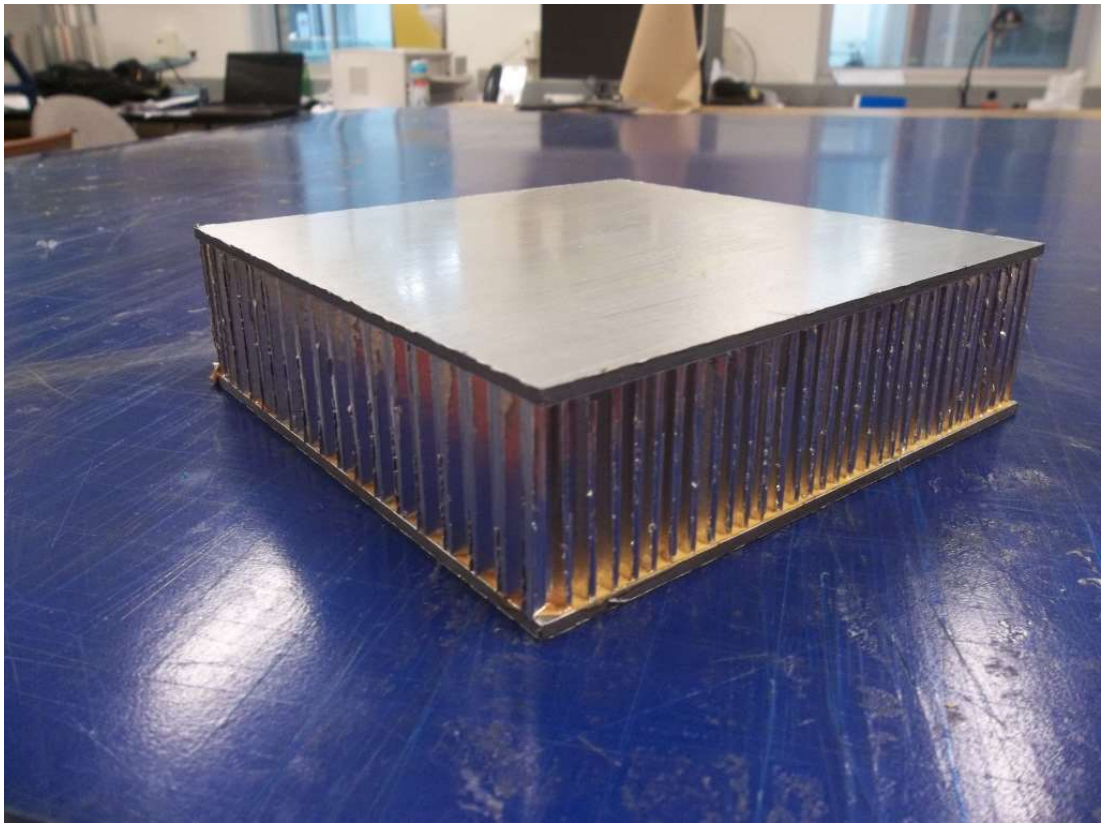

Figure 4.3: Typical hybrid composite sandwich panel

4.5 Testing

4.5.1 Radiation Testing

The ground based radiation sources used in this experiment were chosen based on availability and relevance to space radiation environment in Molniya, a highly elliptical orbit of interest to this study. Even though the exact satellite service environment is difficult to replicate in terrestrial test sites, the radiation sources used in the study have energies comparable to those experienced in Molniya. A significant portion of proton spectra in Molniya have energies less than 70 MeV and fluxes in the range of 10^2 to 10^7 protons/ cm^2s [7, 83]. Similarly, the electrons in Molniya have energies less than 10 MeV with significant portion of the spectra have energies less than 3 MeV and fluxes in the range of 10 to 10^5 electrons/cm^2s [7, 83]. The proton and electron sources used in the experiments had energies of 70 MeV and 10 MeV respectively. The set-up at the electron test facility allowed the measurement and comparison of transmitted TID to evaluate the shielding effectiveness of various materials. However, the set-up at the proton test facility allowed the measurement of Water Equivalence Thickness (t_{WET}), which is defined as the thickness of a body of water that is required to stop the incident proton beam with an energy, E, and equivalent to thickness of "*t*" of a material required to stop the same beam. Hence, for a given areal density, if material A has a higher t_{WET} than material B, then material A would have a higher radiation shielding effectiveness.

Eight (8) panels, identified in Table 4.2 were manufactured and tested. t_1 and t_2 correspond to two different thicknesses of the same panel composition ($t_1<t_2$). The TID and t_{WET} for the three constituents of the solid hybrid composite face sheet panel, namely the PFC, the CFC, and the Al were measured and compared with the simulated values generated using MULASSIS to validate

its simulation accuracy. Further, the TID and t_{WET} of the hybrid composite face sheet (DFC) and the hybrid composite sandwich panel (DSP) were measured and compared with those of Al face sheet and Al sandwich panel (ASP), to evaluate their relative merit. Since the areal densities of these panels varied slightly due to manufacturing variabilities, each panel with 2 to 3 areal densities were tested to generate TID versus areal density and t_{WET} versus areal densities. These curves for various panels were compared.

The samples were kept inside the test room for two days after irradiation to allow the irradiation levels (due to activation) in the test panels to reduce to a safe value for handling, before shipping back to the University of Manitoba.

4.5.1.1 Proton Radiation Testing

The cyclotron accelerator of TRIUMF located on the campus of the University of British Columbia, Canada was used in this study. The cyclotron generated a proton beam with an energy of 70 MeV and the intensity of the beam was set to 5nA (2×10^8 protons/cm^2.s). This energy was degraded to 63 MeV when it entered the test set-up shown in Figures 4.4 and 4.5, which is a modified version of that used in ocular therapy at TRIUMF [84].

The proton beam was collimated onto the test panel using two collimators. Two ion count chambers filled with inert gas were used as detectors. The Diagnostic Ion Chamber (DIC) behind the first collimator measured the ion count due to incident proton beam, while the Back-up Ion Chamber (BIC), placed behind the test panel, measured the ion count due to proton beam leaving the test panel and the IC Cover. The ratio of the ion count from the BIC to the ion count from the DIC (BIC/DIC) provided a measure of change in the intensity of the proton beam due to its

Table 4.2: Radiation Test Panels

Test ID	Material	Panel Thickness (mm)	Areal Density (g/cm^2)
PFC	PFC Panel	1.05	0.099
CFC	CFC Panel	0.58	0.087
Al	Al Panel	1.6	0.43
DFC-T1	Hybrid Face Sheet - t_1	2.84	0.39
DFC-T2	Hybrid Face Sheet - t_2	11.36	1.56
DSP-T1	Composite Sandwich Panel - t_1	8.22	1.17
DSP-T2	Composite Sandwich Panel - t_2	17.04	2.73
ASP-T1	Aluminum Sandwich Panel - t_1	5.74	1.24

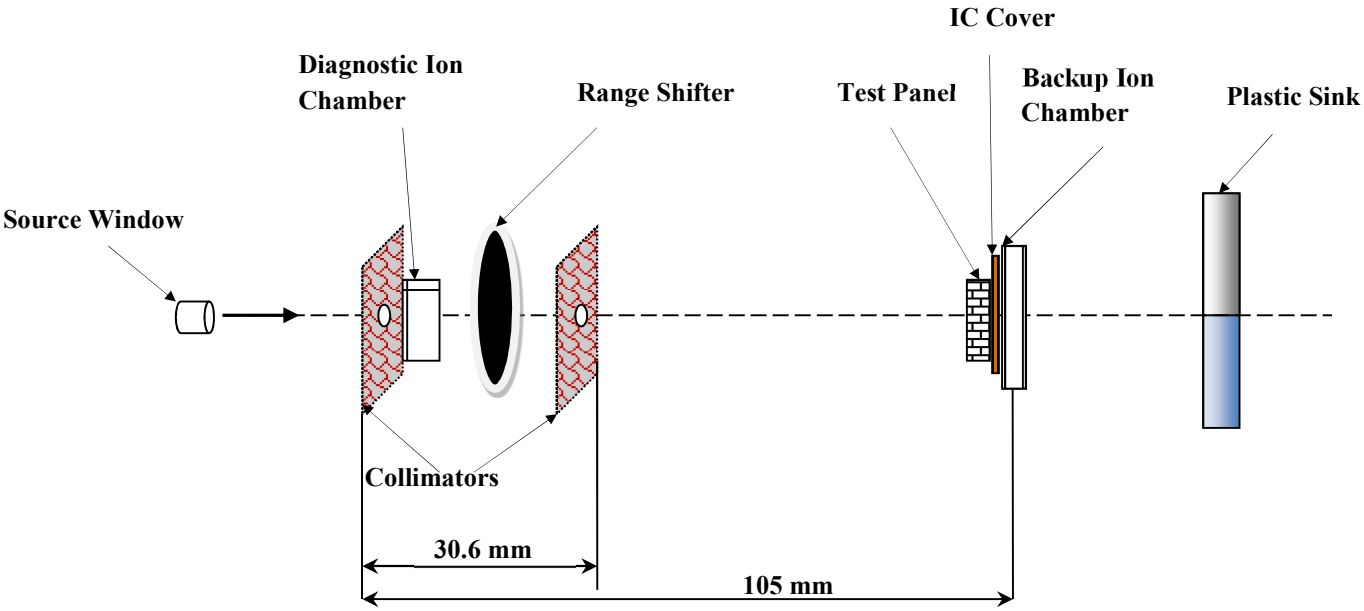

Figure 4.4: A schematic of the proton beam set-up at TRIUMF, Vancouver, Canada

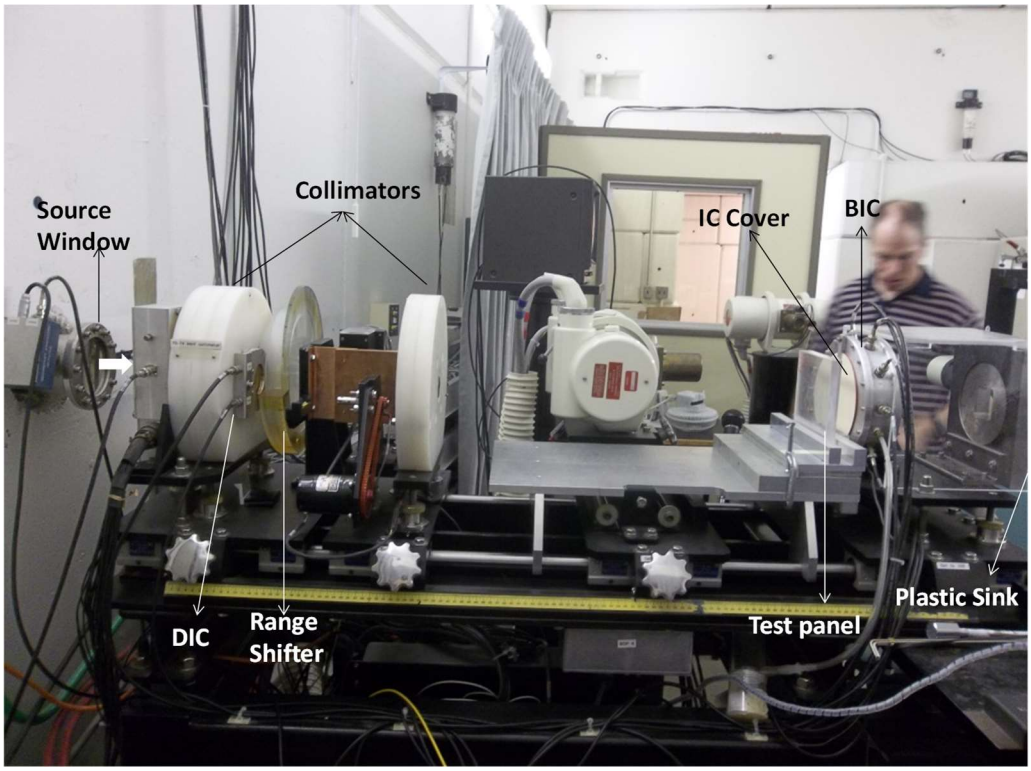

Figure 4.5: Photograph of the proton beam setup with components identified

interaction with the test panel. The IC cover was used between the test panel and the BIC to prevent any accidental damage to the BIC while loading and unloading the test panel.

Since a test panel may not be thick enough to attenuate the incident beam completely, a remote controlled Range Shifter (RS), located between the two collimators and before the test panel, was used to vary the energy of the proton beam incident on the test panel. The RS is a Lucite disc with varying thickness, and the thickness of Lucite in the path of beam was varied by the rotating the disc. The position and thus the thickness of the Lucite in the path of the beam was changed automatically by rotating it.

As a first step, a laboratory calibrated Extradin T1 0.05 cc ion chamber connected to Keithley 616 electrometer was used to provide the absolute dose calibration. The Extradin –T1 was a laboratory calibrated ion chamber. The calibration was done by comparing the dose count of the Exatradin-T1 with that of the BIC introduced in to the beam at the same location; if a pre-established relationship between the two is confirmed, further testing is continued.

After loading the test panel in the path of the proton beam, a coarse scan was performed to locate the Bragg Peak. The RS was increased in steps of 100 in the total range of 0 – 2800 and the ratio of BIC Ion Count/DIC Ion Count was recorded for each step to identify the approximate position of RS around which the Bragg peak was observed. Subsequently, a second finer scan was performed around the Bragg peak to cover a total RS range of 600. During the finer scan, the RS was changed in steps of 10. The rate of increment was 1 increment per second. Thus, the total time taken for one complete scan was 60 s. There was no noticeable irradiation-induced heating since the temperature of the test panel remained between 26 and 28° C.

A representative curve of BIC/DIC versus RS position is shown in Figure 4.6. The ratio of the ion count increased with increase in thickness to a peak value before decreasing and approaching zero value asymptotically. This peak is the well-known Bragg peak, due to secondary particles produced due to interaction of the proton beam with the material. Due to precipitous drop in the ratio beyond the Bragg peak, the RS position value after the peak, corresponding to 90% of the Bragg peak value, was taken to be the stopping range. This RS position ($RS_{90\%}$) was extracted by the software that controls the set-up and used in Eq. (4.1) to determine the $t_{WET,\ RS90\%}$ for the Lucite.

$$t_{WET,\ RS90\%} = 1.156 * (2.23 + 1.0075 * 10^{-2} * RS_{90\%}) \text{ mm} \quad (4.1)$$

This equation has been developed by Blackmore (2000) through a calibration procedure. This $tWET_{,\ R90\%}$ was used along with Eq. (4.2) to determine $t_{WET,\ Test\ Panel}$ for the test panel.

$$t_{WET,\ Test\ Panel} = 30.69 - t_{WET,\ RS90\%} \text{ mm} \quad (4.2)$$

The rationale for these two equations are discussed further in the Appendix C. t_{WET} was determined as a function of areal density for the three chosen materials and compared with the predictions from MULASSIS.

Available conversion charts at TRIUMF provide the energy of the proton beam incident on the test panel as well as multiplication constant to convert ion count into dose in Silicon (Si). This would have allowed simulation of the ratio, Transmitted Dose /Incident Dose = BIC/DIC. However, due to the presence of the IC cover, the transmitted TID was not entirely due to the test panel, which prevented direct evaluation of the transmitted dose instead of $t_{WET.}$

Since the RS degrades the energy of the proton beam to values much below 63 MeV, the experimental results corresponded to a very small energy range (8 -27 MeV). In order to validate the MULASSIS over a wider energy range, its simulations were compared with simulations from another software, SRIM (Stopping and Range of Ions in Matter). The simulation of stopping range of proton in water using SRIM has been well studied and considered to be accurate [46] – within 4.3% for 2010 version.

4.5.1.2 Electron Radiation Testing

The electron test was carried out at Acsion Industries Inc., Pinawa, Manitoba, Canada using its 10 MeV, 4 kW electron accelerator, which produces a pulsating and scanning beam. The test set-up is shown in Figure 4.7. The test panel was placed on a moving conveyor belt exposed to the electron beam as shown in Figure 4.8. The beam delivered electrons with intensity density of ~ 370 μA (1.84×10^{14} electrons/cm^{2}s) on the test panel. Radio-Chromatic dye dosimeters, FWT-60 from Far West Technology, were used as detectors to measure the dose (in Gray) deposited at the center of the panel due to electron exposure. The dosimeter had a thin film, 1 cm × 1 cm in area with an average thickness of 4 -5 microns. After exposure, this film was used along with a read-out unit provided by Far West Technology to determine the dose deposited on the film. As per manufacturer's data sheet, the lowest dose that can be measured by the dosimeter is 4 kGy with an uncertainty of ± 6% at a 95% confidence level.

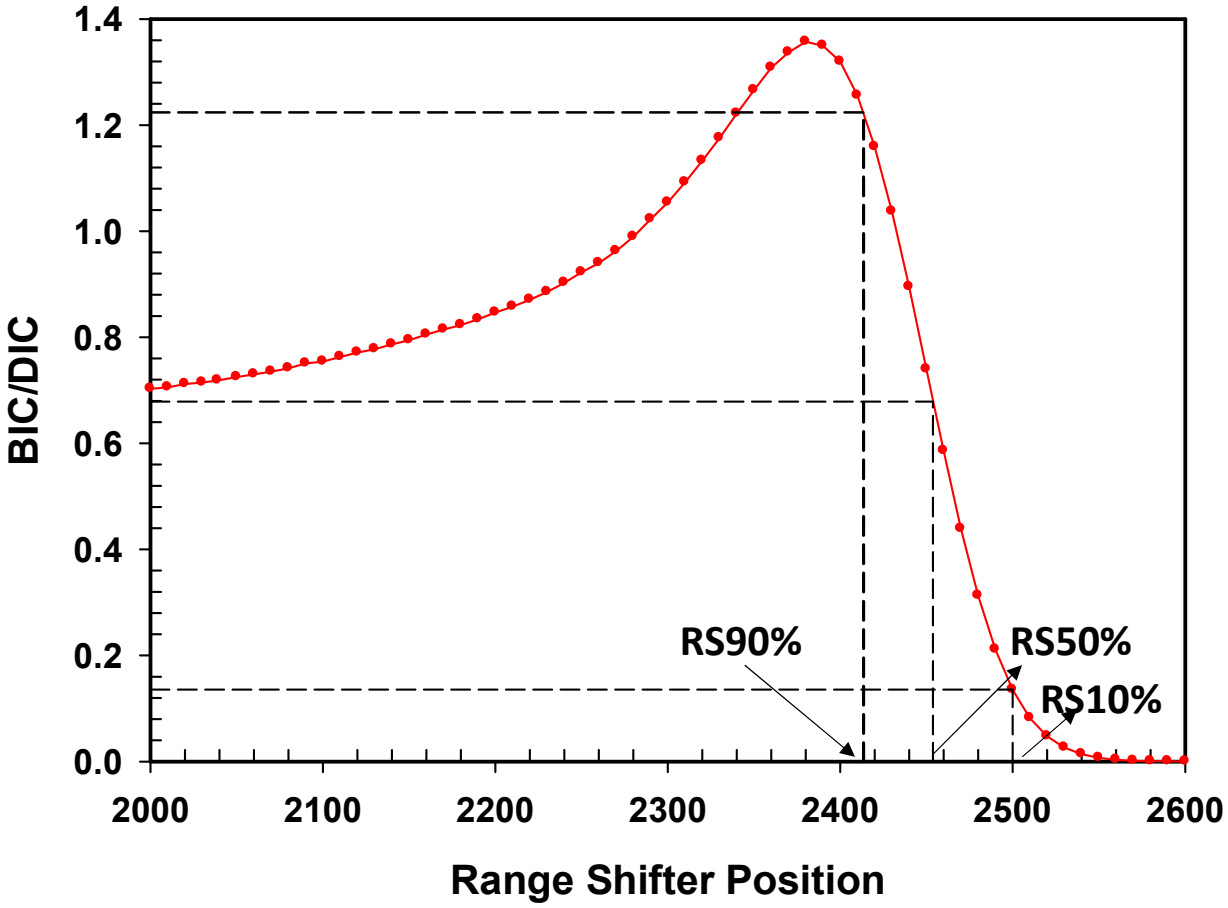

Figure 4.6: Ratio of ion counts recorded by BIC and DIC as a function of range shifter position

Two dosimeters were attached to the front of the panel to determine the average incident dose. Two dosimeters at the back of the panel were used to determine the average dose transmitted through the panel. In addition, multiple panels were stacked to measure the transmitted dose as a function of thickness. In such cases, additional dosimeters were placed between panels to obtain the dose as a function of thickness. Since the dosimeters were calibrated to equivalent absorbed dose in water, a simple conversion Eq. (3) given by the Bragg-Gray relationship (ICRU Report 35, 1984) was used to determine the absorbed dose in Silicon using the dose measured using the dosimeter.

$$D_{Si} = D_{Water} / R_{Water,Si} \quad (4.3)$$

where D_{Si} is the dose in silicon, D_{Water} is the dose measured in water by the dosimeter and $R_{Water,Si}$ is the ratio of the MCSP (Mass Collision Stopping Power) for water to the MCSP for Si. The MCSP values for 10 MeV electrons in water and Si are 1.968MeV $cm^2 \cdot g^{-1}$ and 1.697MeV $cm^2 \cdot g^{-1}$ respectively. Therefore, $R_{Water,Si}$ is 1.968/1.697 = 1.160. The results of absorbed dose in Silicon, from electron exposure, were compared with simulation results using MULASSIS to validate the latter.

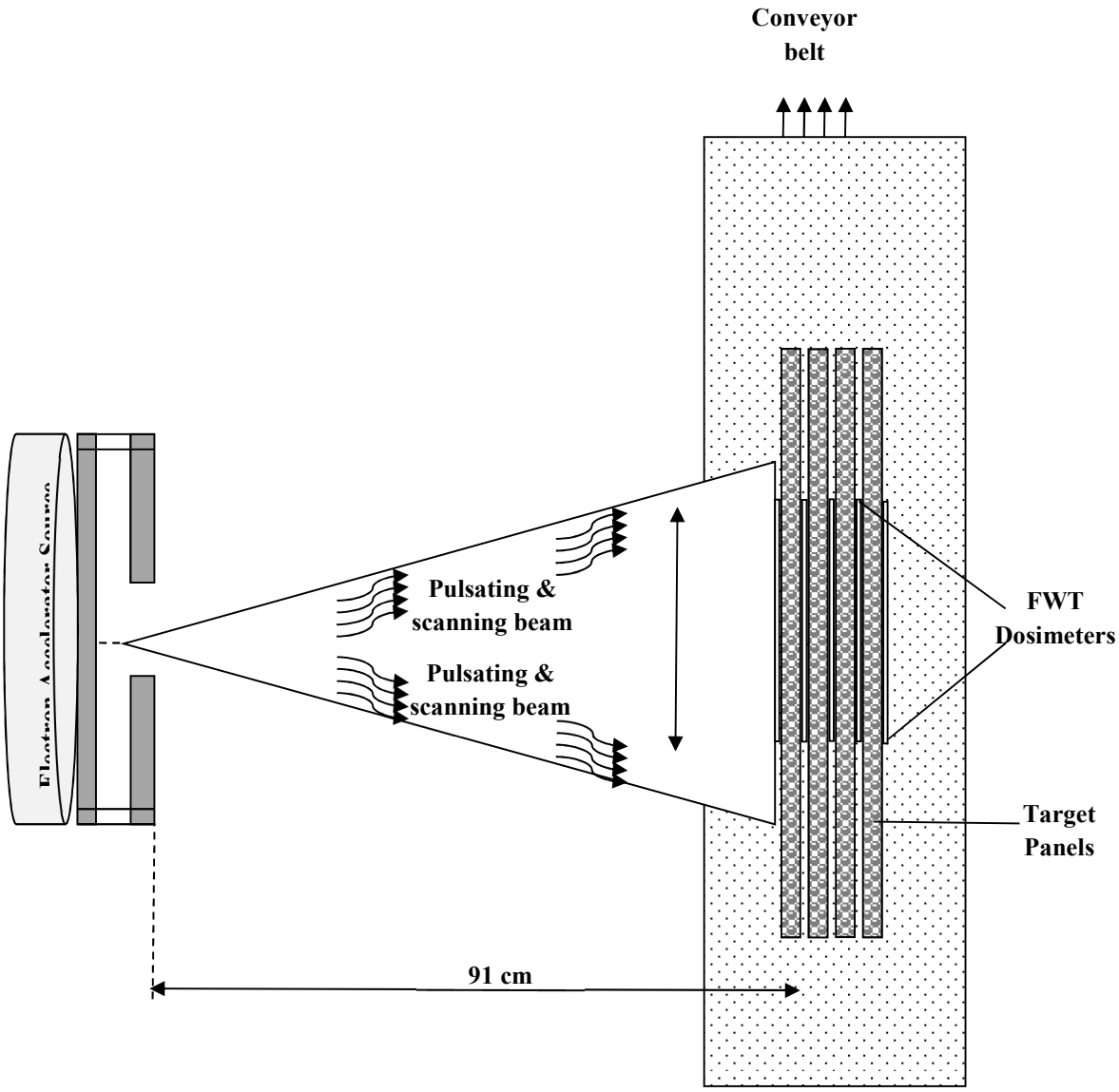

Figure 4.7: Schematic diagram of the electron test set-up

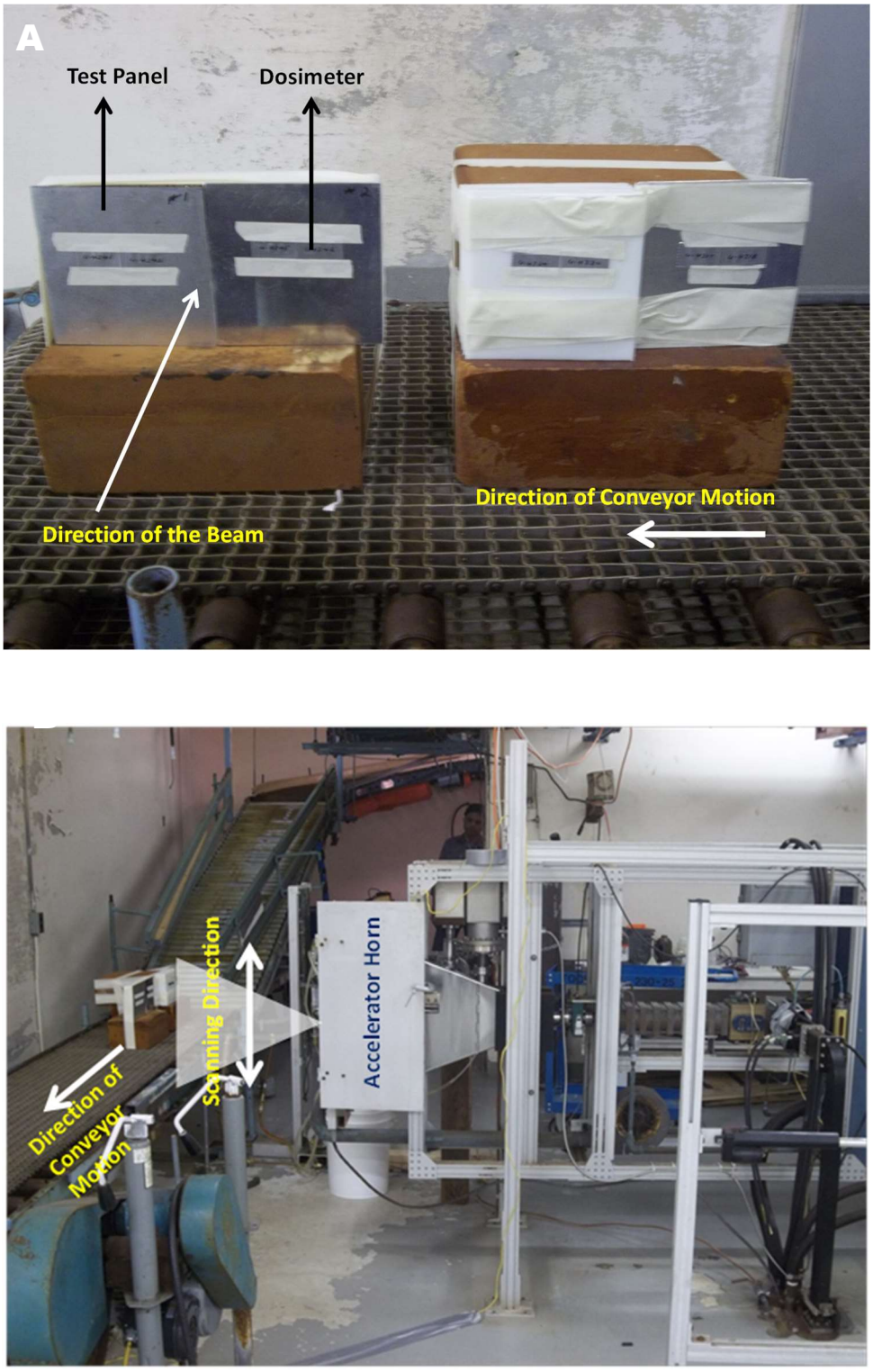

Figure 4.8: Photographs of the electron beam setup with components identified

4.6 Mechanical Testing

4.6.1 Tensile Testing

Tensile tests were performed on the PFC, the CFC, and the hybrid composite (DFC) to determine their mechanical properties. Testing of CFC and PFC were done to make sure that they were well consolidated and/or cured. The properties of these constituents were used in determining mechanical properties of the designed hybrid composite as discussed in Chapter 3 (section 3.8). The measured properties of the hybrid composites were compared with the properties of Al 6061-T6 traditionally used in satellite structures.

4.6.1.1 Tensile testing of PFC

Tensile tests were carried out on PFC test coupons as per ASTM D3039 using a MTS Insight - 820-030-SL- test frame manufactured by MTS System Corp. The load frame was equipped with ±30KN load cell. PFC test coupons, 152.4 mm in length and 25.4mm in width, were cut from the molded composite panels. The ends of each specimen were bonded with carbon epoxy composite tabs (25.4 mm × 25.4 mm), using Devcon 2-ton clear epoxy (ITW Devon®). The adhesive was cured at 60°C for 30 minutes. This allowed gripping of the samples without any premature facture at the clamping points. The tensile test was carried out at a displacement rate of 2 mm/min. Due to the smooth surface and poor bondability of the PFC, neither extensometer nor strain gauge could be attached to the specimen. Therefore, strain was determined using the crosshead displacement. All tests were done at room temperature. Five samples were tested to obtain average properties. Tensile modulus was calculated from slope of the stress – strain curve in the strain range < 0.2%.

4.6.1.2 Tensile Testing of CFC

The procedure was same as that used for PFC. However, the strain was measured using an extensometer of 50.8 mm gauge length.

4.6.1.3 Tensile Testing of Hybrid Composite (DFC)

Tabbing material, 12.7 mm in length and made from woven carbon fiber epoxy composite laminates, (F263-8/T300), were bonded on to two opposite edges of the hybrid composite panel using Cytec Industries Inc.'s adhesive. The adhesive was cured in the Carver hydraulic press at 120 °C for 30 minutes using a pressure of 0.72 tons. The panel with bonded tabs was then allowed to cool down to room temperature under pressure. Test coupons were cut into dimensions as shown in Figure 4.9, using a slow speed Micro-matic Precision Wafering Diamond Cutter from Micromech Corp. at a feed rate of 6 mm/min. Slow speed was used to prevent over heating of the saw and damage to specimen edges. The composite panels were held on the bed of the cutter using double sided tape. The edges of the samples cut were progressively grounded and polished using 180, 240, 320 and 400 grit silicon carbide papers to remove any damage introduced by the cutting.

Strain gauges of type CEA-13-250UW-350 from Micro Measurements Group Inc. were bonded to the test coupons using M-Bond 610 supplied by the manufacturer. Before bonding, the desired area was cleaned using M-prep Conditioner A (alkaline) followed by M-prep Neutralizer B (acidic). The strain gauge was bonded at room temperature with application of thumb pressure for 2 minutes. The test coupons were tested using MTS Insight- 820-030-SL- test frame

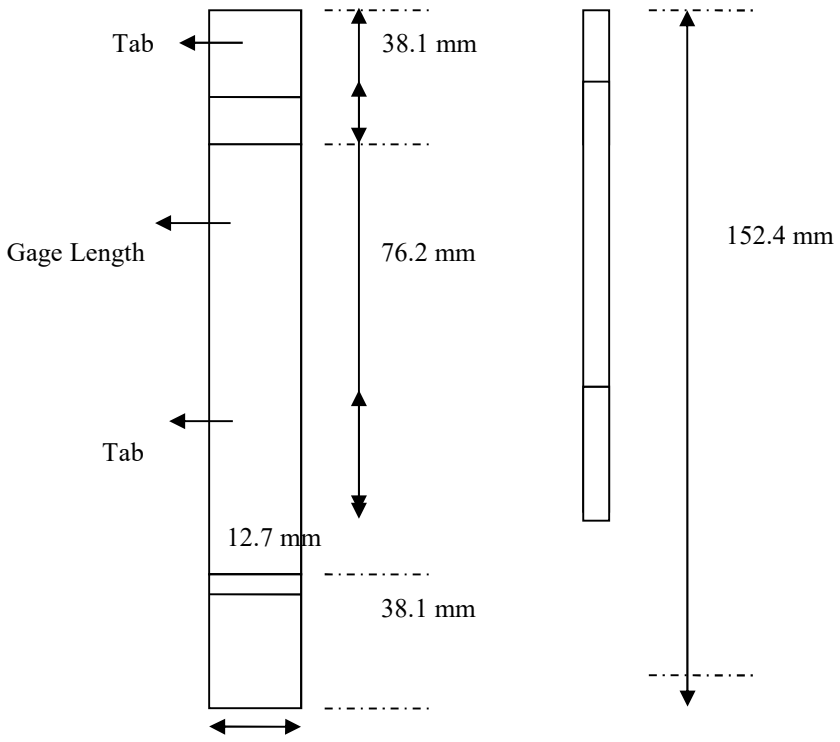

Figure 4.9: Typical test coupon and sample geometry

SCXI-1000 data acquisition system from National Instruments USA, was used to log the strain during tensile test. This system consisted of a SCXI- 1121 signal conditioning module fitted into a SCXI- 1000 chassis and connected to a SCXI -1321terminal block. The SCXI-1000 unit was connected to a computer fitted with PCIe-6251 multifunctional DAQ board and. A Labview based program was used for data sampling and logging at different rates during tests, with the data sampling rate set to 1000 kHz while the logging rate was varied from 1 data point per sec to 1 data point per 300 sec. The hardware was programmed to acquire three independent parameters (strain, position and time) simultaneously for each test.

The load data was collected using the MTS Software (2010) from MTS Insight- 820-030-SL- test frame. The time stamp of the data was used to match the load and the strain recorded using the data acquisition system.

4.6.2 Compression Testing

The compression tests were carried out using Combined Loading Compression (CLC) test method as per ASTM D6641. The method is applicable to general composite that are balanced and symmetric. Also, it can be used for both un-tabbed (Procedure A) and tabbed (Procedure B) test coupons. Untabbed specimens are usually suitable for use with materials of low orthotropy (fabrics and laminates with a maximum of 50% 0° plies, or equivalent). Hybrid composite panels composed of mainly fabrics lamina, therefore untabbed specimen and Procedure A was used. The CLC fixture from Wyoming Test Fixtures Inc. (WTF-EL-335) as shown in Figure 4.10, was used.

The compression test coupons, 139.7 mm in length × 12.7 mm in width as shown in Figure 4.11, were cut from the hybrid composite panel using a slow speed micro-matic precision wafering diamond cutter from Micromech Corp. at a feed rate of 6 mm/min. The edges of the samples cut were progressively ground using 180, 240, 320 and 400 grit silicon carbide papers to remove any defects introduced near the edges due to cutting. A gage length of 12.7 mm was used in the testing.

Strain gauges of type CEA-13-062UW-350 from Micro Measurements Group Inc. were bonded to the test coupons using M-Bond 610. The CLC compression test was carried out using a MTS Insight - 820-030-SL- test frame manufactured by MTS System Corp at a displacement of 1.3 mm/min. The strain data was logged using the data acquisition system discussed in the previous section. Five test coupons were tested and the average value of the result was reported.

Figure 4.10: Compression test set up

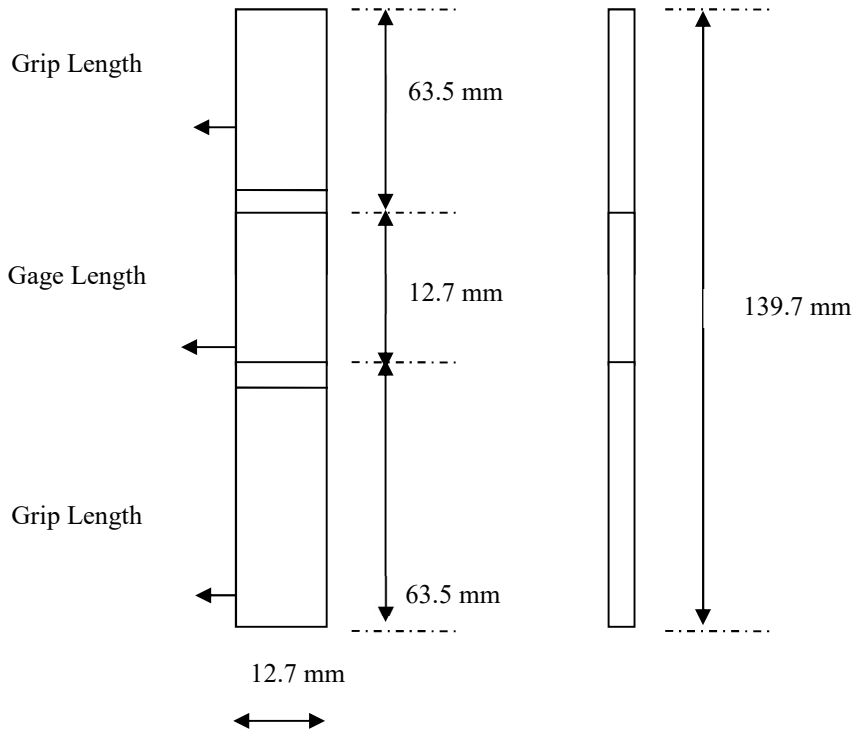

Figure 4.11: Compression test coupon geometry

4.6.3 Shear Testing

V- notched rail shear test method was used to determine the in-plane shear properties of hybrid composite panels in accordance with ASTM D7078/D7078M. The test method is suitable for shear testing of multidirectional composite laminates and textile composites. Flat rectangular coupons with a length of 76.0 mm (3”) and a width of 56.0 mm (2.2”) were cut from the hybrid composite panel and V-notches, as shown in Figure 4.12, were cut using DoALL 16" vertical band saw (Model - 1612). The edges were grind and polish to remove any source of localized deformation.

The edges of the V-notched specimen were clamped in the WTF-NR-120 Utah V-notched rail shear test fixture (Wyoming Test Fixtures Inc.) as shown in Figure 4.13. The gripped areas of the test coupon were roughened using an abrasive cloth (80 grit paper) to prevent any slipping during testing. When the fixture is loaded in tension, the relative displacement between the two halves of the fixture introduces shear stresses in the region of the test coupon between the notches. V-notches increase the magnitude of the shear stress in this region (gage section) when compared to the shear stress in the vicinity of the gripped locations of the test coupon. This localized the failure within the gage section while causing shear stress distribution to be more uniform. Two strain gauges (CEA-06-250UN-350), oriented at ±45°C to the loading axis were bonded to the specimen to measure the strain response. The gauge elements were centered between the notch tips in the gauge section of the specimen. The data was acquired using the DAQ system described in the previous section. The test fixture was mounted between the cross-heads of the MTS Insight - 820-030-SL- test frame and loaded in tension. Five of test coupons were tested and the average value of the result is reported.

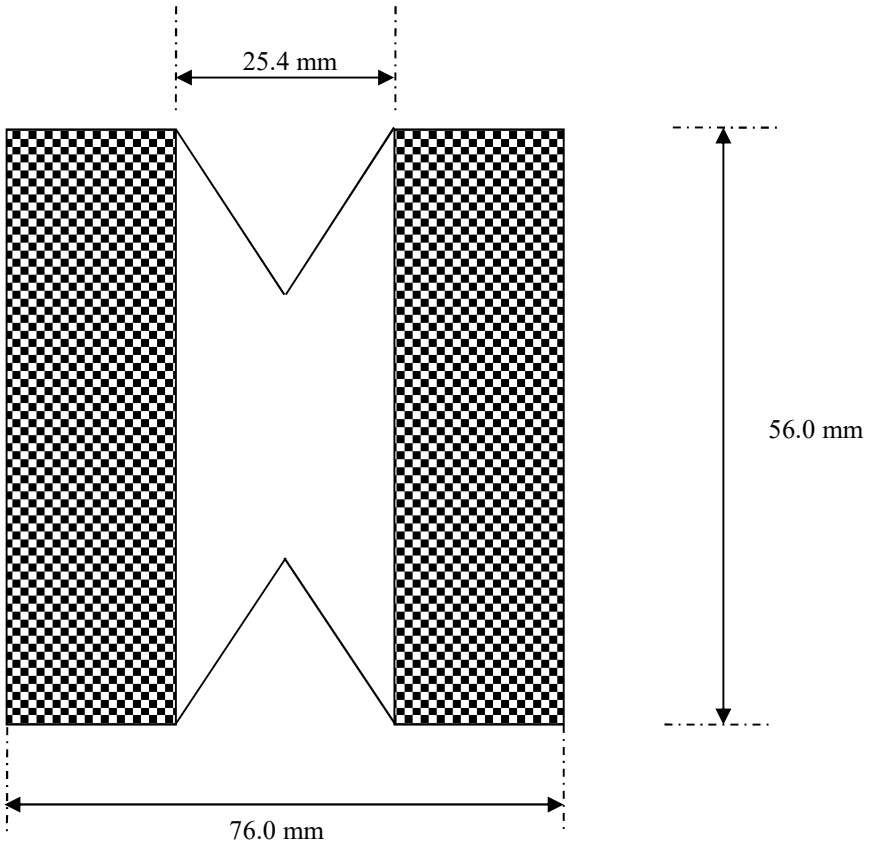

Figure 4.12: V-notched rail shear specimen

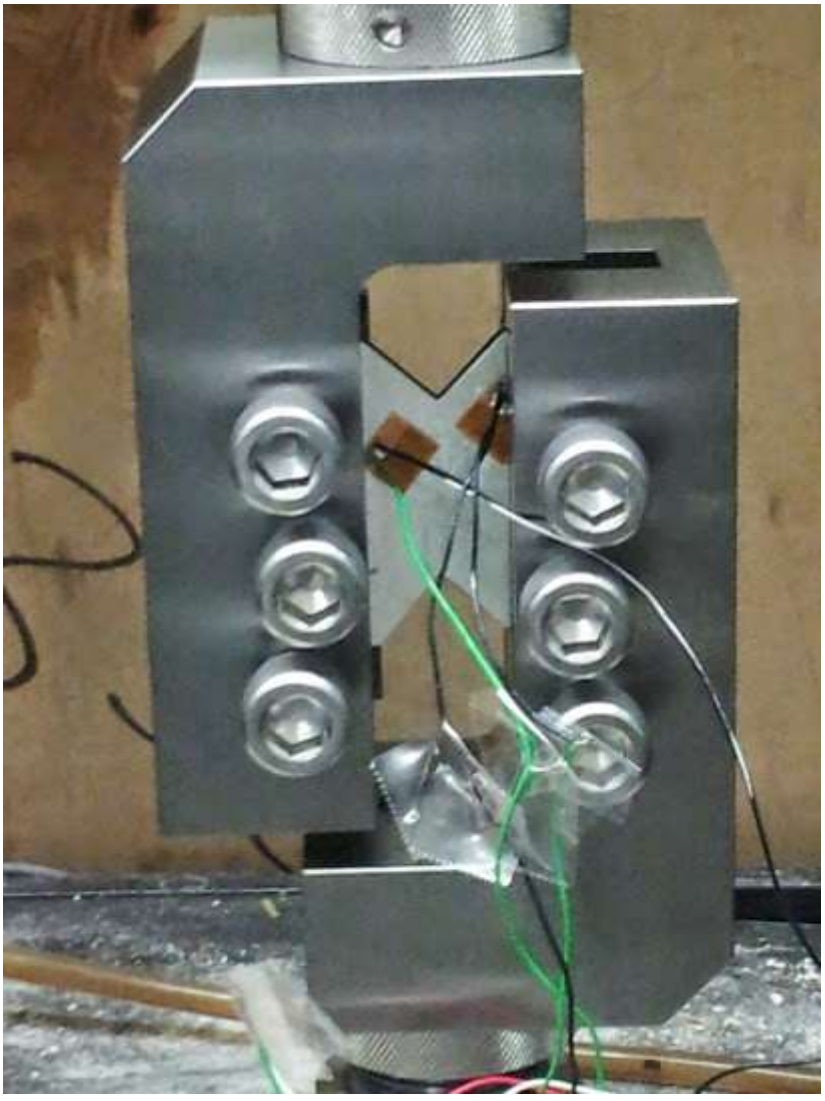

Figure 4.13: V-notched rail shear test fixture with loaded test specimen

4.6.4 Flexural Testing

Flexural testing of hybrid composite was completed using a three-point test fixture as per ASTM D7264/D724M (Procedure A).

Flexural test coupons with dimension shown in Figure 4.14 were cut from the hybrid composite using the procedure discussed in Section 4.6.1 for tensile test. The coupons were tested according to ASTM D7264/ D7264M guidelines with a span length of 95mm and a test speed of 1.0 mm/min using the MTS Insight- 820-030-SL- test frame with ±30 KN capacity load cell. The image of the test setup is shown in Figure 4.15.

Two sets (5 coupons each) of coupons were tested, (a) HC (Hybrid Composite) test coupons without any prior conditioning named “as-prepared samples” and (b) Thermal cycled HC samples. These latter samples were thermally cycled in an Environmental Chamber – model ZBHD-2022 from Associated Environmental System Inc., USA shown in Figure 4.16. The samples were thermally cycled from -60°C to +60°C for 100 cycles using the cycle shown in Figure 4.17 and subsequently subjected to flexural test. This simulates environmental condition experienced by satellite structure space. The ultimate tensile strength (UTS) and the facture mode of each sample were obtained from the test.

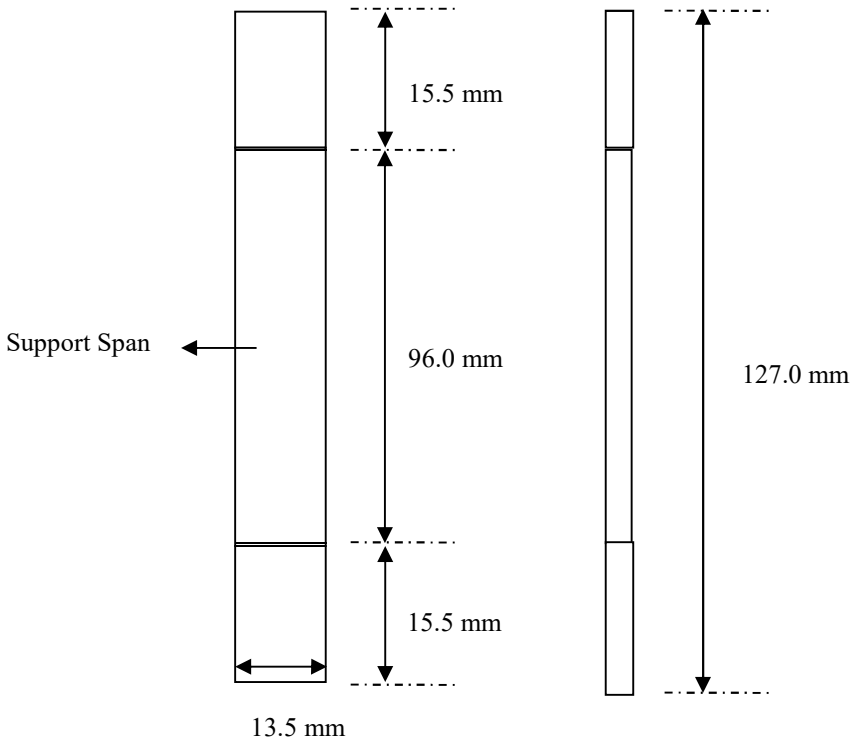

Figure 4.14: Flexural test coupon geometry

Figure 4.15: Flexural test set-up

Figure 4.16: Environmental chamber used in thermal cycling

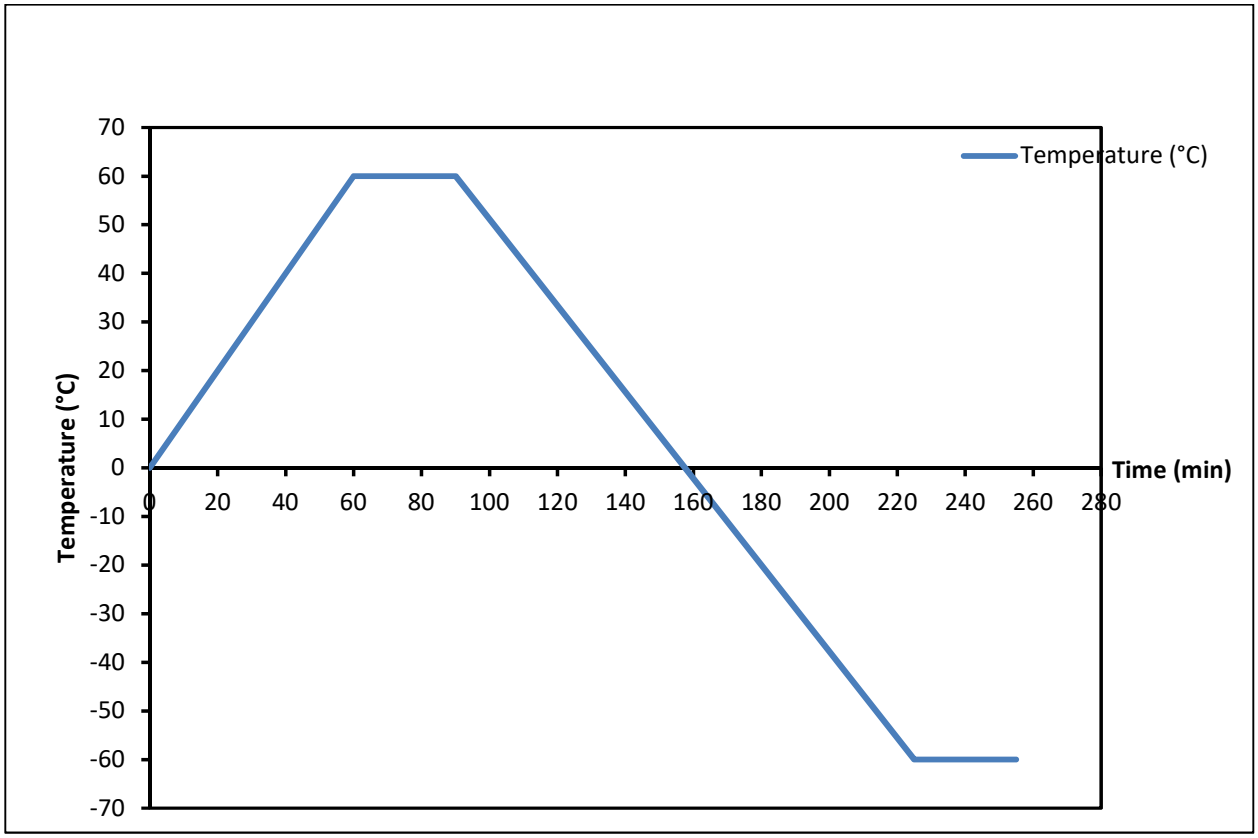

Figure 4.17: Thermal cycle used in conditioning the hybrid composite flexural test coupon

4.6.5 Flatwise Tensile Testing

Flatwise tensile test (FWT) was used to determine the strength of the bond between the Aluminum honeycomb core and hybrid composite face sheet as per the guidelines of ASTM C297 / C297M. This test was accomplished using the FWT 50.8 mm Square Blocks test fixture from Wyoming Test Fixtures Inc. (Model - WTF-FT-57).

Square shaped test coupons (50.8 mm x 50.8 mm) were cut from 152.4 mm × 152.4 mm sandwich panel using low speed 39-1471 Handimet I cutter. Precautions were taken to avoid notches, uneven surfaces and delamination while cutting. Edges of all the specimens were polished using 800 grit silicon carbide paper to remove any effect of cutting.

The top and bottom faces of the test specimens were bonded to two aluminium loading blocks (50.8 mm x 50.8 mm) using Cytec film adhesive cured at 120°C for 30 minutes under low pressure of 0.50 MPa.

The Al blocks, bonded to the test coupon, were mounted on the FWT test fixture as shown in Figure 4.18. The test fixture was subsequently mounted between the cross-heads of the MTS Insight- 820-030-SL- test frame and loaded in tension at the rate of 0.50 mm/min to failure. Ultimate Flatwise Tensile strengths, failure modes and failure locations were recorded. The same procedure was repeated for thermally cycled hybrid composite sandwich test coupons. Five of test coupons were tested and the average value of the result was reported.

Figure 4.18: Flatwise tensile test set-up

CHAPTER FIVE

RESULTS AND DISCUSSION

In this chapter, the experimental radiation test results and mechanical results for the manufactured test coupons are presented and discussed. To begin with the experimental results from radiation testing of the manufactured solid as well as sandwich hybrid composite laminates are compared with simulated results. Results for Al panel as well as Al sandwich panel are also presented and compared with those of composite shields to demonstrate the weight savings achievable with the latter. Subsequently, the experimentally measured mechanical properties are compared with the Al 6061 to demonstrate the ability of the composite panel to meet structural requirements.

5.1 Radiation Test Results

As indicated in 4.5.2, the mono-energetic proton and electron beams available in Canada were used to validate the MULASSIS and the design of the hybrid composite radiation shield. The t_{WET} under proton beam and the transmitted TID under electron beams were experimentally measured and compared with the simulated results to validate MULASSIS. Further, the experimental results for the hybrid composite face sheet (DFC) and sandwich panel (DSP) were compared with those for the Al face sheet and sandwich panel (ASP) to demonstrate the better shielding effectiveness of the former.

5.1.1 Proton Test Results

5.1.1.1 Proton Validation of MULASSIS

For the three constituent materials used in this study, t_{WET} was measured for 1.6 mm and 6.4 mm thick Al (areal densities of 0.43 g/cm^2 and 1.72 g/cm^2 respectively), 1.05 mm thick PE (areal density of .099 g/cm^2), and 0.58 mm thick CFC (areal density of 0.087 g/cm^2). The experimental t_{WET} results are compared with the values simulated using MULASSIS in Figure 5.1.

In order to predict the stopping range in materials, the dose deposited on the Si detector by the proton beam passing through the target panel of a given thickness was simulated. This simulation was repeated by varying the thickness. A typical transmitted TID versus thickness plot at various input proton beam energies is shown in Figure 5.2 for Al.

For a given beam energy, the transmitted TID increases with increase in thickness to a peak value before decreasing and approaching zero value asymptotically. This peak is the well-known Bragg peak, due to secondary particles produced due to interaction of the proton beam with the material. Due to precipitous drop in the TID beyond the Bragg peak, the thickness after the peak, corresponding to 90% of the TID corresponding to the Bragg peak, was taken to be the stopping range. This is also consistent with $RS_{90\%}$ in Eq. (4.1) enabling comparison of the experimental and the simulation results. The stopping range (thickness) is plotted as a function of proton beam energy in Figure 5.3 for Aluminum and water, which was used to determine t_{WET} as follows.

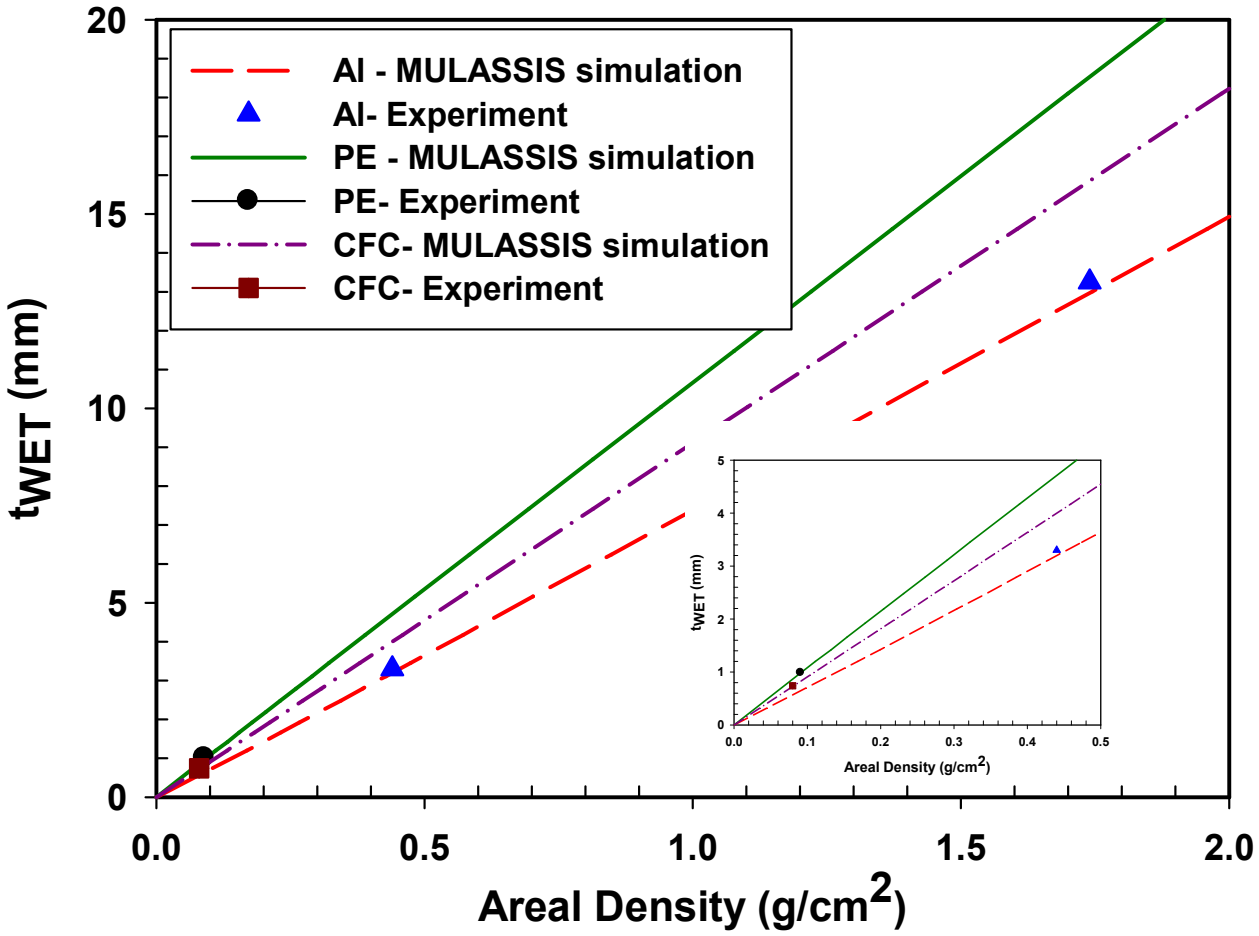

Figure 5.1: Plot of t_{WET} vs areal density (Inset: Enlarged plot of t_{WET} at lower areal densities).

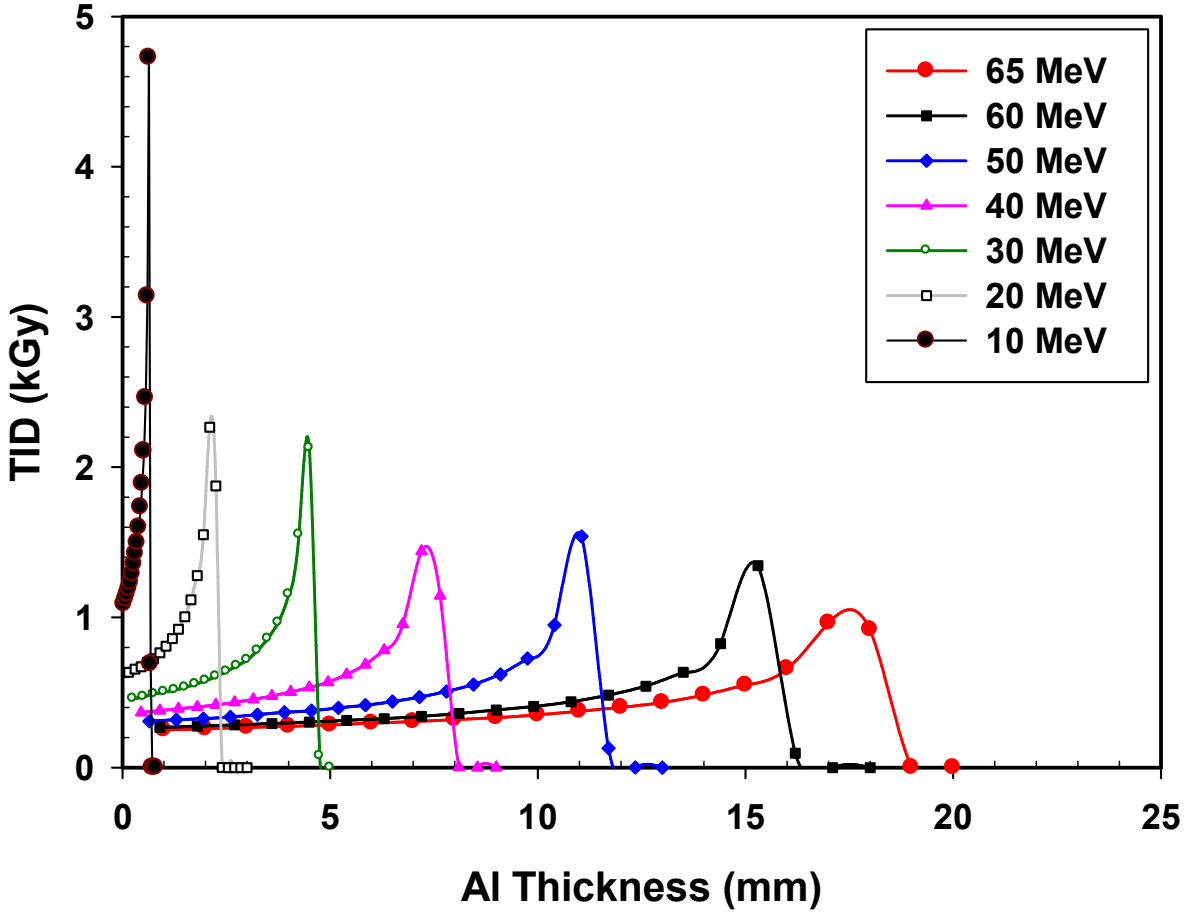

Figure 5.2: Dose – depth profile for transport of proton beam in Al

For a given energy, the stopping ranges (thicknesses) corresponding to Al and water were determined. For example, at 30 MeV, the thicknesses for Al and water are determined to be 4.32 mm and 8.69 mm respectively, as illustrated in Figure 5.3 with dotted lines. This thickness of water (8.69 mm) is the t_{WET} corresponding to the Al thickness of 4.32 mm (i.e. an areal density of 1.16 g/cm^2) to completely absorb the same (30 MeV) incident proton beam. Using this procedure, t_{WET} was simulated as a function of aerial density and compared with the experimental results, as shown in Figure 5.3.

The correlation between experimental and simulated results for Al in Figure 5.1 is excellent with a difference of less than 1%.

Similarly, the relative difference between the simulated and the experimental t_{WET} values for PE and CFC in Figure 5.1 are 5.94% and 1.64%, respectively. These results confirm that MULASSIS can simulate shielding effectiveness of materials against protons within 6%. It can also be inferred from the plot that for a given areal density, PE has the highest t_{WET}, followed by CFC. The Al has the least t_{WET}. Thus, the shielding effectiveness of the three materials against proton increases in this order: Al < CFC < PE.

In addition, SRIM (2013 version) was also used to confirm the predictions of MULASSIS beyond 8 - 27 MeV used in the experiments. Full description of the simulation process can be found in Ziegler et al. [46, 85].

The stopping range (thickness) values simulated using MULASSIS and SRIM are compared in Figures 5.4, 5.5 and 5.6 for Al, PE, and CFC respectively. The maximum difference between the two predicted values, for a given energy, was 5.4 %, 1.75%, and 3.9 % for Al, PE,

and CFC, respectively. Thus, correlation between simulations from MULASSIS and SRIM is considered to be very good. The difference could be attributed to the discrete thickness values used in the simulation. SRIM used a finer 1 MeV energy increment while determining the stopping range and MULASSIS used a coarser energy and thickness increments (in order to reduce the computation time). This may have resulted in slight difference in the predicted Bragg peak values and the stopping range determined using these two codes.

While the experimental data points are limited for direct validation for MULASSIS, excellent indirect validation has been achieved through comparison with SRIM simulations. Nevertheless, further experimentation is required for direct validation.

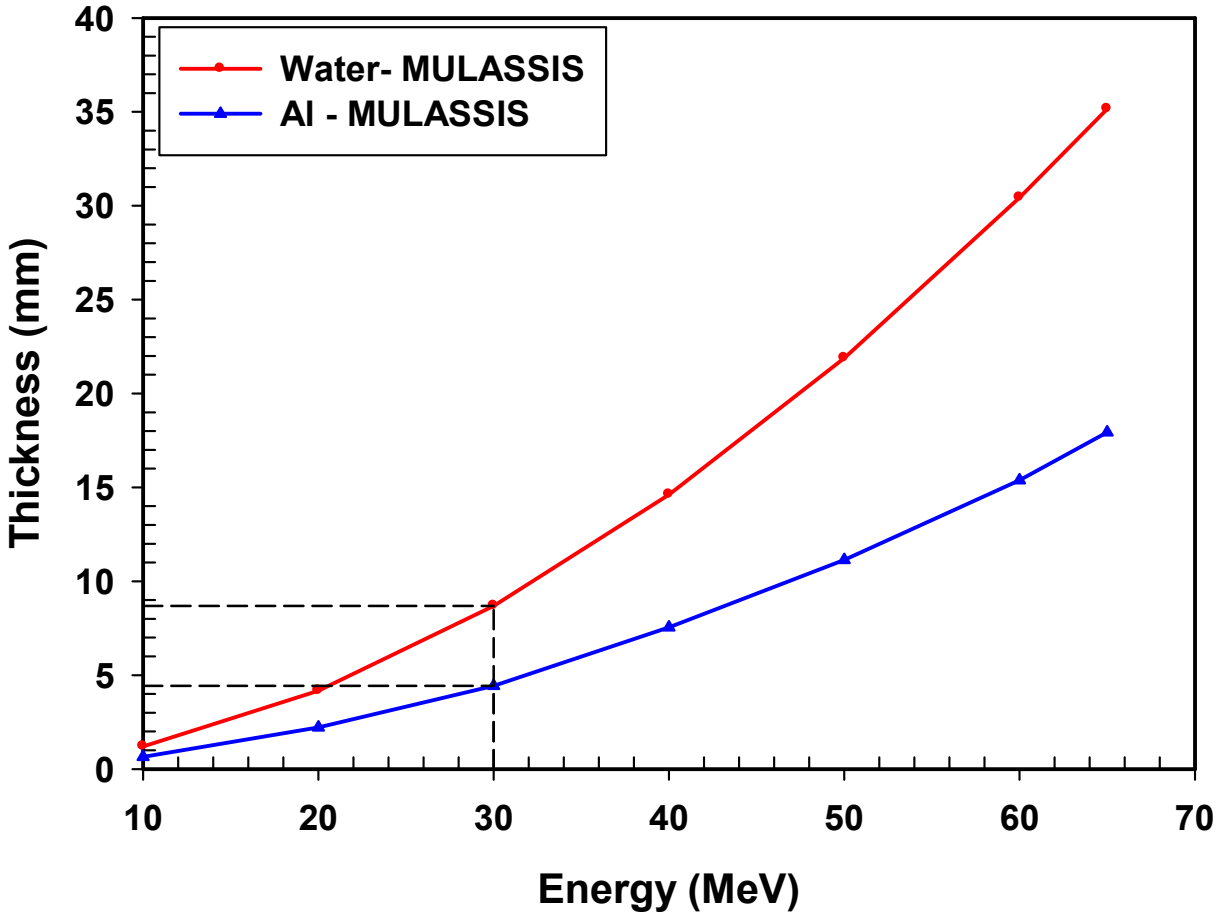

Figure 5.3: Stopping range (thickness) in Water and Aluminum for proton beam with various energies

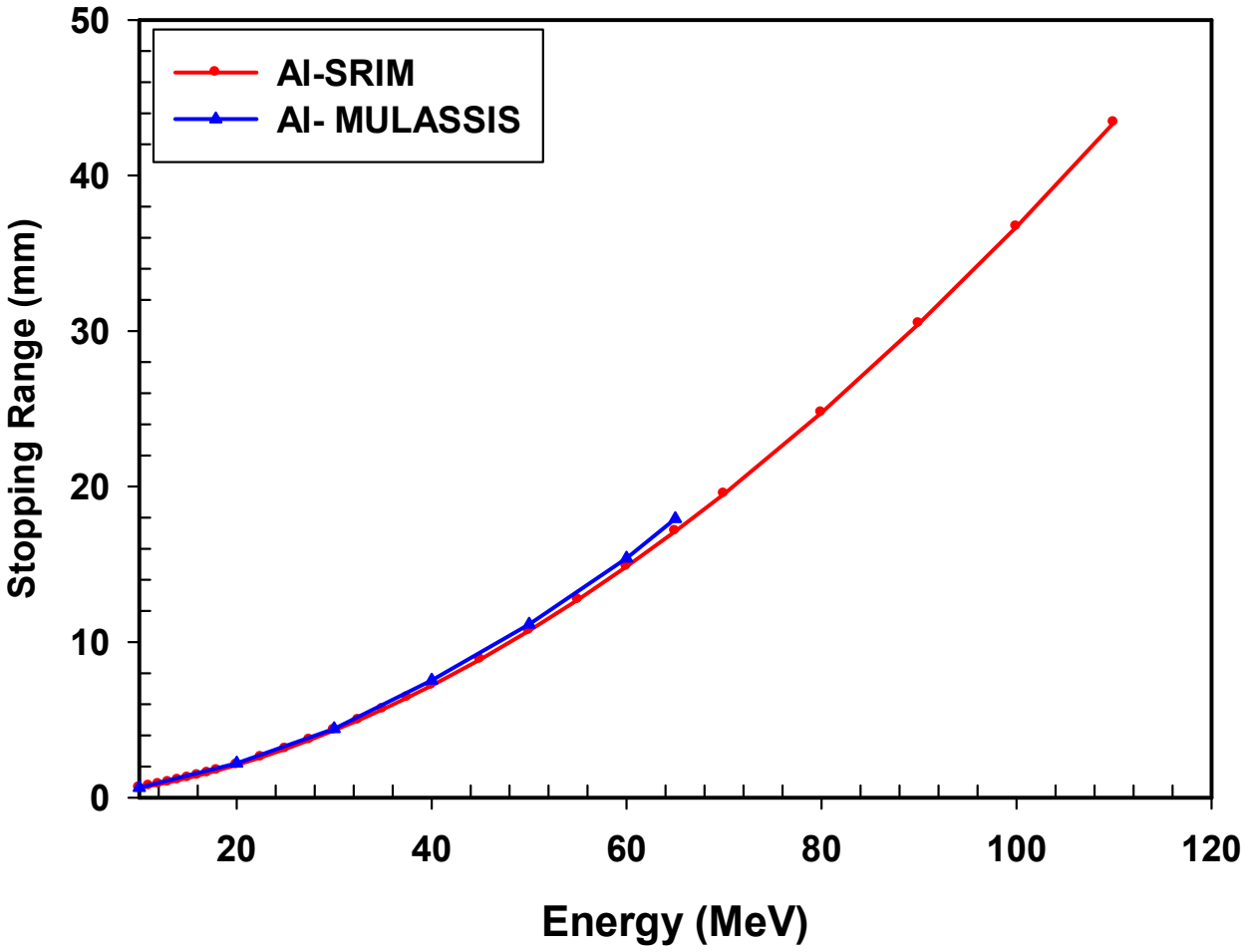

Figure 5.4: Simulated stopping range as a function of proton beam energy for Al using MULASSIS and SRIM

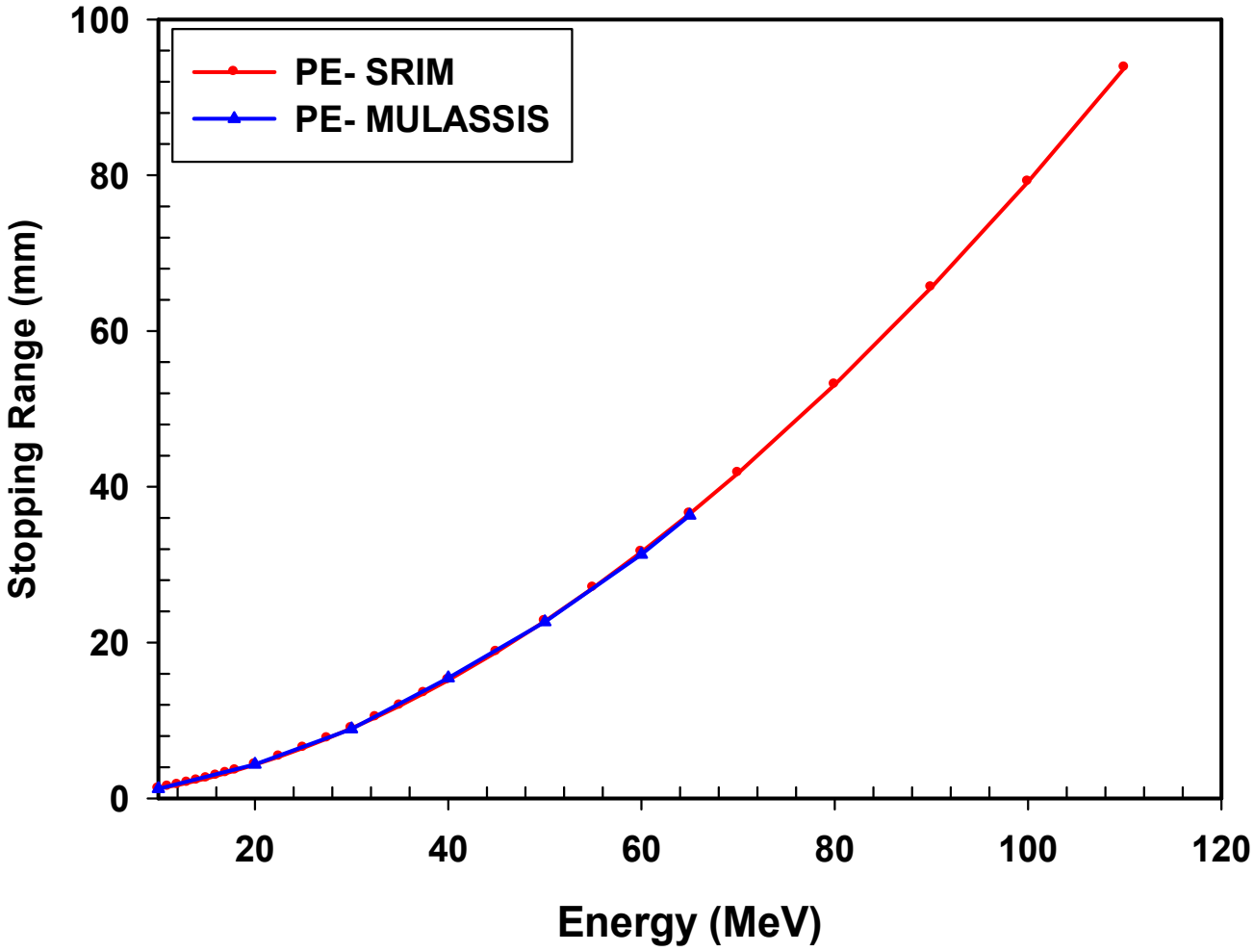

Figure 5.5: Simulated Stopping range as a function of proton beam energy for PE using MULASSIS and SRIM

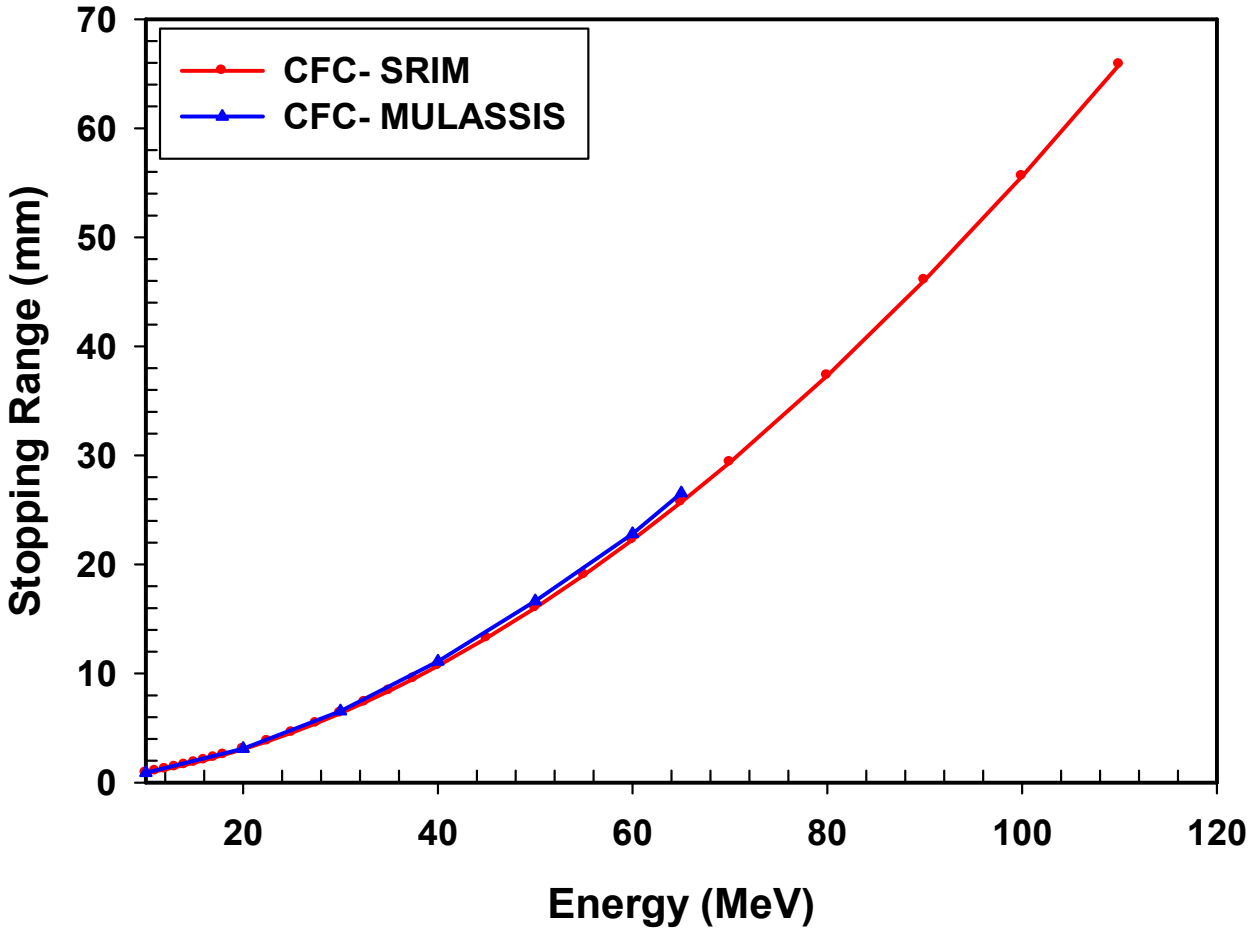

Figure 5.6: Simulated stopping range as a function of proton beam energy for CFC using MULASSIS and SRIM

5.1.1.2 Proton Test Results for Hybrid Composite Face Sheets (DFC) and Sandwich Panels (DSP)

Experimental values of t_{WET} for the hybrid composite face sheet are compared with the predicted results (using MULASSIS) for the various constituents of the hybrid face sheet, namely aluminium (2.71 g/cm^2), PFC (0.95 g/cm^2) and the CFC (1.552 g/cm^2). It should be noted that the t_{WET} for DFC was not simulated since it is not easy using MULSSIS. As shown in Figure 5.7, the experimental values lie between the predicted curves of PFC and aluminium. The t_{WET} and areal density values for the DFC and Al are compared in Table 5.1.

The experimental t_{WET} values for the DFC panels with areal densities of 0.39 g/cm^2 and 1.59 g/cm^2 were 3.54 mm and 15.03 mm respectively. The areal densities of aluminium corresponding to these t_{WET} values, obtained from SRIM are 0.464 g/cm^2 and 1.972 g/cm^{2}respectively. Comparing these areal densities, the weight savings achievable using hybrid composite panel (DFC) over the aluminium in stopping protons with energies corresponding to the two experimental t_{WET} values are calculated to be 18.1% and 19.35% respectively. Similarly, the weight saving of hybrid composite panel over CFC in Figure 5.7 are 2.32% and 3.74%. Thus, the hybrid composite face sheet has higher radiation shielding effectiveness than either the Al or CFC panels with same weight, against protons.

Table 5.1: Comparison of t_{WET} and areal density of DFC with Al

t_{WET}	Areal Density (g/cm^2) Al	Areal Density (g/cm^2) DFC	Weight Savings over Al (%)
3.54	0.464	0.38	18.1
15.03	1.972	1.59	19.4

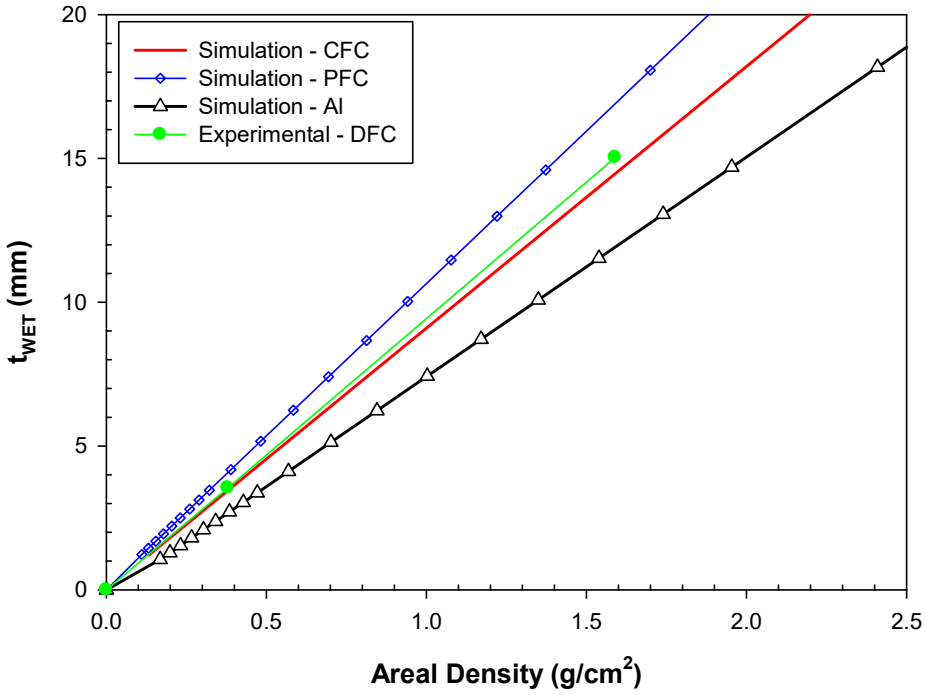

Figure 5.7: Comparison of experimental measured t_{WET} of DFC and SRIM predicted t_{WET} for DFC and its individual constituents

The experimental t_{WET} values for the hybrid composite sandwich panel (DSP) are compared with the experimental t_{WET} values for the aluminium sandwich panel (ASP) in Figure 5.8. The areal density of the Al face sheet in the ASP is same as the areal density of the hybrid face sheet in the DSP. Higher t_{WET} values for the DSP, for a given areal density of the sandwich panel, confirm that the DSP panels have a better radiation shielding efficiency against protons than ASP. The t_{WET} and areal density values for the DSP and ASP are compared in Table 5.2.

5.1.1.3 Effect of Angle of Incidence Beam on Radiation Shielding

The values of t_{WET} for DSP (30°) and ASP (30°) corresponds to the DSP and the ASP panels tested at 30° to the proton beam as shown in Figure 5.9. This was done to evaluate the effect of orientation of the sandwich panel on the t_{WET} since the density of aluminum honeycomb and hence, the amount of aluminum in the path of the beam depends on the orientation of the honeycomb. Also, the path length of the proton beam increases with increase in amount of material (thickness of the face sheet material) as the orientation of the panel changes. As expected, the change in orientation of the plane of the panel from 90° to 30° with respect the beam direction, changes the t_{WET} as observed in Figure 5.8

Table 5.2: Comparison of t_{WET} and areal density of DSP with ASP

t_{WET}	Areal Density (g/cm^2) Al	Areal Density (g/cm^2) DFC	Weight Savings over Al (%)
7.74	1.354	1.17	13.6
15.03	2.301	1.94	15.7

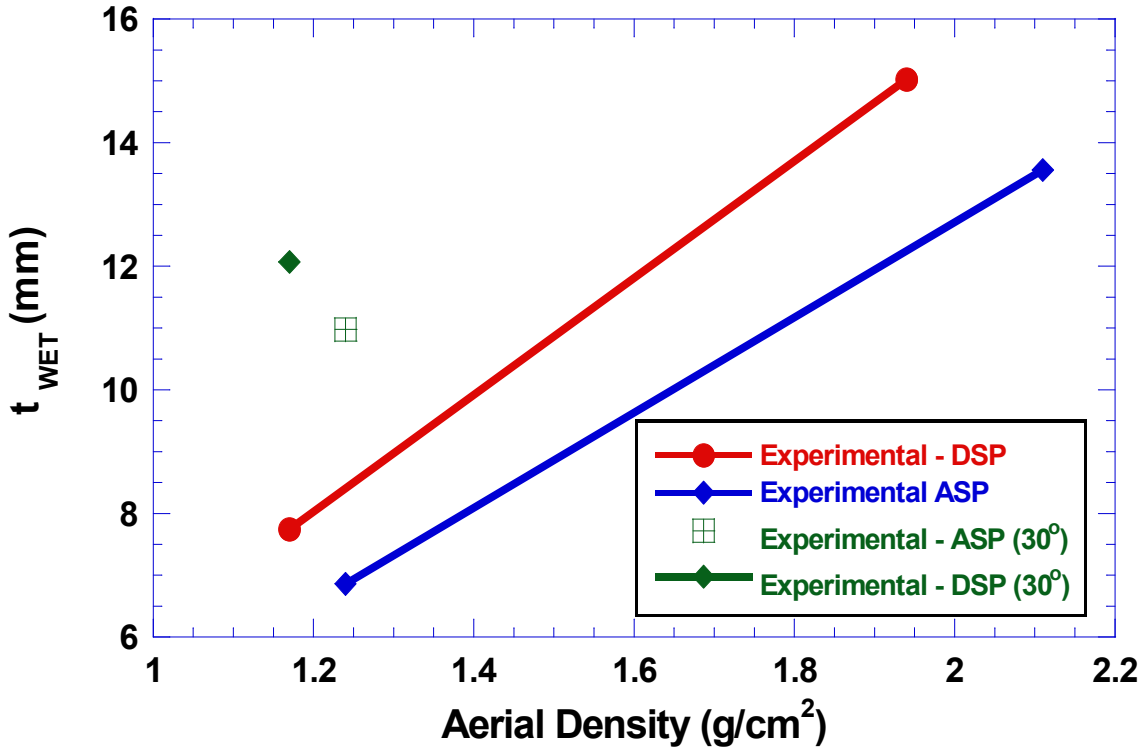

Figure 5.8: Comparison of experimental measured t_{WET} of DSP, ASP, DSP (30°) and ASP (30°)

Figure 5.9: Set-up of DSP panel at 30° angle to the beam direction

In order to confirm the above explanation quantitatively, the experimental t_{WET} values in for ASP are plotted in Figure 5.10 along with the simulated values for Al. While the face sheets were made of Al 1100 (2.71 g/cm^2), the honeycomb core is made of aerospace grade Al alloy (2.64 g/cm^2). Using the volume fraction of Al honeycomb (4.11%) and that of Al 1100 (95.8%) in the ASP, the average density of the Al in the sandwich panel is calculated to be 2.707 g/cm^2. Hence, the SRIM result for 1110 is used in Figure 5.10. The results for ASP are below that of the predicted curve for aluminium as against what is expected. That is, it is expected what the results for both Al and ASP should superpose. This is explained below:

The two Al face sheets in the ASP weigh 209.6 g and hence, the honeycomb 87.14 g. The areal density of ASP used to calculate the t_{WET} for ASP in Figure 5.10 is determined as

$$Areal\ Density\ of\ ASP = \frac{209.6\ g}{15.4 \times 15.6\ cm^2} + \frac{87.14\ g}{15.4 \times 15.6\ cm^2} = 1.24\ g/cm^2$$

While determining the areal density of honeycomb using the above equation, it is assumed that 100% of the 1cm^2 area is covered by the Al material making up the honeycomb. However, the cross section of the Al honeycomb covers only 3.55% of the Al face sheet as shown in Figure 5.11. Hence, the actual aerial densities of honeycomb and ASP are obtained as

$$Actual\ Areal\ Density\ of\ honeycomb = \frac{0.0355\ \times 87.14\ g}{15.4 \times 15.6\ cm^2} = 0.01289\ g/cm^2$$

and

$$Actual\ Areal\ Density\ of\ ASP - T1 = \frac{209.6\ g}{15.4 \times 15.6\ cm^2} + 0.01289 = 0.88534\ g/cm^2$$

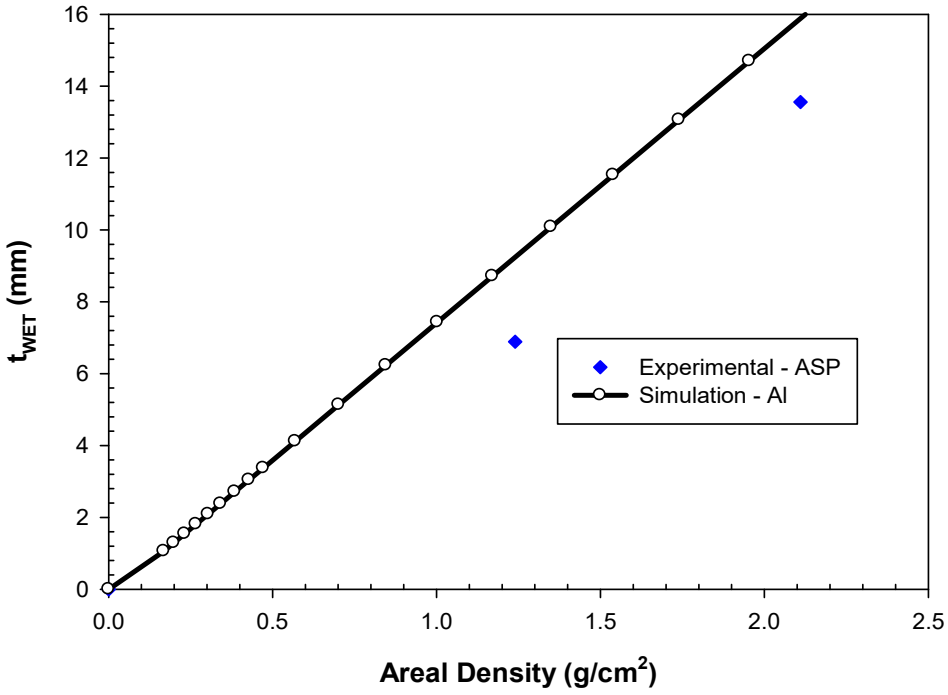

Figure 5.10: Comparison of experimental measured t_{WET} of ASP compared with simulated result of Al using apparent areal density

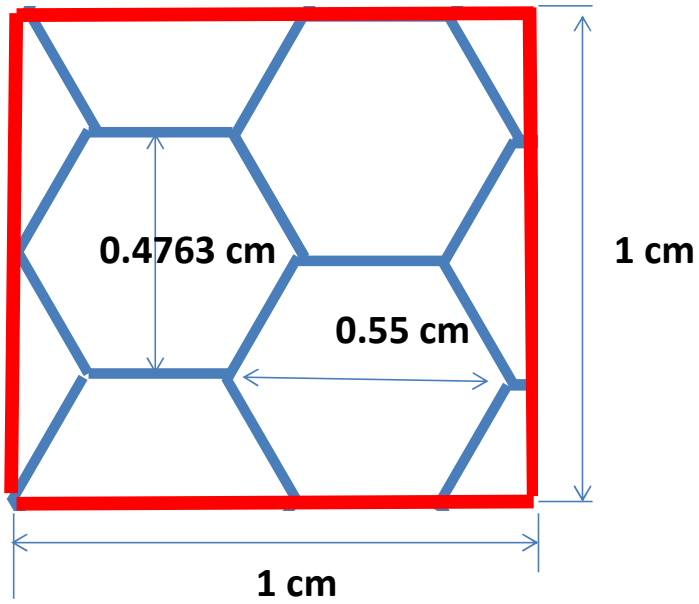

Figure 5.11: Cross section of the Aerospace Al grade honeycomb

Similarly, the actual aerial density for ASP-T2 is 1.7578 g/cm^2. When these two new values were used to plot the experimental t_{WET}, the latter superposes excellently with simulated results for Al (with an error of 1.6%) as shown in Figure 5.12.

Similar reasoning can be extended to explain the lack of superposition between data for DSP and DSP (30^o).

5.1.2 Electron Test Results

5.1.2.1 Electron Validation of MULASSIS

The experimental dose recorded by the dosimeters was converted into dose in Si using Eq. 4.3 and plotted in Figure 5.13 as a function of Al thickness. The value at zero thickness corresponds to the dose incident on the Al panel. The data points are connected by a line to highlight the trend and the line cannot be used to interpolate the values for intermediate thicknesses. The dose increases with thickness initially due to production of secondary particles during interaction of the electron beam with the material. Due to the use of panels with discrete thicknesses in testing, the Bragg peak could not be identified. The dose simulated using MULASSIS is also plotted as a function of thickness in Figure 5.13. The experimental and simulated values are within 2% (referenced to experimental dose) for thicknesses less than 6.4 mm. At higher thicknesses, this difference increases to 74%.

The experimental dose values for PE are compared with simulated dose in Figure 5.14. The difference between the simulated and experimental values varies in the range of 2.7% - 53.6%.

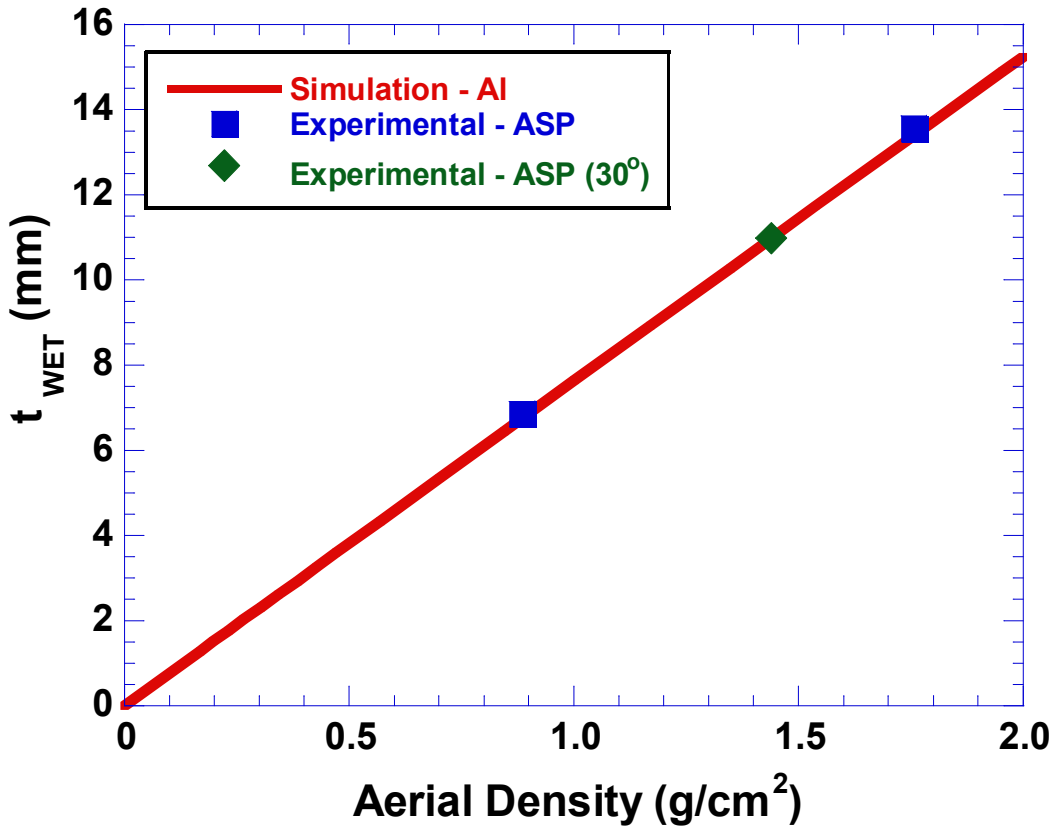

Figure 5.12: Comparison of experimental measured t_{WET} of ASP compared with simulated result of Al using apparent actual density

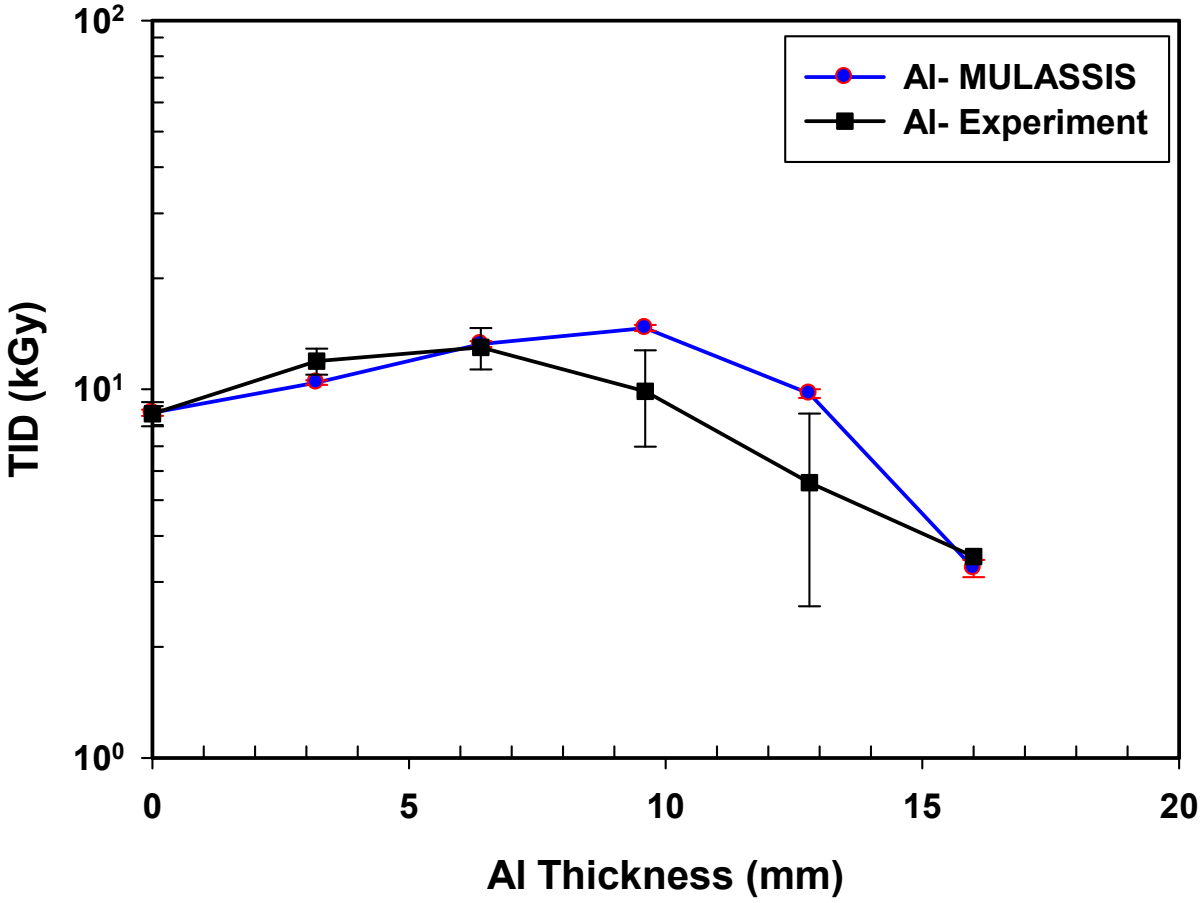

Figure 5.13: Comparison of experimental and simulated dose profile for Al for electron exposure

The experimental dose values for CFC are compared with simulated dose in Figure 5.15. The difference between the simulated and experimental values varies in the range of 2.8% - 33.8 %. The maximum observed difference was least for CFC (33.8%).

For electron exposure, the dose deposited on the Si detector by the electrons transmitted through the panel was simulated and compared with the experimental results. While the simulated dose was the dose deposited on a detector of size equal to the size of the panel, the experimental dose corresponded to the dose deposited on a small 1.5 cm x 1.5 cm area of the dosimeter at the center of the panel. This difference would have resulted in the MULASSIS capturing the effect of particles exiting the panel and scattered over a larger angle than the dosimeter. The higher values for the simulated dose when compared to the experimental dose appear to corroborate this. Since MULASSIS does not allow the size of the detector to be changed, future experiments should consider measuring the dose by using more dosimeters spread across the panel area.

Nevertheless, the correlations between the experimental and simulated values at lower shield thicknesses (< 10 mm) are good, confirming the ability of MULASSIS in predicting the shielding effectiveness of materials against electrons. The experimental dose values are compared in Figure 5.16 for all three materials. It shows that Al is less effective at lower areal densities than PE and CFC but more effective at higher areal densities, under electron exposure. Al generates more secondary particles than PE and CFC due its interaction with the electrons. At lower areal densities, Al is not as effective in absorbing the secondary particles as it is at higher aerial densities, resulting in the observed trend.

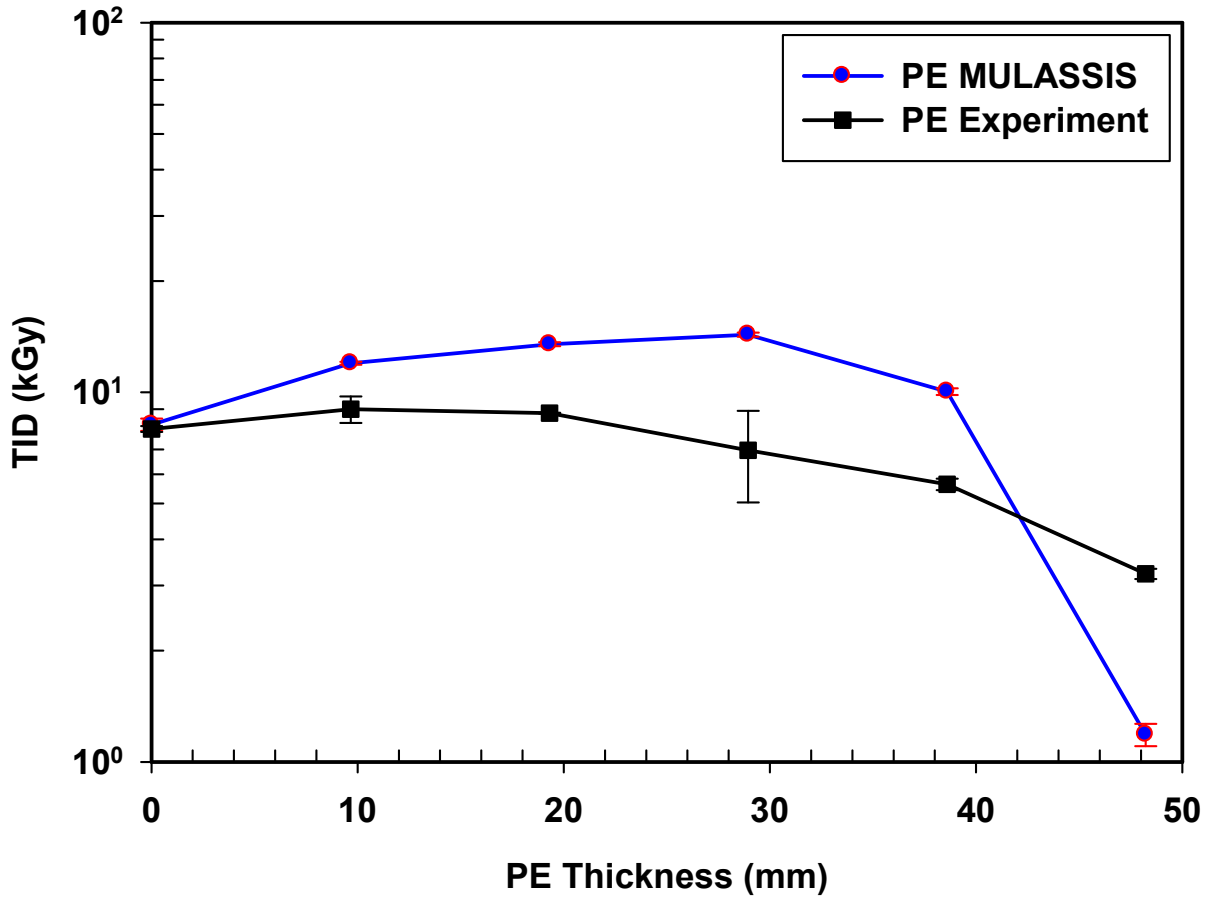

Figure 5.14: Comparison of experimental and simulated dose profile for PE for electron exposure

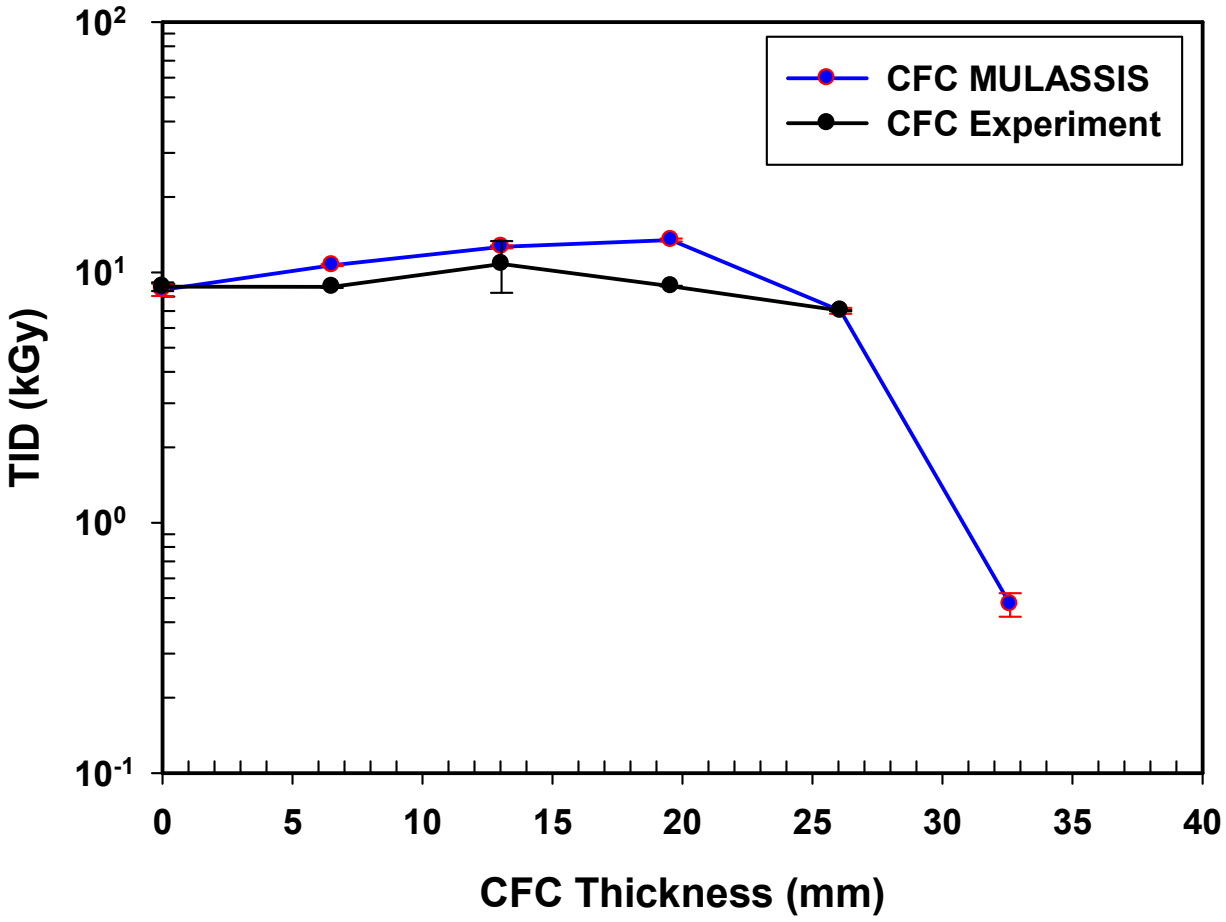

Figure 5.15: Comparison of experimental and simulated dose profile for CFC for electron exposure

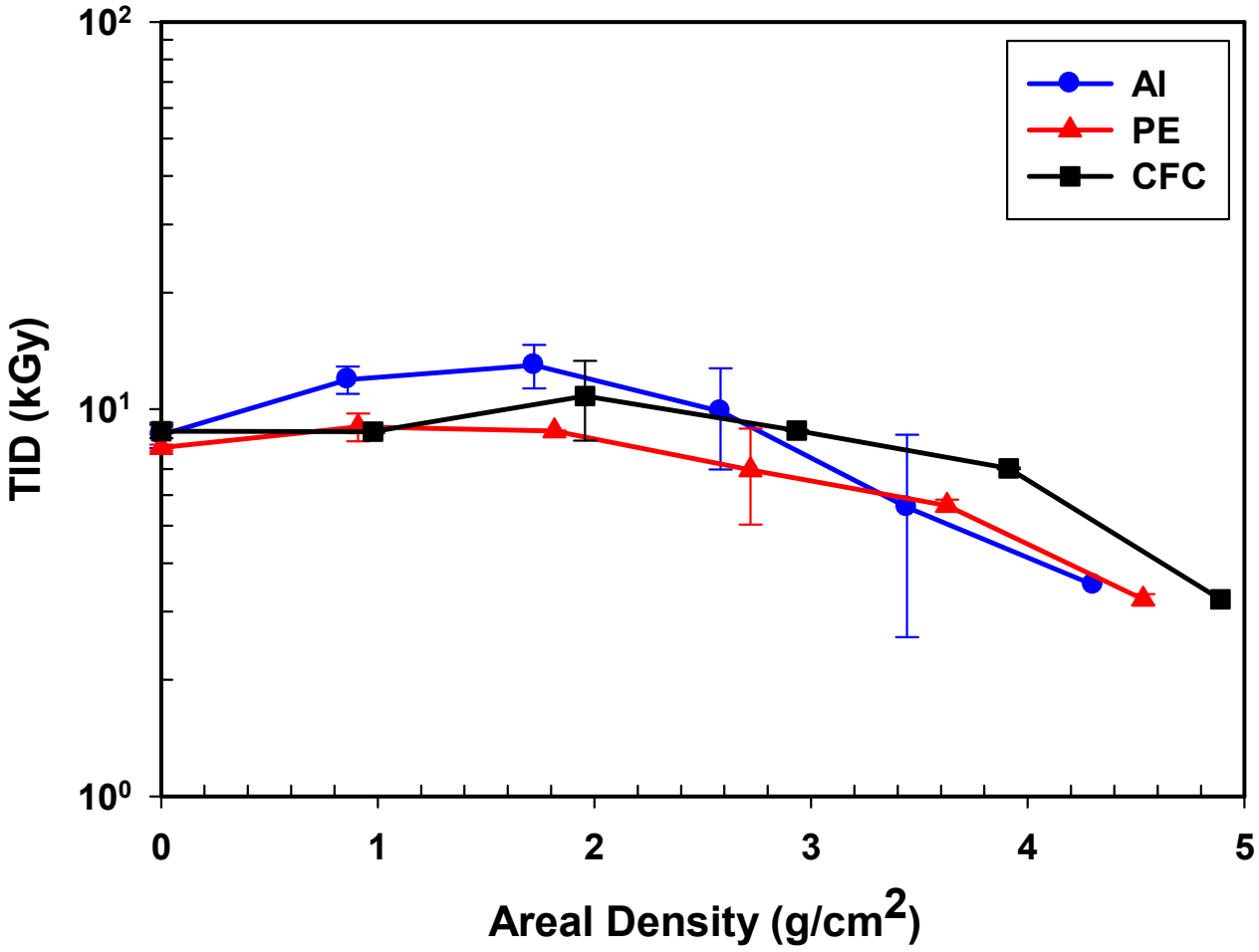

Figure 5.16: Comparison of experimental transmitted dose for three tested materials for electron exposure.

5.1.2.2 Electron Test Results for Hybrid Composite Face Sheet (DFC) and Sandwich Panel (DSP)

Exposure experimental values for the TID transmitted through the DFC panel is plotted as a function of areal density in Figure 5.17. While the trend in experimental values is similar to that in simulated values, the latter values are higher than the former values, which are believed to be due to the difference in size of the detector as discussed in the previous section. The maximum difference between the experimental and predicted values is 48.6%. Thus, these results also validate the MULASSIS.

The normalized dose (TID_{Out} /TID_{In}) for the DFC is compared with that for Al in Figure 5.18. Since TID_{In}, the dose incident on the top surface of the panel, varied slightly from panel to panel, the transmitted TID is normalized with that of the incident value. It can be observed as the increase in dose due to the production of secondary particles is maximum for Al and minimum for PE; CFC and DFC were in between these two extremes. In the areal density range of interest (0-1 g/cm^2) to this project, the normalized dose hardly changes for the DFC, which suggests that electron beams simply pass through the DFC panel, without any interaction.

This is to be expected since the electron beam's energy is very high (10 MeV), which corresponds to the upper limit of the energy of electrons encountered in Molniya orbit. Hence, any weight savings for DFC panel over Al panels, in an electron environment, could not be ascertained from this data. This would require future tests at much lower electron energy levels. Nevertheless, the lower normalized dose values for the DFC panels, in the aerial density range of (1-3 g/cm^2) when compared to Al highlight qualitatively the better radiation shielding effectiveness of the DFC panels over Al in electron environment.

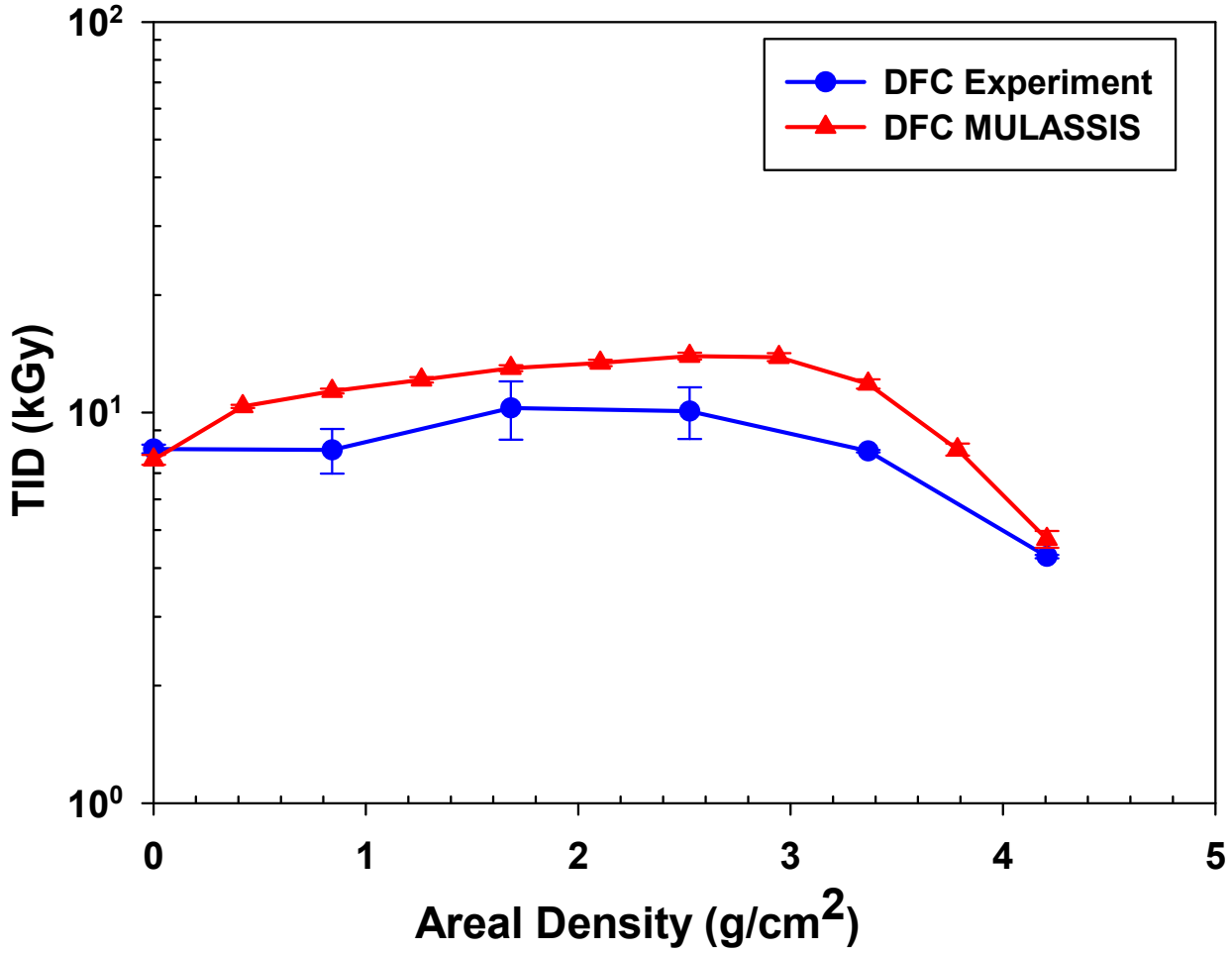

Figure 5.17: Comparison of experimental and simulation results of hybrid composite face sheet (DFC) under electron exposure

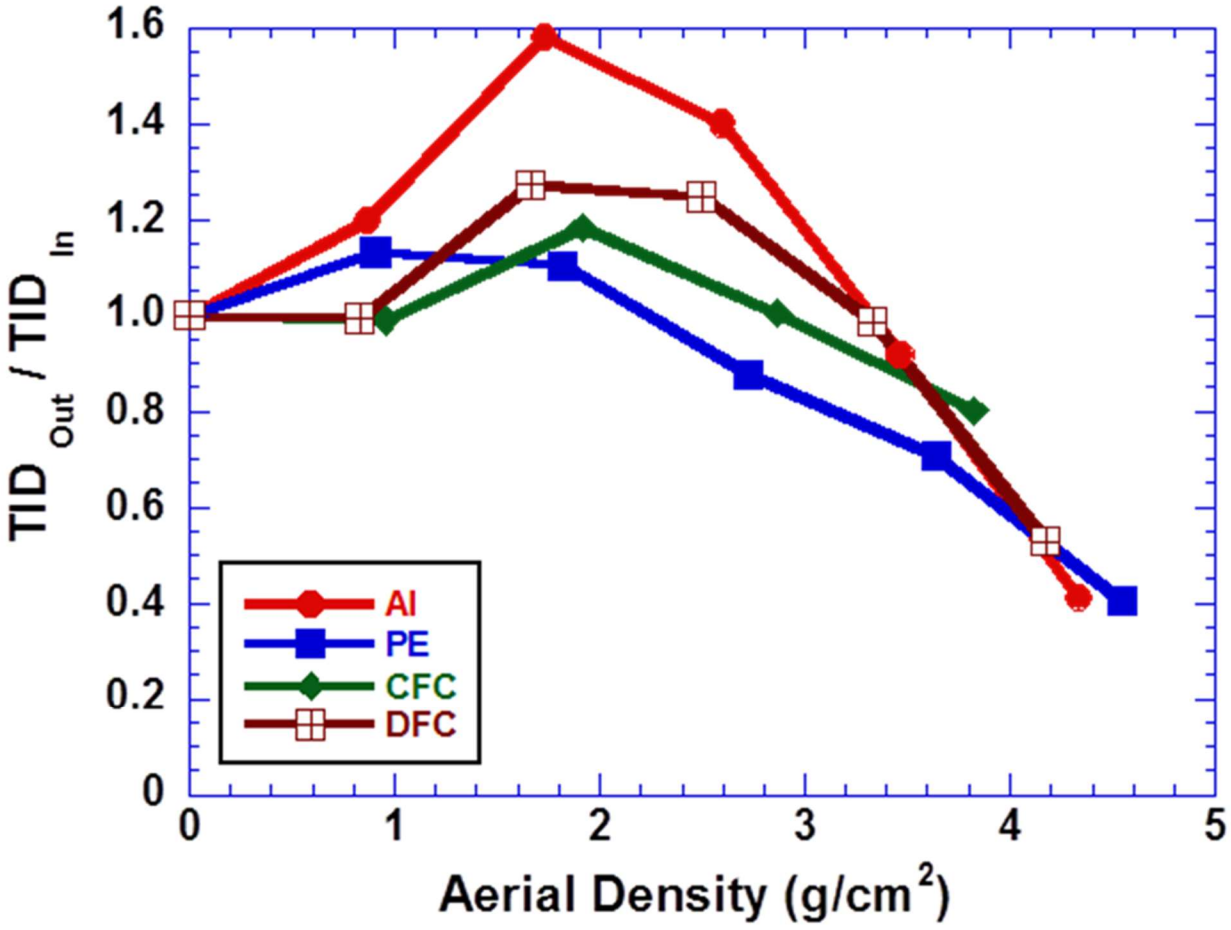

Figure 5.18: Comparison of experimental normalized dose of PE, CFC and DFC with Al under electron exposure

The DSP and ASP panels recorded normalized doses of 1.13 and 1.07 respectively as shown in Table 5.3, which are within the error range of the dosimeter. This suggests that the beam is passing through the panels without much absorption / interaction, due to its high energy.

Hence, 5 DFC panels were introduced before each of the DSP and ASP panels to reduce the energy of the beam entering the sandwich panels as shown in Figure 5.19. Since DFC panels of similar areal density were used, it is assumed that the energy entering the ASP and DSP panels was the same, allowing a meaningful comparison of the dose absorbed by the panels. The dose absorbed by the DSP and ASP panels, in this experiment, were 6.28 kGy and 6.18 kGy respectively. The aerial density of the DSP and ASP panels were 1.17 g/cm^2 and 1.24 g/cm^2, which translates into a weight savings of about 5.6% for the DSP over ASP. This weight savings is expected to be higher for electrons with lower energy levels.

Finally, the effect of lay-up sequence was studied using three lay-up sequences, [Al_4 / CFC $_2$ / PE $_2$], [PE_2 / CFC $_2$ / Al $_4$], and [CFC_2 / Al4 / PE $_2$]. The normalized dose is plotted as a function of thickness and areal density in Figures 20 (a) and (b), respectively.

The differences in normalized dose in these figures clearly establish the effect of lay-up sequence. Al on the surface is better than Al at the bottom in reducing the dose, which validates the design. For a normalized dose, [Al_4 / CFC_2 / PE_2] result in the lowest areal density compared to the other two lay-ups, which is the lay-up sequence used in the design.

Table 5.3: Experimental measured doses for DSP and ASP

Panel	$Dose_{IN}$ (kGy)	$Dose_{OUT}$ (kGy)	$Dose_{IN}$ / $Dose_{OUT}$
DSP	1.354	1.17	1.03
ASP	9.34	10.01	1.07

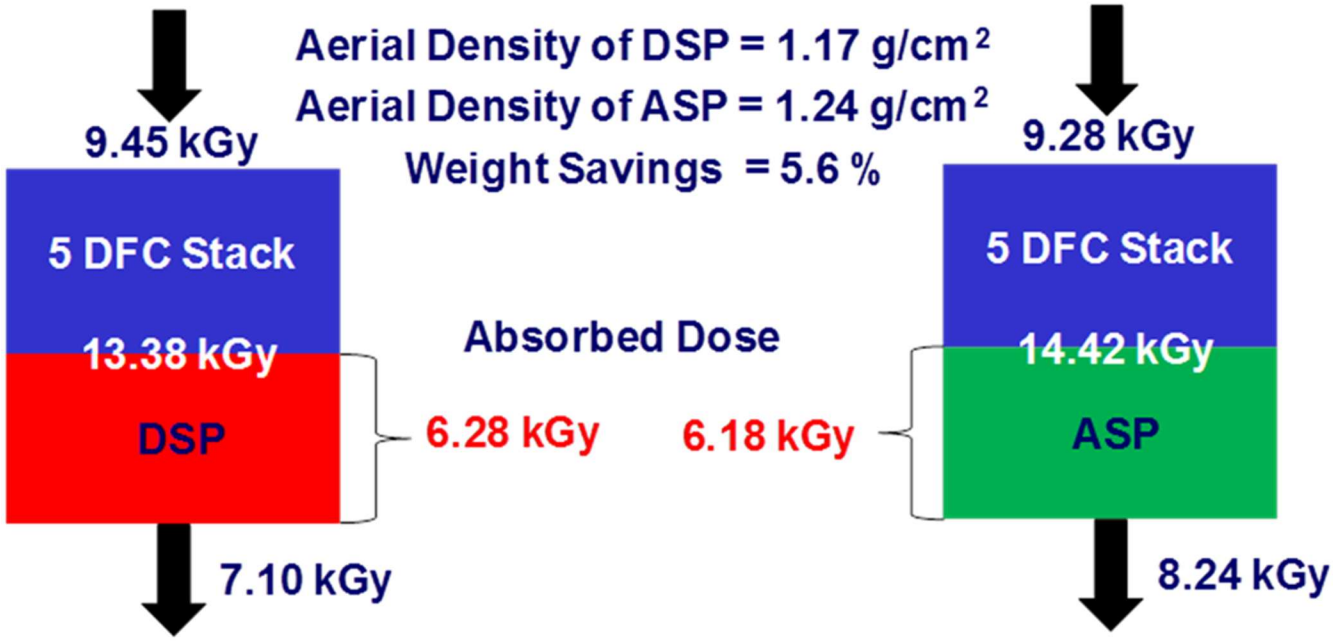

Figure 5.19: Schematic of experimental setup to measure dose absorbed through DSP and ASP

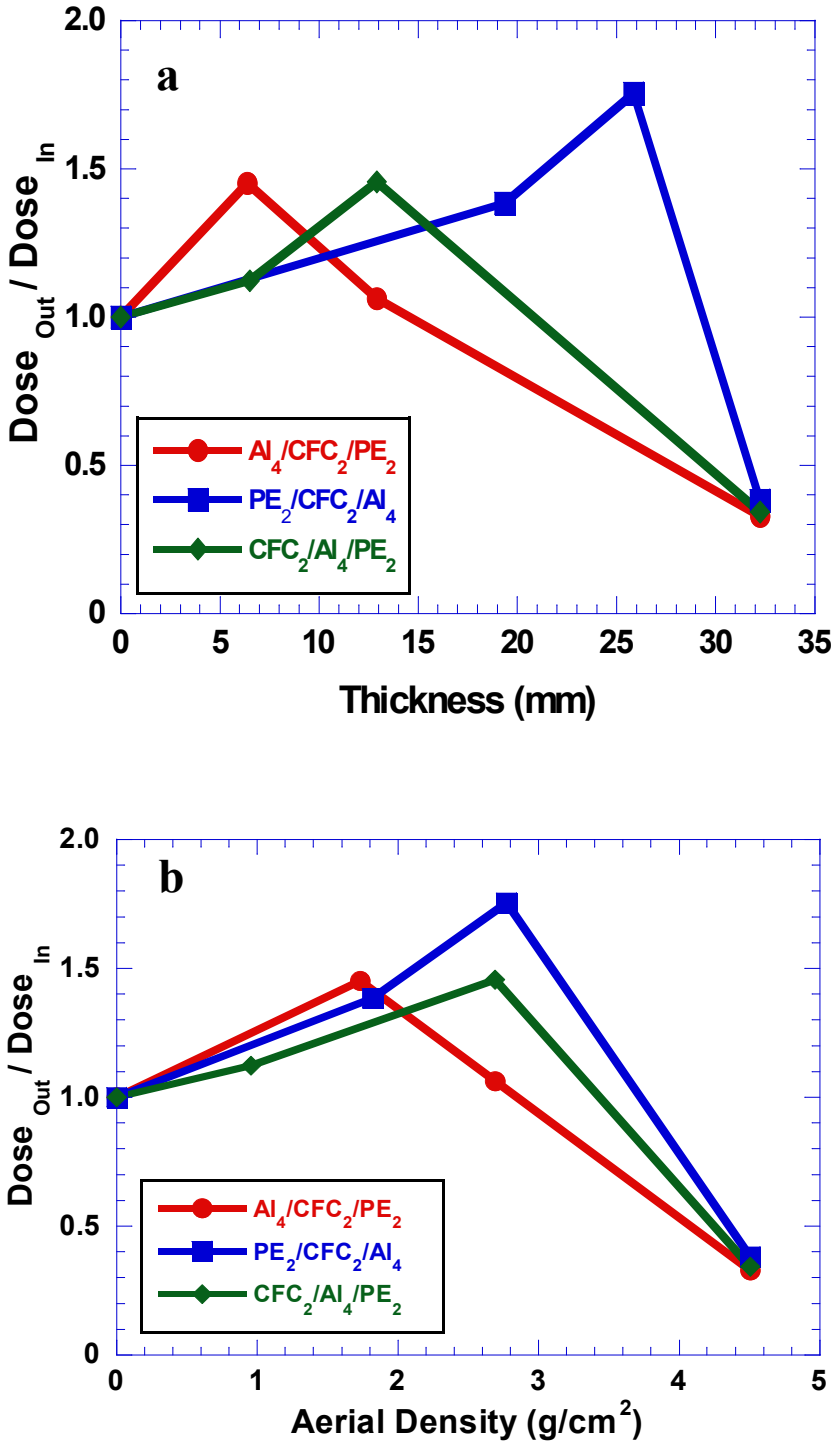

Figure 5.20: Normalized dose as a function (a) thickness and (b) areal density showing the effect of lay up on three lay-up sequence

5.1.3 Summary of Radiation Test Results

The results presented in the previous sections validate the ability of MULASSIS to simulate the TID transmitted through a homogenous and hybrid composite material shielding panels with accuracies in the range of 1.7 – 5.4% for proton exposure and in the range of 6.2 – 48.6% for electron exposure.

The above results also clearly demonstrate that the designed hybrid composite face sheet and sandwich panel have a better radiation shielding efficiency than currently used Al face sheet and Al sandwich panels. The weight savings that can be achieved with hybrid composite over Al to absorb the same amount of energy, calculated in the previous section based on the experimental results, is summarized in Table 5.4.

Predicted weight savings for Molniya is also shown in this Table 5.4, which is different from the experimental values due to the difference between the Molniya's radiation environment and the mono-energetic proton and electron beams used in experimental testing. However, the validation of MULASSIS suggests that the predicted weight savings could be relatively accurate.

It can be inferred that for a mission duration, the transmitted TID for Al is more than that for DFC. Alternatively, to reach a certain limit for transmitted TID (for example, 50 krad shown in the Figure 5.21), the hybrid composite would take ~ 15.9 years while equivalent Al weight would take ~ 19.1 years. Thus, the mission duration of a satellite manufactured with hybrid composite may be extended beyond that for a satellite manufactured with Al panel by additional 3.2 years.

Table 5.4: Weight savings of hybrid face sheet and hybrid sandwich panel over Al in experimental proton and electron, and in simulated Molniya orbit

Material	Weight Savings over Al		
	Proton (Experiment)	Electron (Experiment)	Molniya (Simulation)
Hybrid Face sheet	18.1 to 19.35%	Could not obtain due to high energy of the beam	13% minimum 1 g/cm^2 – Al resulted in a TID of 50 krad and 0.87 g/cc of hybrid composite face sheet resulted in a TID of 46 krad. The weight savings for same TID was not simulated. In this case, the weight savings will be more than 13%
Hybrid Sandwich Panel	13.5 to 15.5%	5.6%	Same as Face Sheet

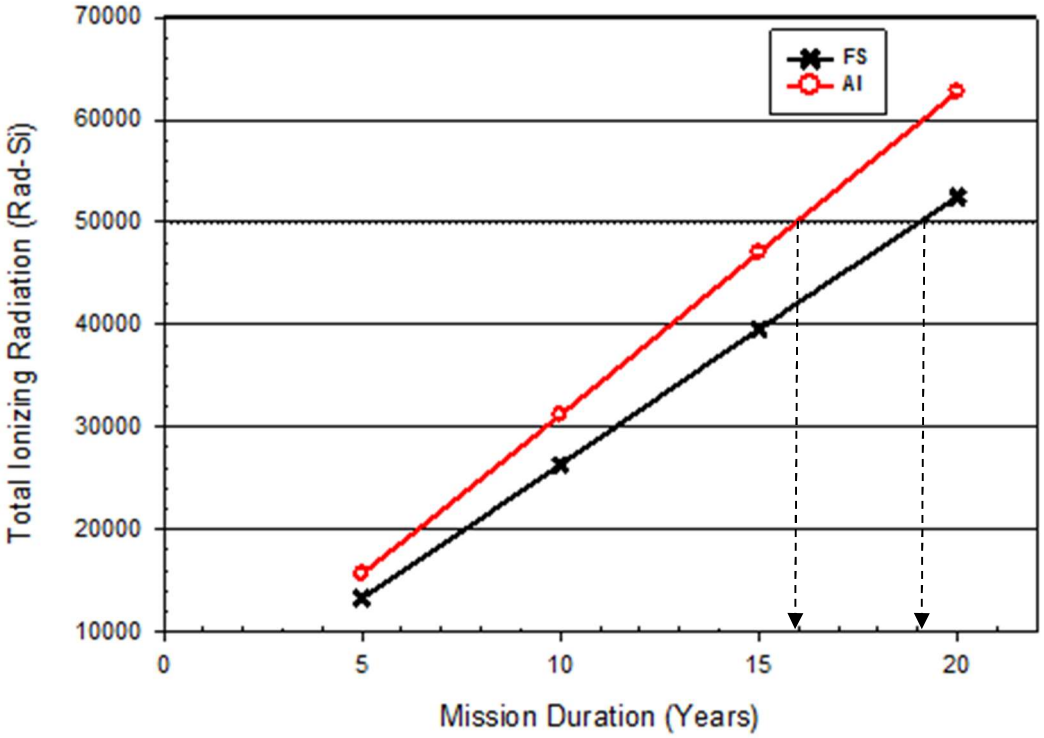

Figure 5.21: Comparison of the TID of hybrid face sheet with Al over mission duration period

5.2 Mechanical Test Results

5.2.1 Tensile Test Results for Hybrid Composite and its Constituents

Using the thicknesses of PFC, CFC, and hybrid composite, the volume fractions of various components of the hybrid composite are estimated and tabulated in Table 5.5. These volume fractions are comparable to volume fractions proposed in Chapter 3 based on design for radiation shielding and structural requirements.

Representative tensile stress-strain curves for PFC, CFC and DFC are plotted in Figure 5.22. It should be noted that PFC and CFC had $0^o/90^o$ fiber orientations. Hence, the properties along the longitudinal and transverse directions were the same. All curves are non-linear and the initial linear portion was used to determine the tensile modulus of each specimen. The average values of the tensile properties determined from these curves are tabulated in Table 5.6. Properties of the third constituent, Al 1100 taken from the literature are included along with the properties of Al 6061 that the DFC is designed to replace.

PFC modulus predicted using the modulus of the UHMWPE fibers and the matrix is 32.7 GPa. This is believed to due to less than perfect impregnation of the PE fiber fabric by the PE matrix. The voids between the yarns were big and were found to be completely filled, through non-destructive testing of the composite using X-ray Micro CT. However, the spaces between the fibers in a yarn were much smaller and are believed to have not been filled by the highly viscous PE matrix despite the application of very high lamination pressure (14.5 MPa). Suggestion to improve this are provided this are provided in section 6.3 of Chapter 6.

Table 5.5: Volume faction of the three constituents in manufactured hybrid composite (DFC)

Layer Material	Volume Faction (%)
Polyethylene fiber composite (PFC)	32.6
Carbon fiber composite (GFC)	62.4
Aluminum (Al)	5

Table 5.6: Average tensile properties of hybrid composite (DFC) and its constituents

Test Specimen	Tensile Modulus (GPa)	Tensile strength (MPa)
PFC	15.1±1.5	500±44
CFC	63.8±1.1	836±74
DFC	45.7±2.2	550±18
Al 1100	68.2 ±4.7	110±14
Al 2024	68.9 ±2.1	314±26

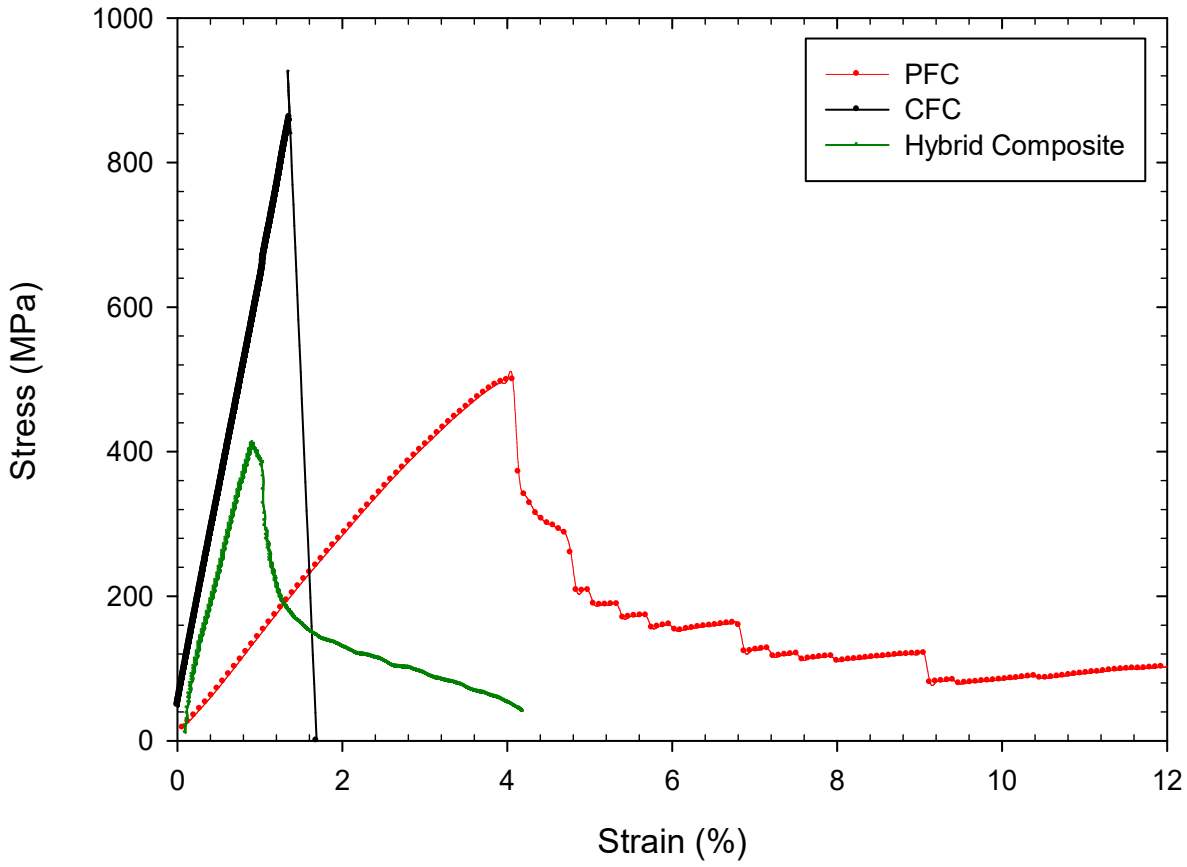

Figure 5.22: Typical tensile stress-strain curves for PFC, CFC and DFC

As expected carbon fiber composite exhibited the highest modulus and strength of 63.8 GPa and 836 MPa respectively. As observed in Figure 5.22, the CFC failed at a very low strain of ~1.6%.

The stress-strain curve for the hybrid composite, DFC, was between those for the CFC and PFC. The modulus of 45.7 GPa is between the modulus values for the CFC and the PFC. and is comparable to the modulus of 48.2 GPa estimated using rule of mixtures, volume fractions in Table 5.5 and moduli of the three constituents in Table 5.6.

The tensile modulus is less than that for the Al 6061. One reason for this is believed to be due to less than optimal impregnation of the UHMWPE fibers by high viscosity polyethylene matrix. A second reason is the use of high strength carbon fibers that have a lower modulus. Use of high modulus graphite fibers, with a modulus higher than the carbon fibers used in manufacturing the face sheet, is likely to increase the modulus to that of Al 6061.

The ductile behaviour of the hybrid composite beyond the peak stress is similar to that of the PFC. While higher than that for the Al 6061, the tensile strength is less than the value of 690 MPa estimated using rule of mixtures, volume fractions in Table 5.5 and strength values of the three constituents in Table 5.6. This suggests premature failure. The top and edge views of the fractured DFC shown Figure 5.23, exhibits failure of the outer Al layer as well as delamination between the DFC and the PFC. Lack of complete failure through the thickness of the test coupon is consistent with low tensile strength and this is due to pre-mature delamination between the CFC and the PFC layers.

Since Al 1100 has the lowest strength, the fracture is believed to have started by the failure of the Al 1100 sheet. The crack subsequently propagated through the thickness of the outer CFC layer. Subsequently, the PFC delaminated from the layers of CFC and Al (still bonded to one another) resulting in the final failure of the composite. This fracture mode confirms that very good bonding was achieved between the Al and CFC during manufacturing. Thus, improving the bonding between the CFC and the PFC layers is likely to increase the strength of the hybrid composite.

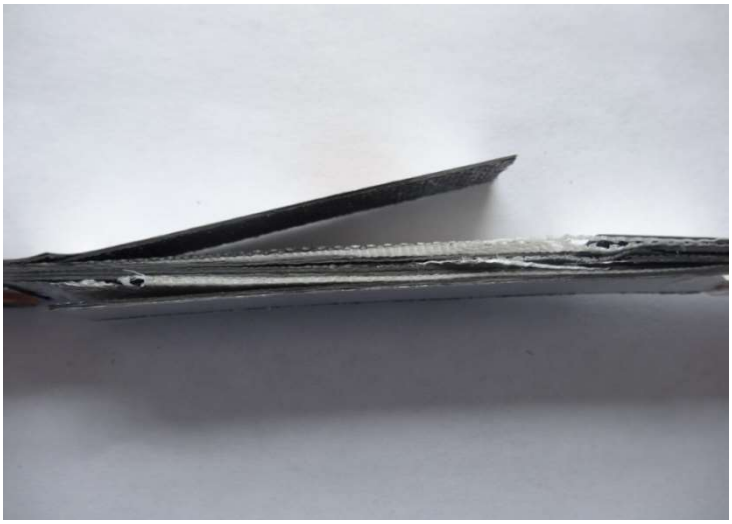

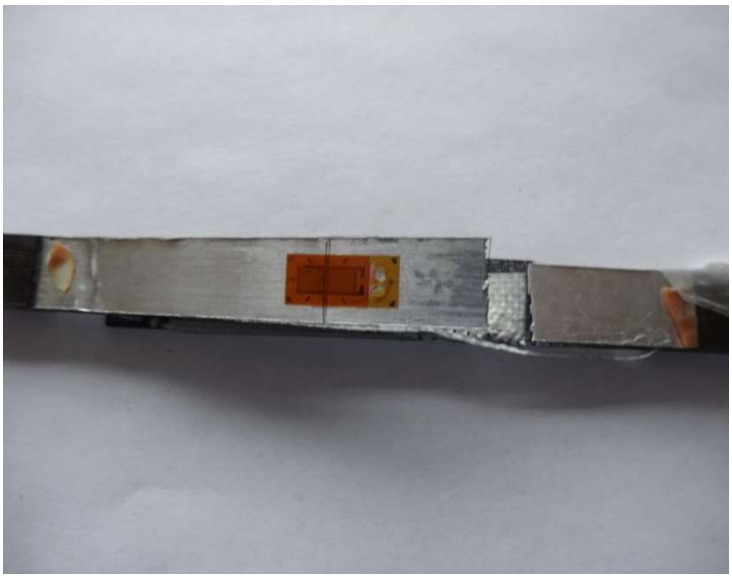

Figure 5.23: The edge and top view of the fractured DFC test coupon

5.2.2 Compression Test Results

A representative compressive test result is plotted in Figure 5.24. In all test specimens, no end crushing was observed and the failure occurred within the gage length. Six samples were tested and the averages of the compressive modulus and compressive strength are reported in Table 5.7. The properties for Al 6061 have been added for comparison and have been taken from literature[71]. The compressive chord modulus was calculated over a range of axial strain ε_x, of 1000 to 3000 micro strain using the Eq. (5.1)

$$E^C = \frac{P_2 - P_1}{(\varepsilon_{x2} - \varepsilon_{x2})wh} \tag{5.1}$$

Where E^c is the compressive modulus, (MPa),

P_1 = load at ε_{x1}, (N),

P_2 = load at ε_{x2}, (N),

ε_{x1} = actual strain nearest lower end of strain range used,

ε_{x2} = actual strain nearest upper end of strain range used,

w = specimen gage width, (mm) and

h = specimen gage thickness, (mm)

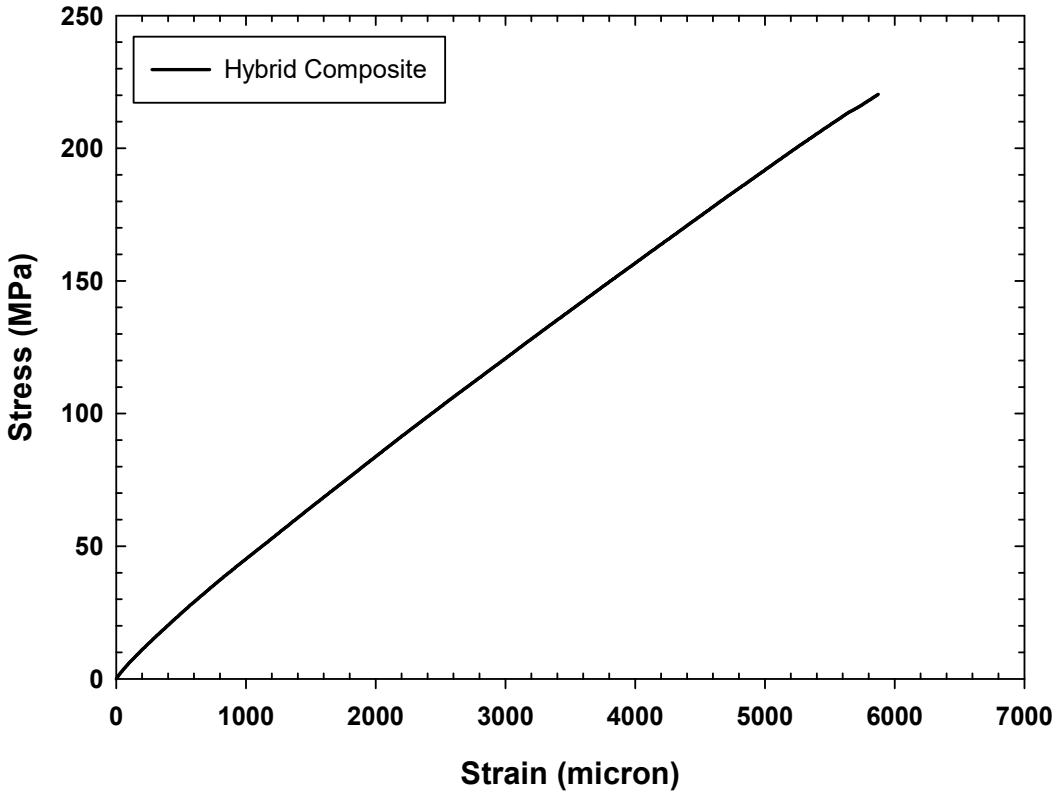

Figure 5.24: A representative compressive stress -strain curve for hybrid composite

Table 5.7: Average compressive modulus and compressive strength of hybrid composite

Test Specimen	Compressive Modulus (GPa)		Compressive strength (MPa)
	Slope Modulus (0-3000με)	Chord Modulus (1000- 3000 με)	
Hybrid composite	39.9±1.6	38.9±1.6	220±113
Al 6061	57.9±2.1	-	406±26

In addition, the modulus was also determined using the slope of the curve in the strain range of 0 - 3000 με. The average compressive modulus of 38.9 GPa, determined using the chord method suggested by ASTM D 6641 is slightly less than that (39.9 GPa) determined from the slope of the stress-strain curve due to increase in non-linearity with increase in strain.

The compressive modulus of 39.9 GPa is less than the modulus of 69.8 GPa for Al-6061. Possible reasons for this are the use of carbon fibers as well as the low compressive modulus of UHMWPE fibers. Use of high modulus graphite fibers, with a modulus higher than the carbon fibers used in manufacturing the face sheet, is likely to increase the modulus.

The reported compressive modulus (~ 39.9 GPa) and compressive strength (220 MPa) values of hybrid composite are almost half the values of Al- 2024. This is unexpectedly low and it is believed that the Combined Loading Compression (CLC) method does not give the true compressive properties of the hybrid composite due to delamination observed between PFC and CFC. This is later confirmed in Section 5.2.4 with flexural test result in which the main destructive force is compressive force.

The images of the fractured test coupon in Figure 5.25 confirm local buckling of layers that caused plastically yielding and lifting of the outer Al layers. Failure of Al layers was not observed suggesting that the load bearing capacity of Al layers was not completely utilized. Delamination between the CFC and the PFC layers, observed in Figure 5.23, is believed to have resulted in the local buckling. Although such delamination was also observed in tensile testing, it occurred at high stresses and over a larger area. However, smaller delamination area observed in compressive specimens suggests that local delamination and buckling resulted in the loss of load bearing capacity of the specimen at relatively low stresses.

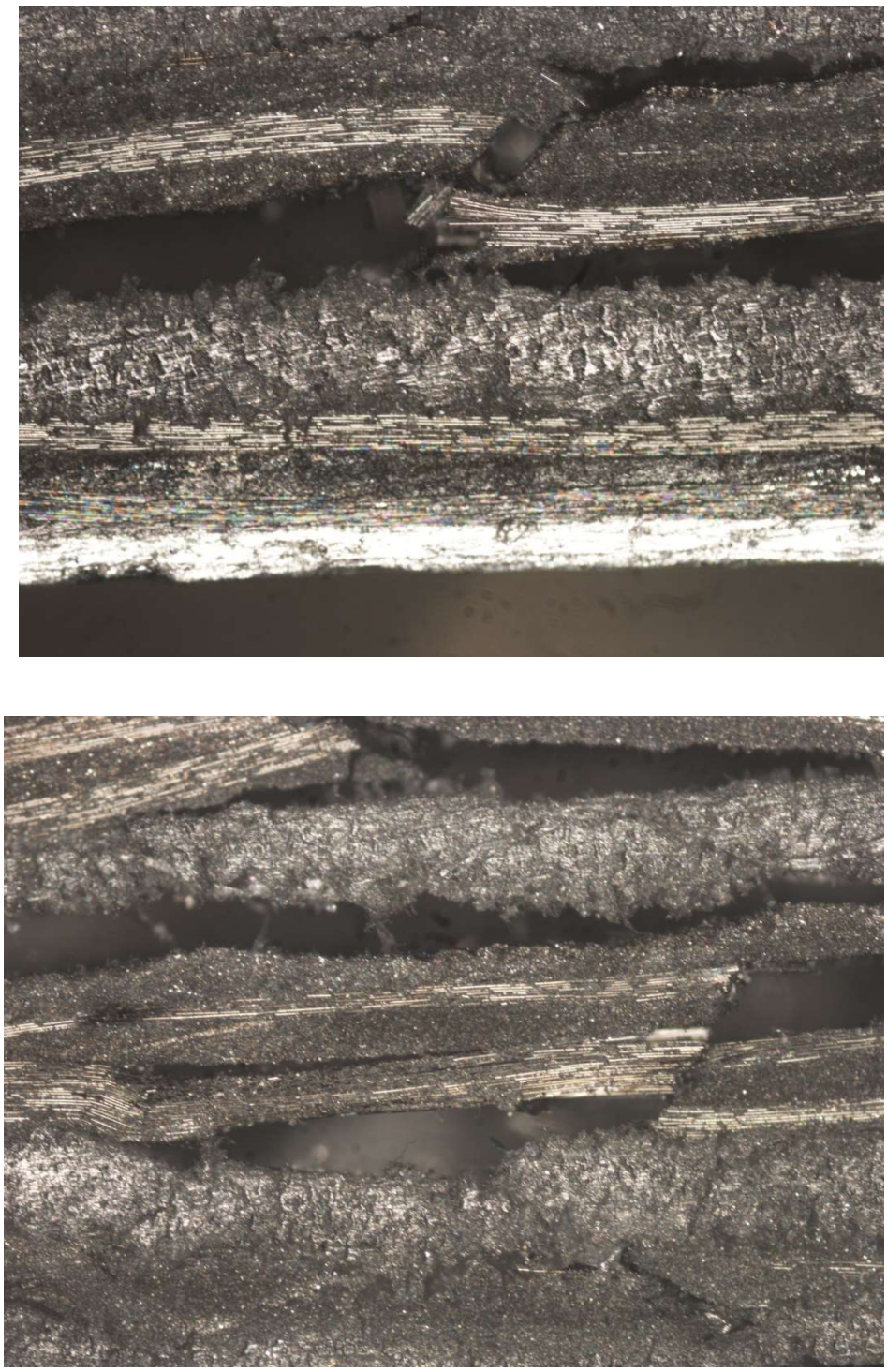

Figure 5.25: Fractured compressive coupon of hybrid composite

5.2.3 In-Plane Shear Test Results

This test was completed as per ASTM D7078. A shear stress versus time plot is shown in Figure 5.26 for one test coupon with fibers in 0/90 orientation. Due to rotation of the fibers and buckling, as shown in Figure 5.27 (see 0/90 specimen), determination of the shear strength is not straight forward. A drop in stress as shown by the arrow in Figure 5.26 is considered to be the shear strength. For specimens that do not show this, stress corresponding to 5% strain is recommended to be the shear strength by ASTM D7078 provided the specimen does not show any buckling (which is not the case in this test). Also, other specimens did not show any drop as shown in Figure 5.28. In such cases, the shear strength was approximated as shown by the arrow in Figure 5.28. Also, due to buckling, shear strain could not be measured until failure.

A typical shear stress-strain curve is shown in Figure 5.28 and a pronounced non-linearity is observed. This non-linearity is more pronounced than that observed in stress-strain curves for tension or compression. Test results are summarized in Table 5.8 for specimens with fibers (in both CFC and PFC) oriented either at 0^o or 90^o to the shear loading direction, as shown in Figure 5.27. The ASTM standard recommends the determination of shear modulus using a chord in the strain range of 1500 – 5500 με. However, due to pronounced non-linearity beyond 3000 με, the shear modulus was determined from the slope of the curve in Figure 5.28 using a strain range of 0 – 3000 με.

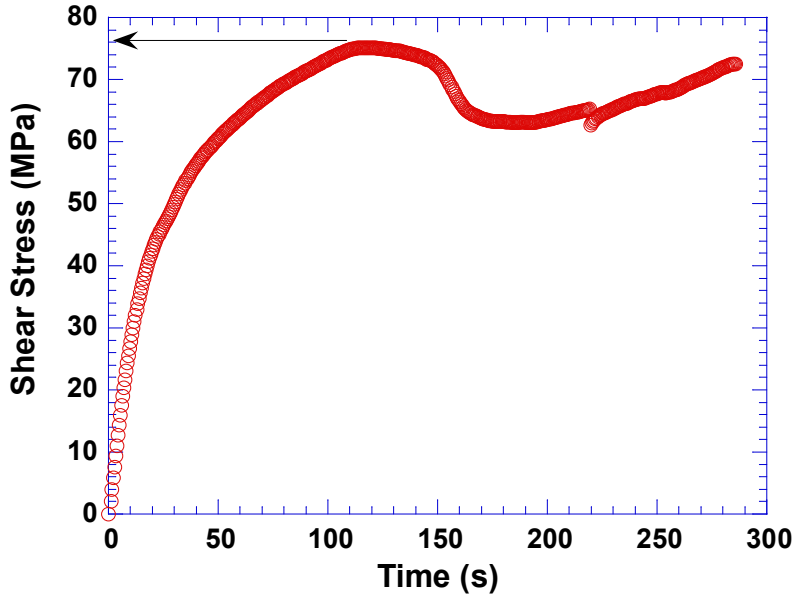

Figure 5.26: Typical shear stress versus time curve for v-notched shear specimen

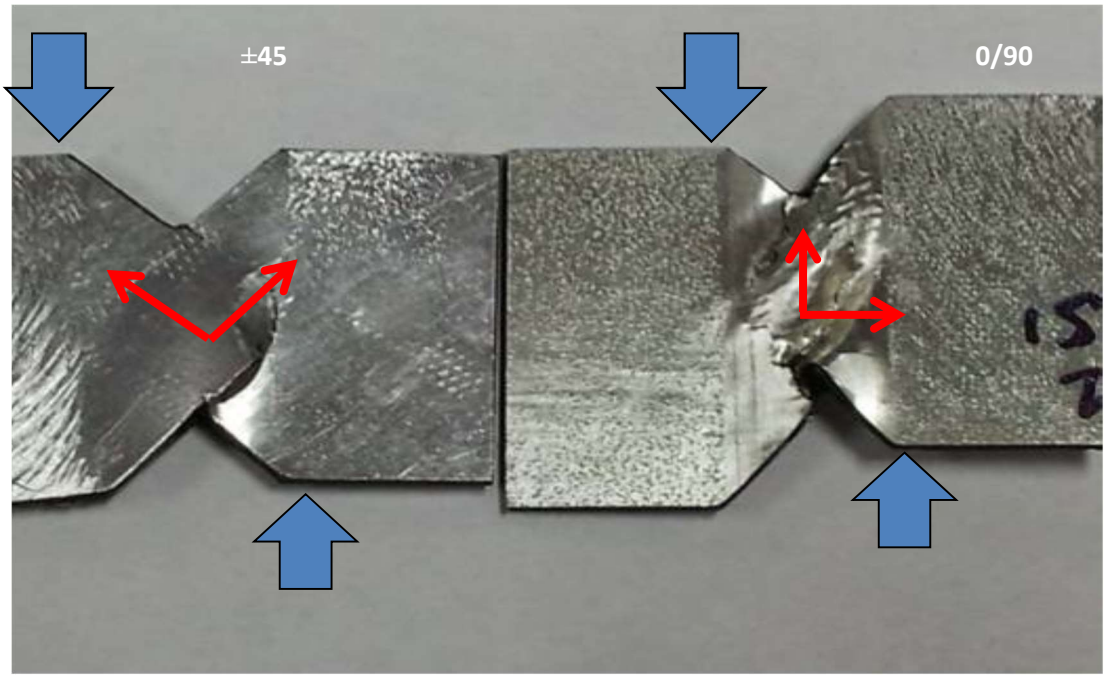

Figure 5.27: Images of test coupons after testing under in-plane shear loading

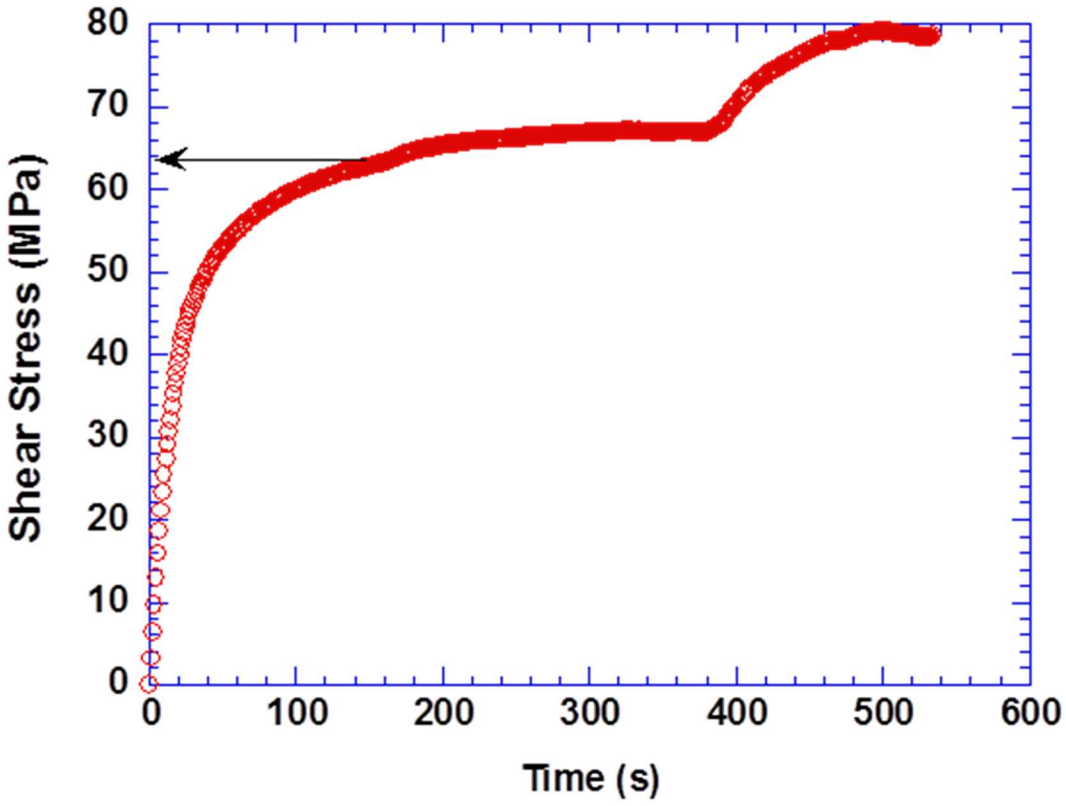

Figure 5.28: Shear stress – test time plot showing no load drop at the initiation of shear failure

Table 5.8: Average shear modulus and shear strength of hybrid composite and Al 6061

Test Specimen	Shear Modulus (GPa) (0-3000με)	Shear strength (MPa)
Hybrid composite [0°/90°]	4.4 ±0.3	27.2±4.6
Hybrid composite [+45°/-45°]	26.3 ±1.4	59.7±15
Al 6061	27.58±2.1	257±26

The average shear modulus of 4.4 GPa is less than that (27.58 GPa) for Al 6061, by 84%. Due to relatively higher volume fraction, both CFC and PFC contribute more to the shear modulus than the Al layers. The shear modulus of PFC is usually low due to poor shear modulus of UHMWPE fibers. Hence, the CFC is the main contributor to the measured shear modulus. However, since the carbon fibers (as well as UHMWPE fibers) are oriented at 0^0 and 90^o to the loading axis (see Figure 5.27), the magnitude of shear load shared by these fibers is low and hence, the measured modulus is mainly due to contribution from the matrix (epoxy in CFC and polyethylene in PFC).

The shear modulus could be improved if the fibers are oriented at 45^0 to the loading direction. New test coupons with fibers oriented at $\pm 45^o$ to the loading direction (see Figure 5.27) were manufactured and tested. A representative shear stress-strain curve is compared in Figure 5.29 with that for $0^o/90^o$ fiber orientation and the results are summarized in Table 5.8. As expected, the new fiber orientation increases the shear modulus substantially.

The average shear modulus of the specimens with $\pm 45^o$ fiber orientation is 26.3 GPa, which is less than the stipulated shear modulus by 4.6%.

The shear strength of the specimens with $0^o/90^o$ fiber orientation is 69.2 MPa, which is lower than the shear strength (257.8 MPa) of Al-6061. Lack of accuracy in the determination of shear strength is believed to be one reason for this difference. Out-of-plane buckling of the layers, as observed in Figure 5.25, is believed to be the second contributor to the low shear strength. A third contributor is the low shear strength of PFC. It should be noted that the shear strength of Al 1100 used in this study is lower than the shear strength of Al 6061 used in identifying the value of 257.8 MPa. Further study is required to improve the shear strength.

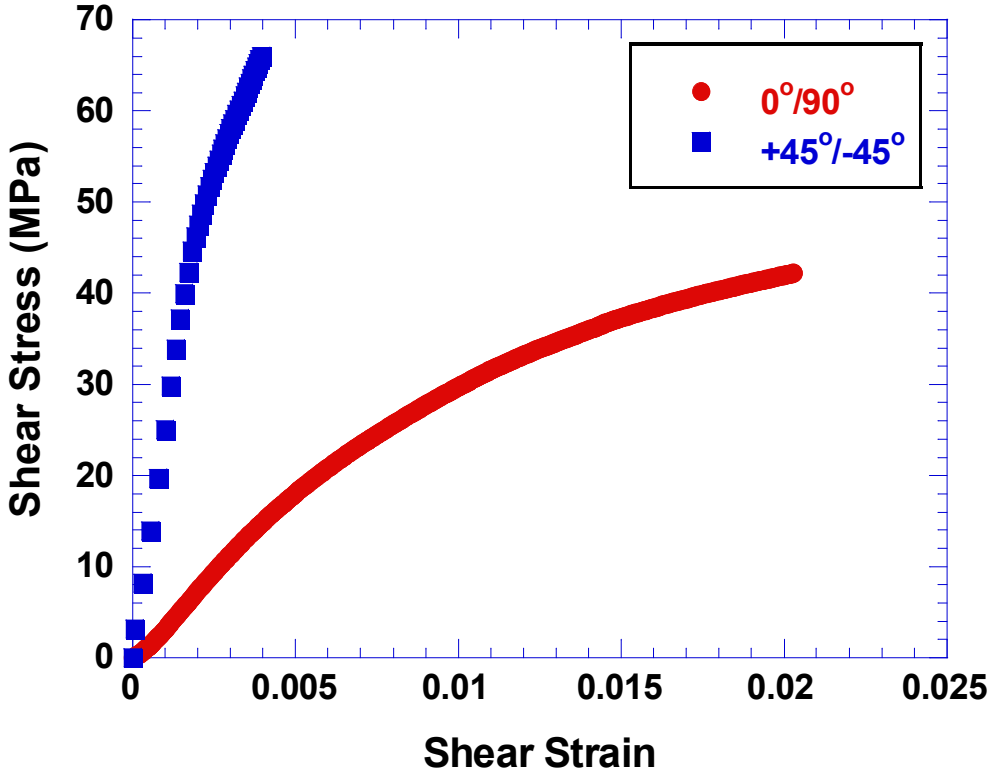

Figure 5.29: Shear stress- strain curve for hybrid composite with $[0/90]_s$ and $[+45°/-45°]_s$ configuration

Re-orienting the fibers from 0º/90º to ±45º changes the failure mode; no buckling is observed as shown in Figure 5.27. However, no improvement in shear strength is observed. Further study is required.

5.2.4 Flexural Test Results

Flexural testing of the hybrid composite was completed as per ASTM C393. All test coupons were tested using a span length of 96 mm (Span length / Thickness = 32) and the total length of the samples was 139.7 mm (5.5 in). A typical flexural stress-time plot for both "as manufactured" and thermally cycled specimens is provided in Figure 5.30. The drop in stress in multiple steps corresponds to sequential development of multiple damage modes.

The flexural strength of "as manufactured" specimens are tabulated in Table 5.9. The average flexural strength is 585 MPa. The failure is always on the compression side and the high value recorded for the flexural strength implies that the compressive strength recorded during compression testing may not be the actual compressive strength.

The flexural strength of coupons subjected to thermal cycling is also tabulated in Table 5.9. The average value of 531 MPa is lower than the value of 585 MPa in Table 5.9 by 9.2%. Further study is required to confirm if this apparent reduction is due to thermal cycling.

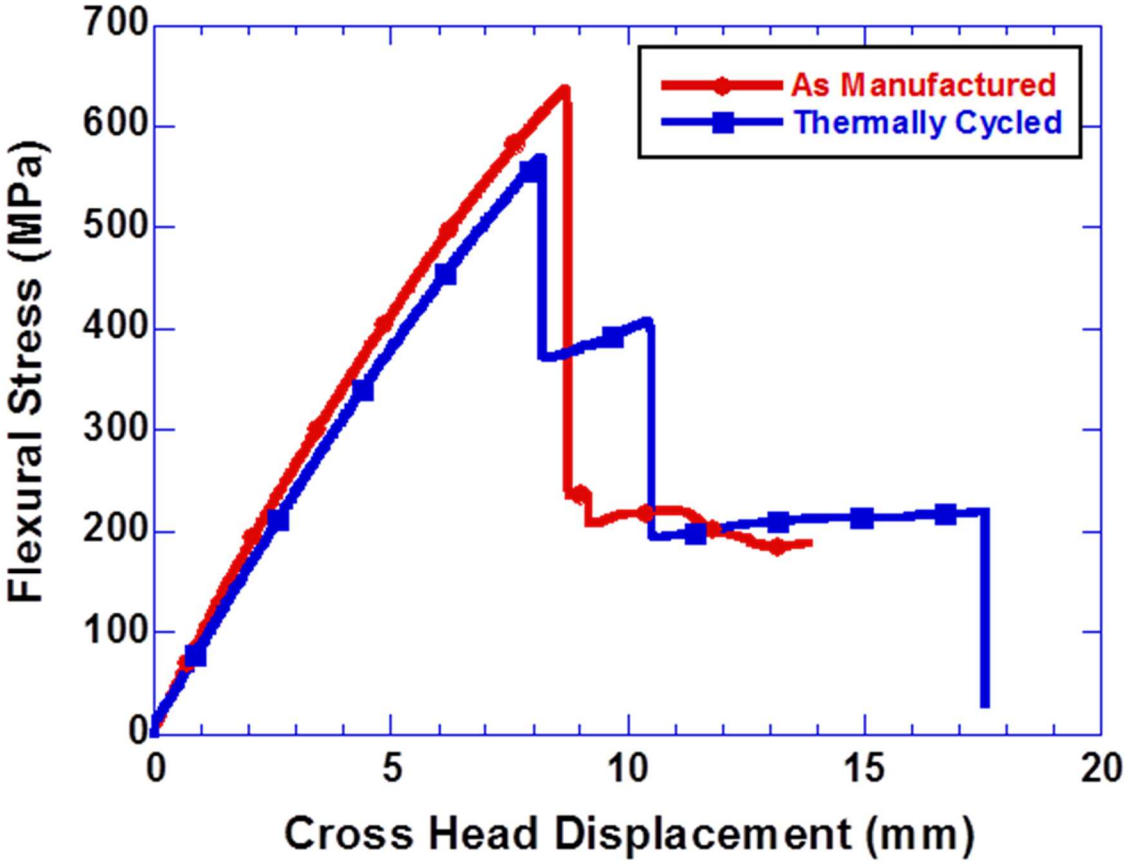

Figure 5.30: Typical flexural stress-time plot for both "as manufactured" and thermally cycled specimens

Table 5.9: Average flexural strengths of as-manufactured and thermally cycled hybrid composite

Test Specimen	Average Flexural Strength (MPa)
As-manufactured Sample	585±28
Thermal Cycled Sample	531±41

5.2.5 Flatwise Tensile Test Results

The strength of the bond between the hybrid composite face sheet and the Al honeycomb core of the hybrid composite sandwich panel was measured at room temperature (25°C) using the flatwise tensile test and the results are tabulated in Table 5.10.

The average value of thermal cycled sample is lower than the "as manufactured sample by value of 5.43 MPa. Instead of separation of the face sheet from the core, the CFC layer delaminated from the PFC layers and this is believed to be the lower recorded value. This delamination was also the cause for lower tensile and compressive strengths. Hence, further effort is required to improve the bonding between the CFC and the PFC layers. After thermal cycling of the samples, no physical damage was observed upon visual examination and under optical microscope. The average value of the flatwise tensile strength remains fairly the same as manufactured sample.

5.2.6 Summary of Mechanical Test Results

The mechanical properties of the hybrid composite, presented in the above sections, are summarized in Table 5.11. The corresponding values for the currently used Al 6061, which the hybrid composite has been designed to replace, is also included in the table. Suggestions to improve the properties are provided as remarks.

In summary, the results presented in this chapter demonstrate that the hybrid composite radiation shield designed in Chapter-4 meets the radiation and structural requirements, thus validate the design.

Table 5.10: Average flatwise tensile strength of as-manufactured and thermally cycled honeycomb sandwich structure based on hybrid composite face sheet

Test Specimen	Average Flatwise Tensile Strength (MPa)
As-manufactured Sample	277.1 ±65.8
Thermal Cycled Sample	262.3±23.8

Table 5.11: Summary of the mechanical properties of the hybrid composite

Property		Al 6061	Experimental for DFC	Remarks
Tensile Modulus (GPa)	Chord	68.9	$44.2^{+1.5}_{-1.1}$ Std. Dev. = 1.1 COV = 2.5%	Likely to meet the requirement if high modulus graphite fibers (IM7) are used
	Slope		$45.7^{+0.9}_{-1.5}$ Std. Dev. = 1.5 COV (Coefficient of Variation) = 3.3%	
Tensile Strength (MPa)	Longitudinal	406.78	$550.2^{+34.8}_{-39.2}$ Std. Dev. = 27.3 COV = 5.0%	Meets the requirement and can be improved if the bonding between the CFC and PFC is improved
Compressive Modulus (GPa)	Chord	70	$38.9^{+1.6}_{-2.3}$ Std. Dev. = 1.8 COV = 4.6%	Likely to meet the requirement if high modulus graphite fibers [IM7] are used and the bonding between the CFC and PFC is improved.
	Slope		$39.9^{+1.6}_{-1.6}$ Std. Dev. = 1.4 COV = 3.5%	
Compressive Strength (MPa)	Longitudinal	406.78	$220.4^{+13.3}_{-10.2}$ Std. Dev. = 9.1 COV = 4.1%	Low strength due to premature failure; flexural test results suggest that this requirement is met; can be improved if the bonding between the CFC and PFC is improved
In-plane Shear Modulus (GPa)	Slope $0^o/90^o$	27.58	$4.4^{+0.3}_{-0.3}$ Std. dev. = 0.3 COV =6.8%	
	Slope ($\pm 45^o$)		$26.3^{+1.4}_{-1.4}$	Upper limit meets the requirement; likely to increase if high modulus graphite fibers [IM7] are used

In-plane Shear Strength (MPa)	0º/90º	257.79	75.1	May be able to improve the strength if high modulus graphite fibers [IM7] are used
	±45º		$59.7^{+15.4}_{-15.4}$	
Flatwise Tensile Strength (Mpa)		Magellan Aerospace Propriety Value	$277.1^{+98.2}_{-40.2}$ Std. Dev. = 65.8 COV = 23.8%	May be able to improve the strength if the bonding between the CFC and PFC is improved
Thermal Cycling	Flexural Strength (MPa)- no Cycling	None	585^{+52}_{-27} Std. Dev. = 28 COV = 4.8%	Confirms that compressive strength is ~585 MPa
	Flexural Strength (MPa) – Thermal cycled	None	531^{+39}_{-56} Std. Dev. = 41 COV = 7.7%	Requires further study to confirm the marginal degradation
	Flatwise Tensile Strength (psi) – Thermally Cycled	None	258	Requires further study to confirm if there is degradation

CHAPTER SIX

CONCLUSION

Satellite missions in HEOs such as Molniya encounter harsh radiation environment and require adequate radiation shielding to protect the satellite electronics and satellite bus. Traditionally used Al would result in heavy shields adding to the cost of launch and mission. Therefore, an alternate light weight shield is required and is not currently available. Moreover, there is no published research on the methodology for the design of radiation shields. Hence, this thesis set out to address knowledge gaps with three specific objectives as stated in 2.4.

6.1 Summary

The tasks that were completed to realize the thesis objectives are as follows:

a. A methodology, for designing a radiation shield that meets both radiation shielding ($TID_{Critical,Transmitted}$ and $TID_{Critical,Absorbed}$) and mechanical property requirements, was developed.
b. Using ESA's SPENVIS, the radiation environment in HEOs for a 15-year was determined.
c. Using (a), (b), and MULASSIS, comparative evaluation of radiation shielding of homogenous materials, polymer composites made up of 2 or more materials, and hybrid composites made-up of polymer composites and homogenous materials was done. In addition, effect of structure of the composites and hybrid composites on radiation shielding was studied. These simulation studies yielded eight hybrid compositions, made up of three constituents namely Al, PFC, and CFC, as possible candidates for the radiation shield.

d. Using lamination theory, the mechanical properties of these eight compositions were evaluated to arrive at two hybrid composites that met the requirements on mechanical property: $Al^{1.5\%}/ ([CFC/ PFC]_{4s})^{67\%/30\%}/Al^{1.5\%}$ and $Al^{2.5\%}/ ([CFC/ PFC]_{4s})^{65\%/30\%}/Al^{2.5\%}$.

e. A two-step manufacturing process was developed to manufacture a hybrid composite with a composition within the range of the two compositions identified in (d). The final composition of the manufactured multifunctional hybrid composite is $[Al/(CFC_2/PFC)_2 CFC_{1/2}]_s$.

f. Using the proton beam at TRIUMF (UBC Campus, BC) and the electron beam at Acsion Inc. (Pinawa, MB), the TID under electrons and t_{WET} (equivalent to TID) under protons were measured for the three constituents (Al, PFC, and CFC) of the hybrid composite and compared with the simulated values to validate MULASSIS.

g. The TID and t_{WET} for the hybrid composite as well as hybrid sandwich composite was experimentally measured and compared with those of Al face sheet and Al sandwich composite to evaluate the relative merits of the former when compared to the latter.

h. Finally, the mechanically properties of the hybrid composite were measured and compared with the published values of Al 6061 to evaluate the relative merits of the former.

Based on the results from the above tasks, presented and discussed in Chapters 3 and 5, the following can be concluded.

- The predictions of MULASSIS correlate very well (within 6% for protons and 2% for electrons for shields with thickness < 6.4 mm) with experimental results, validating the software used in this thesis.

- Low Z polyethylene yields the least shield weight while meeting the radiation shielding criterion, $TID_{Critical,Transmitted}$, when compared to Al in all three HEOs investigated in this study.
- Hybridization of this PE with Al foil is required to meet the second radiation criterion, $TID_{Critical,Absorbed}$.
  - Reinforcement of PE as well as addition of CFC is required to meet the requirements on mechanical properties.
  - Thus, a hybrid composite consisting of AL, PFC, and CFC is required to meet both radiation and mechanical property requirements.
  - The volume fraction and lay-up sequence of these layers influence the radiation shielding of the hybrid composites significantly.
  - The final hybrid composite design for the 15-year mission in Molniya ($[Al/(CFC_2/PFC)_2CFC_{1/2}]_s$) is 13% lighter than Al while meeting the requirements on radiation shielding and mechanical properties.
  - The two-step manufacturing process, developed in this thesis, was able to successfully manufacture the designed hybrid composite, ($[Al/(CFC_2/PFC)_2CFC_{1/2}]_s$).
  - Based on the experimental radiation test results, this hybrid composite and its sandwich version were found to be lighter than Al shield by a maximum of ~19.4% under protons and by ~5.6% under electrons.
  - Experimentally measured mechanical properties of the hybrid composite demonstrated that while some properties were comparable or better than Al 6061, others could be improved through appropriate choice of another carbon fiber composite constituent.

- The above results also clearly demonstrate that the designed hybrid composite face sheet and its sandwich panel version have a better radiation shielding efficiency than currently used Al face sheet and Al sandwich panels, which validates the design methodology developed in this thesis.
- Therefore, the three objectives of the thesis stated in 2.4 have been successfully realized.
- The design methodology developed in this thesis can be extended to design radiation shields for deep space missions.

6.2 Original Contributions

To the best knowledge of the author, the following contributions are the first in this area.

- A design methodology to develop radiation shield for a given satellite mission, which can be extended to deep space mission.
- Comparative study of the radiation shielding effectiveness of homogenous and composite materials as well as the effect of structure of the latter on radiation shielding.
- Experimental validation of MULASSIS.
- An experimentally validated multifunctional hybrid composite radiation shield that is lighter than Al shield, for satellite missions in HEO.

6.3 Recommendations for Future Work

- The MULASSIS software used in this thesis predicts particle transport through materials in 1-D only. In reality, the radiation particle transport through materials will be in 3-D and hence further study using GEANT4 based simulation code like GRAS is

recommended to understand if the prediction in 3-D would improve the accuracy of simulation.

- Validation of MULASSIS software through future experimental radiation tests (both under electron and proton exposure) should consider measuring the dose by using more dosimeters spread across the panel area. Since MULASSIS is limited by the size of the detector, increasing the number of detectors improves the accuracy of the dose measurement and subsequently decreases the maximum observed difference.
- Manufacturing process developed in this thesis is inadequate to ensure complete impregnation of the UHMWPE fiber fabric. Moreover, better bonding between CFC and PFC layers is required to improve the mechanical properties of the hybrid composite. Further research is required to address these issues.
- The use of UHMWPE fiber fabric is manufactured with lower denier tow (than 400 deniers currently used) is recommended in order to allow better impregnation of void spaces between the fibers in a tow by high viscosity PE matrix and subsequently improve the properties of the hybrid composite.
- High modulus carbon fiber composites such as those containing Hexcel IM7 fibers are recommended to improve the modulus of the hybrid composite to the level of Al-6061.
- The effect of long-term exposure to radiation on the mechanical properties of the hybrid composite structure needs to be explored.

REFERENCES

[1] Shin, K., Kim, C., Hong, C. and Lee, H. 2001. Thermal distortion analysis of orbiting solar array including degradation effects of composite materials. *Composites Part B:Engineering*. 32, 4 (2001), 271–285.

[2] Ilcev, S.D. 2010. Highly elliptical orbits (HEO) for high latitudes and polar coverage. *2010 20th International Crimean Conference "Microwave & Telecommunication Technology"* (Sevastopol, Sep. 2010), 396–399.

[3] Joshi, P., Gelb, A., Malonson, M., Lund, E., Green, B., Silverman, E., Segundo, E., Shinn, E. and Long, E. 1999. Light-weight structural materials with integral radiation shielding, thermal control and electronics. *44th International SAMPE Symposium and Exhibition "Envolving and Revolutionary Technologies for the New Millennium"* (Long Beach, CA, 1999).

[4] Maurer, R.H., Fraeman, M.E., Martin, M.N. and Roth, D.R. 2008. Harsh Environments: Space Radiation Environment, Effects, and Mitigation. *Johns Hopkins APL Technical Digest (Applied Physics Laboratory)*. 28, 1 (2008), 17–29.

[5] Heinbockel, J.H., Slaba, T.C., Blattnig, S.R., Tripathi, R.K., Townsend, L.W., Handler, T., Gabriel, T.A., Pinsky, L.S., Reddell, B., Clowdsley, M.S., Singleterry, R.C., Norbury, J.W., Badavi, F.F. and Aghara, S.K. 2011. Comparison of the transport codes HZETRN, HETC and FLUKA for a solar particle event. *Advances in Space Research*. 47, 6 (2011), 1079–1088.

[6] Trishchenko, A.P. and Garand, L. 2011. Spatial and Temporal Sampling of Polar Regions from Two-Satellite System on Molniya Orbit. *Journal of Atmospheric and Oceanic Technology*. 28, 8 (Aug. 2011), 977–992.

[7] Trishchenko, A.P. and Garand, L. 2012. Observing polar regions from space: advantages of a satellite system on a highly elliptical orbit versus a constellation of low Earth polar orbiters. *Canadian Journal of Remote Sensing*. 38, 1 (Jun. 2012), 12–24.

[8] Kroupnik, G. 2011. Polar Communications and Weather (PCW). *Report of the 39th Meeting of the Coordination Group for Meteorological Satellites (CGMS-39), St. Petersburg, Russia. Published and edited for Coordination Group for Meteorological Satellites (CGMS) by CGMS Secretariat, EUMETSAT, Eumetsat Allee 1, D-64295* (St. Petersburg, Russia, 2011).

[9] Mcconnell, J.C., McElroy, C.T., Sioris, C. and Al, E. 2012. PCW/PHEMOSWCA: Quasi-geostationary viewing of the arctic and environs for weather, climate and air quality. *Advances in Atmospheric Science and Applications Conference, ESA ATMOS-2012, Bruges, Belgium, 18– 22nd June, 2012, ©ESA.* (Bruges, Belgium, 2012).

[10] Trishchenko, A.P., Garand, L. and Trichtchenko, L.D. 2011. Three-Apogee 16-h Highly Elliptical Orbit as Optimal Choice for Continuous Meteorological Imaging of Polar Regions. *Journal of Atmospheric and Oceanic Technology*. 28, 11 (Nov. 2011), 1407–1422.

[11] Ilčev, S.D. 2005. *Global mobile satellite communications: For maritime, land and aeronautical applications*. Springer US.

[12] Kaul, R.K., Barghouty, A.F., Penn, B.G. and Hulcher, A.B. 2010. Multi-functional layered structure having structural and radiation shielding attributes. US7855157 B1. 2010.

[13] Sen, S., Schofield, E., O'Dell, J.S., Deka, L. and Pillay, S. 2009. The development of a multifunctional composite material for use in human space exploration beyond low-earth orbit. *Journal of Materials*. 61, 1 (Jan. 2009), 23–31.

[14] Mangeret, R., Carriere, T., Beaucour, J. and Jordan, T.M. 1996. Effects of material and/or

structure on shielding of electronic devices. *IEEE Transactions on Nuclear Science*. 43, 6 (1996), 2665–2670.

[15] Satellite Basics Guide To Satellite-based Solutions - How satellite-based solutions work: 2012. *http://www.intelsat.com/resources/satellite-basics*. Accessed: 2012-01-12.

[16] Banks, B.A., Backus, J.A., Manno, M. V., Waters, D.L., Cameron, K.C. and de Groh, K.K. 2009. Atomic Oxygen Erosion Yield Predictive Tool for Spacecraft Polymers in Low Earth Orbit. *11th International Symposium on Materials in the Space Environment* (Aix en Provence, France, 2009), 10.

[17] ECSS Secretariat 2008. *Space Engineering - Space Environment*. Technical Report ECSS-E-ST-10-04C, ESA-ESTEC Requirements & Standards Division, Noordwijk, The Netherlands.

[18] Barth, J.L., Dyer, C.S. and Stassinopoulos, E.G. 2003. Space, atmospheric, and terrestrial radiation environments. *IEEE Transactions on Nuclear Science*. 50, 3 (2003), 466–482.

[19] Claflin, E.S. and White, R.S. 1974. A study of equatorial inner belt protons from 2 to 200 MeV. *Journal of Geophysical Research*. 79, 7 (1974), 959–965.

[20] Benton, E.R. and Benton, E. V 2001. Space radiation dosimetry in low-Earth orbit and beyond. *Nuclear Instruments and Methods in Physics Research Section B: Beam Interactions with Materials and Atoms*. 184, 1 (2001), 255–294.

[21] Sawyer, D.M. and Vette, J.I. 1976. AP-8 trapped proton environment for solar maximum and solar minimum. *NASA STIRecon Technical Report NSSDC/WDC-A-R/S-76-06* (Greenbelt, Md., 1976).

[22] Vette, J.I. 1991. The AE-8 trapped electron model environment. *NASA STI/Recon Technical Report*. 92, (1991), 24228.

[23] Mazur, J.E., Fennell, J.F. and OBrien, P. 2008. The space environment and its effects on space systems. *Proceeding of 31st Annual AAS Rocky Mountain Guidance & Control Conference* (Breckenridge, CO, 2008), 219 – 230.

[24] Dyer, C. 1998. Space radiation environment dosimetry. *IEEE NSREC Short Course* (Newport Beach, CA, 1998).

[25] Johnston, A. 2000. Radiation damage of electronic and optoelectronic devices in space. *Presented at 4th International Workshop on Radiation Effects on Semiconductor Devices for Space Application* (Tsukuba, Japan, 2000), 1–9.

[26] Heynderickx, D., Kruglanski, M., Pierrard, V., Lemaire, J., Looper, M.D., Blake, J.B., Data, S.P.E.T., Heynderickxl, D., Piercard, V. and Lemairel, J. 1999. A low altitude trapped proton model for solar minimum conditions based on SAMPEX/PET data. *IEEE Transactions on Nuclear Science*. 46, 6 (1999), 1475–1480.

[27] Feynman, J. and Spitale, G. 1993. Interplanetary proton fluence model: JPL 1991. *Journal of Geophysical Research*. 98, 92 (1993), 13281–13294.

[28] Xapsos, M.A., Summers, G.P., Burke, E.A., Barth, J.L. and Stassinopoulos, E.G. 1999. Probability model for worst case solar proton event fluences. *IEEE Transactions on Nuclear Science*. 46, 6 (1999), 1481–1485.

[29] Xapsos, M.A., Summers, G.P., Barth, J.L., Stassinopoulos, E.G. and Burke, E.A. 1999. Probability model for cumulative solar proton event fluences. *1999 Fifth European Conference on Radiation and Its Effects on Components and Systems. RADECS 99 (Cat. No.99TH8471)*. August 1972 (1999), 22–26.

[30] Buhler, C.R. 2005. Analysis of a Lunar Base Electrostatic Radiation Shield Concept. Phase I NASA Technicall Report NIAC CP 04-01 by ASRC Aerospace KSC.

[31] Nymmik, R.A., Panasyuk, M.I., Pervaja, T.I. and Suslov, A.A. 1992. A model of galactic cosmic ray fluxes. *International Journal of Radiation Applications and Instrumentation. Part*. 20, 3 (1992), 427–429.

[32] International Standard Organization (ISO) 2004. Space environment (natural and artificial) – Galactic cosmic ray model. ISO 15390.

[33] Battiston, R., Burger, W.J., Calvelli, V., Musenich, R., Choutko, V., Datskov, V.I., Torre, A. Della, Venditti, F. and Hovland, S. ARSSEM Active Radiation Shield for Space Exploration Missions Active Radiation Shield for Space Exploration Missions.

[34] NASA 1996. Space Radiation Effects on Electronic Components in Low-Earth Orbit. *NASA Technical Publication No. PD-ED-1258*. April (1996), 1–7.

[35] Attix, F.H. 1986. *Introduction to radiological physics and radiation dosimetry*. John Wiley and Sons, Inc.

[36] Dressendorfer, P. V 1998. Basic mechanisms for the new millennium. *IEEE nuclear and space radiation effects conference* (Newport Beach, CA, 1998).

[37] Krane, K.S. and Halliday, D. 1988. *Introductory nuclear physics*. Wiley New York.

[38] Nambiar, S. and Yeow, J.T.W. 2012. Polymer-composite materials for radiation protection. *ACS Applied Materials and Interfaces*. 4, 11 (2012), 5717–5726.

[39] Kim, M.-H.Y., Hu, S., Nounu, H.N. and Cucinotta, F.A. 2010. Overview of Graphical User Interface for ARRBOD (Acute Radiation Risk and BRYNTRN Organ Dose Projection). *38th Committee on Space Research (COSPAR) Scientific Assembly Conference* (Bremen; Germany, 2010), 30–31.

[40] Heinbockel, J.H., Slaba, T.C., Tripathi, R.K., Blattnig, S.R., Norbury, J.W., Badavi, F.F., Townsend, L.W., Handler, T., Gabriel, T.A., Pinsky, L.S., Reddell, B. and Aumann, A.R.

2011. Comparison of the transport codes HZETRN, HETC and FLUKA for galactic cosmic rays. *Advances in Space Research*. 47, 6 (2011), 1089–1105.

[41] Brown, F. Fundamentals of Monte Carlo particle transport: *https://laws.lanl.gov/vhosts/mcnp.lanl.gov/pdf_files/la-ur-05-4983.pdf*. Accessed: 2014-08-01.

[42] Dunn, W.L. and Shultis, J.K. 2012. *Exploring Monte Carlo Methods*. Elsevier, Academic Press, Burlington, MA.

[43] Seltzer, S.M. 1979. Electron, Electron-Bremsstrahlung and Proton Depth-Dose Data for Space-Shielding Applications. *IEEE Transactions on Nuclear Science*. 26, 6 (1979), 4896–4904.

[44] Agostinelli, S. et al. 2003. GEANT4 - A simulation toolkit. *Nuclear Instruments and Methods in Physics Research, Section A: Accelerators, Spectrometers, Detectors and Associated Equipment*. 506, 3 (Jul. 2003), 250–303.

[45] Allison, J. et al. 2006. Geant4 Developments and Applications. *IEEE Transactions on Nuclear Science*. 53, 1 (2006), 270–278.

[46] Ziegler, J.F., Ziegler, M.D. and Biersack, J.P. 2010. SRIM - The stopping and range of ions in matter (2010). *Nuclear Instruments and Methods in Physics Research, Section B: Beam Interactions with Materials and Atoms*. 268, 11–12 (2010), 1818–1823.

[47] ECSS Secretariat 1999. *Thermal cycling test for the screening of space materials and processes*. Technical Report ECSS-Q-70-40A, ESA-ESTEC Requirements & Standards Division, Noordwijk, The Netherlands.

[48] Willis, P. and Hsieh, C.H. 1999. Space Applications of Polymeric Materials. *Proceedings of Society of Polymer Science* (Kobunshi, Japan, 1999).

[49] ECSS Secretariat 2008. *Space product assurance, thermal vacuum outgassing test for the screening of space materials*. Technical Report ECSS-Q-ST-70-02C, ESA-ESTEC Requirements & Standards Division, Noordwijk, The Netherlands.

[50] ECSS Secretariat 2004. *Space product assurance, Data for selection of space materials and processes*. Technical Report ECSS-Q-70-71A Rev. 1, ESA-ESTEC Requirements & Standards Division, Noordwijk, The Netherlands.

[51] Anonymous 2014. *Payload test requirements*. NASA Technical Documents, NASA-STD-7002A.

[52] Czepiela, S.A., McManus, H. and Hastings, D. 2000. Charging of composites in the space environment. *Journal of Spacecraft and Rockets*. 37, 5 (2000), 556–560.

[53] Bogorad, A.L., Likar, J.J. and Herschitz, R. 2007. Charging of composites in space environment: Ground test data. *IEEE Transactions on Nuclear Science*. 54, 6 (Dec. 2007), 1981–1984.

[54] NASA 2011. *Mitigating In-Space Charging Effects —A Guideline*. Technical Report #NASA-HDBK-4002A, NASA Technical Handbook.

[55] Abusafieh, A., Trembly, G., Krumweide, G., Marks, J. and Roske, S. 1999. Development of lightweight radiation shielding composite for electronic enclosures. *44th International SAMPE Symposium and Exhibition (Proceedings)* (1999), 489 – 495.

[56] Brander, T., Gantois, K., Katajisto, H. and Wallin, M. 2005. CFRP electronics housing for a satellite. *European Conference on Spacecraft Structures, Materials and Mechanical Testing* (2005), 753–762.

[57] García, F., Kurvinen, K., Brander, T., Orava, R., Heino, J., Virtanen, A., Kettunen, H. and Tenhunen, M. 2008. Radiation shielding study of Advanced Data and Power Management

Systems (ADPMS) housing using geant4. *IEEE Transactions on Nuclear Science*. 55, 1 (2008), 644–648.

[58] Atwell, W. 2006. Radiation shielding analysis for various materials in the extreme Jovian environment. *Materials Research Society Symposium Proceedings* (San Francisco, CA, 2006), 3–14.

[59] Zhou, J., Moore, J., Calvin, V., Wilkins, R., Vilarino, S.M., Zhong, Y., Gersey, B. and Thibeault, S. 2011. Effects of Extreme Radiation Environment on Composite Materials. *Materials Research Society Proceedings*. 929, (2011).

[60] NASA 1970. *Nuclear and space radiation effects on materials, NASA Space Vehicle Design Criteria- (Structures) - SP-8053*.

[61] Grossman, E. and Gouzman, I. 2003. Space environment effects on polymers in low earth orbit. *Nuclear Instruments and Methods in Physics Research, Section B: Beam Interactions with Materials and Atoms* (2003), 48–57.

[62] Milkovich, S.M., Herakovich, C.T. and Sykes, G.F. 1986. Space Radiation Effects on the Thermo-Mechanical Behavior of Graphite-Epoxy Composites. *Journal of Composite Materials*. 20, (1986), 579–593.

[63] Egusa, S. 1991. Radiation resistance of polymer composites at 77 K: effects of reinforcing fabric type, specimen thickness, radiation type and irradiation atmosphere. *Cryogenics*. 31, 1 (1991), 7–15.

[64] Chaturvedi, S.K. and Chao, C.P. 1995. Thermoelastic constitutive modeling of irradiated polymer composites with matrix property change and fiber/matrix debonding. *Composites Science and Technology*. 54, 2 (1995), 201–210.

[65] Kumar, B.G., Singh, R.P. and Nakamura, T. 2002. Degradation of Carbon Fiber-Reinforced

Epoxy Composites by Ultraviolet Radiation and Condensation. *Journal of Composite Materials*. 36, 24 (2002), 2713–2733.

[66] Hansen, F. DTU Satellite Systems and Design Course Space Environment: *http://www.dsri.dk/roemer/pub/Cubesat*. Accessed: 2013-02-01.

[67] Romeo, R.C., Martin, R.N., Restaino, S.R., Wilcox, C.C., Andrews, J.R., Martinez, T., Santiago, F., Clark, J., Walton, J., Teare, S.W. and Payne, D.M. 2007. Ultra-lightweight , Deployable 1m-Class Optical Telescope for SSA Applications. *Maui Optical and Space Surveillance Technologies Conference* (Maui, Hawaii, 2007), 767–772.

[68] Long, D. 2010. Multifunctional radiation-hardened laminate. US Patents US8460777 B2. 2010.

[69] Heynderickx, D., Quaghebeur, B., Fontaine, B., Glover, A., Carey, W.C. and Daly, E.J. 1998. New features of ESA's space environment information system (SPENVIS). *Proceedings of ESA Workshop on Space Weather - ESA WPP-155* (Noordwijk, Netherlands, 1998), 245–248.

[70] Heynderickx, D., Quaghebeur, B., Wera, J., Daly, E.J. and Evans, H.D.R. 2004. New radiation environment and effects models in the European Space Agency's Space Environment Information System (SPENVIS). *Space Weather-the International Journal of Research and Applications*. 2, 10 (2004), 2–5.

[71] Aluminum 6061 – T6 Technical Data Sheet: *http://www2.glemco.com/pdf/NEW_MARTERIAL_LIST/Alumina 6061-T6.pdf*. Accessed: 2017-01-23.

[72] Kiefer, R.L. 2011. *Polymeric materials with additives for durability and radiation shielding in space*. NASA Technical Report- NNL06AA18A.

[73] Kaul, R.K., Barghouty, a F. and Dahche, H.M. 2004. Space radiation transport properties of polyethylene-based composites. *Annals of the New York Academy of Sciences*. 1027, (Nov. 2004), 138–149.

[74] Abusafieh, A., Trembly, G., Krumweide, G., Marks, J. and Roske, S. 1999. The development of lightweight radiation shielding for electronic enclosures. *44th International SAMPLE Symposium and Exhibition* (Long Beach, California, 1999).

[75] Lei, F., Truscott, P.R., Dyer, C.S., Quaghebeur, B., Heynderickx, D., Nieminen, P., Evans, H. and Daly, E. 2002. MULASSIS: A Geant4-based multilayered shielding simulation tool. *IEEE Transactions on Nuclear Science* (2002), 2788–2793.

[76] Fan, C., Drumm, C.R., Stanley, B. and Scrivner, G.J. 1996. Shielding considerations for satellite microelectronics. *IEEE Transactions on Nuclear Science*. 43, 6 (1996), 2790–2796.

[77] NRC (National Research Council) 2008. *Managing Space Radiation Risk in the New Era of Space Exploration*. The National Academies Press, Washington, D.C.

[78] Swolfs, Y., Crauwels, L., Breda, E. Van, Gorbatikh, L., Hine, P., Ward, I. and Verpoest, I. 2014. Tensile behaviour of intralayer hybrid composites of carbon fibre and self-reinforced polypropylene. *Composites Part A: Applied Science and Manufacturing*. 59, (2014), 78–84.

[79] Peijs, A.A.J.M. and de Kok, J.M.M. 1993. Hybrid composites based on polyethylene and carbon fibres. Part 6: tensile and fatigue behaviour. *Composites*. 24, 1 (1993), 19–32.

[80] Jones, R.M. 1999. *Mechanics of composite materials*. Taylor & Francis, Philadelphia, PA.

[81] Alcock, B., Cabrera, N.O., Barkoula, N.M., Loos, J. and Peijs, T. 2006. The mechanical properties of unidirectional all-polypropylene composites. *Composites Part A: Applied Science and Manufacturing*. 37, 5 (May 2006), 716–726.

[82] Alcock, B. and Peijs, A.J.M. 2013. Technology and development of self-reinforced polymer

composites. *Advances in Polymer Science*. 251, 1 (2013), 1–76.

[83] Emmanuel, A., Raghavan, J., Harris, R. and Ferguson, P. 2014. A comparison of radiation shielding effectiveness of materials for highly elliptical orbits. *Advances in Space Research*. 53, 7 (Apr. 2014), 1143–1152.

[84] Blackmore, E.W. 2000. Operation of the TRIUMF (20-500 MeV) proton irradiation facility. *2000 IEEE Radiation Effects Data Workshop* (Reno, Nevada, USA, 2000), 1–5.

[85] Ziegler, J.F. 1999. The stopping of energetic light ions in elemental matter. *Journal of Applied Physics*. 85, 3 (1999), 1249–1272.

APPENDIX A

RADIATION SIMULATION PROCEDURE USING AVAILABLE MODELS IN SPENVIS

SPace ENVironment Information System (SPENVIS) is a web based interface to model space environment and its effects. User can have access to all SPENVIS's models via its server at https://www.spenvis.oma.be/intro.php. The current version of SPENVIS, is based on version 4.6.8, released on September 2, 2016. The various steps in radiation environment modelling and particle transport simulation through a shield, using standardized SPENVIS's models, are as follows:

Step 1 – Definition of Orbital Trajectory

The orbital trajectory of a satellite in a particular HEO orbit is defined by inputting the orbital parameters into the orbital generator within SPENVIS. The defined orbital parameters include orbital period, perigee and apogee altitudes of the orbit, angle of inclination and finally, the eccentricity of the orbit, which defines its stability. All these parameters are expressed in Table 1.1 for the 3 HEO's defined for the PCW mission. In addition, the number of mission segments and mission duration (15 years for PCW) or expected date to terminate mission are input into the orbital generator.

Step 2 – Definition of Radiation Environment

The cumulative radiation exposure experienced by a satellite in the orbit defined in Step 1 is simulated using standardized radiation models available in SPENVIS. AP-8 model simulates the trapped proton flux with a minimum threshold exposure flux of 1 #particle/cm^2/s. AE-8 model

simulates the trapped electron flux with a minimum exposure flux of 1 #particle/cm^2/s but with a confident level of 50%, which corresponds to the average model flux. The JPL model is used for simulating the long term solar particle fluence with a confidence level of 90%. The model yield fluences outside the magnetosphere, which is then corrected for magnetic shielding by setting quiet magnetosphere "ON" in all direction. Solar particle fluences are blocked by the planet's magnetic field if present and this agrees well with what is expected for Earth's satellite orbit like HEO. Lastly, the GCRs are simulated using ISO 15390 standard model, the solar activity data is based on mission epoch defined in Step 1 with quiet Earth's magnetic shielding.

A "combined run" button calls up all the above models for consecutive runs, simulating the combined radiation effect of all radiating particles. The outputs of each radiation models (that is, the output fluence for each radiating particle) are provided independently in Comma Separated Values (CSV) format. The output results serve as input for dose analysis in the next step.

Step 3 – Multi-Layered Shielding Simulation (MULASSIS)

MULASSIS, a space radiation analysis tool, can be assessed from SPENVIS website, as one of the web based space environment models developed within SPENVIS. The following steps are used in the simulation:

Step 3.1 – Define Geometry, Number of Layers, Material Composition of the Target Shield and Detector

A planar geometry (with infinite length and width and finite thickness) is defined to represent the shield. The number of layers in the shield and the thickness of each layer are defined. The material composition of each layer is defined based on set of pre-defined materials included in MULASSIS material library. In addition, one can also input user-defined material by inputting the chemical

composition and mass density (areal density) of the material for a chosen layer. The detector is defined as additional planar layer behind the target shield with a composition of Si or SiO_2.

Step 3.2 – Specify the Source Particle Type and Energy Spectrum

The radiation environment is selected based on the source, which can be either "mission spectrum" or "user defined". When "mission spectrum" is selected, it automatically inputs the simulated fluences for HEO orbit analysis in Step 2. While simulating radiation tests using terrestrial facilities, the TID calculation is obtain by making use of "User defined" option is used. The fluence and the energy range cut off for each radiating particle (as encountered in the testing site) are appropriately defined and input.

Step 3.3 – Analysis Parameters and Simulation

The type of output parameter required within each layer is defined under "Analysis Parameters". Simulation is started by clicking "RUN". $TID_{Absorbed}$ and $TID_{Transmitted}$ for each layer with range of error is provided in a formatted Report File and Comma Separated Values (CSV) format.

APPENDIX B

DETERMINATION OF EQUIVALENT CHEMICAL COMPOSITION

The equivalent chemical formula for the CFC layer was determined using following steps:

Step 1: Determine the volume fraction by of each constituent in the CFC layer.

Step 2: Determine the mass fraction of each constituent.

Step 3: Convert fractional mass to equivalent chemical formula.

These steps are explained below:

Step 1:

The CFC is made up of carbon fiber (V_f = 60%) and epoxy matrix (V_f = 40%) as per the material data sheet from the material supplier, Hexcel Corporation. Also, the epoxy was defined to be made up of 50% by volume of Diglycidyl ether of bisphenol-A (DGEBA) with a chemical formula $C_{21}H_{24}O_4$, and 50% by volume of 4,4'diamine-diphenylmetane (DDM) with a chemical formula $C_{13}H_{14}N_2$

Step 2:

The volume fraction of each constituent in the CFC layer, as determined in Step 1, is converted into mass fraction using equation (A1)

$$Mass\ Fraction\ (M) \quad = \frac{V_i \times \rho_i}{\sum_i (V_i \times \rho_i)} \qquad (A1)$$

The mass fractions of the constituents of CFC composition, obtained using Eq. (A1), are tabulated in Table A1. Similarly, the mass fractions of DGEBA and DDM in epoxy are calculated and the values are tabulated in Table A2.

This was followed by obtaining the weighted fraction of each element within the two molecules using Eq. (A2) as shown in Tables A3 and A4.

Table A1: Mass Fraction of CFC

Constituent	Carbon	Epoxy
Symbol	C	$(C_{21}H_{24}O_4) + (C_{13}H_{14}N_2)$
Density (ρ) g/cm^3	1.7	1.2
Volume fraction (V)	0.6	0.4
Mass ($\rho \times V_f$)	1.02	0.48
Mass fraction (M)	$W_c = 0.68$	$W_e = 0.32$

Table A2: Mass Fractions of Constituents of Epoxy

Constituent	DGEBA	DDM
Symbol	$C_{21}H_{24}O_4$	$C_{13}H_{14}N_2$
Density (ρ) g/cm^3	1.16	1.05
Volume fraction (V)	0.50	0.50
Mass ($\rho \times V_f$)	0.58	0.525
Mass fraction (M)	$W_1 = 0.524886878$	$W_2 = 0.475113122$

Table A3: Mass fractions of elements in DGEBA.

Elemental mass fraction in DGEBA ($C_{21}H_{24}O_4$)				Total
Symbol	C	H	O	
# of Molecules (#M)	21	24	4	
Atomic Mass (A)	12.0107	1.00794	15.9994	29.01804
Mass (A × #M)	252.2247	24.19056	63.9976	340.41286
Elemental mass (m)	0.740938	0.071062	0.188	
Elemental mass fraction (m_1) in W_1 of DGEBA ($m_1 = m \times W_1$)	0.388908	0.0373	0.098679	
Elemental mass fraction (m_2) in W_e of Epoxy ($m_2 = m_1 \times We$)	0.124451	0.011936	0.031577	

Table A4: Mass fractions of elements in DDM.

Elemental mass fraction in DDM ($C_{13}H_{14}N_2$)				Total
Symbol	C	H	N	
# of Molecules (#M)	13	14	2	
Atomic Mass (A)	12.0107	1.00794	14.00674	27.02538
Mass (A × #M)	156.1391	14.11116	28.01348	198.26374
Elemental mass (n)	0.787532	0.071174	0.141294	
Elemental mass fraction (m_1) in W_1 of DGEBA ($m_3 = n \times W_1$)	0.374167	0.033816	0.067131	
Elemental mass fraction (m_2) in W_e of Epoxy ($m_4 = m_3 \times We$)	0.119733	0.010821	0.021482	

$$Elemental\ mass\ fraction\ (m) = \frac{(A_i \times \#M_i)}{\sum_i (A_i \times \#M_i)} \qquad (A2)$$

The mass fraction of C, H and O in DGEBA and the mass fraction of C, H and N in DDM are calculated by multiplying the elemental fraction m and n with W_1 and W_2 respectively, obtained in Tables A2. These values are tabulated in Tables A3 and A4, respectively.

Step 3:

The mass fraction of each element constituent of CFC are added up to obtain the total elemental mass fraction (i.e. sum all C, H, O and N molecules to obtain elemental mass faction). The elemental mass fractions are then normalized with atomic mass to define the equivalent chemical formula for CFC as shown in Table A5.

Table A5: Conversion of mass fraction to equivalent chemical formula.

From Frac. by Mass to Chemical Formula					
Material Name	CFC				
Material Density (ρ)	1.5 g/cm3				Sum (or Minimum)
Symbol	C	H	O	N	1
Total elemental mass fraction ($\sum_i m$)	0.924184	0.022758	0.03008	0.022607	0.001614
Atomic Mass (A)	12.0107	1.00794	15.9994	14.00674	
Elemental mass (B) = ($\sum_i m$)/A	0.076946732	0.022579	0.001881	0.001614	0.001614
Molecular Content = ($\frac{B}{MIN\ B} \times 100$)	4769	1399	116	100	
Chemical Formula	C-4769	H-1399	O-116	N-100	

APPENDIX C

Determination of t_{WET}

The Equations (4.1) and (4.2) discussed in section 4.5.2.1 have been developed by Dr. Blackmore and his colleagues [84] at TRIUMF through a calibration procedure discussed below. Since the BIC/DIC curve in Figure 4.11 is asymptotic beyond the Bragg peak, it is difficult to determine the RS position for which the BIC/DIC value reduces to zero, i.e. complete absorption of the incident radiation. Hence, it is assumed that the BIC/DIC value drops precipitously to zero for range shifter positions greater than that corresponding to RS90% (i.e. complete absorption), where RS90% is the RS position, beyond the Bragg peak, for which the BIC/DIC value is 90% of the peak value. The range shifter position is a unit-less quantity.

A body of water was placed in the path of the beam after the RS (made up of Lucite) and a miniature ion chamber (instead of BIC) immersed in water was used to determine the ion count at a location within the body of water. For a given Lucite thickness in the path of the beam, the position of the miniature ion chamber within water (i.e. thickness of the body of water) for which the ratio of the ion count registered by the miniature ion chamber to that recorded by the DIC was 90%, was recorded and taken to be the $t_{WET,RS90\%}$ for that Lucite thickness. This procedure was repeated for various Lucite thickness values and the relationship between the two was determined to be

$$t_{WET,\,RS90\%} = 1.156 * t_{Lucite,\,RS90\%} \quad \text{mm} \tag{B1}$$

where $t_{Lucite,\ RS90\%}$ is the thickness of the Lucite that was rotated into the path of the beam. The Lucite thickness is related to the RS position as per Eq. (B2) and hence, RS position is recorded during experiment and used along with Eq. (B2) to determine the Lucite thickness required in Eq. (B1).

$$t_{Lucite,\ RS90\%} = (2.23 + 1.0075 * 10^{-2} * RS90\%)\ mm \qquad (B2)$$

2.23 mm in Eq. (B2) corresponds to minimum thickness of the Lucite in the range shifter. At a zero value for RS, no Lucite was in the path of the beam. When the RS position value was increased from zero, Lucite, with a thickness as determined by using Eq. (B2), was rotated into the path of the beam. Eq. (4.1) in section 4.5.2.1 was obtained by combining Eqs (B1) and (B2).

The rationale for Eq. (4.2) presented in section 4.5.2.1 is as follows.

In the presence of only a body of water, 34.15 mm of water is required to completely absorb the incident proton beam with 63± 1 MeV as shown in Figure B1(a). During experimentation, a combination of RS, test panel, and IC cover was used to absorb this energy as shown in Figure B1(b). The IC cover was used to prevent any accidental damage to the BIC while mounting the test panel near the BIC. The $t_{WET,\ IC\ Cover}$ for this has been determined to be ~3.46 mm.

If only RS is used in the path of the beam along with the IC cover in place, 26.55 mm of Lucite with a $t_{WET,\ RS90\%}$ of 30.69 mm (= 34.15 – 3.46) is required to completely absorb the incident proton beam. However, in the current experiment, the test panel was mounted just before the BIC with the IC cover in place. The position of RS was changed to record the ratio of BIC to DIC counts covering the Bragg peak. The total thickness of the material in the path of the beam was

$$t_{total} = t_{\text{Lucite (RS)}} + t_{\text{Test Panel}} + t_{\text{IC Cover}} \quad \text{(B3)}$$

The equivalent water body thickness corresponding to t_{total}, as shown in Figure B1(a), is

$$t_{WATER} = t_{\text{WET, Lucite (RS)}} + t_{\text{WET, Test Panel}} + t_{\text{WET, IC Cover}} \quad \text{(B4)}$$

Hence,

$t_{\text{WET, Test Panel}} = t_{WATER} - t_{\text{WET, RS90\%}} - t_{\text{WET, IC Cover}}$

$= 34.15 – 3.46 - t_{\text{WET, RS90\%}}$

$t_{\text{WET, Test Panel}} = 30.69 - t_{\text{WET, RS90\%}}$ mm, which is Eq. (4.2) identified in section 4.5.1.1.

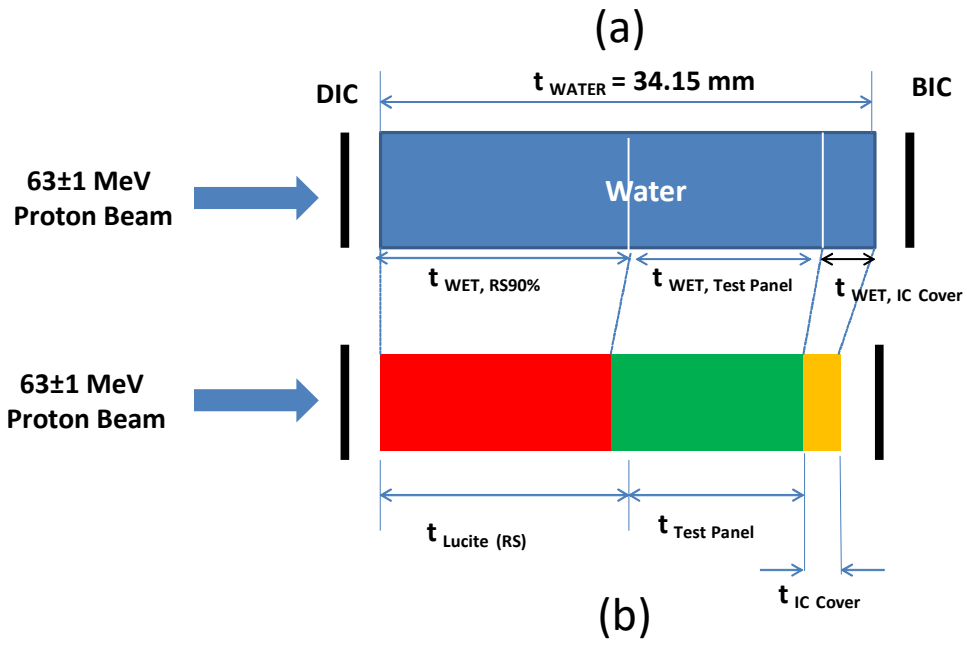

Figure B1: Schematic illustration of (a) Thickness of water to completely absorb the incident proton beam and (b) Thickness of combination of RS, Test Panel, and IC cover to completely absorb the incident proton beam. Equivalent water thickness for RS, Test Panel, and IC Cover are also identified in (a)